HERSCHEL SPACE OBSERVATORY

HERSCHEL EXPLANATORY SUPPLEMENT VOLUME III

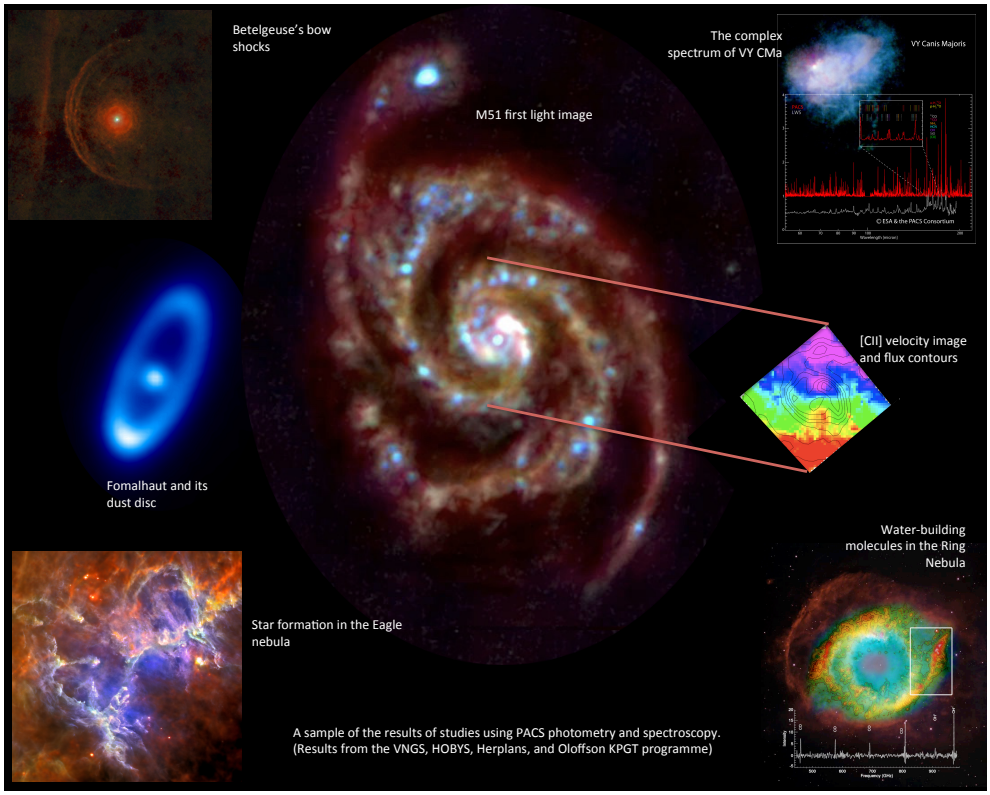

THE PHOTODETECTOR ARRAY CAMERA AND SPECTROMETER (PACS) HANDBOOK

HERSCHEL-HSC-DOC-2101, version 4.0.1, April 30, 2019

PACS Handbook

Version 4.0.1, April 30, 2019

This document is based on inputs from the PACS Consortium and the PACS Instrument Control Centre. The name of this document during the active observing phase of *Herschel* was *PACS Observer's Manual*. This version is the final version of the Handbook, with any subsequent updates being minor.

Document editors and custodians:

Katrina Exter, ESAC, (custodian) with:
Zoltan Balog, MPIA
Luca Calzoletti, ESAC
Ulrich Klaas, MPIA
Dieter Lutz, MPE
Roberta Paladini, NHSC
Elena Puga, ESAC
Pierre Royer, KUL

Contents

Chapter 1

Introduction

1.1 The Observatory

The *Herschel* Space Observatory (Pilbratt et al., 2010) was the fourth cornerstone mission of the ESA science programme. It was aimed at high spatial-resolution observations in the far-IR and sub-millimetre regime; in fact it was the first space observatory to cover this part of the spectrum. It was named after Sir William Herschel, the discoverer of infrared radiation.

Herschel was launched on the May 14th, 2009 aboard an Ariane 5 rocket together with Planck. It was placed on a Lissajous 700,000 km diameter orbit 1.5 million kilometers away from Earth at the second Lagrange point of the Earth–Sun system. The mission ended on April 29th, 2013 when its coolant ran out; the final command on June 17th was to put it into a safe disposal-orbit around the Sun.

The *Herschel* mirror, which was radiatively cooled, had a diameter of 3.5 m, and it was the largest mirror launched at the time. The telescope performed photometry and spectroscopy in the 55–670 μm range with three science instruments – PACS, SPIRE, and HIFI – which were housed inside a superfluid helium cryostat. PACS (Photodetector Array Camera and Spectrometer) provided *Herschel* with capabilities for spectroscopy and broad-band imaging in the 50–210 μm range. A high-level description of the *Herschel* Space Observatory is given in Pilbratt et al. (2010). The first scientific results were presented in the special volume 518 of *Astronomy & Astrophysics* journal.

PACS was designed and built by a consortium of institutes and university departments from across Europe under the leadership of the Principal Investigator Albrecht Poglitsch at Max-Planck-Institute for Extraterrestrial Physics, Garching, Germany. Consortium members came from: Austria: UVIE; Belgium: IMEC, KUL, CSL; France: CEA, OAMP; Germany: MPE, MPIA; Italy: IFSI, OAP/OAT, OAA/CAISMI, LENS, SISSA; Spain: IAC.

1.2 Purpose and Structure of Document

The purpose of this handbook is to provide relevant information about the PACS instrument, to help the reader understand how the instrument was designed, how it worked when observing astronomical targets, and the scientific use that the data can be put to. Chp. 2 is an overview of the instrument design. Chp. 3 is an overview of how the observations were performed and how the observers could

modify their observation requests to suit their needs. Chps **??** and **??** are about the in-flight performance of the photometer and spectrometer parts of PACS, and how there data were affected by this. Chp. 6 is about the astronomical models used for the calibration of photometry and spectroscopy, and the calibration work itself is presented in Chps 7 (photometry) and 8 (spectroscopy). Chp. 9 is about the data-reduction pipelines, and in Chp. 10 is an explanation of the products provided for any observation downloaded from the Herschel Science Archive. Finally, in Chp. 11 source-specific product and analysis advice is given.

1.3 Key PACS publications

For a detailed description of the PACS instrument and its in-flight performances, we refer you to Poglitsch et al. (2010). Links to other important publications and to the wealth of technical notes and publications are given where they are relevant. These can all be found on the *Herschel* Explanatory Legacy Library pages.

1.4 Acknowledgements

This handbook is provided by the *Herschel Science Centre*, based on the PACS Observer's Manual, the extensive user documentation, and a wealth of technical notes written by the PACS Consortium and PACS Instrument Control Centre. A list of people involved in the ICC, too long to include here, can be found on this HCS web-page.

To cite this document, please use: The PACS Handbook, 2017, HERSCHEL-HSC-DOC-2101 v2.0.

1.5 Changes to this document

This is the final version of the PACS Handbook. The performance chapter has been included and the spectroscopy calibration chapter improved. The final advice on use of PACS products has also been added.

1.6 List of Acronyms

AOR	Astronomical Observation Request
AOT	Astronomical Observation Template
APE	Absolute Pointing Error
BOLC	Bolometer Controller
CoP	Commissioning phase
CS	PACS Internal Calibration Source
CB	Calibration Block
CRE	cryogenic amplifier/multiplexer circuit
CUS	Common Uplink System
DECMEC	Detector and Mechanism Controller
DP	Data Processing
DPU	Digital Processing Unit
DTCP	Daily telecommunications period
EEF	Encircled Energy Fraction
EMC	electromagnetic compatibility
ESA	European Space Agency
ESAC	European Space Astronomy Centre, based near Madrid, Spain
FIR	Far Infrared Radiation
FMILT	ILT done on the PACS Flight Model (the actual instrument)
FoV	Field of View
FPU	Focal Plane Unit
FSILT	ILT done on the PACS Flight Spare
FWHM	Full Width Half Maximum
HCSS	Herschel Common Software System
HIFI	Heterodyne Instrument for the Far Infrared
HIPE	*Herschel* Interactive Processing Environment
HK	Housekeeping
HSA	The *Herschel* Science Archive
HSC	The *Herschel Science Centre* (based in ESAC)
HSpot	*Herschel* Observation Planning Tool
IA	Interactive Analysis
ICC	Instrument Control Centre
IFU, IFS	Integral Field Unit, Integral Field Spectroscopy/Spectrograph
ILT	Instrument Level Test (i.e. ground tests of the instrument without the spacecraft)
LSR	Local Standard of Rest
MOC	Mission Operation Centre
NDR	non-destructive read-outs
NEP	Noise-Equivalent Power
OD	Operational Day
OBCP	On-board control procedure
OBSW	On-board software

PACS	Photodetector Array Camera and Spectrometer
PDRG	PACS Data Reduction Guide
PPE	PACS Products Explained
PSF	Point Spread Function
PV	Performance Verification (phase)
RMS	Root Mean Square
RPE	Relative Pointing Error
RSRF	Relative Spectral Response Function
SBP	Standalone Browse Product
SD	Science Demonstration (phase)
SED	Spectral Energy Distribution
SEU	Single Event Upset
SIAM	Spacecraft-instrument alignment matrices
SMCS	Scalable Multichannel Communications Subsystem
SNR, S/N	Signal-to-Noise Ratio
spaxel	A spatial pixel, a pixel of an IFU, containing a full spectrum of its patch of sky
SPG	Standard Product Generation
SPIRE	Spectral and Photometric Imaging Receiver
SPU	Signal Processing Unit
SSO	Solar System Object
TM	Telemetry

Chapter 2

The PACS Instrument

2.1 Introduction

PACS was designed as a general-purpose science instrument for the far-infrared, operating within the wavelength range 51–210 μm. It incorporated two sub-instruments.

1) An imaging dual-band photometer ($\frac{\Delta\lambda}{\lambda}$ <0.5) operating over an instantaenous field of view (FoV) of 3.5′× 1.75′, with full sampling of the telescope point spread function. Bandpass combinations were either 60–85 μm and 125–210 μm (blue/red filter) or 85–125 μm and 125–210 μm (green/red filter).

2) A medium resolution (R $\sim$ 1500) integral-field spectrograph operating between 51 and 210 μm with a velocity resolution of 75–300 km s^{-1} and an instantaneous coverage of $\sim$1500 km s^{-1} over a field of view of 47″×47″.

The scientific rationale for the photometer and spectrometer design are given in Poglitsch et al. (2010), which also provides a good summary of the PACS instrument, capabilities, and observation techniques, with numerous references to relevant work. For a more technical guide to PACS, we refer you to the PACS Instrument Description Documents (IDD I is the easiest to read, II-III contain more technical descriptions of the components of the PACS instruments; all can be found on the *Herschel* PACS Library pages).

2.2 Instrument design overview

PACS consisted of two units (see Fig. 2.1):

1) the cold focal plane unit (FPU) inside the *Herschel* cryostat on the payload module

2) the warm electronic unit on the *Herschel* service module

The units were connected via a harness. The harness consisted of a cold part inside the cryostat vessel and a warm part outside. Care was taken in the arrangement of the warm harness to optimise electromagnetic compatibility (EMC), e.g. interference of the signals on the harness by electrical switching of the solar panels.

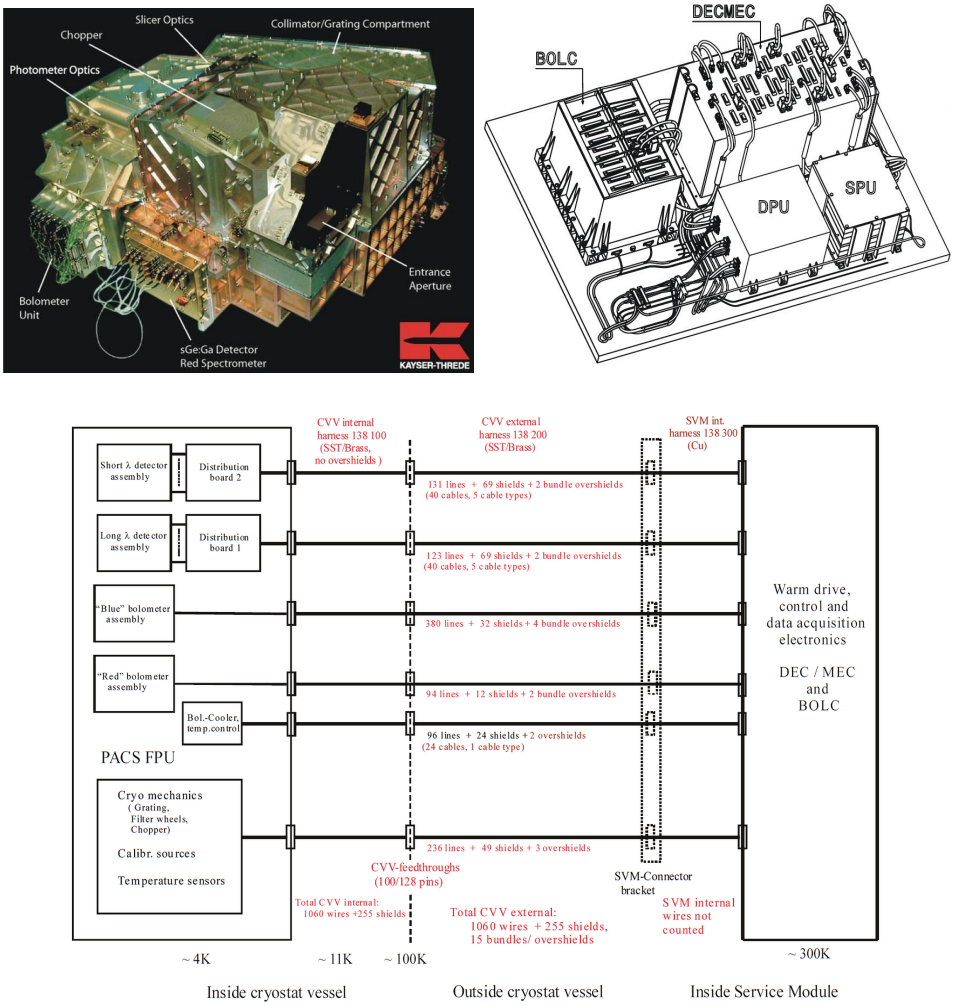

Figure 2.1: The main components of PACS. **Top left**: Cold FPU (T ∼4 K) assembled at Kayser-Threde, Munich, containing the optical elements and the detectors (see Sec. 2.2.2 for details). **Top right**: Warm electronic boxes (T∼300 K) with the on-board CPUs controlling the instrument and receiving engineering and science telemetry. Individual boxes are explained in Sec. 2.2.1. The location of some elements is indicated. **Bottom**: A functional block diagram showing the components of the harness connecting the cold FPU inside the *Herschel* cryostat on the payload module with the warm electronic unit on the satellite service module.

2.2.1 Warm electronics units

The warm electronics unit of PACS had to

1) control the instrument operations

2) execute the data handling

3) provide instrument autonomy for the about 20 h time interval between the Daily Tele-Communication Periods (DTCPs) with the Ground Stations and the Missions Operations Centre (MOC)

These tasks were too voluminous and complex to be handled by a single on-board computer. Therefore, the various functionalities were associated with different sub-units described below. For sub-unit communication the IEEE 1355 (spacewire) interface was adopted as implemented in the Scalable Multichannel Communications Subsystem (SMCS) 332 chip, nominally configured to handle up to 10 Mbit s^{-1}. The warm electronic units were equipped with DSP-21020 microprocessors. Each unit had its own on-board software (OBSW) running under the Virtuoso^{TM} real-time operating system from WindRiver (previously developed by EONIC). DECMEC and SPU RAMs were EDAC (Error Detection And Correction) protected: when the CPU needed to read a memory cell, the content of that cell passed the EDAC unit first. Through the comparison with control bits, EDAC verified the integrity of the content. In case of a Single Event Upset (SEU), EDAC could restore the original content, if only one bit was flipped. The corrected content was transferred to the CPU and written back into the RAM memory cell. Only few EDAC events occurred during the mission. From OD 589 until the end of the *Herschel* mission a special engineering measurement was installed as part of the PACS calibration programme to map affected addresses into configurable Housekeeping as part of long-term trend analysis (see the PACS Routine Calibration Plan sec. 7.4). Details of the OBSW including design, subsystem communications and on-board software update are described in Pezzuto et al. (2012).

2.2.1.1 Digital Processing Unit (DPU)

The DPU was the central PACS on-board computer. It provided the interface of PACS to the satellite and was therefore responsible for receiving and decoding commands either directly from the Missions Operations Centre (mainly for instrument commissioning and contingency recovery) or routinely from the Mission Timeline uplinked in advance and stored on-board. Decoded commands were forwarded to the appropriate subsystems for execution. The DPU monitored the correct execution of all commands and raised error messages in case of a failure. In case of hard limit violations of essential voltage or temperature values, an autonomy function (FDIR = Failure Detection, Isolation and Recovery) was triggered setting the instrument into a safe configuration (Pezzuto et al., 2012). By daily checking of the event log, the MOC staff could recognise quite early on in the DTCP if there was an instrument contingency, and arrange for recovery.

In the opposite data flow direction, all housekeeping and compressed science data from the various subsystems of PACS were collected, formatted into telemetry packets and sent to the satellite mass memory. For details, please refer to the DPU On-board Software User Manual.

2.2.1.2 DEtector and MEchanisms Controler (DECMEC)

The DECMEC received and handled all low-level commands to all PACS systems, except for the bolometers. Tasks that needed to be synchronous (e.g. detector readouts, chopper motion, grating steps) were triggered from here.

The DEC part operated the photoconductor arrays and received their raw data which arrived at a rate of 256 Hz. It also received the digitised bolometer data from BOLC. The detector raw data were then sent on to the SPU for processing.

The MEC part contained drivers and control loop units for all mechanisms, regulated temperatures in the FPU, and generated most of the instrument housekeeping. For special analyses of individual instrument components, diagnostic housekeeping with a rate of 1 kHz was possible. For more detail, please refer to the DEC/MEC User's Manual.

2.2.1.3 BOLometer Controler (BOLC)

BOLC operated the bolometer arrays in the PACS photometer and provided a clock signal to the MEC for the chopper synchronisation in photometer mode. The digitised bolometer signals were sent to the SPU via DECMEC for processing. For details, please refer to the PACS FM Photometer Focal Plane Unit User's Manual.

2.2.1.4 Signal Processing Unit (SPU)

The SPU reduced the raw data rate from the detector arrays, which exceeded the average allowed telemetry rate of 130 kb s^{-1} by far. The SPU performed real-time reduction of the raw data in the time domain, by averaging bolometer frames or fitting photoconductor integration ramps, bit rounding and lossless compression. The compressed science data were sent to the DPU for formatting in the telemetry packets. There were two SPU units, one for the blue photometer/spectrometer channel and one for the red photometer/spectrometer channel.

For a more detailed description of the algorithms employed see Sec. 2.6.

2.2.2 Cold focal plane unit (FPU)

The cold FPU was divided into optically well-separated compartments as shown in Fig. 2.2. The front optics section, common to all optical paths through the instrument, contained the internal calibration sources and the focal plane chopper. Thereafter followed the separate photometer camera and spectrometer sections.

The FPU was mounted on an optical bench together with other two *Herschel* instruments (SPIRE and HIFI) and was kept at the L1 temperature level of ∼3 to 5 K of the cryostat. The spectrometer detectors had thermal straps connected to the L0 temperature level (1.65 K) of the liquid ^{4}He bath inside the cryostat vessel. The bolometer detectors were operated at 285 mK provided by a dedicated ^{3}He sorption cooler, which itself was connected to the L0 level during recycling.

All optical elements and detector units of the FPU are explained in more detail in the following sections.

2.3 Common optics

2.3.1 Entrance optics

The entrance or front optics had instrument-wide tasks. It provided for an intermediate image of the telescope secondary mirror (the entrance pupil of the telescope) with the cold Lyot stop and the first blocking filter (FL_E, see e.g. Sec. 2.4.1), which were common to all the instrument channels. A further image of the pupil was reserved for the focal plane chopper. The focal plane chopper allowed

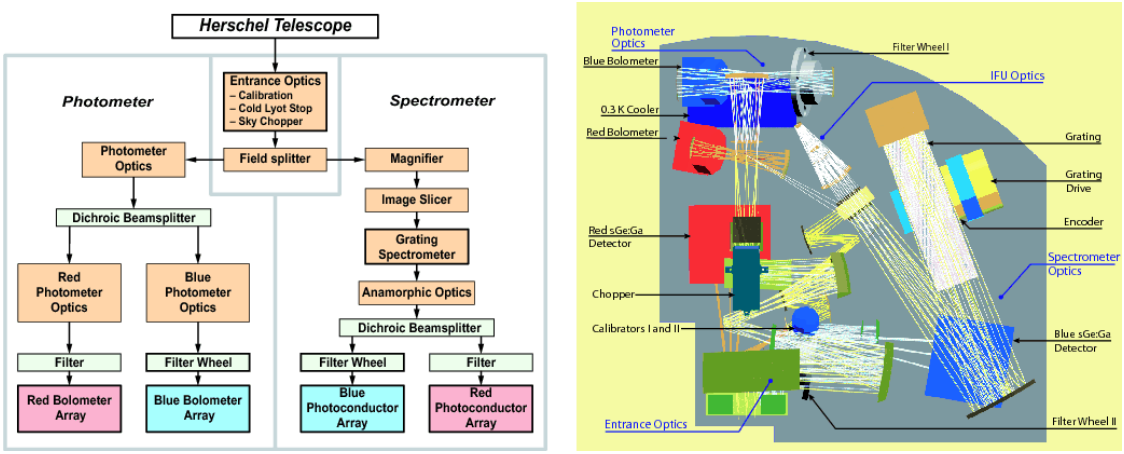

Figure 2.2: **Left**: PACS FPU functional block diagram. The arrows indicate the optical paths through the instrument. Imaging optics are highlighted by the light brown boxes, filter components by the light beige boxes. Blocks containing active components (mechanisms, electronics) are outlined in bold. **Right**: FPU optical layout. After the common entrance optics with internal calibrators and the chopper, the field is split into a spectrometer train and a photometer train. The two bolometer cameras (top left) have partially separate re-imaging optics split by a dichroic beam splitter. Filter wheel I contained the filters for the blue bolometer channel. In the spectrometer train, the integral field unit (IFU) image slicer (middle) converts the square field into an effective long slit for the Littrow-mounted diffraction grating (top right). The dispersed light is distributed to the two photoconductor (Ge:Ga) arrays: the first order to the red array (middle left), 2nd and 3rd order to the blue array (bottom right). The order-sorting filters on wheel II select between 2nd- and 3rd-order light.

spatial chopping on the sky and – through two field mirrors adjacent to the field stop in the telescope focal plane – to switch between field of view on the sky and on either of the two internal calibration sources (see Fig. 2.3, and for more information see Sec. 2.3.3).

In an intermediate focus after the chopper, a fixed-field mirror splits the light off to the spectroscopy channel. The remaining part of the FoV passes into the photometry channel. A footprint of the PACS focal plane is shown in Fig. 2.3. Proper centering of a celestial target in the photometer or spectrometer field of view was therefore achieved by offset pointing the telescope with respect to its optical axis. These offsets were determined during the instrument focal-plane geometry calibration and are listed in the Satellite/Instrument Alignment Matrix (SIAM, see the *Herschel* Satellite Handbook) as PACS instrument apertures P01_0 (photometer; $\Delta Y = 12.50''$, $\Delta Z = 631.51''$) and P02_0 (spectrometer; $\Delta Y = 7.05''$, $\Delta Z = 537.33''$). Additional angular offsets that had to be taken into account were the half step-sizes of chopper throws and telescope nodding steps.

2.3.2 Calibration sources

PACS contained two grey-body radiators as internal calibration sources (CS) which were required to mimic the thermal illumination from the telescope, in the pupil and in the FOV. These were placed near the entrance to the instrument, outside of the Lyot stop (see Fig. 2.2), to have a similar light path for observation and internal calibration. This is essential for removing baseline ripples, which is a serious task with a warm telescope and the associated high thermal background.

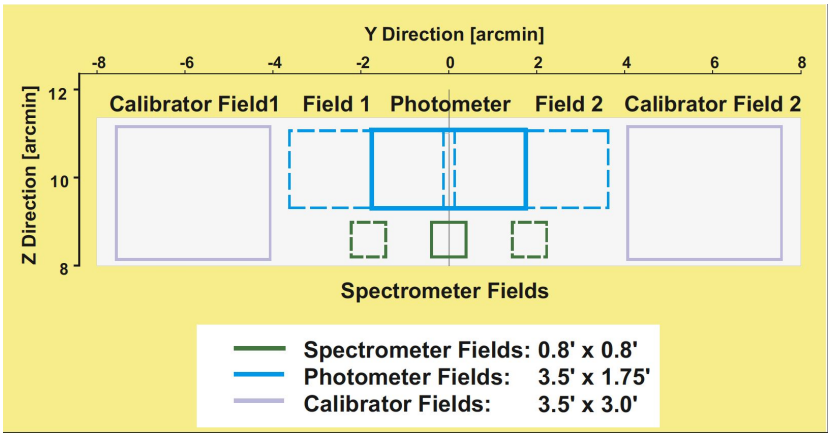

Figure 2.3: PACS telescope focal-plane layout. The axes give the angular offset in the telescope coordinate system with respect to the telescope optical axis when looking towards the focal plane (when looking towards the sky, signs are reversed). Photometer and spectrometer FoV were separated by the fixed-field mirror of the front optics. The smaller spectrometer FoV was offset in the -Z direction by $\Delta Z = 94.2''$. Chopping was along the Y axis direction. On both sides of the sky area in the focal plane, the fields of the internal calibration sources were reachable only by the chopper.

The design of the internal calibration sources is shown in Fig. 2.4. The emitter of the calibration source was a platinum resistance PT500. The required temperature of the grey body was achieved by a heater current flowing over the constant kept resistance. The goal was that the two internal calibration sources should produce radiation loads slightly below (CS1, 48Ω, 55 K) and above (CS2, 58Ω, 60 K) the telescope background at around 100 μm. Their emission was below the telescope background at shorter wavelengths and above at longer wavelengths due to the different emissivity and temperature wrt. the telescope mirror emission. The resistance measurement of the heater allowed a direct determination of the temperature by a four-wire measurement technique. With a 15 bit resolution of the controller, the temperature stability of <5 mΩ corresponding to 5 mK was guaranteed. The heating of the sources was achieved by ballistic heating and needed about 40 min until full temperature stabilisation of the sources was achieved. This was incorporated into the general instrument and detector set-up and took place before a PACS observation block. The sources were kept illuminated until the end of the PACS observation block. The cool-down after switch-off of the sources at the end of the PACS observation block was purely passive and took about >12 h. A detailed determination of heating and cooling time constants is given in (Dannerbauer et al., 2007).

The use of the internal calibration sources for the photometer flux calibration is described in Sec. 7.4.2.2, and for the spectrometer in Sec. 8.2.3.3.

2.3.3 Chopper

The PACS focal-plane chopper was a movable optical element in the PACS instrument light path that moved the centre of the FoV in the focal plane. Its functions were the following:

1) Modulate the incoming beam to be able to subtract the background emitted by the ∼85 K warm telescope, including any drifts and variations of this background slower than the chopper frequency. This was usually done by chopping between a position centred on the source and a

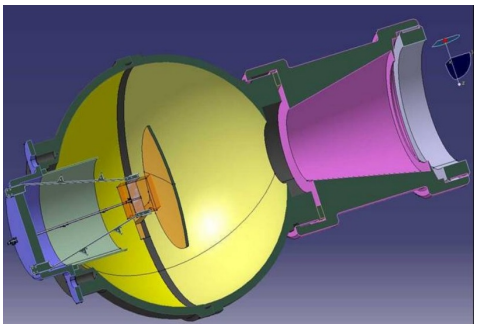

Figure 2.4: Design of the PACS internal calibration source (CS): The radiation emitter at the lower left hand side was a platinum resistor. The four feet carrying the emitter was a glass-fiber board to reduce the thermal heat loss due to low thermal conductivity. The radiation was distributed via a scatter plate in front of the emitter into the integrating sphere to increase the homogeneity at the pupil. The baffle cone at the right hand side including a lens generated the illumination patch covering the field-of-view of the detector.

nearby background reference position on the sky.

2) Mirror one of the two internal calibration sources into the detector field-of-view and to chop between them.

3) Perform step scans with step sizes down to $1''$ to explore the homogeneity and borders of the sky and internal calibration source FoVs.

Design requirements for the chopper were:

- High precision of the end position: $\pm 0.75''$ on sky position and $\pm 1.5''$ on the internal calibration sources. This corresponds to $\sim \pm 0.25$ and $\sim \pm 0.5$ of a blue photometer pixel, respectively.
- Allow chopper frequencies up to 10 Hz.
- A high duty cycle in the chopping pattern (this being a square wave modulation): 80% for sky chopping at 10 Hz, 70% for chopping between the internal calibration sources at 5 Hz.
- Low power dissipation (<4 mW).
- Low microphonic noise.
- Very long lifetime under cryogenic conditions (execute around 630 million chopper cycles).

The chopper and its essential elements are shown in Fig. 2.5. A detailed description of the PACS chopper hardware is given in Krause et al. (2006).

The angular calibration of the chopper (i.e. the relation between the field plate read-out to the angular deflection) was established by the manufacturer (Carl Zeiss AG Oberkochen) with the help of laser measurements. The discrete measurements were interpolated with polynomial functions and the Zeiss calibration was transferred into the PACS instrument system taking into account the different amplification factor (Nielbock et al., 2007). The angular calibration was verified on sky with the help of

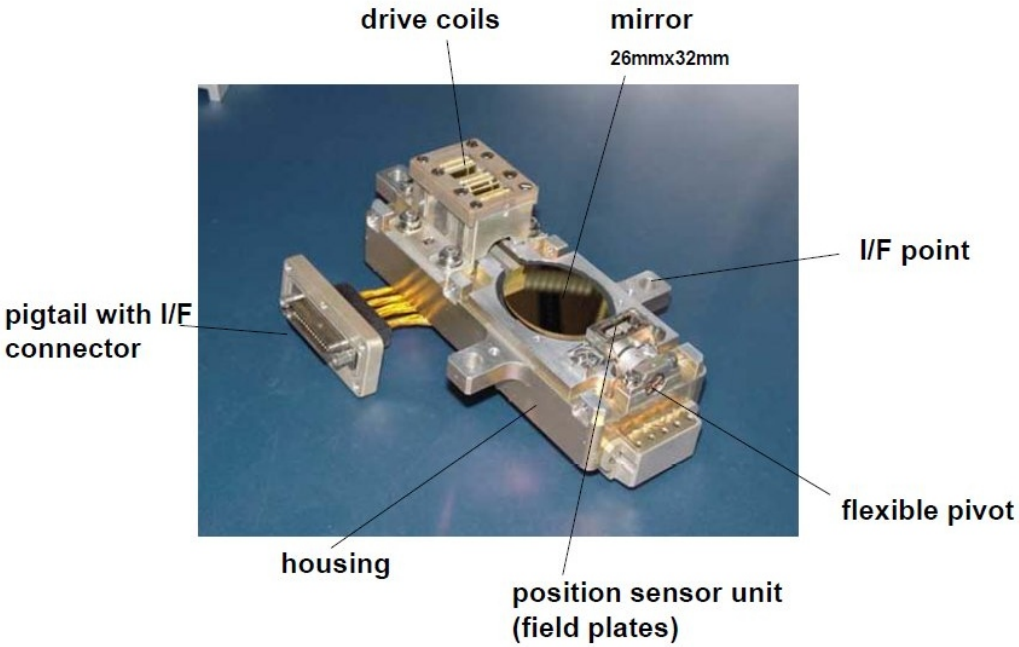

Figure 2.5: The PACS chopper showing its essential elements: The rotation axis of the gold-coated mirror was defined by two flexible pivots on both sides (rotation angle $< \pm 10^o$). Three drive coils provided redundancy for the rotational elongation of the mirror. The rotation angle was monitored by field plates of the position sensor unit and fed back to the chopper control electronics. Three mechanical interface points allowed for a mounting of the chopper accurately in the PACS light path.

double infrared sources with well known separation, and the details, such as measured chopper transition times between the two plateau and the plateau accuracies, can be found in in Bouwman et al. (2009).

To achieve the fast transition times and high plateau position accuracy required, with only small overshoots, an active control loop of the drive had to be developed. The implementation comprised of a PID loop, velocity loop, current feedback loop, and a notch filter for suppression of axial resonances[1]. The chopper control-loop parameters were optimised during a number of on-ground and in-flight tests. One performance example of the chopper during the commissioning in-flight is shown in Fig. 2.6, and details are given in Bouwman et al. (2009). The eventually-used control-loop parameters are stored in calibration uplink file `ConfChopper`. The shortest chopper transition times for the best performing set of control loop parameters are listed in Table 2.1. For a chopper frequency of 5 Hz, the duty cycle was 80% on sky and 78% on the internal calibration sources. Final default operational chopper frequencies were 1.25 Hz (95% duty cycle) in the photometric mode and 2.0 Hz (92% duty cycle) in the spectroscopic mode.

In-orbit performance checks revealed that the overall control-loop gain was dependent on the temperature of the DECMEC warm electronics (Nielbock et al. 2009), with a lower performance at low temperatures. The PACS warm electronics panel was therefore heated to $\geq 0^o$C during all PACS op-

[1] A detailed description of the chopper control is given in (1) the DECMEC User Manual, (2) the PACS Calibration Document (req. 2.3.2)

Table 2.1: Final performance numbers of the PACS chopper for the transition times into the accurate plateau position for the sky range (<15000 ADU) and for the internal calibration source range (>15000 ADU).

deflection angle (ADU)	chopper transition time into negative plateau (ms)	into positive plateau (ms)
3000	17	17
12000	19	20
18000	21	21
21000	22	22

erations, ensuring that the established control-loop parameters gave the optimum performance.

2.4 Photometer

2.4.1 Filters

Far-infrared filters defined the photometric bandpasses of the PACS photometer. Fig. 2.7 shows the filter sets used in the two simultaneously-operated blue and red branches, which were split out by a dichroic. The filter FL_E in the top optics defined the defined the short wavelength edge of the overall PACS wavelength range (52–210 μm). The blue branch contained a filter wheel which allowed one to switch between the blue bandpass (60–85 μm) and the green bandpass (85–125 μm). The bandpass transmission was achieved with a combination of low-pass and high-pass edge-defining filters. In the blue branch, the filter combination FBBP_1/FBBP_2 in front of the blue bolometer camera confined the whole blue-branch range (60–125 μm), while the filter combinations FBBP2_1/FBBP2_2 and FBBP1_1/FBBP1_2 confined the separate "blue" and "green" passbands.

All filters were metal mesh filters with inductive or capacitive grid geometry, either as air-gap or hot-pressed types, and provided by Cardiff University. A review of these metal mesh filters is given in Ade et al. (2006).

The transmission of all PACS photometer filters was measured by transmission spectroscopy. A complete overview is given in Müller et al. (2011). Here the example for the blue bandpass (60–85 μm) is shown in Fig. 2.8.

2.4.1.1 Effective spectral response

The effective spectral response of each bandpass is the product of the dichroic transmission/reflection, the transmission of all edge filters and the bolometer detector absorption. An example of the product of the former two is shown in Fig. 2.8. The bolometer detector absorptions are based on reflection measurements ($absorption = 1 - reflection$). The detector absorption was relatively flat and above 90% in the blue branch and dropping to around 80% for the red branch (see Müller et al. 2011).

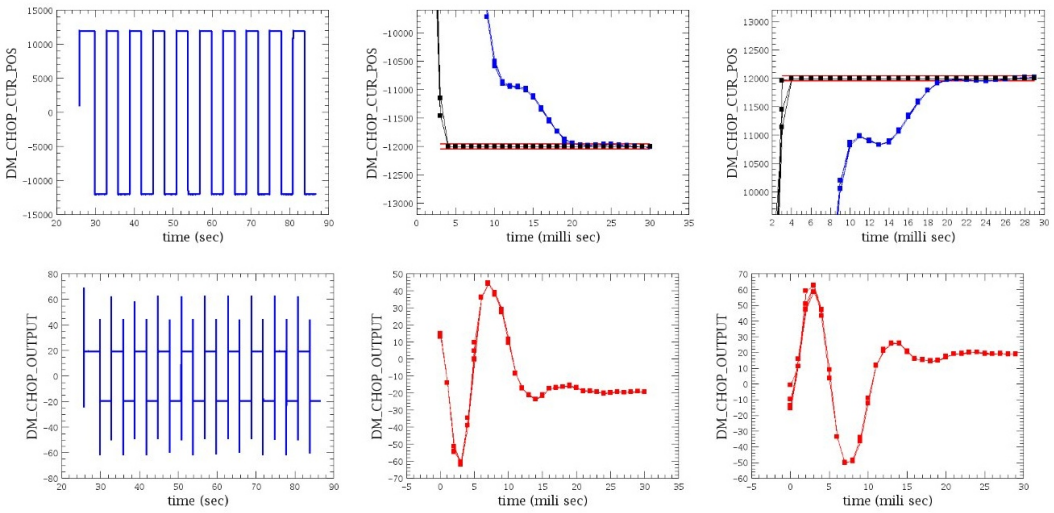

Figure 2.6: Example of a PACS chopper performance test during in-flight commissioning. The upper row shows the position read-out (in ADU), the lower row shows the drive current (in mA). The two left panels display the entire sequence, the central and right panels are a zoom on the critical swing-in phase with all chopper plateaux of the sequence overlaid. A slight jitter between the plateaux can be recognised; this is due to the diagnostic telemetry frequency of 1 kHz (corresponding to 1 ms temporal resolution). In the position read-out, blue symbols represent the actual sensor read-out, black symbols represent the stimulus. The red horizontal lines display the corridor to achieve the required plateau position accuracy.

Fig. 2.9 shows the resulting spectral response of the three bandpasses, the blue or 70 μm band (60–85 μm), the green or 100 μm band (85–125 μm) and the red or 100 μm band (125–210 μm). The filter transmission values are stored in the photometer calibration file `FilterTransmission` and the detector absorption values in the photometer calibration file `Absorption` (see also Table 10.11). The detailed shapes of the spectral response curves were used to derive proper colour correction factors (see Sec. 7.5.3).

2.4.1.2 Filter wheel

The filter wheel assembly is shown in Fig. 2.10. The filter wheel included a disk with the two filter positions, a magnetic motor drive, Hall-effect sensors for position detection and 12 magnets for filter-wheel rotor positioning. The filter-wheel mechanism and magnetic motor were mounted to an adapter plate.

Design requirements for the filter wheel were:

- Precision of end stop: 30′
- Transition time: $\leq$5 s
- Power dissipation per position change: $<$50 mW
- Warming of parts within view of detector: $<$0.1 K

- Operational lifetime: $\geq$20 000 cycles

A description of the filter wheel movement is given in the DEC/MEC User Manual.

The design of the filter wheel for the blue photometer branch was identical with that of the order-sorting filter wheel for the blue spectrometer branch.

2.4.2 Bolometer arrays

The PACS photometer detectors were developed with a novel technology and represented the first filled arrays of fully collectively-built bolometers with a cold multiplexed readout, allowing for a properly-sampled coverage of the full instrument FoV.

2.4.2.1 Bolometer technology

The detection principle of the PACS bolometer arrays was based on resonant absorption of FIR electromagnetic radiation. This was achieved by placing an absorption layer with thermometers (the

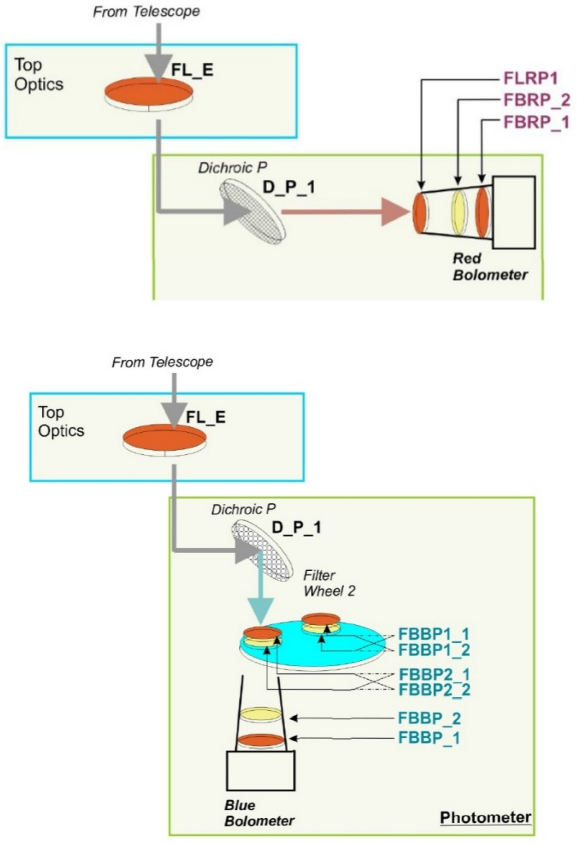

Figure 2.7: PACS photometer filter scheme for the red branch (top: $>$125 μm with dichroic in transmission) and the blue branch (bottom: $<$125 μm with dichroic in reflection). The blue branch contained a filter wheel which switched between the blue bandpass (60–85 μm) and the green bandpass (85–125 μm). The red bandpass was 125–210 μm.

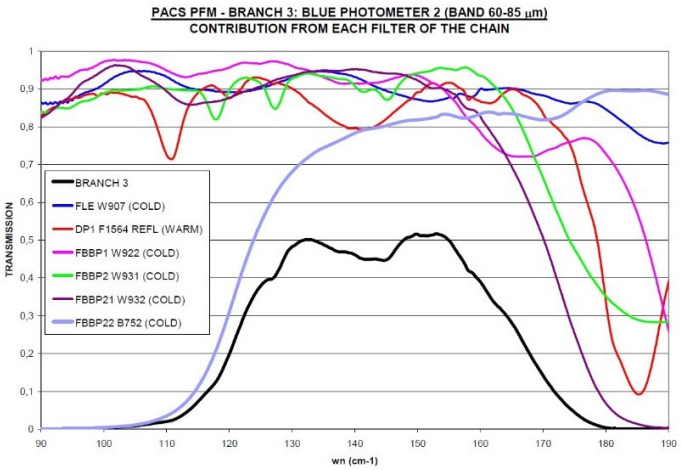

Figure 2.8: Transmission measurements for the PACS FM filter components of the blue bandpass (60–85 μm). Note, that the x-axis is in wavenumber $wn = \frac{1}{\lambda}$; wn = 100 cm^{-1} corresponds to λ = 100 μm. From Müller et al. (2011).

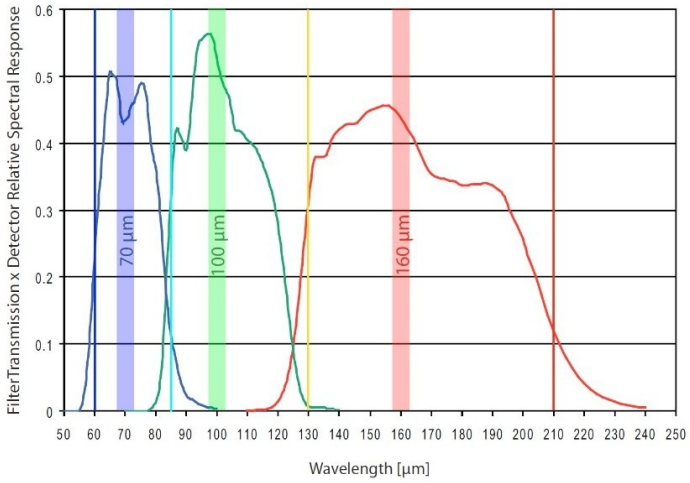

Figure 2.9: Effective spectral response (product of filter transmission and bolometer detector absorption) for the three photometer bandpasses. The reference wavelength λ_0 (cf. Secs. 7.4.2 and 7.5.3) is indicated for each bandpass.

pixels) above a reflector layer, separated by indium bumps to create a resonant cavity (see Fig. 2.11). This arrangement allowed for thermal absorption of close to 100% for wavelengths equal to four times the distance between reflector and absorber. The metal absorber was deposited on a crystalline silicon mesh insulated from a heat sink by four thin silicon rods. The time constant of the detector was given by the heat capacity of the insulated structure and the thermal conductance of the rods. The heat capacity of the sensitive part was optimised by mass reduction and operating it below 300 mK. The temperature elevation of the sensitive part was measured by fitting out the mesh with a semiconductor thermometric structure, a thin ($<$1 μm) and elongated silicon layer heavily doped with phosphorus and 50% compensated by boron ions to achieve a very high impedance ($\sim$TΩ). The thermometer was

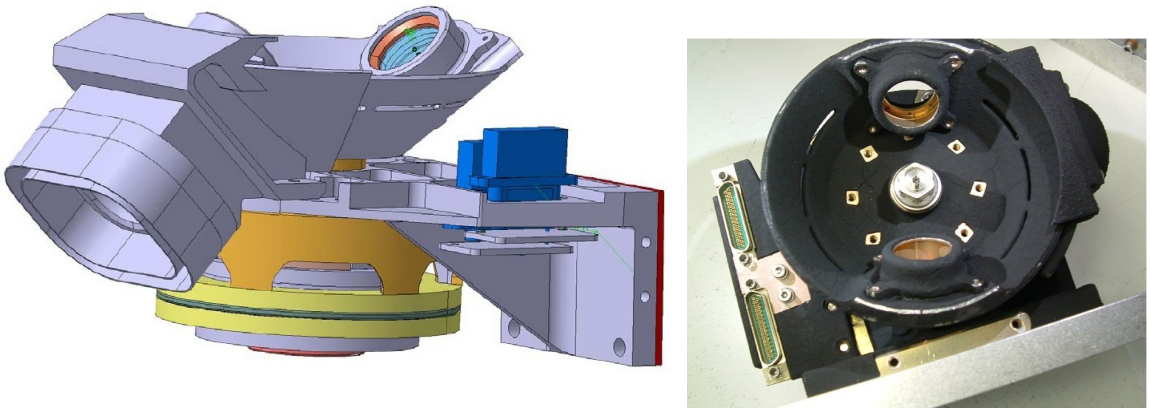

Figure 2.10: PACS filter wheel assembly. **Left**: Design of the filter wheel, showing the disk with the two filter positions and the magnetic motor drive underneath. **Right**: Image of a flight model filter wheel coated with black paint.

electrically insulated from the mesh.

The thermometer impedance changed when being heated by the incoming flux. The output signal of every pixel was the middle point voltage of a resistor bridge consisting of the thermometer resistor on the pixel and a charge resistor located on the heat sink wall and hence kept on the environmental bolometer temperature (Fig. 2.11 middle and right). The charge resistor was identical to the thermometer with respect to doping and geometry. The resulting bolometer output voltage $V_{\rm bolo}$ was hence

$$V_{\rm bolo} = \frac{R_{\rm bolo}}{R_{\rm bolo} + R_{\rm ref}} V_{\rm bias} \tag{2.1}$$

with $V_{\rm bias}$ being the applied detector bias voltage. The bias voltage was tuned to optimise the NEP (Noise Equivalent Power) behaviour and the detector dynamic range (see Sec. 2.4.2.3).

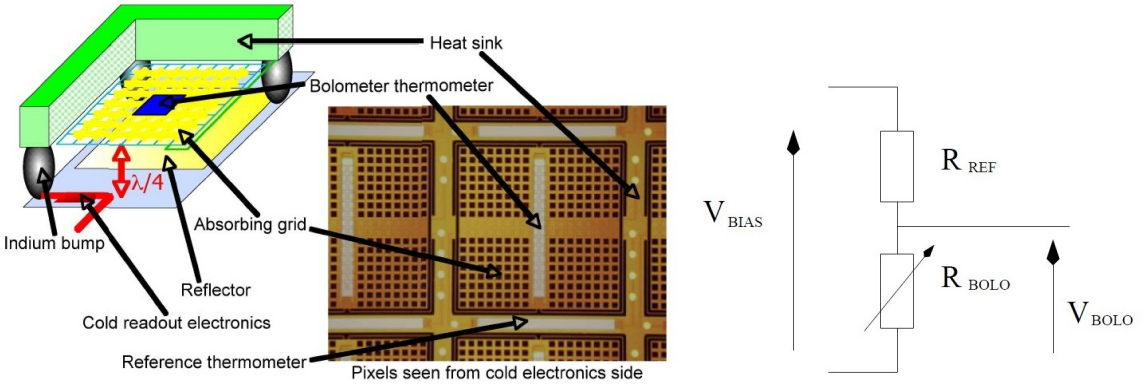

Figure 2.11: **Left**: Structure of a bolometer pixel with the main elements indicated. **Middle**: Absorbing grid of a bolometer pixel as seen from the reflector and cold read-out electronics side. The pixel pitch was 750 μm. The heat sink wall had a width of 70 μm. **Right**: Bolometer thermometer and reference thermometer formed the resistor bridge whose middle point voltage was the bolometer output signal.

Underneath the gold-plated surface of the reflector layer the CMOS[2] read-out and multiplexing circuits were located. CMOS circuits were adopted to ensure electric functionality at the operating temperature of below 300 mK. The multiplexing was mandatory to reduce the number of output channels on the harness: with a multiplexing factor of 16 the number of output channels was 160 for the 2560 individual bolometer pixels. The electric contact between the detector and the read-out circuits was achieved via the indium bumps, which also served to evacuate the power absorbed or dissipated in the detector arrays. Due to the stringent power-dissipation constraint of 10 μW at the 300 mK level, a second readout stage – the impedance adaptation – was located on a a part of the focal plane connected to the satellite 1.65 K (Level 0) level. This buffer stage had enough power to transfer the signals via the harness to the warm electronics. More details of the PACS bolometer technology and manufacturing are given in Billot et al. (2006) and Simoens et al. (2004).

2.4.2.2 Focal-plane arrays

The hybrid technology described in the previous section allowed for the production of detectors with large sensitive surfaces and with sufficiently low heat capacity to avoid requiring a light concentrator, as is in the case of classical bolometer cameras. This solution opened the way for production of filled-arrays collectives. Chips including 16 $\times$ 16 sensitive pixels and chips including 16 $\times$ 16 MOS readout circuits were manufactured and combined into basic units of 256 pixels; also called the detector matrix (see Fig. 2.12 left). These basic units were designed to be buttable on three sides to form larger focal plane assemblies. The PACS Photometer Focal Plane Unit contained two bolometer arrays:

1) The blue channel array for the wavelength range 60–130μm with 2048 pixels in total was a mosaic of 4$\times$2 matrices of 16$\times$16 pixels each (Fig. 2.12 middle).

2) The red channel array for the wavelength range 130–210μm with 512 pixels in total was a mosaic of 2$\times$1 matrices of 16$\times$16 pixels each (Fig. 2.12 right).

As can be seen from Fig. 2.12, there remained small gaps between the matrices. The final detector geometry and orientation with respect to the telescope coordinate system, including optical field distortion, can be seen from Fig. 7.2.

Each focal-plane array was mounted inside a structure connected to the 300 mK level. This temperature level was provided by a ^{3}He sorption cooler (Sec. 2.4.3). The focal-plane array structure was suspended inside a 1.65 K (Level 0) structure by means of Kevlar wires. Filters on the 300 mK level were mounted on top of each bolometer focal plane (see Fig. 2.7). The two photometer cameras had a different magnification to cover the same FoV (3.5$'\times$1.75$'$) with a different pixel scale (3.2$''\times$3.2$''$ and 6.4$''\times$6.4$''$ for the blue and red arrays) for proper over-sampling of the PSF.

2.4.2.3 Read-out electronics

Fig. 2.13 shows a simplified representation of the bolometer read-out electronics, which allows one to identify a number of essential operational voltages.

1) The leftmost blue box represents the detector layer with the resistor brigde (Fig. 2.11 right). The so-called polarisation bias voltage $V_{\rm bias}$ = VH - VL is defined by the two voltages VH and VL.

[2]Complementary Metal-Oxide-Semiconductor

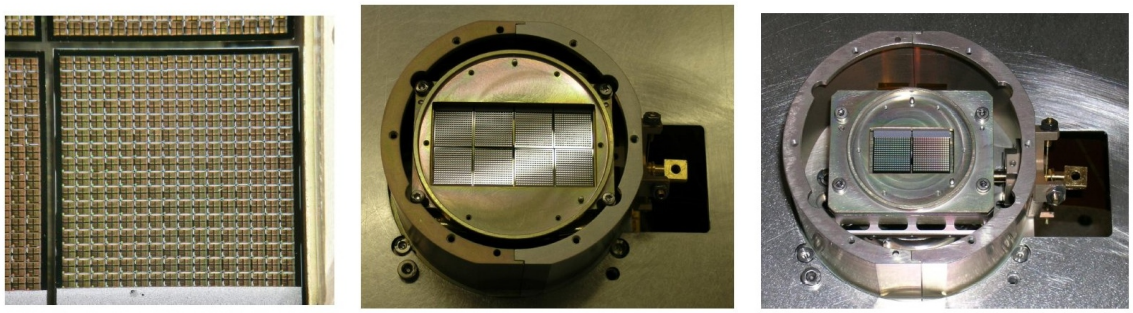

Figure 2.12: **Left**: Zoomed view of a PACS bolometer basic unit, a matrix with 16 × 16 multiplexed bolometers integrated in the blue focal plane array. Matrix dimensions were 12.63 mm×15.78 mm. Middle: PACS blue focal plane array consisting of 8 matrices and a total of 64×32 pixels. **Right**: PACS red focal plane array consisting of 2 matrices and a total of 32×16 pixels.

Nominal bias voltages were 2.6 V for the blue array and 2.0 V for the red array. V_{bolo} could only be transferred when it was in the voltage range 250 to 650 mV, otherwise read-out circuit (CL) saturation occurred (see Sauvage et al. 2008 for a detailed description).

2) The orange box is the read out electronics on the 300 mK level; this is part of the hybrid bolometer matrix. It offered a constant reference voltage VRL which could be switched to and transferred through the read-out electronics instead of the bolometer voltage V_{bolo}. This allowed the operation of the read-out electronics and optimisation of its settings without any detector signal. VRL was also an important component for one of the bolometer read-out modes (see Sec. 2.4.2.4).

3) The red box is the buffer stage on the satellite 1.65 K (Level 0) level. VH_BLIND was analog subtracted from the transferred signal and could thus be used for dynamic range adjustment. The read-out circuit transfer function was determined by the VRL–VH_BLIND calibration (Sauvage et al. 2009).

4) The green box was located inside the warm electronics unit BOLC (cf. Sec. 2.2.1). There the signal resolution could be adjusted for the ADC by selecting between two gain settings: high-gain mode (5 μV/ADU) and low-gain mode (20 μV/ADU). Low-gain mode offered thus a higher dynamic range which was nominally a factor of 4, but the available flux range was limited by ADC saturation (see Sauvage et al. (2008) for more detail).

A more detailed description of the PACS photometer read out electronics can be found in the PACS FM Photometer FPU User's Manual.

2.4.2.4 Detector read-out modes

The PACS photometer read-out electronics offered two read-out modes.

1) Direct mode: either the bolometer voltage V_{bolo} or the reference voltage VRL was continuously transferred. The signal from VH_BLIND was analog subtracted and the resulting signal was converted into digital units by BOLC with a frequency of 40 Hz.

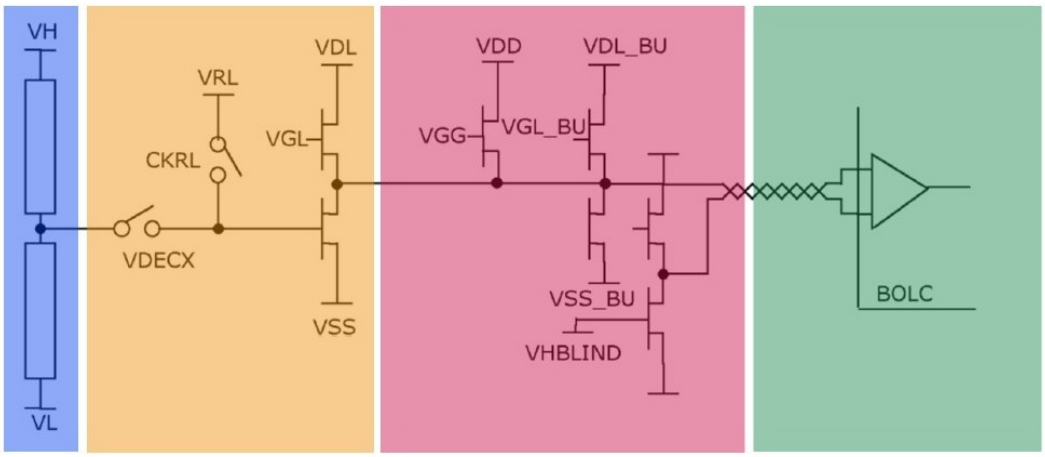

Figure 2.13: Simplified representation of the many-stage bolometer readout electronics. Blue: detection layer; orange: read out layer; red: buffer stage; green: BOLC (warm electronics).

2) Double-differential correlated sampling (DDCS): the V_{bolo} and VRL signal were interleaved using switches controlled by VDECX and CKRL (see Fig. 2.13). The signal from VH_BLIND was analogically subtracted from the mixed signals and the result was converted into digital units by BOLC with a frequency of 40 Hz. The two successive conversions were subtracted from each other to generate the final differential signal.

Double-correlated differential sampling was considered to be more robust to the electrical offsets and drifts that could be generated in the read-out chain downstream of VRL, in particular those caused by electromagnetic interference on the harness. The performance of both read-out modes was tested and compared during the *Herschel* PV Phase and in the end the direct mode was selected as operational read-out mode as it was considered stable and provided a somewhat better sensitivity than DDCS.

2.4.3 Cooler

A ^{3}He sorption cooler produced the operational temperature of 285 mK for the bolometer arrays. The *Herschel* flight model cooler is described in detail in Duband et al. (2008). Fig. 2.14 gives a 3D view of the device showing its main components. The evaporator contained a porous material, an alumina sponge (91 % Al_2O_3 / 9 % SiO_2), which trapped the liquid ^{3}He during the cold state. This liquid ^{3}He evaporated providing the cooling to the detector focal plane. When all the liquid ^{3}He had been evaporated into the gas phase, it needed to be recycled. The gaseous ^{3}He flew into the sorption pump which contained active charcoal for adsorption of the gas. An important monitoring parameter both for the cooler recycling procedure and the detector operation during the cold phase is the evaporator temperature TEMP_EV.

2.4.3.1 Procedure of the cooler recycling

Fig. 2.15 right shows the evolution of the temperatures relevant for the cooler during the various steps of the recycling process as monitored via Housekeeping (HK) parameters from temperature sensors. In this figure, at the beginning the evaporator temperature (TEMP_EV) was $\sim$ 2 K indicating that the

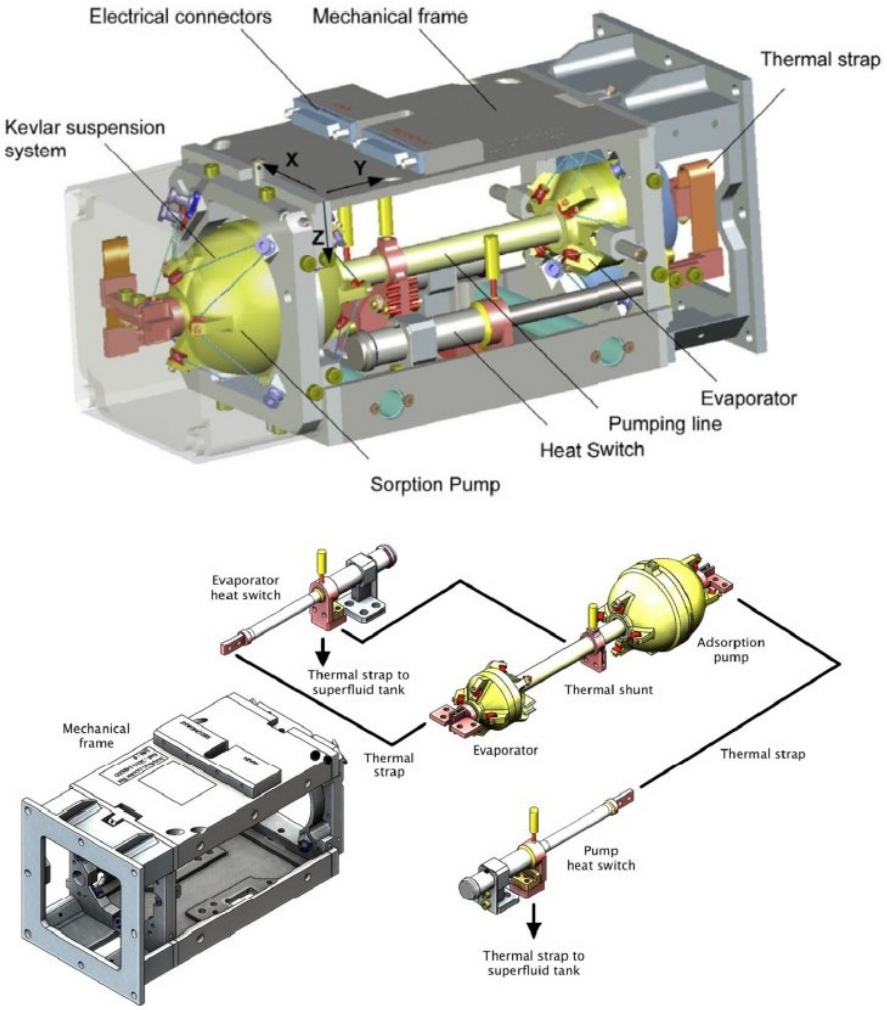

Figure 2.14: Overall 3D view of the PACS cooler identifying its main components. The bottom figure presents an exploded view identifying the elements represented schematically in Fig. 2.15.

cooler had run out of liquid coolant. The recycling procedure was completely controlled via heaters and heat switches integrated into the cooler (Fig. 2.15 left). The heat switches were of the gas-gap type, where the presence or absence of gas between two interlocked copper parts changed the heat flow between them. Gas handling was achieved by means of a miniature cryogenic adsorption pump (Duband, 1995).

The first 15 minutes served to settle the thermal environment. The pump heat switch (HSP in Fig. 2.15 left) had to be open, so that the pump did not dissipate heat into the instrument. The evaporator heat switch (HSE in Fig. 2.15) was closed so that the evaporator thermalised with the 2 K level and did not warm up too much while the pump was heated, and thus still trapped condensing gas. The heat switches HSP and HSE were closed by applying a current and opened by setting the current to zero.

The recycling proper started with heating the sorption pump (SP) to desorb the gas that had been trapped in the active charcoal. After 35 min the heater current was lowered to keep the pump at the required temperature of about 40 K. At this time, ^{3}He out-gassed from the pump and condensed.

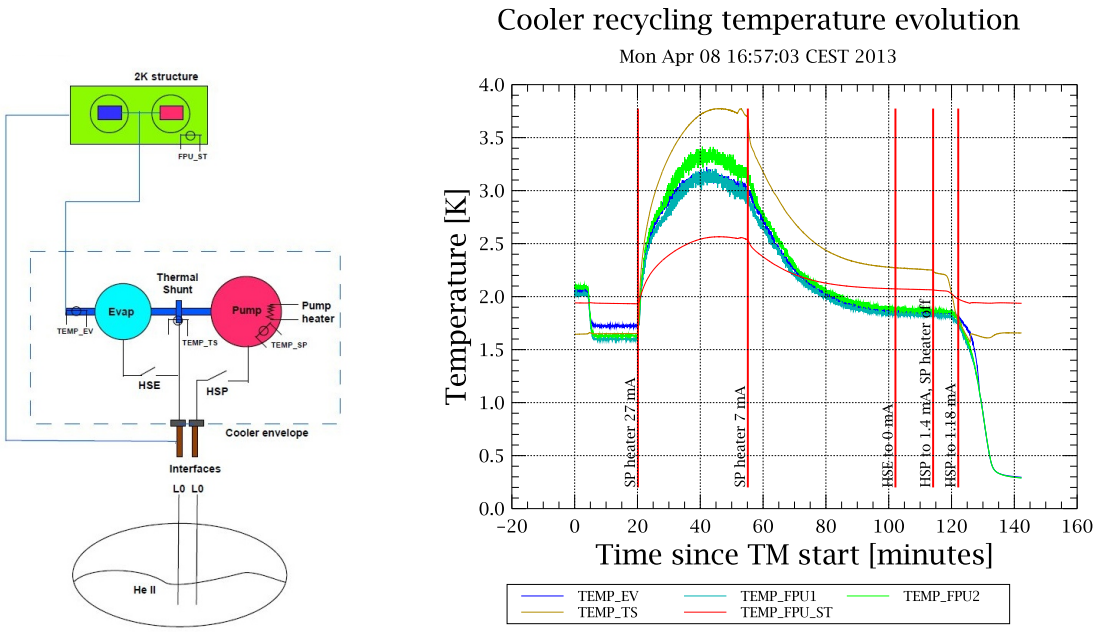

Figure 2.15: **Left**: Schematic drawing of the PACS cooler elements and the thermal connections to the PACS bolometer detector FPU (in green) and the liquid ^{4}He Level 0 bath of the *Herschel* cryostat at ∼1.7 K. **Right**: Evolution of temperatures relevant for the PACS cooler monitored by sensors and provided in the PACS instrument Housekeeping (HK) during the cooler recycling process.

TEMP_EV rose following the temperature rise of the pump due to the enthalpy of the hot gas coming from the pump and not all being removed by the thermal shunt, and also due to the latent heat of ^{3}He. Since the evaporator and the shunt were connected to the same thermal strap, all variations happening at the shunt were also registered by the evaporator temperature sensor (TEMP_EV). TEMP_EV decreased when the pump was kept at the required temperature. At around 80 min TEMP_EV dropped below the 2 K level. The finally achieved TEMP_EV in this step characterised the efficiency of the recycling.

After 82 min the evaporator heat switch (HSE in Fig. 2.15) was opened (HSE = 0 mA) to thermally isolate the evaporator. To establish the cooling functionality the pump heater was switched off after 94 min and re-connected to the 2 K level by closing the pump switch (HSP in Fig. 2.15). Once the pump was connected to the 2 K level the charcoal in the pump started pumping and the ^{3}He pressure dropped. The thermally-insulated liquid ^{3}He decreased in temperature to below the 300 mK level which was reached after around 142 min.

The cooler recycling procedure with the tuned time-steps as described above proceeded fully automatically. The duration of the PACS-only cooler recycling block was 142.37 min, the duration of the parallel-mode cooler recycling block 172.53 min. The procedure was implemented by means of the *Herschel* Common Uplink System (CUS). It is documented in Sauvage et al. (2014).

2.4.3.2 Establishment of the Cooler Hold Time Relation for *Herschel* Mission Planning

For an efficient *Herschel* Mission Planning it was necessary to have a reliable prediction of the cooler hold time $t_{\rm hold}$ for PACS photometer operations. The cooler hold time was defined as the period between TEMP_EV going below 300 mK at the end of the recycling process (cf. Sec. 2.4.3.1 and Fig. 2.15) and TEMP_EV exceeding 320 mK when the cooler was exhausted.

The essential parameter determining the length of the cooler hold time was the time when the PACS bolometer detectors were biased for measurement. This period was set by the orbit prologue and epilogue, which were engineering-type AORs setting and resetting the detector bias and bracketing the sequence of science AORs. The "biased time" $t_{\rm bias}$ was defined as the period between the start of an orbit prologue and the end of the subsequent orbit epilogue.

Such a dependence was monitored right from the beginning of the mission and after about three quarters of a year there were enough statistics to derive the relation

$$t_{\rm hold}(h) = 72.97\,h - 0.20 \times t_{\rm bias}(h) \tag{2.2}$$

established from all complete cooler periods up to OD 270, irrespective of the start conditions or whether it was a PACS-only or parallel mode cooler recycling. This relation was used in the scientific mission scheduling until the end of the mission, with a last PACS cooler recycling on OD 1443 (cf. 2.17). The formula was applied for determination of the cooler hold time following both a PACS-only and a parallel mode (together with the SPIRE cooler) recycling.

In Eqn. 2.2, $t_{\rm hold}$ can be written as $t_{\rm hold} = t_{\rm idle} + t_{\rm bias}$, with $t_{\rm idle}$ being the fraction of the hold-time period with the PACS bolometer detectors not biased, e.g. during spacecraft operational maintenance windows or SPIRE-only operations with both the PACS and SPIRE cooler in recycled state.

In case $t_{\rm idle} \sim 0$, then Eqn. 2.2 can be re-written as

$$t_{\rm bias,max}(h) = \frac{72.97}{1.2}(h) = 60.8\,h \tag{2.3}$$

This meant that a contiguous block of about 2.5 ODs of photometer observations could be scheduled, thus minimising the cooler recycling frequency. The remaining 0.5 OD was usually filled with PACS spectrometer observations, which did not requiring any ^{3}He cooling, by switching between the two PACS sub-instruments.

Since the cooler hold time relation in Eqn. 2.2 was determined for the point in time when the evaporator temperature exceeded an out-of-limit value of 320 mK, a safety time buffer was included when using this relation for mission planningSince the evaporator temperature increased very steeply only at the end of the cooler hold time (see Fig. 2.16), a buffer of 1.5 h was initially deemed sufficient. However, inspection of photometer calibration observations, scheduled deliberately at the end of the cooler period for cross-calibration with subsequently-scheduled PACS spectrometer observations of the same target, showed that there was already an increase in the evaporator temperature (cf. the course of the temperature in Fig. 2.16 with an increase of up to 5 mK for the cycle labeled A093), which had an impact on the photometric calibration accuracy. This effect is described in detail in Moór et al. (2014) and characterised by appropriate correction functions (see Sec. 7.4.2.4) which put all photometric measurements on a homogeneous temperature reference level. Despite the final calibration and correction of this effect, it was decided to increase $t_{\rm buffer}$ to 3 h, which meant that the evaporator temperature increased by at most 1 mK at the end of the cooler period (see the cycle labeled A133 in Fig. 2.16). This meant a maximum contiguous PACS photometer operation of 57.8 h.

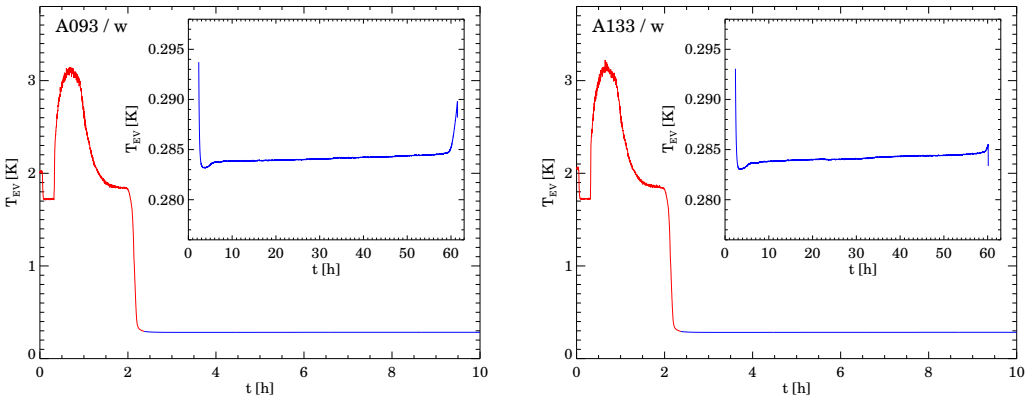

Figure 2.16: Individual PACS-only cooler cycles (labeled "A" plus a sequence number): The figure in the main panel shows the course of the evaporator temperature (T_EV) during the first 10 h following the start of the recycling, whereby the red part represents the proper recycling process, the blue part the beginning of the subsequent operational period. The inserts are a zoomed view with adapted dynamic range of T_EV over the full operational period. **Left**: Cycle A093 on OD 842 with a maximum contiguous bias period of nearly 59.2 h (t_{buffer} = 1.5 h in hold time calculation). **Right**: Cycle A133 on OD 1354 with a reduced (t_{buffer} = 3.0 h in hold time calculation) contiguous bias period of 57.8 h. For the latter one the final steep temperature increase is less than 1 mK.

2.4.3.3 Mission Statistics of Cooler Recycling

A total number of 239 PACS cooler recyclings was performed during the *Herschel* mission, the first on OD 26 for PACS commissioning and the last on OD 1443. 139 cooler recyclings were performed as PACS only, 100 recyclings in parallel with the SPIRE cooler recycling. It should be noted that the parallel cooler recyclings were not only performed for parallel mode observations of PACS and SPIRE, but also for separate PACS and SPIRE observations during the subsequent hold-time periods. The SPIRE cooler hold time was restricted to about 48 h; the difference between the PACS and SPIRE cooler hold times was usually covered by PACS photometer observations to achieve the highest possible efficiency of each cooler recycling with regard to the foreseen and available photometer observing program.

Fig. 2.17 shows the relation of the cooler hold time versus the biased time for all complete cooler cycles during the mission (192 out of 239, 115 out of 139 PACS only, 77 out of 100 parallel). The plot of all complete hold times of the entire mission shows some fine differences between the different modes and start conditions. The PACS-only recyclings starting from a warm cooler cluster close to the relation established from all complete cooler periods up to OD 270 (red line) with a dispersion of $\sim \pm 0.5$ h. The parallel cooler recyclings starting from a warm cooler are slightly shifted to an about 1 h shorter cooler hold time with a similar dispersion. This one hour lower efficiency was easily covered by the buffer time applied for mission planning aspects. Statistics for the cooler recyclings starting from a still-cold cooler are poorer, but there is some indication that the hold times both for PACS-only and parallel cooler recycling were about 0.5 h longer than for the warm start PACS-only cooler recyclings.

A more detailed statistics and description of the PACS cooler holdtime is given in Sauvage et al. (2014). The PACS and SPIRE cooler recyclings were also utilised to determine the lifetime of ^{3}He in

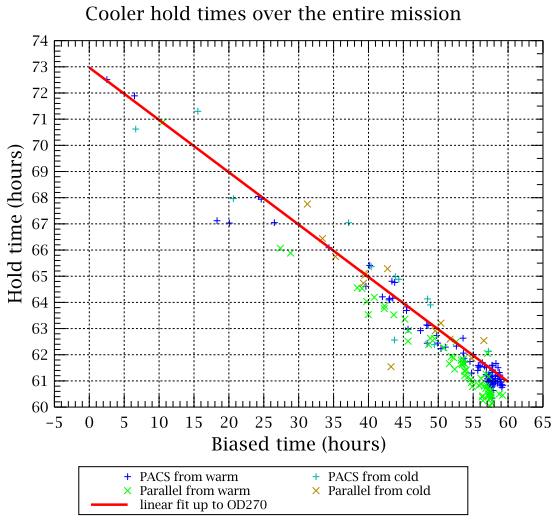

Figure 2.17: Statistics of the cooler hold time versus bolometer-biased time over the entire *Herschel* mission. Hold time and biased time are defined in the text at the beginning of Sec. 2.4.3.2. Symbols and colours represent PACS-only or parallel mode cooler recyclings and the start conditions from a warm, i.e. exhausted liquid ^{3}He, or a cold, i.e. still available liquid ^{3}He, cooler. The operational guideline established from the relation of all cooler periods up to OD 270 (Eqn. 2.2) is shown as the red line.

the *Herschel* cryostat. A description of this method is given in the *Herschel* Satellite Handbook.

2.5 Spectrometer

The power emitted or absorbed by a single spectral line in the FIR is normally several orders of magnitude lower than the power in the dust continuum over a typical photometric band. Sensitivity is thus the most important parameter for optimisation with FIR instruments. The PACS spectrometer was an Integral Field Unit (IFU). An IFU allows simultaneous spectral and spatial multiplexing, which in turns allows for the most efficient detection of weak individual spectral lines with sufficient baseline coverage and a high tolerance to pointing errors without compromising spatial resolution, as well as for spectral line mapping of extended sources regardless of their intrinsic velocity structure.

With a background-limited detector (as is the case for PACS), the best sensitivity is obtained when the spectrometer satisfies the following conditions: the detection bandwidth is not greater than the resolution bandwidth, which in turn is matched to the line width of the source; and the line flux from the source must be detected with the highest possible efficiency in terms of system transmission, and spatial and spectral multiplexing. These were all taken into account when designing the PACS spectrograph.

2.5.1 Instrument design

The PACS spectrometer was an Integral Field Unit (IFU) with a slightly-irregular grid of 5×5 spaxels covering a FoV of $47'' \times 47''$. It covered the wavelength range from 51 μm to 210 μm, in two

channels that operated simultaneously in a blue and a red band, split at $\sim$ 100 μm. The Littrow-mount grating spectrometer offered a resolving power of 1000–4000, i.e. a spectral resolution of 75–300 km s^{-1} depending on wavelength; for a fixed grating position the instantaneous coverage was about 1500 km s^{-1}.

PACS allowed simultaneous imaging at every wavelength over its entire FoV. The 5×5 spaxel grid was created thus: an image slicer employing reflective optics split the 2D FoV into five slices which were arranged along an entrance slit to the grating (see Fig. 2.18). A detailed description of the slicer optics is given in a paper on the similar SOFIA experiment FIFI LS (Looney et al., 2003). Each of the five slices was then divided into five by the fact that each detector array behind the grating and that received the light from each slit was a 5×18 grid (with the 18 consisting of 16 active detectors and 2 unused ones).

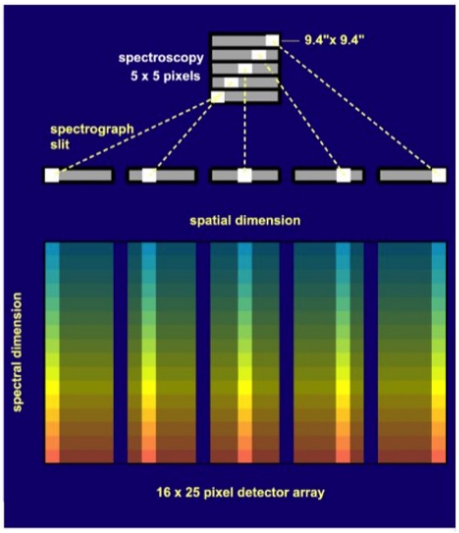

Figure 2.18: The Integral-field spectrometer concept: projection of the focal plane onto the detector arrays in spectroscopy mode. At the top is the $47'' \times 47''$ FoV on the sky. The image slicer re-arranges the 2D field along the entrance slit of the grating spectrograph such that, for all spatial elements in the field, the spectra are observed simultaneously. Note, the blank space left between the slices to reduce cross-talk between leftmost and rightmost pixels of adjacent slices (see also Fig. 2.27).

The grating was Littrow-mounted, i.e. the entrance and exit optical paths coincided. It could be operated in first, second, or third order: the first order covered 102–210 μm, the second order 52–72 μm or 68–105 μm, and the third order 53–73 μm (design values – actual filter edges deviate slightly from these values). Anamorphic collimating optics expanded the beam to an elliptical cross-section to illuminate the grating over the length required to reach the desired spectral resolution. The grating was actuated by a cryogenic motor with arcsecond precision, allowing for spectral scanning/stepping patterns to be used for coverage of extended wavelength ranges. The resulting the high data-redundancy aided in the detection of drifts in detector responsivity between individual pixels.

The settling time for typical motions used in the PACS AOTs was sufficiently short to allow for grating scans at various sampling densities (Sec. 3.3.2).

The light from the first diffraction order was separated from the light of the two other orders by a dichroic beamsplitter and passed into two optical trains feeding the two detector arrays (red: stressed, blue: unstressed) for the wavelength ranges 102–210 μm and 51–105 μm. Anamorphic re-imaging

optics was employed to independently match the spatial and spectral resolution of the system to the square pixels of the detector arrays. The filter wheel in the short wavelength path selected the second or third grating order.

Both spectrometer detector arrays (red and blue) operated simultaneously, always obtaining "prime" and "parallel" camera data. Coverage of the full PACS spectral range could so-be obtained by using the appropriated grating orders and data from both detector arrays together.

2.5.2 Image slicer

The image slicer's main function was to transform the 5×5 spaxel array at its focal plane into a linear 1×25 array at the entrance slit to the grating spectrometer. The slicer assembly consisted of three mirrors sets, which are sketched in Fig. reffig:imageslicer:

- The slicer stack: five identical spherical field mirrors, individually tilted, which formed separate pupil images for each slice on the set of five capture mirrors.
- The capture mirrors recombined the separate beams into the desired linear image on the set of five spherical mirrors at the exit of the slicer assembly.
- The field mirrors at the exit recombined the pupils separated in the slicer into a common virtual pupil. The collimators of the spectrometer will later form an (anamorphic) image of this virtual pupil onto the grating. At the same time, the field mirror apertures served as the entrance slit of the grating spectrometer.

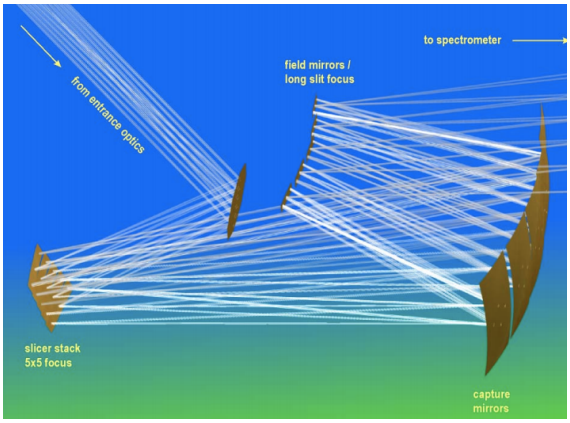

Figure 2.19: The mirrors used to cut the FoV of the PACS IFU into five rectangular segments.

The image slicer was the most critical element of the PACS optics. In Fig. 2.20, the diffraction throughput of the spectrometer optics is shown: the diffraction losses occur mainly in the image slicer.

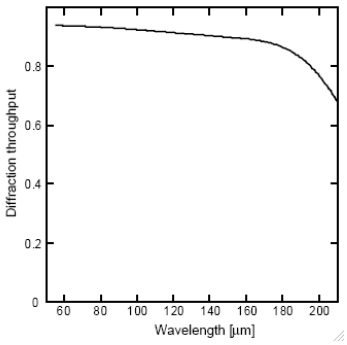

Figure 2.20: The diffraction throughput of the spectrometer optics

2.5.3 Littrow spectrometer

The entire grating assembly consisted of a Littrow-mounted grating, a mounting bracket that interfaced with the FPU structure, the actuator with redundant coils that provided positioning of the grating, the redundant position sensors, a launch-lock mechanism with redundant coils for the launch-lock actuator, the redundant temperature sensors, and the duplicated cryo-harness (see Fig. 2.21).

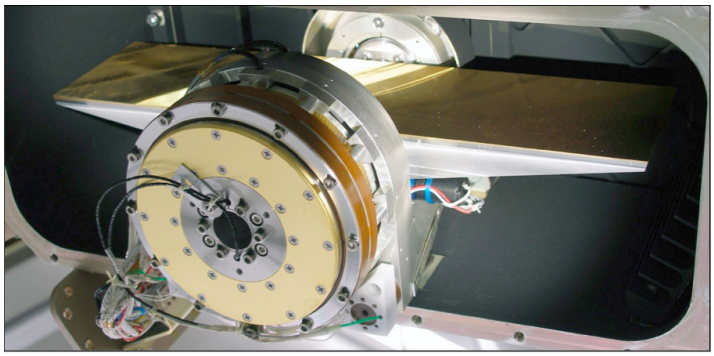

Figure 2.21: Flight model grating unit. A torque motor was used to actuate the grating angle, which was measured with sub-arcsecond precision by an inductosyn angular resolver.

The spectrometer used a reflective diffraction grating in Littrow mount, i.e. the incoming and diffracted beam are nearly collinear. The Littrow configuration provides a good compensation of image aberrations in the collimator, and this is especially important in the case of a complex collimating system such as the PACS spectrometer.

An anamorphic collimator system consisting of two crossed off-axis parabolic-cylinder mirrors was used. This collimates the beam to the required illumination diameter along the grating, while keeping beam, mirror, and grating dimensions small ($\sim$80 mm) in the cross-dispersion direction.

The grating was a diamond-ruled aluminium grating. The grating blank had a length of 320mm with a groove period of 8.5 ± 0.05 grooves/mm, with a total of approximately 2720 grooves. The reflection grating was originally envisaged to operate in the first (105–210 μm), the second (72–105 μm) and the third diffraction order (53–73 μm). Tests carried out early in the mission showed that the second order could be usefully extended down to 52 μm. These ranges were chosen by the angle the grating was set to: grating deflections from 25 to 70 degrees covered the full wavelength range of each order.

A graphical correlation of the grating angle of incidence versus order and wavelength is given in Fig. 2.22.

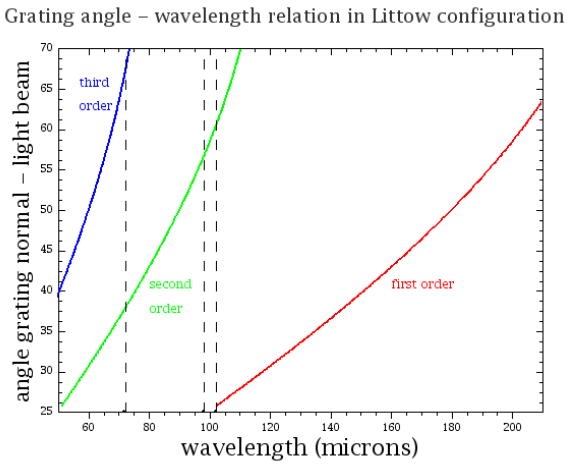

Figure 2.22: Relation between grating angle and wavelength.

A plot of the calculated grating efficiency also shows the location of the "stray orders": Fig. 2.23. At each intended wavelength setting of the grating some parasitic orders were also diffracted with appreciable intensity, most notably the 0th order (mirror-like reflection). This light exited from the grating at different angles from the intended order, and had to be suppressed by baffles around the grating and collimators to avoid "ghost" spectral lines showing up on the detector. A field stop at the exit of the spectrometer helped to further suppress stray-light and also wavelengths beyond the 16-pixel instantaneous spectral range.

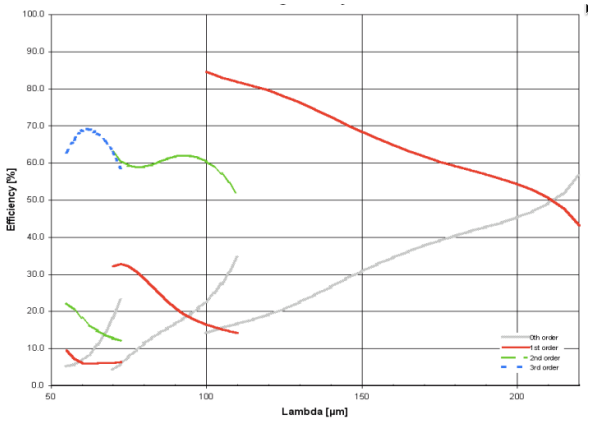

Figure 2.23: The calculated grating efficiencies and stray orders.

2.5.4 Filters

The filters of the PACS spectrograph fulfilled two purposes: they limited the detection bandwidth, i.e. they acted as order-sorting filters; secondly, they reduced the radiative thermal load on the 1.7 K and,

in particular, on the 0.3 K level. Since the performance requirements in terms of out-of-band suppression could not be met by one filter, the necessity of a chain of filters provided a certain freedom in the positioning of the filters, and the main optimisation parameter for that was stray-light suppression. The combination of filters, however, was solely driven by the need for maximum in-band transmission at the required out-of-band suppression which, in turn, was defined by a set of critical template observations.

The light paths though the filters are demonstrated in Fig. 2.24.

- A dichroic beam splitter reflected the 2nd and 3rd orders toward the blue detector, and the 1st order ("R1") towards the red detector.
- At the entrance (pupil) of the red detector housing, a fixed filter selected the 1st grating order. Inside the red detector housing a gratuitous flat-fold mirror was necessary to avoid exceeding the instrument envelope.
- The separation of the orders for the blue light happened at the entrance (pupil) of the blue detector housing. A filter wheel rotated two order-selection filters into the beam.

The blue filters worked by suppressing contributions by the other orders the detector was sensitive to. Filter "A" selected the 3rd order (B3A) and filter "B" the 2nd order (B2B). During flight it was realised that the blue end of the 2nd order, which could also be selected in filter "A", would provide spectra with a greater sensitivity than those of 3rd order, and this range was therefore also offered (B2A). Fig. 2.25 shows the total system transmission for three of the bands (B3A, B2B, and R1).

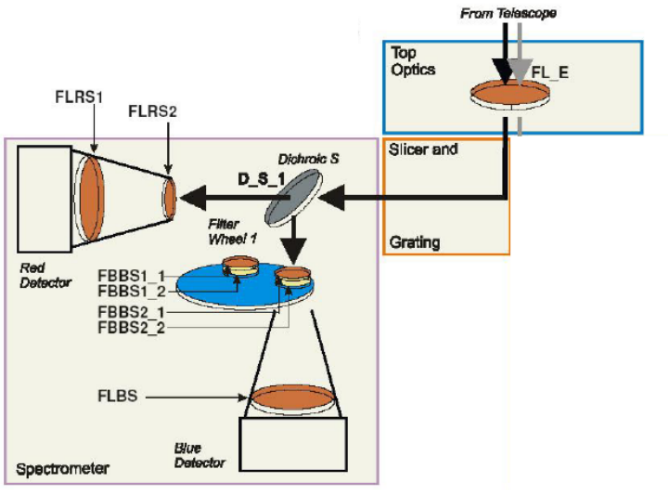

Figure 2.24: Overview of the filter arrangements in PACS. The light passes through the image slicer and grating and is then directed to the spectrometer side (left side of the image). The red and blue light are split by a dichroic. The blue light passes through a filter wheel to select orders two and three.

There was no band-limiting filter at 210 μm except implicitly by the diminishing response function of the detectors. All other order borders were defined by band-passes and blocking edges. Since the filter edges were not perfectly steep, however, the last few microns at the longward end of each order

were contaminated by short-wavelength leakage from the next higher grating order, this being mostly a problem for the red filter (Sec. 8.2.3.2).

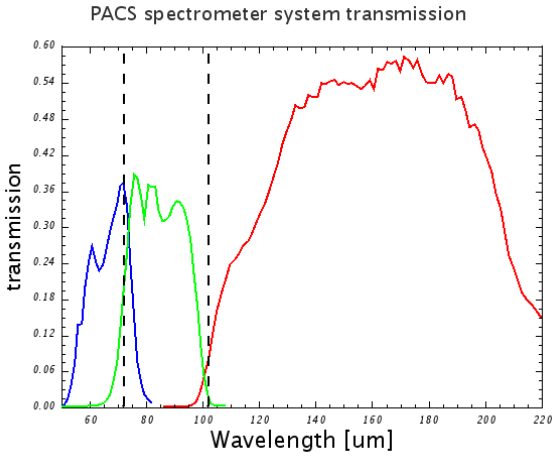

Figure 2.25: Transmission of the spectrometer filter chains. The graph represents the overall transmission of the combined filters in each of the three grating orders of the spectrometer. The vertical lines mark the edges between spectral bands. Band B3A (blue), B2B (green) and R1 (red) are shown.

2.5.5 Photoconductor arrays

The spectrometer detector array of PACS is described in Rosenthal et al. (2002). It consisted of two 16×25 arrays of gallium-doped germanium (Ge:Ga) photoconductor detectors. These detectors are extrinsic photoconductors, i.e. absorption of an FIR photon generates a free carrier by ionisation of a shallow, localised state bound to a dopant atom. Unstressed Ge:Ga photoconductors are sensitive in the wavelength range 40–130 μm, so a stress was applied to one of the arrays improve the long-wavelength sensitivity to 210 μm. The stressing mechanisms ensured a homogeneous stress on each pixel along the entire row of 16 spectral elements. A low mechanical stress was also applied to the blue detectors, of about 10% of the level used for the red detectors. The low-stressed detector is also referred to as "unstressed". A schematic of the design of a highly-stressed detector module is show in Fig. 2.26.

The detector arrays consisted of a stack of 25 "modules" (one of which is shown in Fig. 2.26) with 16 "spectral pixels" each, situated within individual integrating cavities for good quantum efficiency, and with light cones for area-filling light collection in the focal plane. These 25 modules created the 25 (5×5) spaxels of the PACS IFU (see Fig. 2.27). In fact, there were 18 spectral pixels in each module, but pixel 0 and 17 did not collect science data: these were an open and a dummy channel. The first had no detector but could be used to measure read-out systematics, and the second was a resister providing a perfectly known signal which could be used to check for other systematics. However, the data from these two channels were never required for any investigations. (There was also a dummy position for a module nr. 26, but with no detectors actually present.)

The 25 modules were operated at the (stressed) or slightly above the (unstressed) "Level 0" cryostat temperature ($\sim$ 1.65 K). For the unstressed detector array, a heater was attached to the housing to create a slightly higher operating temperature (2.5 K). Each module was read out by a cryogenic

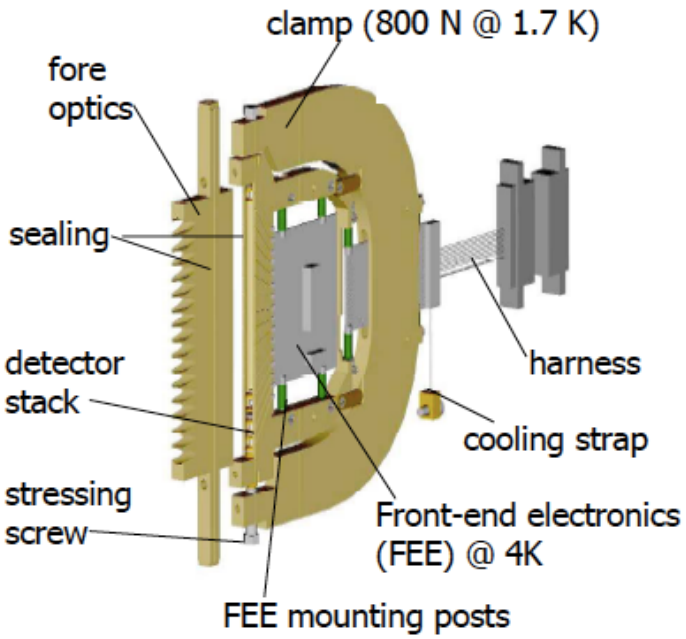

Figure 2.26: Schematic of the design of a single high-stressed detector module for PACS. The stress to the stack of 16 detector pixels was applied via one stressing screw. A clamp allowed a controlled adjustment of the stress. The detector channel was decoupled from the rest of the detector housing to keep the detector channel stress-free. The front-end electronics (FEE) was integrated in the U-shaped clamp. The FEE at a temperature of about 4 K were thermally isolated from the housing at a temperature of about 1.7 K for the high-stressed array and about 3 K for the low-stressed array. The modules were integrated into a housing which was coupled to the cooling system via a cooling strap.

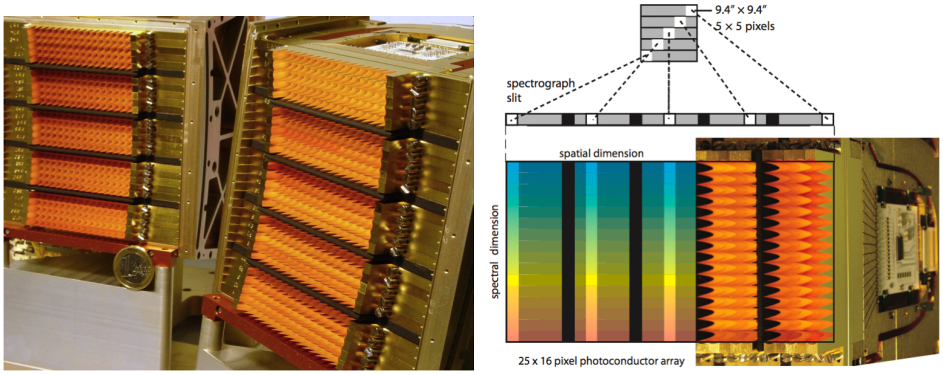

Figure 2.27: **Left**: The Ge:Ga detector arrays: The 25 modules (corresponding to 25 spatial pixels) in the red and blue arrays integrated into their housing. **Right**: showing the detector arrays together with the IFU concept. Part of the red photoconductor array with its area-filling light-cones and CREs are shown scaled to the schematic picture of the 25 by 16 array.

amplifier/multiplexer circuit (CRE) in CMOS technology. The readout electronics was integrated into the detector modules, but operated at "Level 1" temperature (3–5 K). Light cones in front of

the actual detector block provided an area-filling light collection in the focal plane, and fed the light onto the individual integrating cavities within which each individual detector crystal was located (this maximised the quantum efficiency). The light cones also acted as a very efficient means of suppressing stray-light, because their solid angle acceptance was matched to the re-imaging optics such that out-of-beam light was rejected.

The photocurrent from the detector crystals was integrated on a capacitor. The capacitance was switchable between four values from 0.14 to 1.15 pF to provide sufficient dynamic range for the expected astronomical flux range. It was expected that for most astrophysical sources the input flux would be dominated by the telescope background, so that the largest fraction of observations would be performed with the lowest capacitance setting. This was confirmed by the extensive CoP programme which searched for the optimal detector settings (see Royer et al. 2009). A higher capacitance setting could be selected for observations of bright sources (Sec. 3.3.2), however since the saturation level changes very little with capacitance (Sec. 8.2.6), this mode was offered to optimised observing time rather than to avoid detector saturation.

The signal from the detector consisted of integration "ramps": the infalling signal was integrated over a preset interval (i.e. the count level continuously increased), at the end of which the integration process was reset. A "ramp" therefore consists of a set of values where each value is the integrated signal *from the starting time until the current time*. During the integration interval, the voltage signal was read-out in a non-destructive way with a frequency of 256 Hz. At the end of the integration time, the voltage was cleared and the integration began again. One integration ramp then has 256/(reset interval) number of samples within it.

The CoP programme to optimise the detector settings led to a choice of ramps of 32 samples, i.e. an integration time of 1/8 second, for all spectrometer AOTs and both cameras. However, for reasons of bandwidth (see Sec. 2.6.2.2), the signal downlinked from the telescope were not the raw integration ramps readouts themselves, but the on-board fitted *slopes* of these ramps. Hence, a spectrometer observation of n seconds always resulted in $18 \times 25 \times 8n$ samples for each camera, i.e. 8 measures per second for each detector pixel (see also Sec. 2.6.2.3). Some examples of integration ramps can be found in 8.2.6.

Each of the 25 modules recorded an instantaneous spectrum from each of the 16 pixels, that is, for each fitted integration ramp time interval, one value of the slope is returned for each of the 16 pixels in each of the modules, and this being at a single grating position (and obviously for a single sky position). For an explanation of how the components of PACS moved during an observation to collect the requested spectra, see Sec. 3.3.

The optimum bias values determined by the PV programme were 42 mV in the blue and 100 mV in the red. At its optimum settings, the median NEP values were of the order 5×10^{-18} WHz$^{-1/2}$ for the stressed detectors and 1×10^{-17} WHz$^{-1/2}$ for the unstressed detectors. Only a small fraction of pixels suffered from excess noise; the identification of these can be found in the calibration file `NoisyPixelMask`(Sec. 10.5) and in the mask NOISYPIXELS in the lower-level pipeline products, Sec. 9.2.1.1).

Photoconductor arrays are known to show a fast and a slow component in their response; for the second, they can show a delayed response (from minutes to hours in duration) to changes in the illumination or to ionising irradiation. Characterising and dealing with these detector responses changes (from spiking glitches to long-term response gradients) was an important part of the CoP programme, and in the design of some of the pipeline tasks. Self curing via an IR "background" radiation is known to be a method to reduce some of the slow response effects. Thermal heating and IR flashing (via a

heater and a flasher which were integrated with the spectroscopy detector unit) and bias boosting were tested for their efficacy in self-curing the PACS detector. This was done via a series of proton irradiation tests carried out between 2004 and 2006 (resulting in a series of reports that can be found on HELL L3). However, these tests established – and the CoP tests then confirmed (Sec. 8.1) – that with the right combination of bias level, ramp-length, and with signal chopping (which was the method used in-flight), the best detector performance could be achieved without self-curing.

2.6 On-board data handling

The *Herschel* satellite RF communication system was an X-band system providing a downlink data rate of up to 1.5 Mbit s^{-1} at L2. With the Daily Telecommunication Period (DTCP) lasting for 3 h (since ESA's Deep Space Network Antennae at New Norcia and Cebreros had to be shared with other missions), this meant an average data rate of 150 kbit s^{-1} over the nominal length of an Operational Day (OD, ∼24 h). The prime instrument had an average data rate of 130 kbit s^{-1}, including instrument house-keeping (HK) data.

The PACS instrument had by far the largest number of pixels and hence the highest data rates of all *Herschel* instruments. The bolometer arrays (see Sec. 2.4.2) had 2048 pixels for the blue channel and 512 pixels for the red channel. Both were read out with 40 Hz and 16 bit precision. This led to a raw science data-rate of 1600 kbit s^{-1}[3] for the photometer. In addition, a header consisting of sixteen 32-bit parameters was attached to each science data frame for each array, adding another 40 kbit s^{-1}. In spectroscopy each camera contained 25 spatial columns with 16 spectral elements (see Sec. 2.5.5). Both arrays were read out non-destructively with 256 Hz and 16 bit precision.

In fact, there were actually 18 pixels, but the two extra were an open and a resistor pixel and they were not used in the mission. There were also 26 spatial columns, but only 25 actually contains detectors. Hence, the *actual* detector was a 25×16 array, but the formal instrument configuration was 26×18.

The DECMEC unit (see Sec. 2.2.1) provided the spectrometer science data of each array to the SPU units in 234 words of 32 bits, corresponding to 26×18 pixels, some containing dummy values. This corresponded to a total raw science data rate of 3744 kbit s^{-1}. The spectroscopy header had the same 16 parameters, resulting in a data rate of 256 kbit s^{-1}. The raw data rate therefore exceeded the average prime instrument data rate of 130 kbit s^{-1} by factors of 14 and 34, respectively. Even the raw spectroscopy header would have exceeded the allowed rate by a factor of 2. Therefore, the on-board signal processing software had to include data reduction and lossless compression algorithms to adhere to the allowed data rate.

The PACS data-rate was monitored as part of the PACS instrument housekeeping daily trend analysis (various trend plots and event reports can be found on this HSC archive page). Examples of these trend plots are shown in Figs. 2.30 and 2.31.

2.6.1 Data gathering

Fig. 2.28 shows the data flow from the detector units via the harness through the warm electronics units to telemetry packets stored on the *Herschel* mass memory prior to the daily telecommunication period with the ground station. The raw detector array data were gathered by the DECMEC, bolometer

[3] 1024 is used as base for quantities in kbit

data via the BOLC. The data were structured into frames, attached with a header consisting of sixteen 32 bit words and sent to the Signal Processing Units (SPUs). This header contained parameters such as observation identification and information about the instrument set-up, and the compression mode to be used by the SPU. The SPUs reduced and compressed the data according to the data type and compression mode. The data were shipped in packets to the Digital Processing Unit (DPU) which had an interface to the satellite Central Data Management System (CDMS). Regardless whether PACS was operating in photometry or spectroscopy, the data flow of the long wavelength arrays (the red channel) and the short wavelength arrays (the blue channel) went separate ways through dedicated DECMEC and SPU units. Only the DPU handled the reduced and compressed data of both channels together, packing them into telemetry packets before storage on the solid state mass memory.

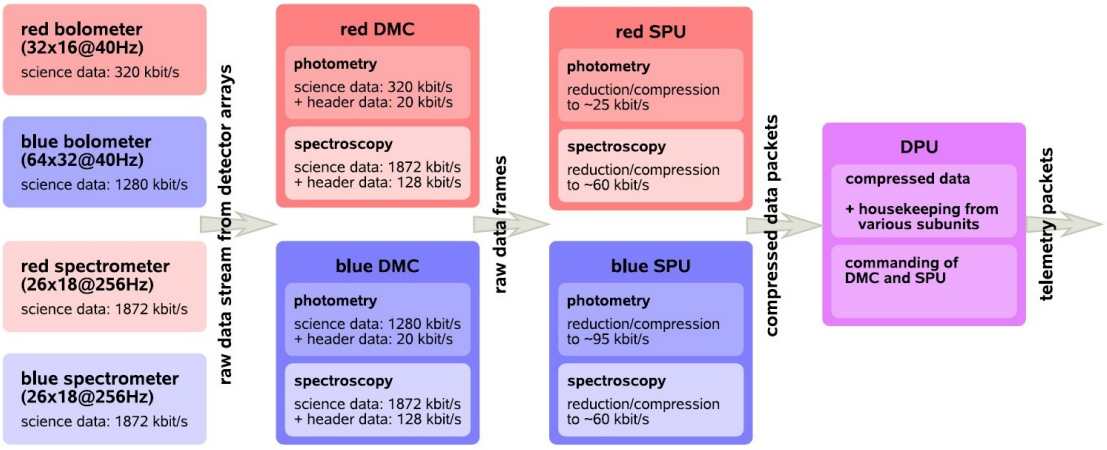

Figure 2.28: PACS data flow from the detectors via the warm electronic units to telemetry packets stored on the *Herschel* mass memory prior to the daily telecommunication period with the ground station. From left to right: either the bolometer arrays or the stressed Ge:Ga arrays were used, depending on the observation mode. Their detector raw data were gathered by the DECMEC (via BOLC for bolometer data), which structured them into data frames by attaching a 64 byte header. These data frames were forwarded to the blue and red SPU for reduction and compression. The SPUs produced a compressed data stream sliced into packets that got wrapped by the DPU to become standard telemetry packets. Aside from the nominal science data flow, each sub-unit sent Housekeeping (HK), a set of diagnostic counters and physical values, sampled with a time intervals of 2 s.

For a more detailed overview of the on-board software see Pezzuto et al. (2012). Detailed descriptions of the on-board software of the individual warm electronics units are given:

1) for the Digital Processing Unit (DPU) in *Herschel* PACS DPU OBS User Manual.
2) for the DEtector and MEchanisms Controler (DECMEC) in the DEC/MEC User's Manual.
3) for the BOLometer Controler (BOLC) in PACS FM Photometer FPU User's Manual.
4) for the Signal Processing Unit (SPU) in *Herschel*/PACS SPU High Level SoftWare User's Manual.

The crucial unit in reducing the incoming raw data to the acceptable telemetry volume were the two

Signal Processing Units (SPUs). An overview of the steps the data underwent there is shown in Fig. 2.29.

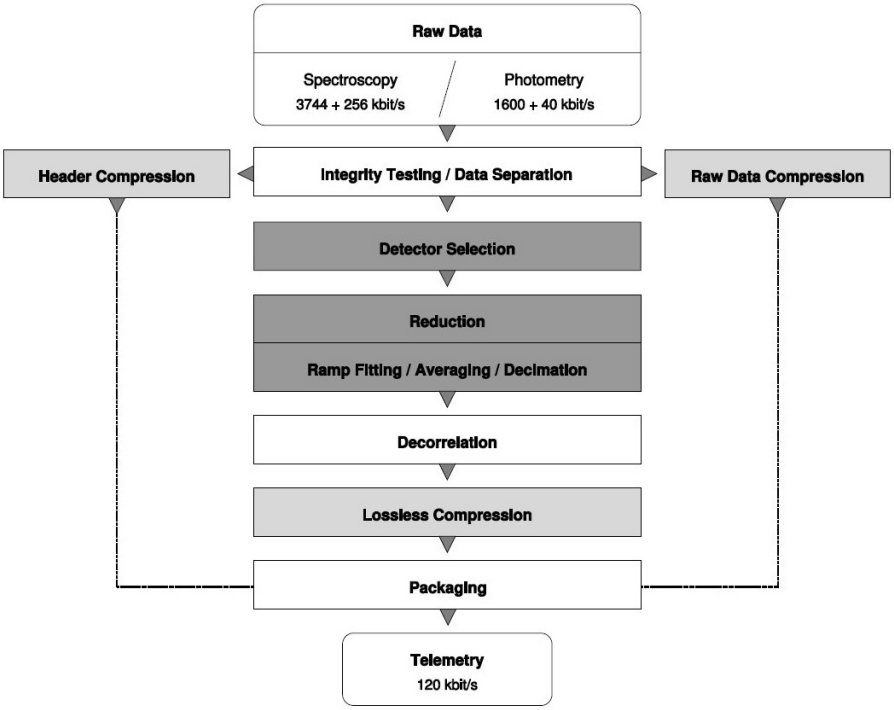

Figure 2.29: PACS data-reduction and compression steps inside the SPU. Modules where raw data were irreversibly reduced are high-lighted by dark grey colour. Incoming data were tested for their integrity, the headers were separated from the data and passed through the header compression subroutine. Raw data of a few pixels were routed outside the normal data processing for inclusion of compressed raw data in the downlink stream. The bulk science data were filtered with the detector selection table mask and passed onto the reduction module. The reduction module conducted averaging or ramp fitting including optional bit rounding. The data were prepared in the de-correlation stage for lossless compression. The data streams that went through different paths were finally reunified and sent to the DPU in form of packets.

An overview of the SPU software can be found in in Ottensamer and Kerschbaum (2008). The available SPU algorithms are described in HERSCHEL/PACS SPU High Level Software Specification Document, Appendices A & B. Detailed considerations on and illustrations of the SPU High Level Software development are given in Ottensamer (2009). The following sections provide a summary of the most essential features.

2.6.2 On-board data reduction

2.6.2.1 Detector selection

Detector selection for each detector array offered the possibility to select only a subset of pixels. e.g. to downlink raw data for this subset. Detector selection was handled by the SPU via uploadable tables that were written into the SPU memory as part of the AOT prologue. These tables were part of the

PACS uplink calibration tables, and hence of the mission configuration, and were stored within the *Herschel* Common Science System (HCSS). They had a unique identification number that allowed the reconstruction of the array geometry on ground. Detector selection tables were stored within the *Herschel* Common Science System (HCSS). Ottensamer et al. (2004) shows the detector selection table graphical user interface within the HCSS.

A detector selection table was used to extract the active pixel data from the total amount of spectrometer detector data words including also dummy values.

During the PV phase a few calibration observations with dedicated detector selection tables were performed:

1) Spectrometer calibration observations in support of dynamic range and ramp linearity assessment were executed in lossless compression mode to obtain raw ramps for each Ge:Ga/CRE module[4].

2) Photometer observations in the so-called Transparent Mode were obtained to test a compressed sensing strategy (cf. Sec. 2.6.3.4)[5].

2.6.2.2 Averaging

One major data reduction factor in photometry was the averaging of 4 consecutive frames in PACS prime mode. For the parallel observing mode, 8 consecutive frames of the blue array and 4 consecutive frames of the red array were averaged to comply with the parallel SPIRE photometer data-rate. This meant data-reduction factors of 4 for the photometry prime mode and 7.2 for the photometry parallel mode, at the expense of temporal and, with regard to scan maps, spatial resolution. Reducing the read-out frequency from 40 to 10 Hz meant for the standard scan speed of $20''\,s^{-1}$ an averaged sampling point every $2''$, i.e. 0.63 of a blue pixel and 0.31 of a red pixel side length, which still provided a good oversampling of the PSF. The situation was different for the blue parallel mode and the high scan speed of $60''\,s^{-1}$ with an averaged sampling point every $12''$, i.e. 3.75 times a blue pixel side length, which led to a significant smearing of the point spread function as shown in Sec. 7.3.2.

In chopped photometry the data frames were synchronised with a movement of the chopper via a flag in the header, signaling the start and end of a chopper plateau. This way it was guaranteed that averaging did not occur during a chopper transition.

Averaging of 4 frames reduced the noise by a factor of 2 or 1 bit. Nevertheless the reduction gain was not sufficient for all photometer settings that lossless compression alone could achieve the final data rate. Depending whether the observation was in high gain or low gain (cf. Sec. 2.4.2.3), an additional bit rounding was necessary. This is discussed in Sec. 2.6.2.4.

For spectroscopy the data sampling was somewhat different. The basic sampling frequency was the non-destructive read-out frequency of 256 Hz while integrating the signal along the ramp. After n-1 non-destructive read-outs (NDRs), with n being typically 32 (ramp length = $\frac{1}{8}$ s) or 64 (ramp length = $\frac{1}{4}$ s), a destructive read-out was executed resetting the integration. The integration ramp was therefore the basic data element of a spectrometer detector pixel with its fitted slope corresponding to the signal. Due to non-linearities of the ramp it was desirable to take the intermediate sampling into account.

[4]Using detector selection tables PACSDetSel_200xx, xx = 1 . . .25 being the number of the module

[5]Only a subset of 256 detector pixels of matrix 6 of the blue array defined by detector selection table PACSDetSel_20090909 was used.

One implementation of spectrometer data reduction was therefore the averaging of a subsample of m non-destructive read-outs, with m being typically 8 or 16 and to transmit the reduced number of $\frac{n}{m}$ averaged ramp samples to ground for reconstruction of the detector integration ramp. There was the option to deselect some critical samples at the beginning of the ramp ("hook" response: see e.g. PICC-MA-TR-043) or at the end of the ramp (destructive read-out affected by the reset) from the average process.

In the early PV phase a variety of SPU settings was tested with respect to data-rate and optimum signal-to-noise. One example is shown in Fig. 2.30 for OD 79. One major block (seen in the time range between ∼32 600 s and 61 500 s) was the optimisation of the spectrometer Astronomical Observation Template (AOT, see Sec. 3.3.2.1) for line spectroscopy. Several identical observing blocks with different scan parameter combinations and and two different SPU settings were inter-compared. One SPU setting used sub-sample averaging of 4 × 16 NDRs (no deselection of NDRs) for a $\frac{1}{4}$ s reset interval, another used ramp fitting of 32 NDRs for a $\frac{1}{8}$ s reset interval. A clear dichotomy could be recognised: the ramp-fitting mode yielded a data rate of below 120 kbit s^{-1}, the ramp averaging mode yielded data rates above 160 kbit s^{-1}, so not complying with the allowed average data rate. For the red spectrometer detector the optimum reset interval was actually $\frac{1}{8}$ s, and so a subsample averaging of 16 NDRs would have meant only 2 average points per ramp; this would not allow for a determination of an uncertainty of the slope. A subsample averaging of 8 NDRs, to have 4 averaged points, would have required already a bit rounding of 2 (see Sec. 2.6.2.4 for a description of the combined averaging and bit rounding algorithm). Therefore, finally the ramp-fitting mode (see Sec. 2.6.2.3) was selected as the operational SPU reduction mode for spectrometer data.

2.6.2.3 Ramp fitting

The default data reduction mode in spectroscopy became the fitting of the ramp slope or the fitting of several segments of the ramp (subramp fitting) on board. Synchronisation of the SPU processing with the ramp start was achieved via dedicated header parameters. The applied algorithm was

$$slope = \frac{\sum_{i=1}^{n} x_{\rm i} \sum_{i=1}^{n} y_{\rm i} - n \sum_{i=1}^{n} x_{\rm i}\, y_{\rm i}}{(\sum_{i=1}^{n} x_{\rm i})^2 - n \sum_{i=1}^{n} x_{\rm i}^2} \tag{2.4}$$

with x being the sample number of the ramp or subramp, y being the corresponding voltage read-out of the integration capacitor and n being the number of samples used in the (sub)ramp fitting.

Also here the option to deselect some critical samples at the beginning of the ramp ("hook" response) or at the end of the ramp (destructive read-out affected by the reset) from the fitting was possible. There was also the option of glitch detection and excluding the affected ramp parts from the slope determination. However, none of these options were ever used.

As outlined in the previous section, the final basic spectrometer detector pixel data set was the integration ramp with 32 read-outs (reset interval of $\frac{1}{8}$ s). The final decision with respect to the spectrometer on-board data reduction was to fit the whole ramp (no NDR deselection and no glitch detection) and transmit the slope of the ramp as the reduced data set.

Although ramp fitting was the default for spectroscopy, the full raw ramps were also downlinked for one spectral pixel of one module of the red and blue detector arrays. The purpose of this was to have access to some raw data from which in particular to check for saturation (see Sec. 8.2.6 for the calibration; Sec. 9.2.1.1 for pipeline details). The spectral pixels were the most responsive ones of

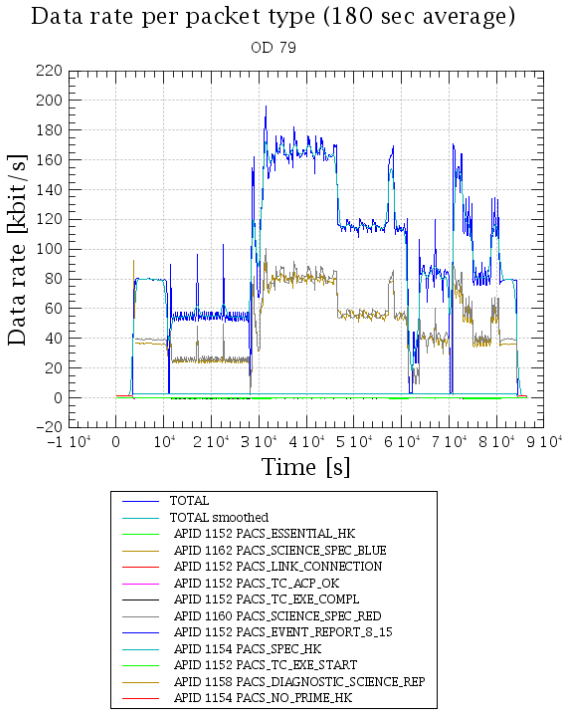

Figure 2.30: PACS prime mode data rate for the spectrometer on OD 79, when a variety of SPU reduction modes were inter-compared. In the time period between 28 500 s and 32 600 s dedicated SPU setting tests according to Performance Verification Phase Plan, section 6.17 were executed showing a large variation of the data rate. Between 32 600 s and 61 500 s line spectroscopy AOT validation repeating the same observing blocks on the same target were executed (cf. PV Phase plan, section 6.24). A dichotomy in data rate can be recognised: whenever subsample averaging was performed, the data rate was above 160 kbit s^{-1}, when slope fitting was performed, the data rate was below 120 kbit s^{-1}.

the central modules, the assumption being that the science target would most likely be located in this centre of the FoV.

2.6.2.4 Bit rounding

The noise in the bolometer high-gain setting mode was actually oversampled, using a too-large bit span. 2 bits of rounding were already sufficient to solve the data-rate issue, the additional quantisation noise amounted to only 1–4% total noise increase. The most efficient implementation in terms of CPU load was to include the rounding process in the averaging step. The combined averaging and rounding algorithm can be written as

$$m_{\mathrm{r}} = \frac{1}{2^r\, n} \sum_{i=1}^{n} x_{\mathrm{i}} + \frac{1}{2} sgn \sum_{i=1}^{n} x_{\mathrm{i}} - \frac{rand(1)}{2^r\, n} \tag{2.5}$$

where n is the number of samples to average and r the number of bits of additional rounding, *sgn* is the sign function. Statistically-correct rounding involves random number generation: rand(1) is a random number being 0 or 1.

Originally r = 2 bit was applied to all photometer high gain measurements. Trend analysis of the PACS data rate revealed that there was margin left in the data rate to reduce the bit rounding for prime mode observations. From OD 173 (02-Nov-2009) onward, the bit rounding for prime mode observations was released to r = 1 bit. Considerations to dispense with bit rounding during scan map mode were finally withdrawn in spring 2010 due to the very small improvement in noise performance accompanied by a significantly increased data rate which could have violated the overall data rate constraint during long ODs.

The spectrometer reduction mode sub-sample averaging with bit rounding, which however was finally not used for operations, applied the same algorithm.

2.6.3 On-board data compression

2.6.3.1 Header compression

Efficient lossless header compression made advantage of the structured content of the headers, which contained parameters staying the same for several frames or counters increasing or decreasing in a steady manner. Only a few parameters, such as the chopper or grating positions, were affected by a 2-bit noise. The principal algorithm used for header compression is published in Ottensamer et al. (2004). This included subtracting header frames from each other which reduced constants to zeros and counters to constants. All words containing zeros were removed by storing their original position in a binary mask. The remaining data were packed with the entropy encoder *RZip*.

2.6.3.2 De-correlation

The detector data were prepared in the de-correlation stage for lossless compression. The purpose of this stage was to produce a data set as sparse as possible. This was accomplished by separating signal and noise, with the signal part comprising the actual source signal and the bias offset including any form of drift as well as the chopping pattern and the noise part comprising the read-out noise around zero. This determined the final compression efficiency.

For the photometer data a differentiation (differencing) for each pixel was chosen as the first de-correlation step. After re-ordering of the data a second differentiation (differencing) followed at the frames level. This was essential for chopped data sets to remove the chopped pattern from the noise part. The two differentiation steps increased the noise by 1 bit, but the result was, that only 5–10% of the de-correlated values exceeded an 8 bit range, even for chopped observations, which was a good starting point for the lossless compression.

For the spectrometer data the de-correlation was done in a different way. Each processing buffer held 4 ramps per pixel. The first step was the differentiation of each ramp. One crucial step was then the subtraction of a key-ramp (the compression scheme was therefore called rampdiff): The first one in the buffer was subtracted from the remaining ones. The residuals were then differentiated another time to remove offsets due to the chopping. There remained one large offset value per pixel made up of bias, offset noise and read-out noise. To bring these large offset values closer to zero, a mean integer value was calculated and subtracted. This value had to be included in the compressed data stream to undo this step during the on-ground decompression. The sequence of subtraction steps increased the noise by slightly more than half a bit. The grating order (selected by the filter wheel setting) had no effect on the read-out noise and affected the data compression only slightly. However, different capacitor

settings had a large influence on the resulting signal and noise, which drove the data rate through the entropy.

2.6.3.3 Lossless compression

The best way to deal with the noise was by not trying to compress it, but to efficiently encode it to the entropy[6] limit. Both photometer and spectrometer reduction schemes produced a data stream of 3–6 bits signed noise around zero with certain peaks taking the full 16 bit range. Before passing the data to the entropy coder the input values were mapped to positive (unsigned 16 bit). Arithmetic compression was optimal to encode the de-correlated data sets down to the entropy limit. Limited CPU resources excluded a fully adaptive data model. Since the full 16 bit range had to be encoded, yet 90–95% of the encoding signals were within the 8 bit region, the trick was to handle values 0–254 with a classical cumulative probability table and use the index 255 for values 255–65535, indicating that they were put aside for separate compression with a variable block word length encoder. The "semi-adaptivity" of this model stemmed from the probability table which was replaced whenever 8192 symbols had been encoded. Typical achieved compression factors were 2–3.

2.6.3.4 Compressed sensing

Compressed sensing makes use of the sparsity of astronomical images to optimise the acquisition scheme of the data needed to estimate those images. This can lead to high compression factors (Bobin et al., 2008). During the PV phase, photometer scan map observations in the so-called Transparent Mode were obtained to test this compressed sensing strategy (see the PACS Performance Verification Phase Plan, sec. 6.8). Data were read out and transmitted with the full 40 Hz sampling of the bolometers, but only for the subset of the 256 detector pixels of matrix 6 of the blue array (see Sec. 2.6.2.1 on the usage of a detector selection table). The higher temporal resolution of the scan maps should enable to generate sharper images. An example of the processing method is given in Barbey et al. (2011).

2.6.3.5 Decompression

The decompression software was the reversal of the on-board compression software on ground, which was used to unpack the compressed content of the telemetry packets.

2.6.4 Burst mode

A special PACS telemetry feature was the burst or buffer transmission mode with an increased telemetry data rate of 300 kbit s^{-1} averaged over 30 minutes. This telemetry mode was used for engineering or calibration purposes only, when raw detector data of the whole arrays were needed. The data were not compressed at all, but the price to be paid for a few seconds of raw data was an about 1 min time-out: the data had to be buffered, as they could not be written with the read-out sampling frequency to the on-board memory. For this burst mode also a different bus profile in the DPU–CDMS communication interface had to be selected.

[6] In information theory entropy is a measure for expected uncertainty

Burst mode observations with the photometer were taken in support of measuring the time constants after a flux change by determining the signal dependence on the chopping frequency. These were executed in Performance Verification Phase on ODs 85 and 96 (see the PACS Performance Verification Phase Plan, sec. 6.7), as well as during the Routine Science Phase on ODs 455–457, 830–832, ODs 1193–1195 (see the PACS Routine Phase Calibration Plan, sec. 6.5). Fig. 2.31 shows the example from OD 831, when one out of three measurements was scheduled over the period OD 830–832 to keep the average data rate within the overall data rate requirement of 130 kbit s^{-1}.

In the PACS PV phase, some spectrometer calibration observations were also taken in support of detector dark current as well as ramp dynamic range and linearity assessment: see the PACS Performance Verification Phase Plan, sec. 6.18. These were performed in buffer-transmission mode to obtain raw ramps for all detector pixels. Raw ramps were routinely transmitted for three pixels for all standard spectrometer Astronomical Observations as part of the overall spectrometer data reduction/compression scheme.

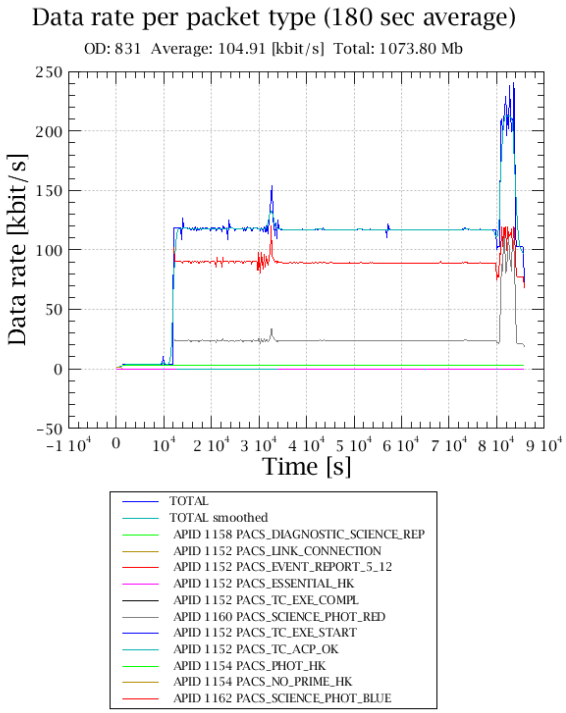

Figure 2.31: PACS prime mode data rate on OD 831 containing a ∼1 h photometer calibration observation with buffer transmission mode (burst) mode TM of raw detector data at the end. The average data rate for the OD was well within the overall data rate requirement of 130 kbit s^{-1}.

Chapter 3

Observing with PACS

3.1 Introduction

Any observation with PACS (or any of the *Herschel* instruments) was performed following an Astronomical Observation Request (AOR) made by the observer. The AOR was constructed by the observer by filling in an Astronomical Observation Template (AOT) in the *Herschel* Observation Planning Tool, HSpot. Each template contained options to be selected and parameters to be filled in, such as target name and coordinates, observing mode etc. How to do this is explained in detail in the HSpot user's manual and the PACS Observer's Manual. In this chapter we do not explain how to fill in an AOT (since that is no longer relevant), rather we explain the choices the observers had to make when creating their AORs, and what the resulting observing modes created were.

If the observation request was accepted via the normal proposal→evaluation→time allocation process, then the AOR content was subsequently translated into instrument and telescope/spacecraft commands, which were up-linked to the observatory for the observation to be executed. One special feature of PACS commanding was the use of On-board Control Procedures (OBCPs), command macros composed of a logical sequence of low-level commands needed to execute a certain type of observation, which were stored on-board. This reduced the telecommand bandwidth considerably, because only the name of the OBCP and the related parameters, whose values depended on the AOT parameter selection of the observer, had to be uplinked as part of the Mission Time-Line. The OBCPs were therefore essential elements of the AOT commanding design. A complete list of all PACS OBCPs and DEC/MEC sequences is given in Feuchtgruber et al. (2010).

The AOTs evolved in the first year of the mission as more efficient ways to carry out observations were created, so some of the standard AOTs used during the Performance Verification (PV) and Science Demonstration (SD) Phases (July–Dec, Oct–Dec 2009, respectively) were subsequently discontinued, and most were slightly changed. Here we concentrate on the final version of each AOT, which were used during the Routine Operations Phase.

Building Blocks: Observations were made up of logical operations, such as configuring the instrument, initialisation, and science data-taking operations. These logical operations are referred to as building blocks (or just "blocks"). The science operations were usually repeated several times to achieve the requested SNR and/or to map a given sky area. Pipeline data reduction modules work on these building blocks under the hood.

3.2 Photometer observations

Since the noise of the bolometer readout system had a strong $1/f$ component, photometer observations were designed such that the signal was modulated with a frequency from 1 to 5 Hz to achieve optimum sensitivity. Signal modulation was possible either by using the focal plane chopper or by scanning with the whole telescope. In the pre-flight design of the PACS photometer AOTs (see Sauvage & Okumura, 2005), utilisation of the chopper was considered to be the more efficient. Besides a chop-nod point-source AOT, a small-source AOT and a chopped-raster AOT were designed using a combination of telescope raster execution and chopping. These three modes were tested during the AOT validation in the PV Phase, together with the scan map technique with the chopper mirror staring in the optical zero position. These AOT validation tests showed the scan map technique was superior to the chop/nod technique. Chopped small-source and raster mode were therefore abandoned and made inaccessible in the HSpot user interface. The chop-nod point-source mode was maintained, because it provided accurate astrometry for the *Herschel* Pointing Calibration program (performed throughout the mission) and an independent reliable and low-cost observing method to test the photometer flux calibration consistency. With the invention of a special point-source mini-scan map mode, utilisation of the chop/nod point source AOT was no longer recommended to the general observer, and it was used exclusively by the PACS ICC calibration team.

Three photometer AOTs were fully validated and released to the observer community.

1) Point-source photometry with the chop-nod technique with the restrictions outlined above (see the "Point/Compact Source Observations: Mini-Scan Maps & Chop-Nod" release note).

2) Scan map technique, for large maps and for mini maps for point source photometry (see "Prime and Parallel scan mode" release note and the "Point/Compact Source Observations: Mini-Scan Maps & Chop-Nod" release note).

3) Scan map technique within the SPIRE/PACS parallel mode (see "Prime and Parallel scan mode" release note).

All photometer configurations performed dual band photometry with the possibility to select either the blue (60–85μm) or the green (85–125μm) band for the blue channel, and the red band (125–210μm) was always included. The two bolometer arrays provided full spatial sampling in each band.

Source flux estimates given by the observer drove the selection of the photometer gain setting for the ADC conversion. The default was the "high" gain, while "low" gain offered a larger dynamic flux range. Above the saturation thresholds given in Table 3.1, the AOT-to-ICP (Instrument Command Parameter) logic switched to the low-gain setting. The given flux thresholds were quite conservative estimates, to ensure that saturation occurred only for a small percentage of pixels, even for the detector matrices with the highest signal dispersion. The more homogeneous behaviour of the matrices in this setting allows for the measurement of higher fluxes. As the PACS "low" gain setting did not improve the dynamic range by the nominal factor of 4 in the ADC signal conversion, due to saturation occurring in the read-out circuit prior to reaching saturation of the ADC range, the extension of the flux range was limited to less than a factor of 2. A description of how the saturation estimates were derived is given in Sauvage et al. (2008).

Table 3.1: Bolometer readout saturation levels for the high gain setting. These numbers are conservative to ensure that saturation was avoided for most of the detector pixels.

filter	point source [Jy]	extended source [GJy/sr]
blue	220	290
green	510	350
red	1125	300

3.2.1 Scan map

The scan technique was the most frequently used PACS observing mode. Scan maps were performed by slewing the *Herschel* telescope at a constant speed along parallel lines, as shown in Fig. 3.1. The available satellite speeds were 10, 20, 60″/s, but during the mission the 10″/s was made inaccessible to the general observer, because the 20″/s achieved the same performance within a shorter time. The number of scan legs, the scan-leg length, the scan-leg separation, and the orientation angles (either in array or sky reference frames) were freely selectable by the observer to obtain the required map size and sensitivity depth. The sensitivity could also be increased via a repetition parameter, repeatedly executing the scan map n times.

To improve the map cosmetics (destriping) and to permit use of various mapmakers (cf. Sect. 9.1.1) it was recommended to execute a cross-scan map as well as the scan map. An optimum orientation of the array for large maps was $\sim 45^o$, and 135^o for the cross-scan, in the array reference frame, to avoid artifacts by the inter-matrix gaps[1] (Fig. 3.1). The performance for a given map configuration and repetition factor could be evaluated and optimised during observation planning via sensitivity estimates and coverage maps in HSpot.

3.2.2 Point source photometry (mini-scan map)

A special map design was created for point source photometry with scan maps. The orientation of the array was here rather 70^o in scan and 110^o cross-scan. Scan leg separations of 3–4″provided a very high map coverage and redundancy with many pixels seeing the source. The scan-leg length was of the order of 3′ and 10 scan legs provided a sufficient width of the map. Compared to the chop-nod point-source observation mode (see below), the advantage of the mini-scan map mode was a better characterisation of the source vicinity and larger-scale structures in the background due to a larger useful area, more homogeneous coverage inside the final map, the higher redundancy with respect to the impact of noisy and dead pixels, the absence of confusion by “negative beams”, and the better sensitivity of the scan technique.

[1] As of OD 208 the actual orientation angle of PACS photometer prime mode scan maps was set to a -2.5^o smaller value than the nominal one given by the observer to compensate for the slight rotation of the photometer array with respect to the satellite coordinate system, as shown in Fig. 7.2

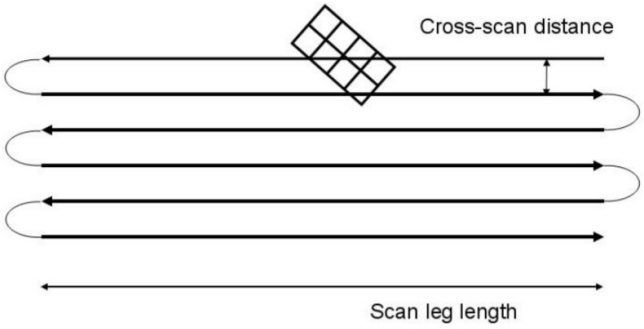

Figure 3.1: Illustration of the photometer scan map scheme with an example of six scan legs. After finishing the first leg, the telescope turned around and continued with the next scan line in the opposite direction. The specified reference scan direction was the direction of the first leg. An optimum orientation of the PACS blue photometer array with respect to the scan direction is indicated. The rotation by about 45^o in the array reference frame improved the map coverage and avoided artifacts by the inter-matrix gaps.

3.2.3 Point-source photometry (chop-nod)

The chop-nod point-source mode used the PACS chopper to move the source on-array by about $50''$, corresponding to the size of about 1 blue/green bolometer matrix (16 pixels) or the size of about half a red matrix (8 pixels), with a chopper frequency of 1.25 Hz. The nodding was performed by a satellite movement of the same amplitude but perpendicular to the chopping direction. This chop-nod scheme is shown in Fig. 3.2. The offset of $50''$ between the source images on the array meant that this was approximately the length of the useful sky area.

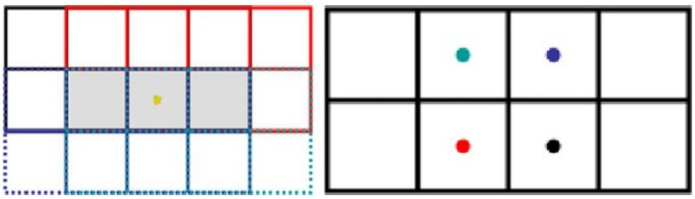

Figure 3.2: Illustration of the detector footprint of the blue detector array on the sky (left) and the chop-nod point-source pattern (right) produced on the detector during the execution of the chop-nod point source AOT. The detector array with a field of view of $3.5' \times 1.75'$ consisted of eight individual sub-matrices. The source was offset by about $50''$ horizontally by chopping (no dithering) and also by about $50''$vertically by the telescope nodding. The colours reflect the four combinations of the nodding and chopping positions attained during the observing sequence: black: nodA chop1, red: nodA chop2, blue: nodB chop1, cyan: nodB chop2.

At each nod position the chopper executed 3×25 chopper cycles. The 3 sets of chopper patterns were either on the same array position (no dithering) or on 3 different array positions (dither option). In the latter case the chopper pattern was displaced parallel to the chopper deflection by $8.5''$ ($2\frac{2}{3}$ blue

pixels or $1\frac{1}{3}$ red pixels). Each chopper plateau[2] lasted for 0.4 s (16 readouts on-board) producing 4 frames per plateau in the telemetry downlink. The full 3×25 chopper cycles per nod position were completed in less than 1 minute. For repetition factors larger than 1, the nod-cycles were repeated in the following way (example for 4 repetitions): *nodA-nodB-nodB-nodA-nodA-nodB-nodB-nodA*, to minimise satellite slew times.

3.2.4 SPIRE–PACS parallel

The SPIRE–PACS parallel scan mapping mode allowed one to obtain simultaneous five filter photometry in two PACS bands (70 or 100μm and 160μm) and the three SPIRE bands (250, 350, and 500μm). Due to the fixed $21'$ separation of the PACS photometer and SPIRE photometer footprints in the *Herschel* focal plane, only large maps were efficient i.e. had sufficient common overlap in this observing mode. Offered scan speeds were 20 and $60''$/s. The orientation angle with respect to the array was fixed to the optimum SPIRE orientation angle, which was 42.4^o and 317.6^o (-42.4^o) for scan and cross scan. Compared to the PACS prime mode, with the SPU averaging 4 consecutive frames, in the SPIRE/PACS parallel mode 8 frames were averaged for the blue/green filter, while for the red filter the averaging was identical with the prime mode. This led to a noticeable smearing of the PACS point spread function, in particular for the fast scan speed of $60''$/s (cf. Sect. 7.3.2). Another difference was in the data compression step, for which 1-bit more was rounded for SPIRE/PACS high-gain observations. For all other aspects the PACS instrument set-up was identical with the prime mode.

3.3 Spectrometer observations

During a PACS spectrometer observation, data were collected continuously while various parts of the instrument or telescope were moving: the grating, to cover the wavelength range of the observation; the chopper, to observe on-source and off-source sky positions; and the telescope itself, nodding to observe on-source and off-source sky positions or to move in a raster pattern. The choices of the observers in their AORs dictated the range of movements of the grating, chopper, and the telescope nodding; the choices made depended on the size of their astronomical source, the crowdedness of the field, and spectral coverage desired.

The AORs were designed by the observers from a set of inputs in the standard AOTs.

- The [rimary source of emission in all PACS spectra is that of the telescope mirror. To be able to observe a clean telescope background spectrum to subtract from the data of the astronomical target, it was necessary to observe an off-source sky position. Two ways were offered to set the **background measurement method** of the AOR: *chop-nod* and *unchopped*.

- **Three spectral coverage modes** were offered: *line-scan*, *range-scan*, and *SED range-scan* spectroscopy. The central wavelength, spectral range, and the sampling density could be chosen by the observer.

- Depending on whether observing a small source or an extended source, the **spatial coverage** choices were: *pointed* or *mapping*.

[2] plateau refers to a single chopper, nod, or grating position where a sequence of data-points were collected

The two AOTs that were offered via HSpot for the PACS spectrometer were line and range spectroscopy. (A wavelength switching mode was offered early in the mission, but was discontinued after the PV phase.) It was within these two AOTs that all the other selections could be made.

There are two AOT release notes for the unchopped mode: for line and range scan modes, and for the unchopped line scan bright line mode. For the chop-nod mode there are also two release notes: for the SED and range scan mode, and for the line and range scan modes. For the discontinued wavelength switching mode, there is just one release note.

All spectrometer observations began with a modulated chopped measurement on the two internal calibration sources with the grating at a fixed position (at the "key wavelength" nearest to the range requested in the science observation: a list of the key wavelengths is given in Table. 8.3). The "calibration block" measurement started during the slew of the spacecraft to the target. Data obtained in this block was used for the flux calibration in one of the data-reduction pipelines, and this calibration is explained in Sec. 8.2.3.1.

Before explaining the choices observers could make in their AORs, it is appropriate to explain the format of the data down-linked from *Herschel*. A raw PACS spectrometer spectrum is a time-line data-stream. Once set on a source, the detector integrated the infalling signal over 1/8 second (i.e. each infalling photon increased the counts) before a reset occurred, and the integration would begin again. Each integrated 1/8 second "ramp" was fitted with a low-order polynomial within the PACS SPU (Sec. 2.6.2.3); and so each single data-point transmitted to the ground was this fitted slope, in units of ADU/reset interval.

3.3.1 The background measurement method

Two observing methods were offered to allow the background spectrum to be measured: chop-nod (a.k.a. chopping), and unchopped. (The "background" could include any intervening astronomical emission, but primarily it was the spectrum of the telescope mirror.) The first was the main observing mode: it used a rapid chopping between the on-source position and an off-source position using an internal mirror, combined with a nodding movement of the telescope. The second mode was the choice for observations of sources in crowded fields, where no suitable off-position within the chopper throw could be found; instead, the telescope nodded between the on-source pointing and a chosen off-source pointing.

3.3.1.1 Chop-nod mode

The chopping and nodding movements occurring during a chop-nod observation are demonstrated in Fig. 3.3. A high-frequency chopping between the source and a background position took place while the grating moved along its requested range and back again, gathering signal from the source. The telescope would then move (nod) to a near-by position, and the sequence of chopping between the source and a background would begin again. The reason for the nodding is that the line-of-sight through the mirror to the two chopper positions was sufficiently different that the telescope background spectrum was not the same. In nod A, the on-source position was at chop- and the off-source position was at chop+, but since the intrinsic telescope spectrum at these two chopper positions was not the same, simply subtracting off-source from on-source would not remove the telescope background. Therefore in nod B, the on-source position was at the chop+ and the off-source position was at the chop-, and

the combination of all four of these signals *would* remove the telescope background spectrum (see Sec. 8.2.2.1 for more detail).

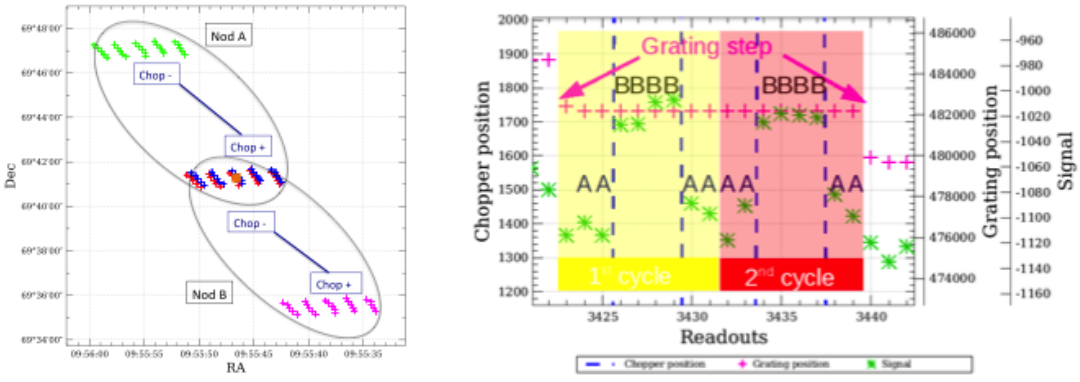

Figure 3.3: An explanation of the chop-nod observing pattern. **Left:** each coloured set of 5x5 crosses is the footprint of the PACS IFU (each cross is a spaxel). In each telescope nod position – A and B – the chopper flipped at high frequency between a minus and a plus (-,+) position. The source (orange square) is located at nodA,chop+ and nodB,chop-, while nodA,chop- and nodB,chop+ are off-source (background) positions. **Right:** In this plot you can see the signal taken at the chop+ and chop- positions, with two AABBBBAA chopping cycles at each grating position, where A and B here refer to chop+ and chop-, *not* the nod.

Three chopper "throws" were offered: 1.5′ (small), 3′ (medium), or 6′ (large). Ideally the two on-source positions (i.e. nodA,chop+ and nodB,chop-) should overlap exactly, but in reality – and due to the curved nature of the chopper path (see chp. 4.5 of the Observer's Manual) – there were slight spatial offsets between the footprints. The small chopper throw was the recommended one since the offset here was the smallest.

The user could chose the number of repeats of the nodA-nodB pattern to request. Increasing the number of nodding sequences was done to improve the SNR of the final spectra. However, it was also possible to increase the line repetition factor to improve the SNR (Sec. 3.3.2), and this was more time-efficient: for a low number of repetitions (~ 6) it was recommended to repeat the line rather than the nodding sequence.

3.3.1.2 Unchopped mode

The unchopped mode was for observations where no emission-free background region within the reach of the chopper was available. The observing pattern in the unchopped mode depended on whether the AOT chosen was line or range scan.

For the line-scan AOT, the entire spectrum (for each spectral line requested) was observed in nod B, the on-source position, and the telescope then moved to nod A, the user-selected off-source position. This had to fall within 2° of the on-source position. The entire on-off nod sequence could be repeated a user-requested number of time.

For the range can AOT it was necessary to define a second observation, ideally taken consecutively (at least within 60 minutes) with the on-source observation, to observe an off-source position. (Note

that not all observers requested an off-source position, and some used a single off-source position for several on-source positions.) The on-source and off-source AORs then had to be concatenated so that the HSC knew they were to be executed as a single block. For range scan AORs which requested the entire band (SEDs), it was possible to split the off-source observation into two observations, i.e. one before and one after the on-source observation, and both could then have half the on-source integration time. In the SPG pipeline, however, only one off-source observation is subtracted from an on-source observation.

In later versions of HSPOT the observer could set a switch (which became a Meta datum) to indicate whether the AOR was the off-source or the on-source observation. This was for information purposes, and it was not always set.

One disadvantage of the unchopped mode is that it is less robust to the short-term responsivity changes caused by cosmic ray hits in the Ge:Ga detector pixels ("transients"[3]). The multiple consecutive ramps taken at each grating plateau was done not just to improve the SNR at each wavelength, but to also minimise the effect of these transients. To minimise the effect of the transients (which are especially important in the unchopped mode), the up/down grating scan was made faster in this mode than in the chop-nod mode, and every line repetition requested by the observer was doubled internally. The duration of a single grating plateau was [4 integrations] x [1/8 sec integration time] = 1/2 seconds, i.e. 1/4 of that for the chop-nod mode.

3.3.2 The spectral coverage and sampling

Three spectral coverage modes could be chosen, of which only two survived the entire mission:

- **Line spectroscopy** (a.k.a. line-scan). A limited number of defined central wavelengths could be covered with a pre-determined spectral range. The fixed angular range scanned by the grating mechanism was optimised for a given diffraction order to ensure the detection of the full profile of an unresolved line with sufficient continuum coverage symmetric to the line centre.
- **Range spectroscopy** (a.k.a. range-scan). A limited number of spectral ranges could be requested. The upper limit was the full range of the filter band, this then being **SED** mode. The wavelength range was scanned by stepping through the relevant angles of the grating with a selectable grating sampling density (high or Nyquist).
- A *wavelength switching* mode was offered during the first few months of the mission but was then decomissioned in favour of the unchopped line spectroscopy mode.

Spectral lines or ranges could only be requested for a pre-defined combination of spectral bands. The bands that could be chosen in HSPOT were R1 (103–220 μm) + B2B (71–105 μm), or R1 + B3A (51–73 μm). For observations in the 51–55 μm region, band B3A is affected by a red leak : it was recommended to instead use the range spectroscopy AOT from where band B2B could be selected (Sec. **??** and Sec. 5.4). If the observer wanted to mix bands, they needed to create separate AORs and concatenated them, so that they would be sure to be observed consecutively.

Note that the pipeline cuts out all data from the blue camera below 55 μm and above 95 μm, and from the red camera above 190 μm, as these ranges are affected either by the band edge or order leak (Sec. 5.2.3 and Sec. 8.2.3.4).

[3]Transients are events (such as cosmic ray hits, high flux levels, ...) that caused a short- or long-term change to the response of the detector.

At each point in time, each of the 16 pixels of the PACS modules[4] "saw" a slightly offset wavelength compared to its neighbour. This was to improve the spectral sampling when the data from all 16 pixels were combined into a single spaxel-spectrum by the pipeline. In addition to this, in the SED AORs where multiple repeats on the wavelength range were requested, a spectral dither was implemented; this also improved the spectral sampling and the data redundancy. The spectral coverage of this combined spectrum is always slightly lower at the edges of the range, where not all 16 pixels contribute to the spectral coverage, and hence the edges of the spectra have the lowest SNR and more errant features. For line scans, the spectral range with uniform data coverage (the region of highest sensitivity) is at least ~ 4 times larger than the width of an unresolved line. (The dataset called "coverage", found in the Level 2 cubes, is a measure of the number of data-points in each spectral bin: Table 10.9). For range scans, the region of uniform coverage is larger, and for the full SEDs only a few wavelength bins at the spectral edges are so-affected.

Data from the red and blue camera was always obtained simultaneously, and the camera with the selected spectral range was known as the "prime" (nominal), the other camera was then the "parallel". If the observer specified a line in a blue band, then the parallel red band would be at a wavelength $2\times$ (B2B) or $3\times$ (B3A) that of the blue wavelength, and similar applies if the spectral line chosen falls in the red band. The choices observers could make when defining their AOTs is given in Table. 3.2. Note that it was possible to chose a wavelength range in one camera that resulted in a wavelength range in the other camera that fell outside of the band limits (these ranges would then be cut out by the pipeline).

In both the line and range spectroscopy AORs, the grating step size (i.e. the distance between consecutive wavelengths) was set by the chosen band and the spectral sampling *of the prime camera*. The step sizes set for the red and blue cameras are not the same: see Tables 3.4 and 3.3 in the following sections. For instance, the 80–90 μm range is observed as a prime range with step size 188 in the 2nd order, but this range is also observed as the parallel for observations with the prime range 160–180 μm in 1st order, for which the grating step size is 240. This second spectrum has a sub-optimal wavelength sampling in the blue range. Archive users should bear this in mind when looking at spectral ranges from the parallel camera, especially when comparing similar spectral ranges from the prime and parallel cameras.

Observers were asked to input the expected line and continuum fluxes from their source. This was used by the uplink logic to set the integrating capacitance (Sec. 2.5.5), particularly to minimise the chance of saturation. Based on the continuum and line flux estimates entered by the observer, the expected maximum photoconductor signal level was estimated by the observing logic. The appropriate integrating capacitance of the CRE was then chosen for the entire observation to avoid saturation.

3.3.2.1 Line spectroscopy

At each grating plateau[5], 8 integrations of 1/8 sec integration time were taken. With two on-off-off-on cycles per plateau, the total time was 2 seconds.

In line spectroscopy it was possible to chose a combination of 10 lines and/or line repetition factors: anything from 10 separate lines with only 1 "repetition" to 1 line with a 10 repetitions. The repetition factor refers to the number of consecutive grating up-down scans. This could be combined in the

[4]The PACS detector consists of 25 modules with 16 pixels measuring the spectrum of each module: Sec. 2.5.5. The pipeline turned this 25×16 into the 5×5 spaxels in the PACS cubes.

[5]plateau refers to a single chopper, nod, or grating position where a sequence of data-points were collected

Table 3.2: The choices of bands that observers were offered in HSPOT. For a prime range chosen from band 1, a parallel range came in band 2, and vice versa.

AOT	Band 1	Wavelength (μm)	Band 2	Wavelength (μm)	Sampling
Line scan	B3A	51–73	R1	146–220	deep
	B2B	71–105	R1	140–210	deep
	R1	102–146	B2A	51–73	deep
SED	B2A	51–73	R1	102–146	Nyquist
	B3A	51–73	R1	153–219	Nyquist
	B2B	71–105	R1	140–219	Nyquist
Range scan	Any range within the SED limits could be chosen				Nyquist/deep

AOR with any number of nod repetitions. For the unchopped mode, while the user could chose the number of repeats to do on each spectral line in the on-source position, but in the off-source position the grating scan was done only once for each line.

The spectral coverage ranged from 0.35 μm in the blue order 3 to 1.8 μm in the red. The sampling density per resolution element is higher than 3 samples per FWHM of an unresolved line in each of the 16 pixels of each module and at all wavelengths. The scanning parameters, including grating steps, sizes, wavelength coverage, range, and spectral density, are given in Table 3.3. Fig. 3.4 is the visualisation of a chop-nod line scan AOT, and Fig. 3.5 of an unchopped line scan AOT. For the unchopped mode, more steps where taken than in the chop-nod mode, resulting in a longer wavelength coverage with the same spectral sampling, however as less time was spent at each grating position, the overall integration time was similar for the two modes.

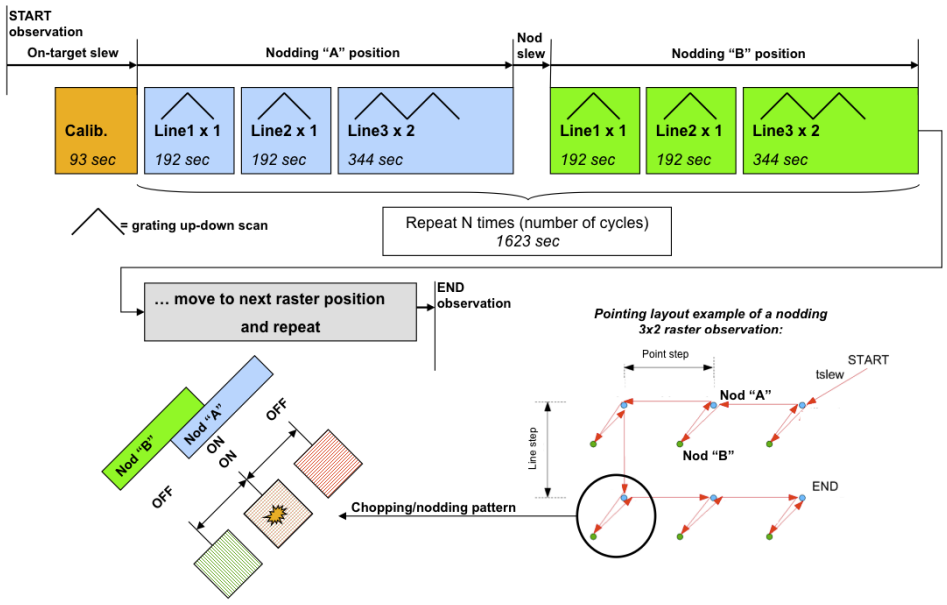

Figure 3.4: The observing pattern for chop-nod AOTs. **Upper** part shows how the requested spectral ranges fit into the nods. **Lower left** shows the chopping pattern (see also Fig. 3.3). **Lower right** part shows the pattern of nod A–nod B for a mapping observation (Sec. 3.3.3).

The bright line mode offered a shorter spectral coverage and a shorter observing time. For the *chop-nod bright line mode*, up and down grating scans were still performed in this mode, but with only 10

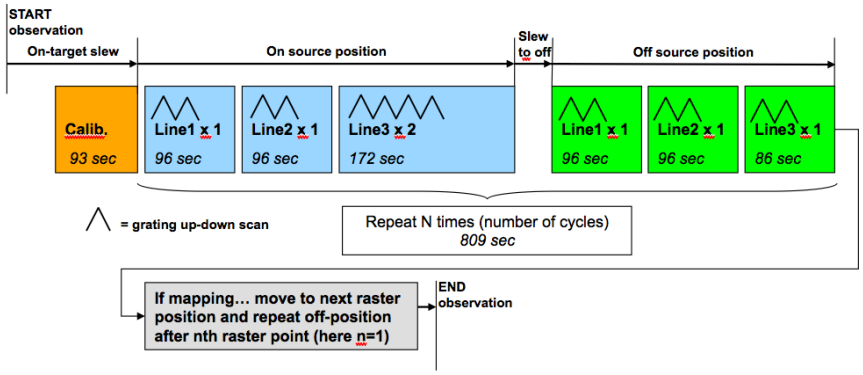

Figure 3.5: The observing pattern for unchopped AOTs, showing how the requested spectral ranges fit into the on-source and off-source nods, and that the repetition of the off-source scans was always only one.

grating steps taken, the on-sky time was about 3 to 4 times shorter than in the standard mode. The minimum total observing time (one line, one cycle) was about half that of the standard mode, and it was about twice less sensitive. In the bright line mode – even for unresolved lines – the central 3 pixels in the 16-pixel modules do not see the continuum, as they scan over the line profile only. For the *unchopped bright line mode*, fewer grating steps were also taken, 50 rather than 75, resulting in a reduced wavelength coverage and an integration time reduced by by 1/3. Everything else remains the same.

A catalogue of common spectral lines was offered in HSPOT for users to chose from, or they could request their own wavelength. If the observed specified a redshift, the wavelength range would be shifted by the appropriate amount.

3.3.2.2 Range spectroscopy

Range spectroscopy AOTs allowed observers to chose their own wavelength range; this was used to cover broad lines, several lines at once, or the entire chosen band in one go ("SED" mode).

Chosing ranges: A combination of 10 ranges and/or range repetition factors was allowed: anything from 10 separate ranges with repetition factor 1 to 1 range with a 10 repetitions. As with line spectroscopy, the default was to do each grating scan twice (up and then down), so for these a repetition factor 2 meant that it was done four times. This could be combined in the AOR with any number of nod repetitions.

Chosing the SED: This mode allowed the observer to observe the entire range of the band chosen. Only one choice of band (one blue+red combination) could be chosen in a single AOR, but users could ask for multiple range and nod repetitions factors. To observe the entire spectral range of PACS (the entire SED), the red and blue camera ranges with two separate observations was necessary.

Two spectral sampling densities were offered: high, which gave the same sampling as for line spectroscopy, or Nyquist, which was shallower by a factor 10–13 and hence allowed for faster grating scans. Nyquist sampling was the only choice possible for the SED mode, as otherwise the observation would have taken too long. The scanning parameters, including wavelength coverage, range, and

Table 3.3: The grating, wavelength range, and sampling details for line spectroscopy AOTs. The oversampling factor gives the number of times a given wavelength is seen by multiple pixels in the homogeneously-sampled part of the spectrum. "Bright" and "faint" refer to bright-line or normal spectral mode.

Band	Mode	Wavelength	Grating step size		Grating steps		oversample factor	
		range (μm)	faint	bright	faint	bright	faint	bright
B3A	CN	51–73	168	384	48	10	41.1	80
B3A	UN	51–73	168	384	75	10	41.1	80
B2B	CN	71–105	188	368	46	10	36.2	80
B2B	UN	71–105	188	368	75	10	36.2	80
R1	CN	103–220	240	344	43	10	27.9	80
R1	UN	103–220	240	344	75	10	27.9	80

Band	Wavelength	Instantaneous coverage		FWHM	
	μm	μm	km s^{-1}	μm	km s^{-1}
B3A	55	0.26	1420	0.021	114
B3A	70	0.28	1400	0.020	98
B3A	72	0.14	580	0.013	55
B2B	75	0.43	1720	0.039	156
B2B	90	0.24	1220	0.036	121
R1	105	1.06	3030	0.111	318
R1	158	0.87	1650	0.126	239
R1	175	0.78	1340	0.124	212
R1	210	0.50	715	0.098	140

spectral density, are given in Table 3.4. The instrument FWHM in this mode is the same as is given in Table 3.3.

Table 3.4: The grating and spectral sampling details for range spectroscopy AOTs The oversampling factor gives the number of times a given wavelength is seen by multiple pixels in the homogeneously-sampled part of the spectrum. The Instrument FWHM is the same as for line-scan AOTs: Table 3.3.

Band	Wavelength	Grating step size		oversample factor	
	range (μm)	Nyquist	SED	Nyquist	SED
B3A	51–73	168	2220	41.1	3.1
B2A	51–73	188	2300	36.7	3.0
B2B	71–105	188	2400	36.2	2.8
R1	102–220	240	2500	27.9	2.7

To improve data quality for Nyquist sampled observations, a spectral dithering scheme was implemented: if the line repetition factor was > 1, then subsequent scans were performed with a small spectral offset; this improved the spectral sampling of the combined spectrum.

To increase the depth of high sampling density range scans, even for relatively short ranges, observers were advised to increase the range repetition *and* the number of nodding cycles. As the timescale of the drifts in detector sensitivities should be considered shorter than an hour, they will be better corrected with shorter nodding cycle durations.

3.3.2.3 Wavelength switching

The wavelength switching mode was superceeded by the unchopped line scan mode after the PV phase, which it was aimed at the same sorts of observations but produced superior results. The continuum flux level recovered by the wavelength switching mode is not preserved, and line profiles are not reliable if: a noticeable gradient is present in the continuum flux over the performed wavelength throw, or if blends or line forests disturb the wavelength-switch interval.

In wavelength switching mode, the line was scanned with the same grating step as in chopped line spectroscopy, i.e. every spectral pixel was sampled at least every 1/3 of a resolution element. This step was called a "dither" step. At every dither step, the signal was modulated by moving the spectral range over about half of the FWHM of an unresolved line. This allowed one to measure a *differential* line profile, canceling out the background. The modulation on every scan step followed an AABBBBAA pattern, where A is a detector integration at the initial wavelength, and B is a detector integration at the wavelength-switched wavelength. This cycle was repeated 20 times in one direction, and repeated in the reverse wavelength direction. The switching amplitude was fixed for every spectral band.

To create the clean source spectrum, an off position was visited at the beginning and the end of the observation (via a telescope movement, not a chopper throw), where the same scan was was performed every two or more raster positions.

3.3.3 The spatial sampling

A single pointing was the basic PACS spectroscopy observation. Its FoV was $47''\times47''$ with square spaxels of about $9''.4$ on a side – these spaxels are not completely contiguous and are distributed on a slightly irregular 5×5 grid (e.g. see Fig 5.9). The beam of PACS varies from about $9''$ to $13''$ over the spectral range of PACS: it is clear that a single pointing therefore spatially undersamples the beam.

Pointed observations were suited for point and slightly extended sources, for which post-pipeline correction tasks allow a fully-calibrated spectrum to be extracted from the cubes produced for single pointing observations. The point and slightly-extended source calibrations are explained in Secs 8.3.3 and 8.3.4). However, many extended sources that were slightly smaller or larger than the field-of-view of the PACS IFU were also observed in this mode. Archive users of this data should bear in mind the limitations of undersampling the beam for these observations.

A mode called *Pointed with dither* was offered prior to launch to perform a small (1×3) raster with $2''$ step size. However, during the PV Phase it was found that for sources with a well-known and confined photocenter, the pointing accuracy of *Herschel* was sufficient to allow for a reproducibility of the line fluxes on the percent level with well-behaved line centres and shapes. This mode was therefore discontinued in favour of the Pointed mode.

Observers wishing to cover either a larger field or a slightly-larger field with finer spatial sampling could use the **mapping mode**. Mapping observations came in three flavours: tiling, Nyquist mapping, or oversampled mapping, and these are summarised in Table 3.5 (Table 10.7 is also a good reference). Fig. 3.6 shows the pointing pattern of the recommended raster patterns for a Nyquist-sampled mapping observation.

For the *tiling mode*, the sampling of the beam is the same as with pointed observation. *The Nyquist mode* obviously Nyquist-sampled the beam. The steps are in this mode are larger than a spaxel, but, as can be seen in Fig. 3.6, the resulting sampling is finer than a spaxel. For the oversampled mode

Table 3.5: The recommendations for raster settings for the various mapping modes. Y and Z direction are the in the instrumental plane (Y is in the PACS chopping direction).

Mode	Offsets (Y,Z)		Nr. of steps		Use case
	blue	red	blue	red	
Tiling	34″–47″		any		To create a larger field where the spatial sampling was less important
Nyquist	14.5″,16″	22″,24″	3×3	2×2	To Nyquist sample the beam at the wavelength of the observation
Oversample	3″,3″	4.5″,4.5″	3×3	2×2	To oversample for the best image reconstruction

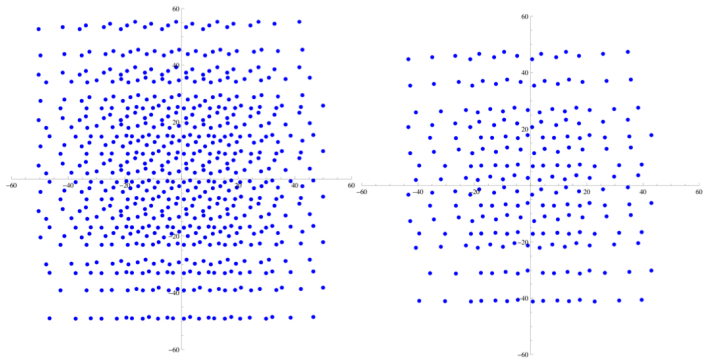

Figure 3.6: Spatial sampling by all PACS spaxels when using a 5×5 raster with step size 14.5″×16″ for the blue camera (left), and a 3×3 raster with step size 22″×24″for the red (right) camera.

where the beam is oversampled, the very small step sizes allow for a better image reconstruction using the mosaic tasks of the pipeline, and this mode was suited for science cases where the source's morphology was of prime interest.

In mapping AORs, it was necessary to set the number and spacing of the raster steps. For chop–nod observations the map could only be defined in instrument coordinates (Y and Z), and the map size was restricted to 6′×6′ so clean offset positions with the large chopper throw could be obtained. In the unchopped mode the map could be defined in instrument or sky coordinates, with a maximum size of 2°.

When defining their mapping AORs, observers using the unchopped mode had to be careful about where to place and with what frequency to observe their off positions: see Sec. 3.3.1. For the chop-nod mapping modes, the only extra restriction was that only the large chopper throw was possible.

For mapping observations, the observer could specify the number of raster positions to place between visits to the off-source block, e.g. for a 2×2 raster, asking for a repeat of 4 would result in the off-source block taking place at the end of the raster.

Chapter 4

In-flight Performance: Photometer

4.1 Introduction

This chapter gives the final calibration accuracies for PACS photometry observations and the details of the performance of the instrument in-flight: in short, the necessary information to optimally interpret PACS observations.

4.2 Saturation thresholds

Table 3.1 in Sect. 3.2 lists the saturation levels used by the observation planning to switch between "high" and "low" gain setting for the ADC conversion. These numbers were conservatively-chosen to ensure that saturation was avoided for most of the detector pixels. In fact, the different matrices making up the PACS photometer arrays showed quite different dispersions in dynamic range and hence in saturation level. Table 4.1 provides an estimation of saturation thresholds obtained using an image simulator, depending on whether none of the pixels, 50% of the array pixels, or all of the array pixels become saturated.

Table 4.1: Estimated flux thresholds, meaning saturation of the pixels for none of, half of, and all of the pixels for the nominal high-gain and bright-source low-gain setting.

filter	high gain saturating flux for % of pixels			low gain saturating flux for % of pixels		
	0% [Jy]	50% [Jy]	100% [Jy]	0% [Jy]	50% [Jy]	100% [Jy]
blue	125	751	1251	250	876	1502
green	331	1434	2317	552	1655	2758
red	1213	3639	4852	1213	4367	7278

For scan maps, where many detector pixels cross the source, considerably higher saturation levels than those given in Table 3.1 could be achieved. This is demonstrated in the brightest calibration sources observed with PACS: the two Galilean moons Ganymede and Callisto, both with fluxes of about 1330 Jy at 70 μm (Müller et al., 2016). Fig. 4.1 shows one of the scan maps and its corresponding coverage map[1]. In this most critical filter with regard to saturation levels. The coverage map shows clear dips at the mid-positions of the two moon images, indicating that some of the pixels had to be excluded in image reconstruction because they were saturated. At Callisto's position the coverage decreases from a value of about 6200 to 3368, which means that only 54% of the available pixels contributed to the reconstructed image at this point, hence a saturation of about 46%. This is even more favourable than what would be expected from Table 4.1, where above 876 Jy half of the pixels should be saturated and 1500 Jy is the absolute limit for all pixels. This is likely because the bright source does always cross a full detector pixel, but just an edge, so reducing the percentage of saturated pixels.

The brightest PACS photometer primary flux calibration source, Uranus, with a maximum measured flux of about 900 Jy at 70 μm on OD 789, (Müller et al. 2016), was observed in low gain mode; its coverage map (Fig. 4.1) indicates a slight decrease in coverage and hence a saturation of 4–5%.

Hence, the coverage map is a good diagnostic tool to detect noticeable or severe saturation for a very bright source. For a detailed analysis of which pixel was saturated in which frame the Level 1 saturation masks can be inspected (cf. PACS Data Reduction Guide: Photometer, section 4.2).

4.3 Sensitivity and flux uncertainty

4.3.1 Sensitivity prediction

The sensitivity prediction for a given observing time t_{obs}[2] was calculated in HSpot as:

$$\frac{S}{N} = \frac{f_\nu}{f_{1\,\sigma,1\,s}} \sqrt{n_{\rm rep}\, f_{\rm t}^{\rm (AOT)}\, t_{\rm obs}} \tag{4.1}$$

with $f_{1\,\sigma,1\,s}$ being the 1 σ ($\frac{S}{N}$ = 1) flux uncertainty achievable with an integration time of 1 s, and $f_{\rm t}^{\rm (AOT)} = \frac{t_{\rm sint}}{t_{\rm obs}}$ being the fraction of the on-source integration time to the observing time, and $n_{\rm rep}$ the number of repetitions of the basic observing pattern. For on-array chopping $f_{\rm t}^{\rm (AOT)} = \varepsilon_{\rm chdutycyc}$ (duty cycle of the chop pattern $\geq$90%), for off-array chopping $f_{\rm t}^{\rm (AOT)} = \frac{\varepsilon_{\rm ch}^{\rm (duty)}}{2}$, and for scan mapping $t_{\rm sint}$ is the sum of all times the source crosses any pixel of the array (the coverage).

Eq. 4.1 shows that the S/N prediction scales linearly with the source flux and with the square root of the on-source integration time.

[1] The coverage map gives the sum of all complete (= 1.0) or partial (< 1.0) coverage occurrences of each map pixel by any physical detector pixel, reduced to the specified drop size, from all unmasked read-out frames along the scan time-line. It is one extension of the Level 2 or 2.5 photometry FITS files, cf. PACS Products Explained document.

[2] $t_{\rm obs}$ is defined as the time to execute the basic AOT observation pattern on the sky; the total time $t_{\rm tot}^{\rm (AOT)}$ includes the number of repetitions $n_{\rm rep}$ and the overheads such as instrument set-up, internal calibration, and target acquisition

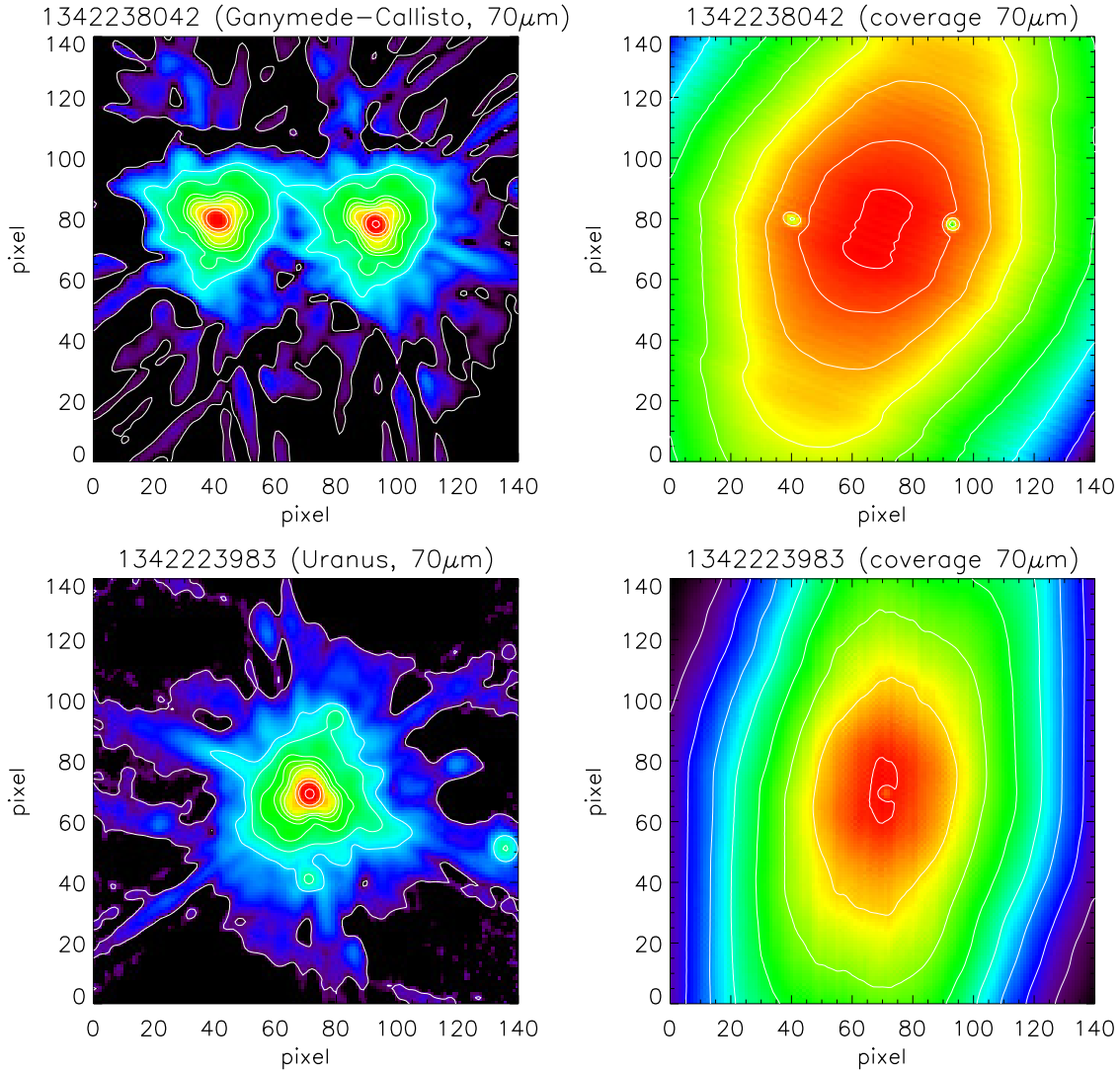

Figure 4.1: Check for saturation by very bright sources. **Upper left**: Scan map (OBSID 1342238042 on OD 981) of the two Galilean Moons Ganymede (left) and Callisto (right) at 70 μm in the low gain setting. The map is fully corrected for the motion of Callisto's during the observation, while Ganymede has a residual proper motion leading to a slight elongation of its image. **Upper right**: Corresponding coverage map showing reduced coverage (green dots) at the mid position of the two moons' location due to partial saturation. The contour line circumventing the dip in coverage at Callisto's mid position corresponds to a coverage value of 6200. The minimum coverage measured at the mid-position of Callisto is 3368. **Lower left**: Scan map (OBSID 1342223983 on OD 789) of Uranus. **Lower right**: Corresponding coverage map showing reduced coverage at Uranus' mid position. The contour line circumventing the dip in coverage at Uranus' mid position corresponds to a coverage value of 615. The minimum coverage measured at the mid-position of Uranus is 581.

Pre-flight, $f_{1\,\sigma,1\,s}$ was modeled by instrument specific parameters (see e.g. presentations by A. Poglitsch on PACS Instrument Model and Performance Prediction for SVR 1 and SVR 2) according

to:

$$\frac{f_\nu}{f_{1\,\sigma,1\,s}} = \frac{f_{\rm PSF}\ F_{\rm photband}}{NEP} \tag{4.2}$$

with NEP (Noise Equivalent Power in W/$\sqrt{Hz}$) being the signal power of a bolometer pixel that gives a $\frac{S}{N}$ = 1 in a 1 Hz output bandwidth (e.g. chopping with 1 Hz, integrating on-source for 500 ms) as a measure of the sensitivity of a photodetector. The NEP of the PACS bolometers had two components: (1) the detector read-out noise $\mathrm{NEP_{det}}$ and (2) the photon noise of the telescope background $\mathrm{NEP_{back}}$. The detector read-out noise depended on the read-out mode (cf. Sect. 2.4.2.4), with the direct mode being more sensitive and the double differential correlated sampling (DDCS) being more robust against EMC– the direct mode was finally the one used during the mission. Calculation of the $\mathrm{NEP_{back}}$ required a telescope model with background and stray-light temperatures and emissivities and the knowledge of the detector quantum efficiency. The factor $\mathrm{f_{PSF}}$ is the coupling factor of the array to the sky giving the fraction of the point-spread function centred on one pixel.

As shown in Sect. 7.4.2,

$$\begin{aligned} F_{\rm photband} &= T\ A_{eff} \int_{\lambda_1}^{\lambda_2} \frac{c}{\lambda^2}\ f_{\nu,s}(\lambda)\ S(\lambda)\ d\lambda \\ &= T\ A_{eff}\ f_{\nu,1}(\lambda_0)\ \frac{c}{\lambda_0} \int_{\lambda_1}^{\lambda_2} \frac{1}{\lambda}\ S(\lambda)\ d\lambda \\ &= T\ A_{eff}\ \frac{c}{\lambda_0}\ \frac{\Delta\nu_0}{\nu_0}\ K_{cc,s}\ f_{\nu,s}(\lambda_0) \end{aligned} \tag{4.3}$$

Hence,

$$f_{1\,\sigma,1\,s} = \frac{NEP}{f_{\rm PSF}\ T\ A_{eff}\ \frac{c}{\lambda_0}\ \frac{\Delta\nu_0}{\nu_0}\ K_{cc,s}} \tag{4.4}$$

In Table 4.2 relevant numbers are listed for each filter. The NEP was determined by reading the noise at the typical operational frequency of 2 Hz from a representative noise power spectrum (NPS) such as shown in Fig. 4.2, calculating

$$NEP = \frac{NPS(@2\,Hz)}{R^{\rm nom}} \tag{4.5}$$

The point-spread function fraction, centred in a pixel, was determined using the Encircled Energy Fraction calibration files and making the simplification of a round pixel with radius r having the same area as the squared pixel with side length d

$$r = \sqrt{\frac{d^2}{\pi}} \tag{4.6}$$

The 1 σ,1 s sensitivities $\mathrm{f}_{1\,\sigma,1\,s}^{NEP}$ calculated according to Eq. 4.4 are listed in the second last column of Table 4.2.

Table 4.2: Determination of 1 σ,1 s sensitivity $f_{1\,\sigma,1\,s}$. For the calculation, an effective telescope area $A_{eff} = \pi\,(\frac{3.33}{2.})^2 = 8.709\,m^2$ and a constant transmission factor T = $0.9315 \cdot 0.99^{16} = 0.7931$ have been used. $K_{cc,s}$ has been set to 1.0.

λ_0 (μm)	NPS(@2 Hz) (V/$\sqrt{Hz}$)	R^{nom} (V/W)	NEP (W/$\sqrt{Hz}$)	$\Delta\,\nu_0$ (Hz)	$\frac{\Delta\nu_0}{\nu_0}$	f^{pixel}_{PSF}(r)	$f^{NEP}_{1\,\sigma,1\,s}$ (mJy)	$f^{HSpot}_{1\,\sigma,1\,s}$ (mJy)
70	$7.0{\cdot}10^{-6}$	$2.58{\cdot}10^{10}$	$2.72{\cdot}10^{-16}$	$6.48{\cdot}10^{11}$	0.151	0.162 (1.8″)	37.5	30.6
100	$7.0{\cdot}10^{-6}$	$3.30{\cdot}10^{10}$	$2.12{\cdot}10^{-16}$	$5.09{\cdot}10^{11}$	0.170	0.118 (1.8″)	51.1	36.0
160	$1.0{\cdot}10^{-5}$	$4.07{\cdot}10^{10}$	$2.46{\cdot}10^{-16}$	$3.54{\cdot}10^{11}$	0.189	0.160 (3.6″)	62.9	68.5

During the mission, $f^{HSpot}_{1\,\sigma,1\,s}$ was updated according to the in-flight measured sensitivities from deep-field maps and chopped measurements of faint point sources. The comparison of both the two modes showed that the scan map technique (typically with the scan speed of 20″/s) better suppressed the detector low-frequency noise than on-array chopping (typically with chopper frequencies of 1.25 Hz), hence $NEP_{scanmap} < NEP_{chopnod}$ (this was handled by different columns for $f_{1\,\sigma,1\,s}$ in the calibration up-link table PHOTnoise). The values listed in the last column of Table 4.2 are the ones for scan-map photometry.

4.3.2 Noise properties

The PACS photometer noise spectrum had two contributions, (1) from the actual bolometers, the high impedance end of the circuit, and (2) from the subsequent readout electronics chain. The readout electronics generated a flat noise spectrum (Johnson noise) and a low-frequency noise excess at frequencies below ~1 Hz. The noise spectrum of the bolometers was similar, with a low-frequency noise excess and a white noise component at higher frequencies. The bolometer noise was inherently low-pass filtered by the electro-thermal time constant (~30 ms). The shape of the observed noise spectrum can be decomposed into three regimes.

1. A low-frequency excess noise below ~1 Hz due to slow drifts in the bolometer and electronics signal offset.
2. A white noise regime between 1 and 5 Hz. The flattening of the blue matrix spectrum in Fig. 4.2 means that the white noise component becomes comparable to the low-frequency noise above 1 Hz.
3. A white noise contribution from the electronics only above 5 Hz. Since the nominal sampling frequency in-flight was 10 Hz due to on-board averaging, the noise spectrum in Fig. 4.2 is sampled up to 5 Hz, so that the imprint of the bolometer time constant is not visible.

The noise spectra shown in Fig. 4.2 have the shape of a power law of the form $f^{-\alpha}$ with $0.4 \lesssim \alpha \lesssim 0.5$.

One method to remove low-frequency noise is the high-pass filtering method, which subtracts from each detector signal time-line, the time-line filtered by a running-box median filter of a specified radius expressed in readouts (see Sect. 9.1.1.3 for details). Popesso et al. (2012) investigated the resulting

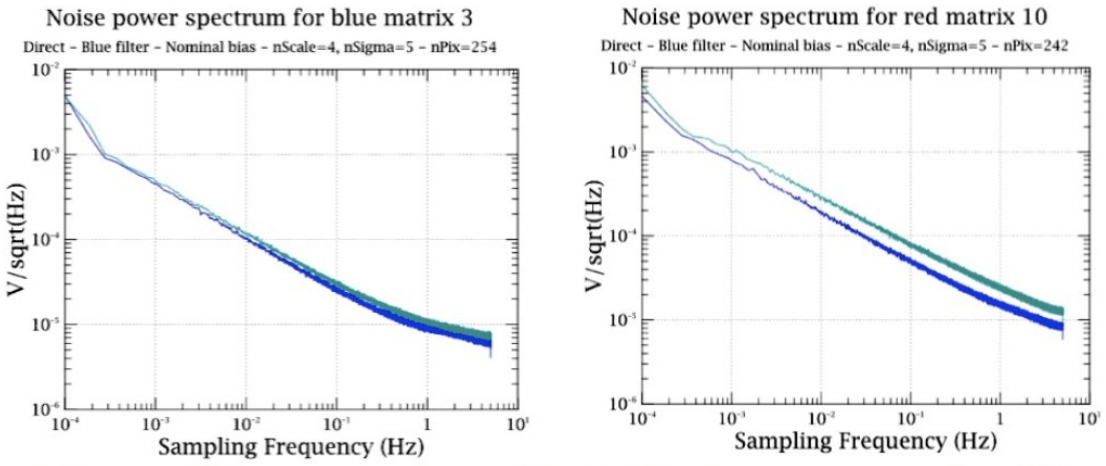

Figure 4.2: Noise power spectrum (NPS) averaged over a whole blue (**left**) and red (**right**) bolometer detector matrix (16×16 pixels). Cyan and dark blue curves represent ground and in-flight measurements (Billot et al., 2010).

noise in detail and its dependence on the selection of the mapping parameters high-pass filter radius, pixel fraction (ratio of the drizzling drop size to input pixel size), and map output pixel size, and including the effects of correlated noise due to the high-pass filtering and map projection. The general noise is described by three parameters, a, b and f, which themselves are parametrised each by sets of 20 parameters given in Table 9 of Popesso et al. (2012)

$$\alpha(\lambda) = \sum_{0\le i+j+k\le n}^{n=3} a_{ijk}(\lambda)\, hpf^i\, outpix^j\, pixfrac^k \tag{4.7}$$

$$\beta(\lambda) = \sum_{0\le i+j+k\le n}^{n=3} b_{ijk}(\lambda)\, hpf^i\, outpix^j\, pixfrac^k \tag{4.8}$$

$$f(\lambda) = \sum_{0\le i+j+k\le n}^{n=3} c_{ijk}(\lambda)\, hpf^i\, toutpix^j\, pixfrac^k \tag{4.9}$$

$$k = 0, n; j = 0, (n-k); i = 0, (n-k-j)$$

The noise per pixel uncorrected for correlation is given as:

$$\sigma_{\rm pix}^{\rm uncorrel}(\lambda)\ \ [Jy] = 10^{\alpha(\lambda)\cdot log(coverage_{\rm pix}) + \beta(\lambda)} \tag{4.10}$$

with $\rm coverage_{pix}$ taken from the accompanying coverage maps[1].

The global noise per pixel corrected for correlated noise contributions is then given by

$$\sigma_{\rm pix}^{\rm global}(\lambda) = f(\lambda)\ \cdot\ \sigma_{\rm pix}^{\rm uncorrel}(\lambda) \tag{4.11}$$

Eqns. 4.10 and 4.11 are the basis for determining the values in the error maps associated with Level 2 products of scan maps generated with the high-pass filtering method (c.f. Herschel Product Definition Document, Sect. 4.1.5).

For a comparison with the sensitivity performance values given in Table 4.2, the following calculation is done

$$f^{\mathrm{HPF}}_{1\,\sigma,1\,s} = \sqrt{N_{\mathrm{pix}}(r_{\mathrm{aperture}})} \cdot f(\lambda) \cdot \sqrt{\frac{\frac{FWHM_{\mathrm{PSF}(\lambda)}}{v_{\mathrm{scan}}}}{1\,s}} \cdot \sigma^{\mathrm{uncorrel}}_{\mathrm{pix}}(HPFrad_{\mathrm{opt}}(\lambda), \mathrm{pixfrac} = 1.0, \mathrm{outpix} = \mathrm{native\,size}, \mathrm{coverage} = 1.0) \quad (4.12)$$

where $\sigma^{\mathrm{uncorrel}}_{\mathrm{pix}}(HPFrad_{\mathrm{opt}}(\lambda), \mathrm{pixfrac} = 1.0, \mathrm{outpix} = \mathrm{native\,size}, \mathrm{coverage} = 1.0)$ is the noise per pixel uncorrected for correlation calculated with the optimum high-pass filter radius for the corresponding filter, drop size and output pixel size equal to native pixel size and a coverage equal to 1 pixel, according to Eq. 4.10. The time a similar source level is seen by a pixel is derived from $\mathrm{v_{scan}}$, the scan speed (20″/s assumed), and $\mathrm{FWHM_{PSF(\lambda)}}$, the full width half maximum of the point-spread function. The noise has to be accumulated inside the measurement aperture, thus is weighted by $\sqrt{N_{\mathrm{pix}}(r_{\mathrm{aperture}})}$ of the number of pixels inside an aperture.

Table 4.3: Determination of 1 σ,1 s sensitivity $\mathrm{f}^{\mathrm{HPF}}_{1\,\sigma,1\,s}$ with Eq. 4.12 for high-pass filtered maps from the parametrised error calculation according to Popesso et al. (2012). Pixfrac is set to 1.0, the output pixel size is 3.2″ for 70 and 100 μm and 6.4″ for 160 μm and the coverage is set to 1.0.

λ_0 (μm)	HPFrad	α	β	$\sigma^{\mathrm{uncorrel}}_{\mathrm{pix}}$ (mJy)	$\mathrm{FWHM_{PSF(\lambda)}}$ (″)	f	$\mathrm{N_{pix}}(r_{\mathrm{aperture}})$	$\mathrm{f}^{HPF}_{1\,\sigma,1\,s}$ (mJy)
70	15	-0.4994	-1.9562	11.1	5.6	1.5121	9.62(5.6″)	27.6
100	20	-0.4134	-2.2659	5.4	6.8	1.5675	14.19(6.8″)	18.6
160	35	-0.4142	-1.5856	26.0	10.7	1.5950	8.78(10.7″)	89.9

This shows that the 1 σ,1 s sensitivity $\mathrm{f}^{HPF}_{1\,\sigma,1\,s}$ derived from global noise properties of high-pass filtered maps is comparable to the predictions.

4.3.3 Noise properties depending on mapping parameters and map-maker software

The effect of the mapping parameter selection on the noise properties is demonstrated in Fig. 4.3, where three different processing versions of the same mini-map on the star β Gem (OBSID 1342232772) are compared. The left image has a drop size of $\frac{1}{10}$ (pixfrac = 0.1) of the native pixel size (3.2″), which is considerably smaller than the output pixel size of 1.6″. The noise looks only little correlated. The middle image has a drop size identical to the native pixel size and the same output pixel size as the first image. Because the output pixel size is smaller than the drop size, quite a clustering of the noise is visible. This is the effect of correlated noise due to the projection. However, note that the standard deviation measured in the two white boxes is lower than those of the left image. The right image has the same pixel parameters as the middle image, but a softer high-pass filter was used. The noise appears again correlated, but here the low frequency noise is less well suppressed: this can be seen in the more prominent streaks. The corresponding correlated noise correction factors f from Eq. 4.9 are 1.39, 2.34, and 2.60, and the global noise per pixel (f·σ, σ as measured in the maps) is 0.260 mJy, 0.264 mJy, and 0.316 mJy, respectively. Hence, the global noise is identical for the same

HPFrad, whereas it is larger for the larger HPFrad. A more detailed systematic investigation of the noise in high-pass filtered scan maps is given in Klaas and Linz (2016)

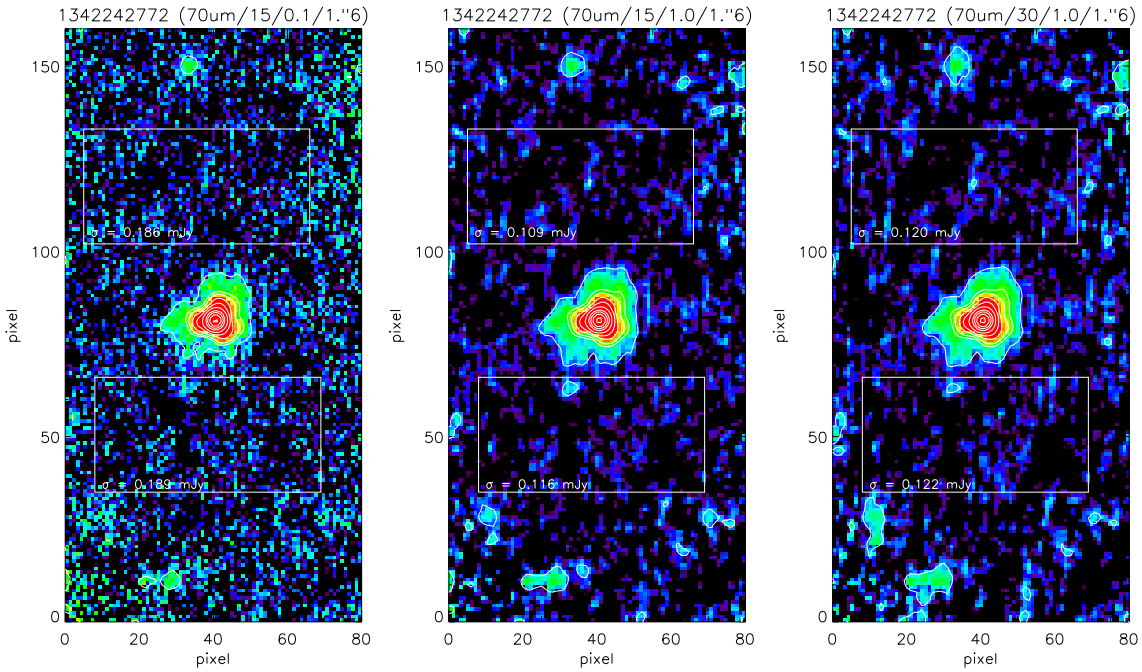

Figure 4.3: Comparison of the results of high-pass filter processing of the same mini-map (OBSID 1342232772) on the star β Gem. Wavelength, high-pass filter radius, ratio of drop size to native pixel size and output pixel size are indicated in the figure title. Identical display cuts have been used for all three images. The indicated σ's are the standard deviation of the fluxes inside the white boxes. See text for an explanation.

Klaas et al. (2017) compared the noise properties of the four main PACS photometer map makers – high-pass filter, JScanam, Scanamorphos and Unimap – for a deep scan map of the faint star HD 152222. Fig. 4.4 shows the area around the star in the 70 μm filter for the four mappers as an example of this study.

- The noise determined from the JScanam map, i.e. uncorrected for noise correlation, is slightly larger (+14%) than that of the HPF map. This indicates that the noise correlation introduced by the JScanam mapper is less than for the HPF mapper. Since both mappers use the same projection algorithm photProject, Klaas and Linz (2017) dug deeper into the issue by conducting a systematic comparison of JScanam-processed maps for different mapping parameter combinations to the corresponding HPF dataset of Klaas and Linz (2016). They determined empirical correlated noise correction factors f for JScanam maps under the assumption that the final corrected noise values are the same for HPF and JScanam maps.
- The noise determined from the Scanamorphos map is slightly smaller (-10%) than that of the HPF map. This indicates that the noise correlation introduced by the Scanamorphos mapper is more than that for the HPF mapper.
- The noise determined from the Unimap map is a factor of 2.1 higher than that of the HPF map. This is explained by the use of the Generalised Least-Squares (GLS) algorithm to remove the

correlated $\frac{1}{f}$-noise by Unimap (Piazzo et al., 2015). The Unimap map noise is hence closest to the real noise level. The correlated noise correction factor f for the selected mapping parameters of the HPF map is 3.13, so that the Unimap noise would need some correction (factor of 1.49) to receive the same global noise value as for the HPF map.

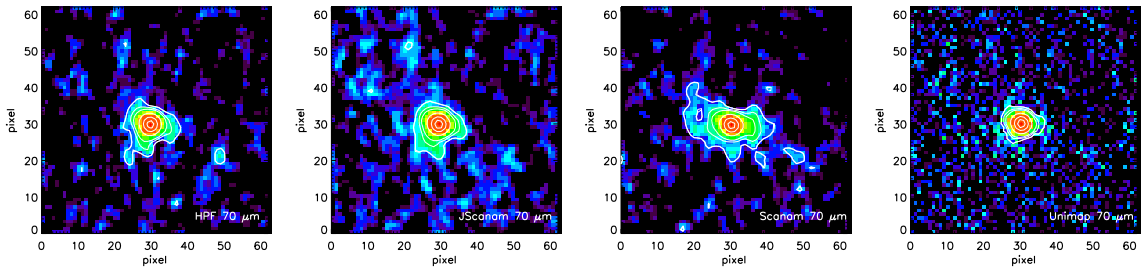

Figure 4.4: Comparison of HD 152222 photometric maps (used OBSIDs are the combinations of 1342240702+03) for different mapper softwares at 70 μm. **From left**: HPF (high-pass filter), JScanam, Scanamorphos and Unimap. Identical drop size (1.0) and output pixel size (1.1″) parameters were used for all mappers. Display cuts are identical for all four images.

4.3.4 S/N dependence on time and flux from observations of faint calibration stars

Klaas et al. (2017) conducted a verification of the predictions of Eq. 4.1, i.e. scaling of the S/N with flux and square root of time for the faint star sample described in Table 6.4.

The S/N of the scan map photometry of the faint stars was determined as

$$\frac{S}{N} = \frac{f_{\mathrm{aper}}}{\sigma_{\mathrm{aper,corr}}} \tag{4.13}$$

with f_{aper} being the part of the source flux measured inside the aperture

$$\sigma_{\mathrm{aper,corr}} = \sqrt{N_{\mathrm{pix}}(r_{\mathrm{aperture}})} \cdot f(\lambda) \cdot \sigma_{\mathrm{pix,uncorr}} \tag{4.14}$$

in analogy with Eq. 4.12. The noise per pixel uncorrected for correlation, $\sigma_{\mathrm{pix,uncorr}}$, was determined with the help of the histogram method described in Klaas et al. (2017) and Klaas and Linz (2016) for coverage values $> \frac{1}{2}$ maximum coverage.

Fig. 4.5 shows several examples of the scaling of S/N, with time represented as integer multiples, i.e. the repetitions of the basic scan-map observation time, and the comparison with the HSpot prediction as formulated in Eq. 4.1.

For 70 and 100 μm measurements, the S/N improves quite closely with the relation $\sqrt{n_{\mathrm{rep}}}$. The ratio of the average measured S/N to the HSpot prediction is 1.14–1.22 at 70 μm and 1.03–1.09 at 100 μm. The HSpot calculation was done for half maximum coverage, so that the measured S/N can be considered as consistent with the HSpot prediction.

For the 160 μm measurements, the S/N improves closely with the relation $\sqrt{n_{\mathrm{rep}}}$ for small n_{rep}. For higher n_{rep} it is obvious that the increase of the measured S/N is flatter. This flattening is caused by

confusion noise, which can be expressed in the following way:

$$\frac{S}{N} = \frac{f_\nu}{\sqrt{\frac{f^2_{1\,\sigma,1\,s}}{n_{\rm rep}\ f_{\rm tAOT}\ t_{\rm obs}} + f^2_{\rm conf}}} \tag{4.15}$$

The constant confusion noise term becomes more dominant the higher n_{rep}, so that the S/N approaches a constant limit. The ratio of the average measured S/N to the HSpot prediction is around 0.80. Note, however, that there is some margin in achievable S/N depending on the selection of the high-pass filter (HPF) radius. In the study of Klaas et al. (2017), an HPF radius of 35 was used. According to the formalism in Popesso et al. (2012), a decrease of the noise by ≈23% between HPF radius = 40 read-outs and HPF radius = 15 read-outs for pixfrac = 1.0 and output pixel size of 2.0″ is calculated.

Fig. 4.6 shows the dependence of the achieved S/N ratios with flux. For the 70 and 100 μm filters, Klaas et al. (2017) verified that the S/N scales linearly with flux over two decades of flux and at least down to total source fluxes of 30 mJy and 18 mJy, respectively. For the 160 μm filter, the linearity with flux could be verified over about one decade in flux down to a total source flux of 85 mJy for repetition factors 1–12. For fainter fluxes measurements with higher ($\geq$ 20) repetitions factors are necessary to achieve a S/N which is sufficiently above values close to the detection limit. As already addressed above, these measurements with high repetition factors are affected by confusion noise and give an increase in S/N that is smaller than expected. Fig. 4.6, 160 μm panel shows one example how measured S/N ratios are matched taking confusion noise into account. Since the confusion noise contribution is not the same in the different source fields, the linearity of the S/N with flux cannot be verified any more straightforwardly in the 160 μm flux range below 85 mJy.

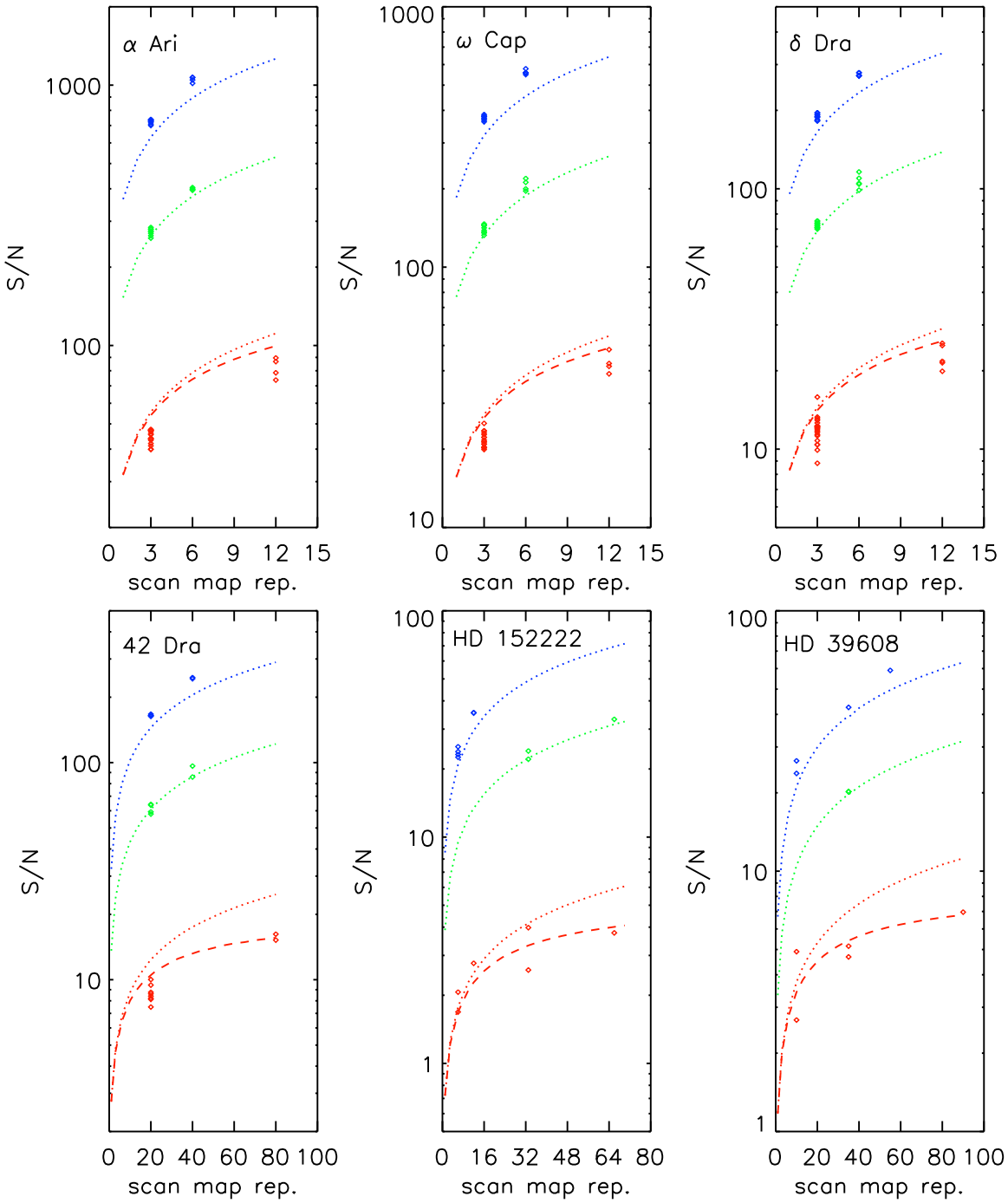

Figure 4.5: Measured S/N ratios for mini scan-map photometry of faint stars depending on the number of repetitions. Blue, green and red symbols represent measurements in the three filters 70, 100, and 160 μm. The dotted lines in the respective colours show the S/N prediction by the PACS exposure-time calculator of the *Herschel* observation planning tool HSpot for the measured colour-corrected stellar flux. Long dashed red lines indicate the S/N prediction including confusion noise (cf. Eq. 4.15 with f_{conf} = 1.3–1.5 mJy).

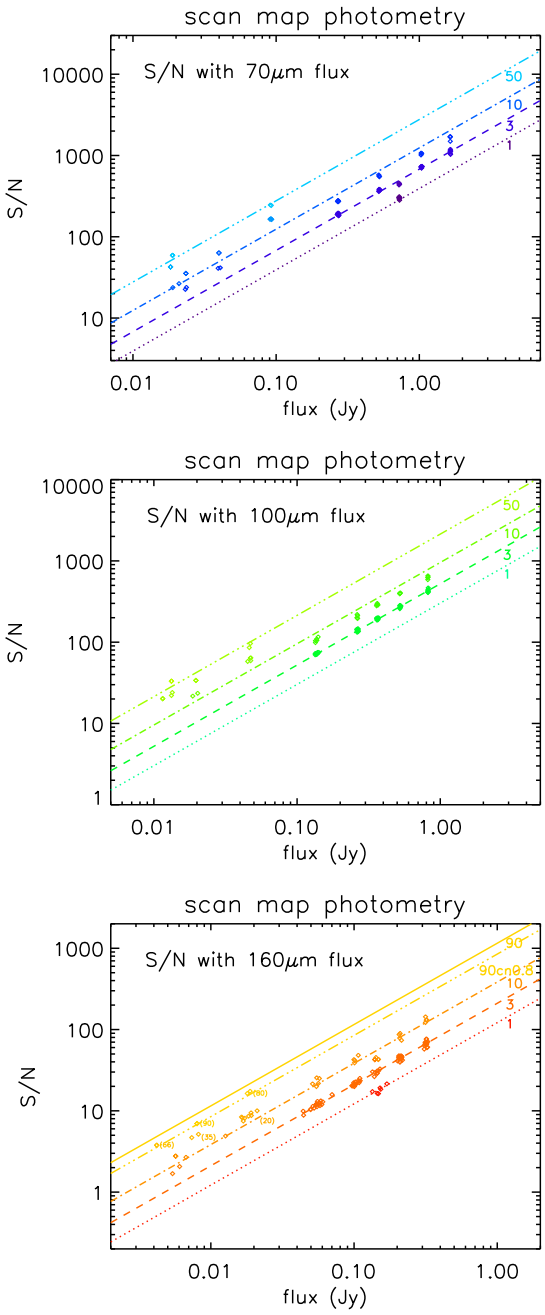

Figure 4.6: Measured S/N ratios for mini-scan map photometry of faint stars depending on the source flux (note: fluxes measured inside the aperture are used here). For better comparability, only measurements with an observational setup identical with the final mini-map set-up (ten 180″ scan legs with 4″ separation and scan speed 20″/s are considered. Lighter colour tones are measurements with higher scan-map repetition factors. Note that here the dotted, dashed, and dashed-dotted lines in different colour tones do not represent the S/N prediction by the PACS exposure time calculator of the *Herschel* observation planning tool HSpot, but are empirical adjustments to the average measured S/N for the respective scan-map repetitions. In the 160 μm panel, numbers in parentheses mark measurements with high repetition factors whose S/N is degraded by confusion noise. This is also indicated by two S/N with flux lines for repetition factor 90, where the lower one includes additional confusion noise of 0.8 mJy.

4.4 Sky confusion

The fainter the source the higher the probability, in particular at 100 and 160 μm, that nearby sources confuse the source flux inside the measurement aperture. Klaas et al. (2017) discuss several examples and the origin of the confusion in the faint star study in detail. Here we include some illustrative examples.

4.4.1 Confusion by neighboring sources

One extreme case of confusion of a faint star by neighbouring sources was encountered in the faint star study by Klaas et al. (2017) for HD 159330. This is demonstrated in Fig. 4.7. While at 70 μm the star ($f_{star,70\,\mu\,m}$ = 65 mJy) is more or less the only visible source inside the field, at 100 μm a small cluster of sources around the star ($f_{star,100\,\mu\,m}$ = 31 mJy) appear, but the star is still the dominant source inside the field. At 160 μm, all surrounding sources are brighter than the star ($f^{expected}_{star,160\,\mu\,m}$ = 12 mJy). The star is blended with the closes source, and hence its local brightness maximum is not as well located on the cross as is the case for the stellar images at 70 and 100μm. It is therefore not possible to obtain reliable photometry for HD 159330 at 160 μm. The compactness of the surrounding sources points to an extragalactic nature of the confusing sources. This is difficult to verify in the optical, since HD 159330 is a 6.2 mag (V band) bright star.

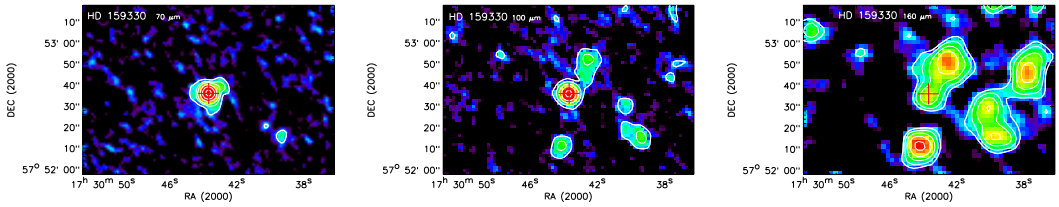

Figure 4.7: Example of confusion by neighbouring sources around the star HD 159330 (OBSIDs 1342213583-86 on OD 628) by comparing maps in the 70, 100 and 160 μm filters. The red cross (arm length equal to 5″) indicates the best common *Herschel* position of the star after frame-centring at RA = 17:30:43.69 and DEC = +57:52:36.0.

For 160 μm source fluxes of 10 mJy and below, the possibility that the PSF of a discrete few-mJy source coincides with any part of the the PSF of the target source is quite high. Differential number counts in cosmological fields, as in fig. 7 of Berta et al. (2011), suggest that there are 9.2×10^3 background sources/deg^2 for $f_{\rm lim} \geq 3.5$ mJy, which gives 0.25 sources per photometric aperture of 10.7″.

The confusion noise in cosmological fields has been determined as $\sigma_{\rm c}$ = 0.27 and 0.92 mJy (for $q = \frac{f_{\rm lim}}{\sigma_{\rm c}} = 5$) at 100 and 160 μm from fields in the *Herschel*-PEP survey (Berta et al., 2011). Information from high-resolution images at shorter wavelengths can help to mitigate the confusion limitations, e.g. Safarzadeh et al. (2015) proposed a technique using graphs and Bayesian priors to improve the photometry obtained from confusion-affected PACS images.

4.4.2 Cirrus confusion

Due to its fractal nature, the infrared emission from background cirrus is not completely removed by the differential measurement techniques used on PACS scan maps, and peaks in cirrus emission will be detected.

A plausible example of cirrus confusion is shown in the left panel of Fig. 4.8 around the faint star η Dra (HD 148387). The map was processed with JScanam which preserves faint extended emission better than high-pass filtering. The map shows a filamentary emission around the star. Indeed η Dra, with $l = 92.6^o$ and $b = +41.0^o$ is located at the edge of the Draco nebula (cf. e.g. fig. 3 in Herbstmeier et al. 1998, a pronounced cirrus cloud. The extract of the *AKARI* Wide-L (140 μm) all sky map[3] (Doi et al., 2015) in the right panel of Fig. 4.8 reveals that η Dra is located at the southern edge of a knot of cirrus with an extension passing north-west into the PACS mapped area. It is obvious that cirrus emission knots lie inside the annulus used to determine the background level. The effect is that too much background is subtracted, leading to a positive excess emission of the source.

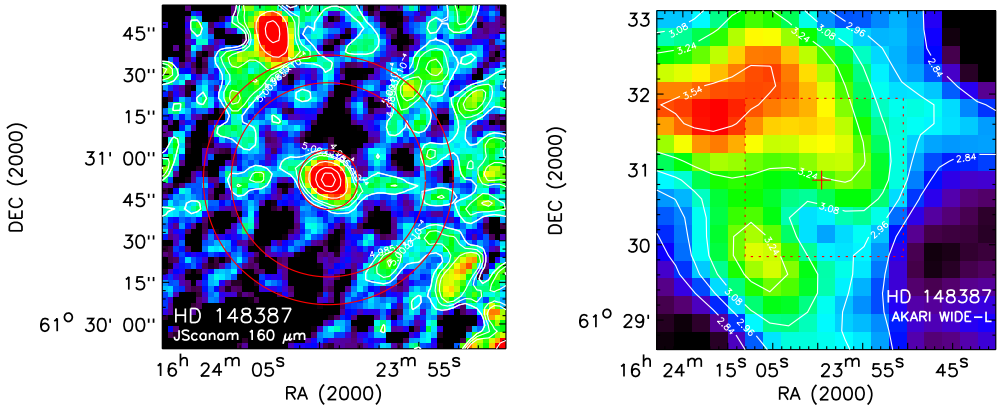

Figure 4.8: Example of cirrus confusion noise around the star HD 148387 (η Dra, OBSIDs 1342186146, ..47, ..55, ..56 from OD 160). The left panel shows a Jscanam map. The innermost red circle is an aperture of 10.7″ radius. The two outer red circles confine a typical annulus used for background determination. The right panel shows the AKARI WIDE-L (140 μm) background emission around the source (red cross), the AKARI map area is about four times as large as the PACS map area, which is indicated by the red dashed square.

Miville-Deschênes et al. (2010) showed with their power spectrum analysis of the Polaris flare, a high galactic latitude cirrus cloud, that the structure of the interstellar medium is well described by a single power law with an exponent α in the order of -3 (-2.7 ± 0.1 for the Polaris flare) at all scales from 30″ to 8^o at the three SPIRE wavelengths 250, 350 and 500 μm, thus extending earlier results from *IRAS* (e.g. Gautier et al. 1992, Miville-Deschênes et al. 2007) and ISOPHOT (e.g. Kiss et al. 2003) to longer wavelengths λ and higher spatial frequencies 1/d. From fig. 3 in Miville-Deschênes et al. (2010) a power $P_0(1/d_0 = 1\,\mathrm{arcmin}^{-1}) = 2.5 \cdot 10^4\,\mathrm{Jy}^2\,\mathrm{sr}^{-1}$ (blue curve) is read for $\lambda = 250\,\mu$m. The cloud has a 250 μm surface brightness $B_0(250\,\mu\mathrm{m}) \approx 20\,\mathrm{MJy\,sr}^{-1}$. Assuming that α and P_0 values

[3] *AKARI* Far-infrared All-Sky Survey maps query service
http://www.ir.isas.jaxa.jp/AKARI/Archive/Images/FIS_AllSkyMap/search/
We use the *AKARI* WIDE-L (140 μm) maps instead of the N160 (160 μm) maps, because the latter ones do not have sufficient S/N over the whole field for illustration of the background structure.

apply also for 160 μm, we can use the formalism in Gautier et al. (1992) to estimate an expected rms cirrus noise as the product of a normalized rms error and the amplitude of the cirrus spectrum.

The normalised rms error is described by the relation:

$$log_{10(normalised\ rms\ error)} = E_0 + \left(1 - \frac{\alpha}{2}\right) \cdot log_{10}\left(\frac{d}{d_0}\right) \tag{4.16}$$

The E_0 are tabulated in table 2 of Gautier et al. (1992) depending on the spatial resolution and the measurement configuration. For a typical PACS 160 μm photometry configuration as shown in Fig. 4.8, the aperture diameter is d = 0.33' (20″) and the central background annulus diameter is θ = 1.33' (80″) giving a separation ratio $\frac{\theta}{d}$ = 4. The resolution ratio at λ = 160 μm is $d \cdot \frac{D}{\lambda}$ = 2.1, with D = 3.5 m. For this combination of α = -2.7, $\log_{10}$(res ratio) = 0.32 and $\log_{10}$(sep ratio) = 0.6, we derive an interpolated E_0(annulus) ≈ -2.824, hence a normalised rms error for PACS 160 μm aperture photometry of $1.11 \cdot 10^{-4}$ sr$^{1/2}$.

The amplitude of the cirrus spectrum is given by

$$A(1/d) = \sqrt{\left(\frac{d_0}{d}\right)^{\alpha} \cdot \left(\frac{B(\lambda)}{B_0(\lambda)}\right)^3 \cdot P_0(1/d_0)} \tag{4.17}$$

making use of the relation P $\propto$ B^3.

For B = 5 MJy sr^{-1} we obtain A(3 arcmin^{-1}) = 4.5 Jy sr$^{-1/2}$ and an expected rms cirrus noise of 0.5 mJy for the measurement aperture d. For computation of a point source representative sky confusion noise, we multiply with the aperture correction factor c_{aper}(160 μm) = 1.56, hence $N^{PACS}_{\text{cirr conf,PS}}$($\lambda$ = 160 μm,B = 5 MJy sr^{-1}) = 0.8 mJy

Klaas et al. (2017) obtained a cirrus noise estimate by proper scaling of the sky confusion noise (1 σ) as parametrised by Kiss et al. (2005) for ISOPHOT measurements which is described by

$$N^{\text{PACS}}_{\text{cirr conf,PS}} = 3.54 \cdot 10^{-2} \cdot C_1 \langle B^{ISM}_{160} \rangle^{\eta} \tag{4.18}$$

with C_1 = 3.37±1.01 mJy and η = 1.46±0.17. For B^{ISM}_{160} = 5 MJy sr^{-1} this formula gives $N^{PACS}_{\text{cirr conf,PS}}$($\lambda$ = 160 μm,B = 5 MJy sr^{-1}) = 1.3±0.7 mJy.

One should note that both estimates give rms noise values based on statistical analysis. Peaks and depressions can significantly deviate from the average. Calculating the cirrus noise from the surface brightness of a larger area will often underestimate the local cirrus noise.

4.5 Determination of the surface brightness offset related to the sky background

Since *Herschel* was only passively cooled, with a main mirror temperature of around 89 K, the signal from the PACS photometer pixels is dominated by the telescope background (cf. e.g. Klaas 2016). Consequently, a differential measurement mode and data analysis must be applied to remove this background. As this includes subtracting the large-scale sky background, the zero level of the extended emission is lost. Because the majority of PACS targets were compact sources, well confined inside the map area, there was no need to reconstruct the total sky background and this is why this was not a PACS calibration requirement. However, for some studies of extended galactic emission, the

knowledge of the total local surface brightness is of advantage (e.g. Abreu-Vicente et al. 2017, Juvela et al. 2015) and therefore some guidelines and recipes that have been used to determine the surface brightness offset of the sky background are given here.

Cold FIR and sub-mm space telescopes with relatively wide beams can reliably measure the lowest sky backgrounds of few MJy sr^{-1}. In particular, all-sky survey missions such as IRAS (Wheelock et al. 1994, $\sim$4′ beam), COBE/DIRBE (Hauser et al. 1998, $\sim$ 42′ beam), Akari-FIS (Doi et al. 2015, $\sim$1.5′ beam) and Planck-HFI (Planck Collaboration et al. 2016a, 4.6′–9.7′ beam) can provide useful reference datasets. With the exception of COBE/DIRBE, which had an absolute calibration source on-board, the absolute calibration of these missions was done with point-like celestial standard sources; the Planck HFI 545 and 857 GHz filters were calibrated against planets, the longer ones against the CMB dipole. This calibration required an accurate knowledge of the beam solid angle at all wavelengths, to convert from Jy/beam into MJy/sr. IRAS (60, 100 μm), COBE/DIRBE (60, 100, 140 μm) and Arkari-FIS (65, 90, 140, 160 μm) have a proper wavelength overlap with the PACS filter bands. Arkari-FIS 140 μm WIDE-L band should be preferred over the N160 band because of the much better sensitivity and S/N. COBE/DIRBE is quite accurate, but its beam size is not very compatible to the PACS pixel scales. Planck maps are very accurately calibrated (<6.5%, Bertincourt et al. 2016), but there is no wavelength overlap with PACS filter bands and assumptions about the shape of the background SED must be made. The best-calibrated IRAS products are the IRIS maps (Miville-Deschênes and Lagache, 2005). Akari maps, which have the best spatial resolution, were calibrated against COBE/DIRBE and achieve an uncertainty of better than 10% in the WIDE-L band for surface brightnesses >25 MJy sr^{-1} (Takita et al. 2015). Important steps in the offset determination are

1. The colour correction of the reference maps with regard to the PACS band. Usually a single modified blackbody of the form ν^{β} B(T,ν) with β = 1.8 – 2.0 and T = 15 – 20 K is assumed as reference SED. Planck and IRAS data can be used to derive a colour temperature (e.g. Abreu-Vicente et al. (2017)). There also exist two component models, e.g. of Meisner and Finkbeiner (2015).

2. The convolution of the PACS images to the resolution of the reference maps, including re-griding to the pixel size of the reference maps. For the convolution, either Gaussian approximations or the true PSFs can be applied (e.g. Juvela et al. 2015).

The latter step is necessary so that the intensity distribution in the PACS maps is as close as possible to the top of the intensity distribution in the reference map, thus allowing the offset determination by linear fits between the PACS image intensity values and the reference image intensity values.

The longer wavelength *Herschel*-SPIRE photometer has an excellent overlap of its 350 and 500 μm filters with the Planck HFI 545 and 857 GHz filters, thus for the SPIRE photometer maps the absolute flux offsets can be determined by cross-calibration against a corresponding Planck map. The following steps, as described in the SPIRE Data Reduction Guide, section 6.10.1, have been used to determine this offset:

1. Colour-correction factors for the Planck maps to convert them to the SPIRE band passes were determined. A modified blackbody spectrum ν^{β} B(T,ν) with β = 1.8 was applied, and the colour temperature determined from the HFI-545 to HFI-857 ratio map. The HFI 857 GHz map was converted to the SPIRE 250 μm and 350 μm band response, and the HFI 545 GHz map to the SPIRE 500 μm band response.

2. The SPIRE maps were converted from Jy/beam to MJy/sr with the appropriate conversion factors for the effective beam solid angles.
3. SPIRE maps were convolved to the HFI beam resolution.
4. A first estimation of the offset was obtained from the difference map of the HFI and the convolved SPIRE maps.
5. With the first offset estimation applied to the full resolution SPIRE maps, the SPIRE maps were embedded in the HFI maps and the composite map was convolved to the HFI beam resolution.
6. The SPIRE map part was de-embedded from the convolved composite map. This act to minimised edge effects before the second difference map is generated.
7. A second estimation of the offset was obtained from the difference map which, was applied as the final offset to the full resolution SPIRE maps without offset.
8. Since the gains for SPIRE and HIFI vary somewhat from the ideal value 1.0, appropriate gain-correction factors could be applied in the offset determination process. The comparison of the absolute gain photometric calibration between HFI and SPIRE is described in detail in Bertincourt et al. (2016).

The procedure described for SPIRE flux offset calibration should also work for the PACS 160 μm band, although the extrapolation of the source background SED introduces a higher uncertainty in the gain and offset values. It will not work for the PACS 70 μm band, since at this wavelength another dust grain population (small grains which are not in thermal equilibrium) is the dominant emission source (e.g. Draine and Li 2007, Planck Collaboration et al. 2014). In the PACS 100 μm band there is still a fair contribution by large dust grains, but there is some contribution by smaller dust grains.

A somewhat more sophisticated method of combining PACS data with Planck data, while attempting to include both a constant offset intensity level and scale-dependent background variation to the PACS map, is described by Abreu-Vicente et al. (2017). The Planck data set transferred to the PACS 160 μm filter is constructed from the Planck all-sky model intensity distribution (Planck Collaboration et al., 2014, 2016b), convolved with the 160 μm bandpass response and converted to the central wavelength monochromatic flux density with the 75″ pixel scale of the Planck healpix data. The Planck map and the PACS map are then Fourier transformed and combined in Fourier space with the appropriate weightings. The final combined image is then the result of an inverse Fourier transform.

4.6 Anomalies and quality control

Anomalies occurred at various points during the mission, and it was the job of Quality Control (QC) at HSC to spot these. Fortunately, few PACS photometer measurements were noticeably affected by either satellite events, instrument anomalies, problematic instrument settings, or space-environment influences. Measurements which suffered from suboptimal instrument performance or instrument/satellite events or anomalies have a corresponding entry in the Quality Control Report (QCR) Summary associated with the *Herschel* Science Archive (HSA) product listing. Quality flags are described in the *Herschel* Product Definition Document Quality Control section. Detailed information on the satellite and instrument events can be found in the Spacecraft Activities and Events Log [password required] and from the MOC daily, weekly and monthly reports on mission and systems status. In the following we describe the most relevant PACS photometer issues in more detail.

4.6.1 Loss of half of the red photometer array from OD 1375 onwards

All PACS red photometer observations starting from 2013-02-17T01:59:31Z, at the end of the mission on OD 1375, show a saturated red matrix #9 with fixed readings FFFF, so that only half of the red photometer array remained operational. In case of sparsely-sampled maps, as with SPIRE-PACS parallel mode, this can mean that the map contains holes. An example is shown in Fig. 4.9. It is important to note that the effect may not be obvious at first glance, and inspection of the QCR is strongly recommended.

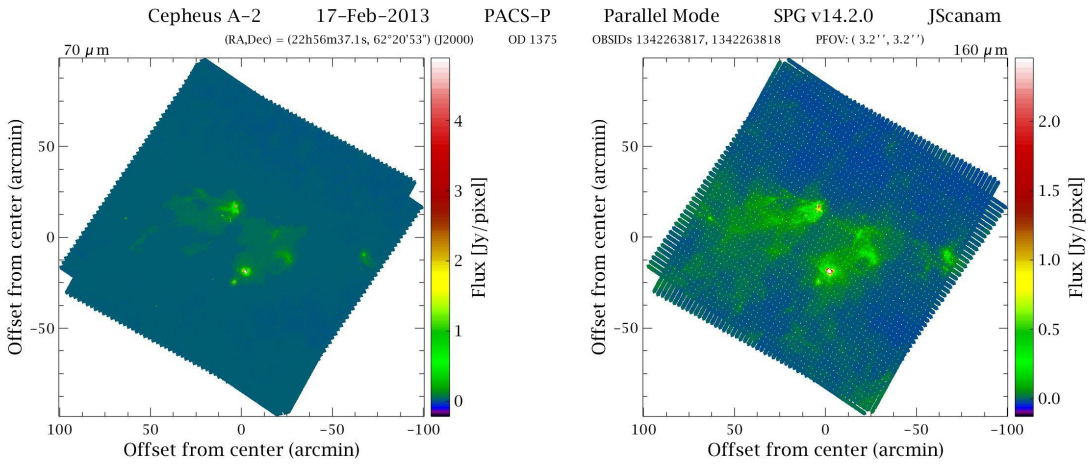

Figure 4.9: Postcard preview of the PACS maps from a SPIRE-PACS parallel mode observation on OD 1375. While the 70 μm map shows full coverage of the mapped area, the 160 μm map shows a hole pattern due to the missing half of the red array.

The effect of the lost red sub-array on mini-map photometry (c.f. Sect. 3.2.2) is shown in Fig. 4.10. The affected map from OD 1377 is compared against a complete map with practically identical orientation on the sky from OD 833 with the following conclusions:

1. The map from OD 1377 is considerably smaller, in particular in the direction south of the star.

2. While the star is located inside the maximum coverage area (at 99.8% of the maximum coverage value 5318.0) in the complete map, it is outside the maximum coverage area (albeit still at 90.8% of the maximum coverage value 2987.3) in the affected map. The coverage ratio OD 1377 / OD 833 is 0.56 for the maximum values and 0.51 at the peak position of the star.

3. Due to the considerably lower coverage (<50%), the noise in the southern box is considerably higher and the noise ratio OD 1377 / OD 833 $\frac{0.116}{0.080}$ = 1.45 is close to $\sqrt{2}$. However, the ratio of the noise ratio determined from the northern box is $\frac{0.079}{0.071}$ = 1.11, because also the coverage ratio is ≈0.75. The average noise ratio from both boxes is $\frac{0.097}{0.076}$ = 1.28, i.e. better than $\sqrt{2}$. The fluxes measured inside a 10.7″ aperture by Klaas et al. (2017) are 151.8 mJy for the OD 1377 map and 152.8 mJy for the OD 833 map.

4. Thus, overall the OD 1377 160 μm observation yields a better S/N than would be expected in case of loss of half of the detector pixels.

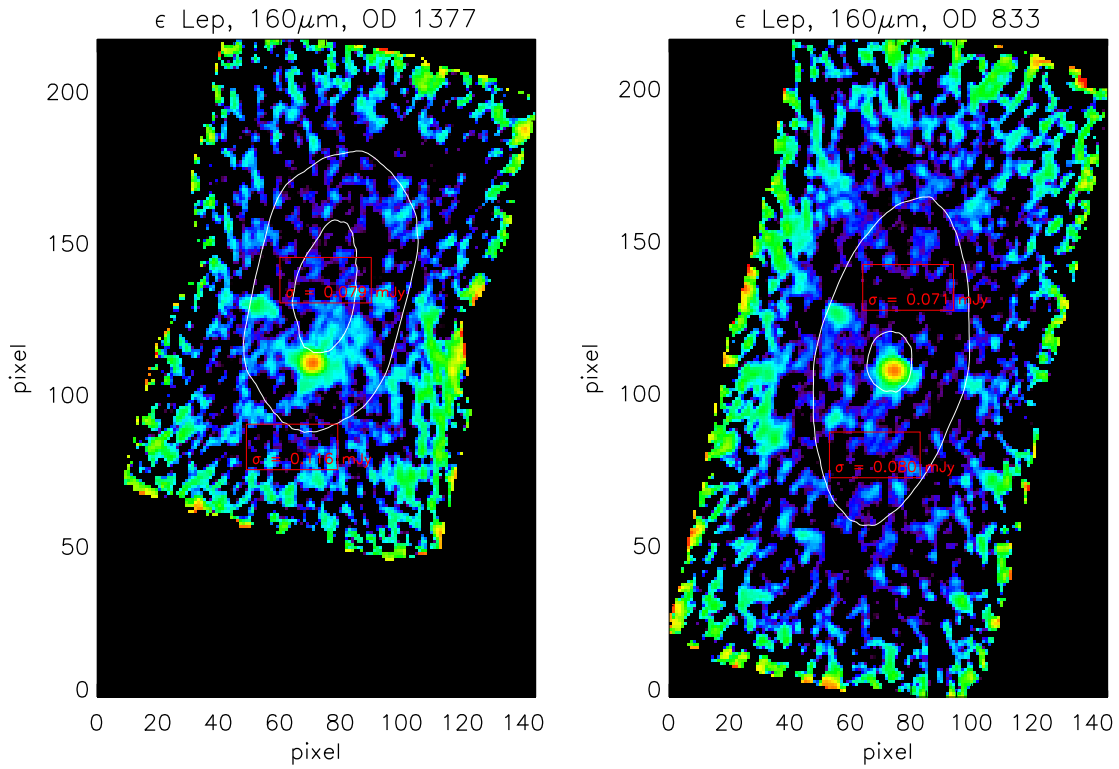

Figure 4.10: Effect of the lost red sub-array (matrix #9) from OD 1375 onwards on mini-map photometry. The overlay of 4 scan maps in the 160 μm filter (two each at 70^o and 110^o map orientation with regard to S/C orientation, 10 scan legs with 180$''$ length and 4$''$ separation) from OD 1377 (OBSIDs 1342263902+903+904+905) is compared with a corresponding one with identical map orientation from OD 833 (OBSIDs 1342227297+298+299+300), i.e. 1.5 year before. The white contours indicate 50% and 95% coverage, respectively. The two red boxes indicate the areas for pixel noise $\sigma_{\rm pix}$ determination.

4.6.2 SPU-S failures due to Single Event Upsets (SEUs)

Twice during the *Herschel* Routine Science Phase there was a Single Event Upset affecting PACS photometer observations with particle hits into the SPU-S (c.f. Sect. 2.2.1.4), the signal processing unit for the blue photometer, interrupting the link to the PACS digital processing unit DPU (c.f. Sect. 2.2.1.1) so that no bolometer science data could be transmitted anymore. This happened on OD 807 at 2011-07-30T02:31:30Z and on OD 1096 at 2012-05-13T22:40:09Z. Both SPU-S failures were cured by a manual PACS power re-cycling during DTCPs 809 and 1098, respectively. During the period between the occurrence of the failure and the power re-cycling, data of the red bolometer array were transferred without any problem. On OD 808 there is only a set of SPIRE-PACS parallel observations. The blue maps are missing in the HSA, and the appropriate QCR flag is set. On OD 807 there is only one pair of failed PACS prime observations, but there were a large number of PACS prime observations on ODs 1096/1097. Since one out of two filters was missing for each prime-mode observation, all were declared failed and were repeated on later ODs. The red bolometer science observations of this period are flagged to be available but are currently not offered in the Herschel Science Archive.

4.6.3 Observations with pointing affected by a thermoelastic drift

The general description of *Herschel*'s pointing performance is presented in the Herschel Mission & Satellite Overview Handbook, section 5.4.3. The knowledge of *Herschel*'s Attitude and Orbit Control system (AOCS) evolved during the mission and so did the pointing quality and pointing reconstruction accuracy (Sánchez-Portal et al., 2014). Post-mission, two essential improvements in the pointing reconstruction with regard to Absolute Pointing Error (APE) and Pointing Drift Error (PDE) were achieved, namely the correction for star-tracker distortions (Sánchez-Portal, 2015, Pointing Updates in HCSS 13.0 Description and performance) and the gyro-based attitude reconstruction (Stephenson, 2016). Both corrections were implemented in HIPE and applied when generating the SPG products that populate the HSA. There is, however, one known but uncorrected AOCS effect which affects the pointing accuracy of a small subset of observations in the HSA. These are observations taken in the warm attitude range with Solar Aspect Angles (SAA) in the interval 110^o to 119.2^o or β-angles between -29.2^o and -20^o (note: the star tracker pointed to opposite direction to the telescope boresight) and in particular when remaining for several hours in this attitude range. In these cases, thermo-elastic deformations of the star-tracker platform occurred, leading to pointing offset drifts along the S/C z-axis. Esquej and Sánchez-Portal (2017) established a relation between Δz-offsets caused by thermo-elastic deformations and the temperature reading of the mostly unused redundant star tracker STR2, which they implemented in an astrometry correction script for observations affected by a thermoelastic drift. If the best astrometry is needed for such observations, and if they are flagged in the Quality Control Report (QCR) Summary with "observation at warm beta angle" and a comment 11Star Tracker 2 temperature ¿ -15 C", then the correction script should be applied. If the comment says "observation immediately preceded by X-hours warm beta period" this is not necessary.

Chapter 5

In-flight Performance: Spectrometer

5.1 Introduction

This chapter provides a summary of the performance of the PACS spectrometer in-flight, of its flux calibration accuracy, and of its spectral and spatial calibration accuracies.

5.2 Flux calibration accuracies

Technical detail on the flux calibration accuracies can also be found in Sec. **??** and it is recommended to read that section. The flux calibration concept and derivation is explained in Chp. 8.

The PACS flux calibration used difference schemes for chop-nod and for unchopped observations. *For the chop-nod observations* it was possible to use data from the the off-source chopping positions to derive the instantaneous detector response at any given time during the observation: the signal from the telescope is so much greater than that from the astronomical "background", so data from these off-source chop positions are effectively measurements of the telescope emissivity, taken continuously throughout an observation. The measured signal of the telescope background is compared to the expected emissivity – derived from an empirical model of the telescope emissivity that was fitted to full-range spectra of Ceres and Pallas taken throughout the mission – to obtain the conversion from detected fluxes to correct *relative* fluxes over the spectrum. The *absolute* level of the flux was set using the absolute scale of the telescope emissivity model, which was fine-tuned using the 109 PACS key-wavelength flux-calibration measurements taken of fiducial stars and asteroids that form the backbone of the flux calibration for PACS spectroscopy (and photometry). *For the unchopped observations*, the observing design did not include observations of the telescope background taken continuously during an observation – rather they were taken as a single block – so instead the detector response is determined from measurements of the internal calibration sources taken at the beginning of all observations. The emissivity of these calibration sources was also calibrated against the flux calibration measurements of the fiducial stars and asteroids.

The PACS spectrometer flux calibration accuracy for the two schemes is slightly different. For both, the accuracy is limited by detector response drifts and slight pointing offsets, which act to modify the flux distribution over the FoV of the observed sources, and are a larger source of error compared to the systematic uncertainties of the calibrators and their models. These limit the absolute flux accuracy

and the relative accuracy within a band. Note that the impact of pointing offsets affects the calibration sources (and hence the flux calibration) *and* any particular observation of a point source, and while they are less important for semi-extended and extended sources, they still have some impact here. Response drifts are important for all and any observation.

The flux calibration of PACS is based on point sources, and hence the calibration uncertainties have been computed for point sources. These same uncertainties apply to extended sources if one considers only single spaxels; how to combine the uncertainties for aperture-integrated fluxes (i.e. for a source spread over spaxels or as mapped in a mosaic cube) is explained in Sec. 5.2.8.

Most of this information in this section is also reported in the Spectrometer Calibration document, however the values reported here are more recent.

A handy summary of the flux calibration accuracies can be found in the spectrometer quick-start guide.

5.2.1 Absolute flux calibration accuracy

The absolute flux calibration accuracy applies to single line fluxes or continuum flux densities at a given wavelength, in any spaxel. Beware of the extra correction needed for the flux falling out of the spaxel(s) for point sources (see later).

The absolute flux calibration accuracy was assessed by comparing the measured flux density at the key wavelengths in every band to the expected (model) flux density for over 100 measurements of fiducial calibration stars and asteroids. Two scatter plots, showing the final calibration results, are given in Fig. 5.1 (these plots are an update to those in this technical note from 2011).

- The standard deviation of the ratio measured/expected flux density over all measurements is 6 to 12% in all bands.
- The systematic error is 1%.

One fiducial calibration star, HD161796, was measured 120 times in the chop-nod mode, 5 times in the unchopped mode. These observations allow one to assess the continuum flux reproducibility: Fig. 5.2.

- The stochastic error (standard deviation) on the reproducibility is better than 4%.
- The peak-to-peak reproducibility variations are better than 15%.

The peak-to-peak scatter is the safest value to take for the absolute calibration uncertainty. This is because this value includes the errors imparted by pointing jitter, pointing offsets, and detector response drifts, which affect *all* observations of *any* source to a greater or lesser degree.

5.2.2 Relative flux accuracy within a band and detection limit for broad features

The in-band accuracy is a measure of differences due to the RSRF/telescope background spectrum shape and those introduced by transient effects (e.g. cosmic ray hits on the detector, which temporarily affect its response), and telescope pointing offsets. The in-band accuracy is a peak-to-peak relative

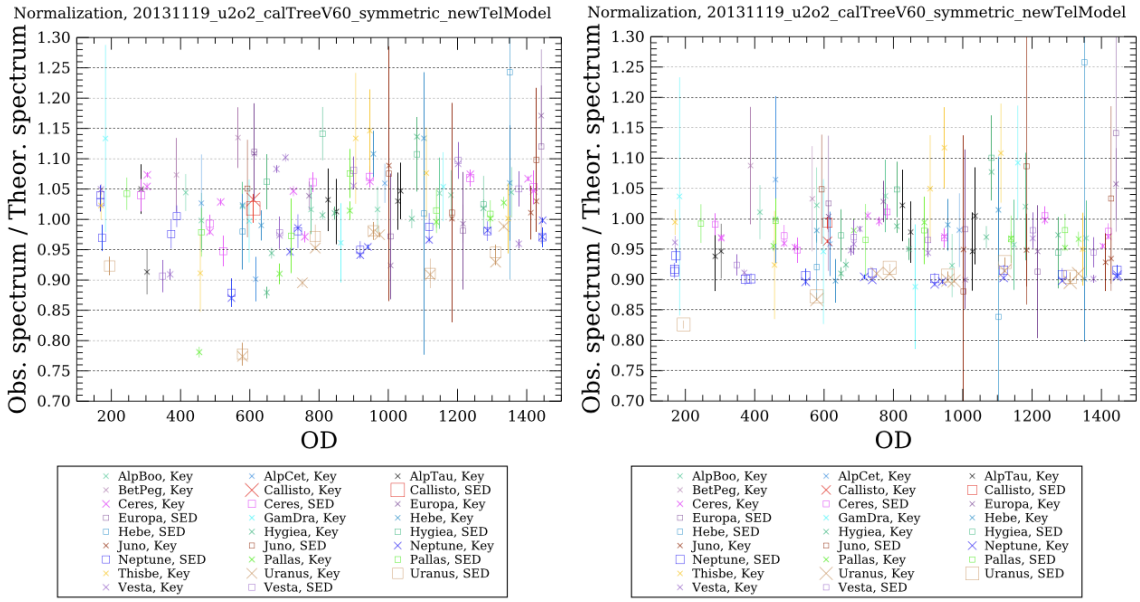

Figure 5.1: The observed-to-expected flux of all the 60 μm (**left**, band B3A) and 150 μm (**right**, R1) key wavelength observations of the celestial calibrators.

accuracy, and it will affect broad spectral features (of width a few micrometers) and the continuum shape. Note that the affect of these will be unique for every observation, so dividing two PACS cubes by each other will not eliminate them.

For chop-nod observations, where the telescope background normalisation calibration scheme is used, the relative flux accuracy within a band is:

- 5% shortward of 150 μm

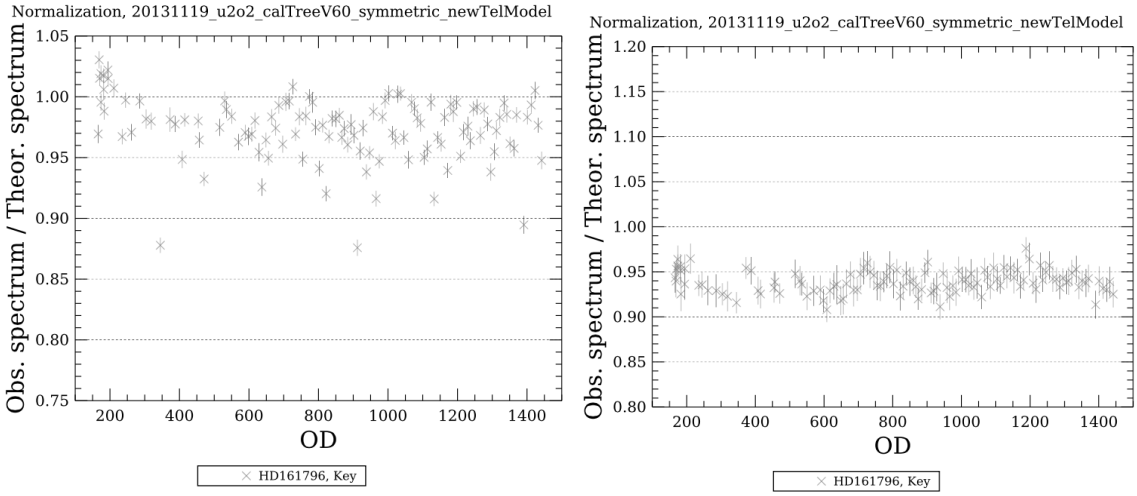

Figure 5.2: Reproducibility measurements of HD 161796 at 60 μm (**left**, band B3A) and 150 μm (**right**, R1).

- 10% longward of 150 μm

For unchopped observations, where the calibration block calibration scheme is used, the relative flux accuracy within a band is:

- 10% across the PACS wavelength range

This is the relative accuracy to assume when comparing line fluxes within a spectral band. When comparing line fluxes across spectral bands, the absolute flux accuracies in Sec. 5.2.1 apply. The relative in-band accuracy is also the limit on the detection of broad spectral features (such as solid-state features, dust continuum shape). These numbers apply to the wavelength regions not affected by spectral leakage; see Sec. 5.2.3.

The in-band accuracies were determined from repeated measurements of the asteroid Pallas in the course of the *Herschel* mission. The observation/model residuals (normalised to the flux at the key wavelength of the band) of the different observations are shown in Fig. 5.3 (which is an update to the figures in this technical note from 2011).

For point sources, it is possible to slightly improve the continuum smoothness (and hence also improve broad-band and faint lines) by using the interactive pointing correction pipeline script provided in HIPE (Sec. 9.2.2). Documentation for this script can be found in the PDRG (spec) and in the point-source documentation found on HELL L2.

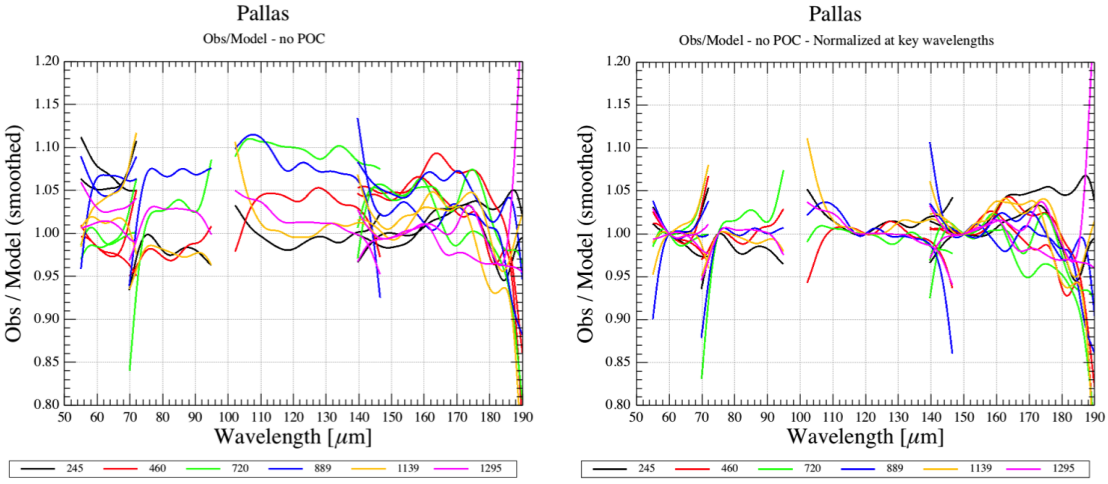

Figure 5.3: The in-band accuracies were determined from repeated measurements of the asteroid Pallas taken throughout the *Herschel* mission. The observation/model residuals (normalised to the flux at the key wavelength of the band) of the different observations are shown in different colours; the numbers in the legend are the OD of the respective observations.

5.2.3 Calibration accuracy above 190 μm

As pointed out in Sec. 5.4 and explained in more detail in Sec. 8.2.3.4, all spectra at wavelengths above 190 μm are contaminated by order leakage from the blue part of the spectrum. This not only affects each observation, but also affects also the flux corrections as applied to standard PACS spectroscopy

observations. A tailored "RSRF" (relative spectral response function) is provided in HIPE to partially correct for this: the fluxes of emission lines will be more correct, however the continuum flux levels will still be extremely unreliable. Using this RSRF, highly-processed data products for all observations that include the spectral range in this "red leak" region have been created, and these are provided via the HSA as "HPDPs" (Sec. 10.4.4.2).

The continuum flux calibration above is 190 μm is totally inaccurate. The accuracy of the line flux measurements is poor: using the HPDPs one needs to multiply all line flux measurements by a factor 1.3 and even then the values should be taken as approximate. More information will be published in a forthcoming paper on the "Cross calibration with Herschel spectrometers".

5.2.4 Calibration accuracy below 55 μm

The region below 55 μm is at the edge of the blue band, and in addition in band B3A this spectral range is affected by order leakage (Sec. 5.4). Therefore, no standard products provided via the HSA include this spectral range. Instead, the uncalibrated spectra are provided as HPDPs (Sec. 10.4.4.2).

5.2.5 Additional continuum flux uncertainties for the chop-nod mode

An additional uncertainty for the absolute level of the continuum arises from the accuracy with which the telescope background spectrum can be determined for any observation. A standard telescope spectrum is used in the calibration scheme for chop-nod observations, and the flux level is adjusted according to the temperature (of the mirror) as recorded in the housekeeping data for each observation before the spectrum is used to convert the observation's fluxes to Janskys. However, it should be noted that since during chop-nod observations the telescope nods between two positions on the sky, with a time gap necessary so the requested spectral range can be covered by the instrument, it is possible that transient effects affect the detector response between the nod A and nod B data being taken. This will affect the certainty of the calibration of the continuum fluxes in the nod A and nod B cubes, and as these are added together at the end of the pipeline, this becomes an additional uncertainty to the continuum level in the science cubes (but *not* to the fluxes of emission lines on top of that continuum). The flux of the telescope spectrum ranges from 300–550 Jy in the blue to 150–300 Jy in the red, and so a drift in the fluxes of even 1% will lead to an uncertainty of 1–5 Jy. In practise we do not see drifts of that level, however we add a note of caution when interpreting continuum flux levels of < 5 Jy.

For a guideline to reproducing the telescope spectrum in HIPE, see this technical note.

5.2.6 Additional continuum flux uncertainties for the unchopped mode

An additional uncertainty for the absolute level of the continuum for all unchopped observations arises from the uncorrected effect of detector response drifts. In the unchopped mode, the off-source data were observed in a block, before, between, or after the on-source data were taken. Long-term "transient" events that often occurred at the beginning of an observation and had a slow effect on the detector response throughout the observation. By changing the response of the detector, the conversion from instrumental units to Jy was essentially rendered incorrect (by a small amount), since the calibration was calculated for single value of the detector response. The Jy that a detector unit was converted to therefore changed slightly through an observation. This had the knock-on effect of making the continuum flux levels apparently change though an observation, and hence when the off-source

data are subtracted from the on-source data, a residual remains, and the resulting continuum level is uncertain.

Based on experiments done in-orbit (see this AOT release note), it was found that reproduction of the absolute value of the continuum in the unchopped mode is not reliable for faint sources, and it was not recommend to use this mode to measure the continuum for continuum sources less than ~ 20 Jy at the desired wavelength. One can hence assume that most observations in this mode were concerned about line emission, rather than continuum fluxes, and archive users should note that having negative continuum levels is most likely a consequence of this additive uncertainty. Tests show that for continuum sources brighter than ~ 20 Jy, the final spectra well matched to a chop-nod equivalent spectrum, but the fluxes are likely to be uncertain in absolute terms by an extra 30%; the shape of the continuum is, however, expected to be reliable.

5.2.7 The additional uncertainties for extended, crowded, semi-extended, or off-centred point sources

The uncertainties discussed previously refer to the spectra of point sources extracted from an observation and to the spectra from any individual spaxel of a cube. When combining the spectra of multiple spaxels–aperture photometry on extended sources–the uncertainties need to be combined. At the practical level, the absolute and relative uncertainties discussed here are uncorrelated when combining spaxel-spectra. Therefore, they should be combined as the sum root of the squares. This is explained below in Sec. 5.2.8.

The flux of all PACS science-grade products are calibrated to be fully correct only for fully-extended sources, i.e. those with a flat or gradual flux gradient (of no more than 20% within a single $47''$ square FoV). Why is this? The detector plane of PACS was not evenly illuminated by the infalling light, with the result that different amounts of flux loss will occur depending on where the source is on the detector plane – a source falling on a low "illumination" part will lose more flux than one falling on a high "illumination" part. A flat source, however, is pretty much the same everywhere on the detector plane and so a general percentage correction is possible. The (flat-source) "extended source correction" was developed to correct for the loss of flux due to this uneven illumination of the PACS IFU for a flat source, and is applied as part of the calibration in the pipeline of PACS. For point and semi-extended sources, correction tasks are provided in HIPE that removes the extended source correction factor and replaces it with a point-source or tailored semi-extended source correction factor, and so the fluxes for these sources are usually well calibrated. For other sources,

- crowded fields
- extended sources with a steeper gradient. e.g. a blobby structure, a central bright area with relatively bright wings, ...
- off-centred point sources
- semi-extended structure

aperture photometry done on the cubes will result in an incorrect measurement because the extended source correction does not fully correct their detected fluxes for the uneven illumination. How incorrect this is depends on the morphology of the source at the wavelength of the observation and its coupling to the detector's beam efficiencies on every pointing (mapping) pattern.

To estimate the inaccuracy in the flux, if you know (or can model/estimate) the surface brightness distribution of the source (i.e. its morphology at the wavelength of your observation), you can apply a "forward projection" in HIPE: this takes in your input surface brightness model/image, and working with the pointing/mapping pattern of your observation, it produces result which folds in the uneven illumination. This can be compared to the observed cube to estimate the inaccuracy in the aperture-extracted fluxes. This is documented in the PDRG (spec) (chps 8 and 9), in documentation provided on the HELL L2 pages, and on the PACS calibration pages at herschel.esac.esa.int/twiki/bin/view/Public/PacsCalibrationWeb. This will work for all the cases mentioned above.

Separate corrections for (slightly) off-centred point sources and semi-extended sources, which are also easier to apply, are also provided. The point-source correction is explained in Sec. 8.3.3 and its application in Sec. 11.2.1. For semi-extended sources see Secs 8.3.5 and 11.2.2. For extended sources see Secs 8.3.4 and 11.2.3.

In addition, in HELL L2 there is a collection of technical notes that explain what to do when dealing with point (centred or not), semi-extended, and extended sources, and these should be consulted for practical advice and examples.

For the semi-extended and extended source flux corrections, you will need to work in HIPE with the products taken from Level 2 or 2.5, and you will need to have an idea of the size and shape of your source. The extra uncertainties that this flux correction "modelling" brings are related to how well you know these information: if you know your source perfectly, the extra errors can be disregarded.

5.2.8 Combining the calibration uncertainties

Most of the calibration uncertainties apply to each and every native 9.4″ spaxel of the *rebinned cubes*, not to the spaxels of the mosaic cubes. Why the difference? Mosaic cubes have smaller spaxels than the rebinned cubes, but for percentage errors this make no difference. However, what does make a difference is that the spectra in each spaxel of the the mosaic cubes are the combination of the spectra from all the rebinned cube spaxels that overlap that piece of sky in the mapping sequence of the observation (this being the way mosaic cubes are created). Hence the mosaic spaxel spectra are *combined data*, and so the errors for these should, strictly-speaking, be computed as the *combination* of the errors from the overlapping spaxels. The error arrays in the mosaic cubes *are* created in this way, however these data errors are separate to the calibration errors. In practise, not only is it too awkward to propagate the calibration errors for each spaxel of the rebinned cube that feeds in to creating each mosaic cube, but as the errors are mostly percentages, it will make little difference. However, it is important to be aware that the calibration errors do apply to each spaxel independently and when combining larger areas of a cube, the errors should be appropriately combined. When considering the additive errors (e.g. those for the unchopped continuum), it is also important to remember that the values quoted are for 9.4″ spaxels, and they should be modified appropriately for the smaller spaxels of the mosaic cubes.

For an observation of any source with PACS, the recommended error budget is:

- For measurements from a single native spaxel:
  - Any single emission line flux: the fitting errors combined, using standard error propagation (i.e. the sum of squares), with the absolute calibration error (Sec. 5.2.1, i.e. 15%).

  - Any emission line flux ratios for lines from within the same band: the calibration errors are uncorrelated, and the absolute flux uncertainty does not play a role, hence the fitting errors are combined in quadrature with the in-band uncertainty (Sec. 5.2.2).
  - Any emission line flux ratios for lines from different bands or different observations: the fitting errors combined, using standard error propagation (i.e. the sum of squares), with the absolute calibration error (Sec. 5.2.1, i.e. 15%).

- For measurements of area-integrated regions of rebinned cubes: as the data errors are unique to each spaxel, they should be combined appropriately (normally the best measure of uncertainty to a PACS line measurement is the RMS in the local continuum), and the the continuum and line calibration errors mentioned in this section should also be combined with this in mind.

- For measurements from mosaic cubes: it is important to remember that since the small mosaic spaxels are created from overlapping large rebinned spaxels, the spectra from neighbouring spaxels of the mosaic cube will have been created from almost the same input spectra – this means that the noise in the spectra will be to some degree correlated. This is especially important for mosaic cubes created from undersampled observations (e.g. tiling and pointed observations).

5.2.9 The data error array in the PACS science-level products

In addition to the calibration errors discussed here, all PACS science products include an error dataset (3d datasets in the cubes and single columns in the tables). The first of the science-level cubes (the rebinned cubes) are created by spectrally rebinning the data of the preceding-level cubes, during which each wavelength bin is therefore fed by many incoming data-points. The standard deviation of these data-points create an "stddev" array, and this becomes an "error" array in the tables and mosaic cubes which are subsequently created from those rebinned cubes (see the PDRG (spec) chp. 7, for more detail). This error is effectively the shot noise in the spectra. It, as well as the actual scatter (the RMS) in any spectrum you are measuring, can be used to estimate the measurement error on spectral line fluxes.

The stddev measures only the scatter in the wavelength bins, it does not include sources of flux uncertainty such as those caused by pointing jitter, long-term transients, or flat-fielding, which tend to affect wavelength ranges slightly longer than a single bin. These sources of error are wrapped up in the calibration errors quoted above.

5.3 A comment on saturated lines

Saturation is flagged near the beginning of the pipeline, before the data have been on-off subtracted or calibrated. The saturation detection is based on a comparison of the counts in the data array with values in the calibration tree. This saturation is stored in an array called SATURATION which is found in all Level 0.5 and 1 products, and in the first cubes of Level 2 – however, note that none of these products are of science quality. The first science quality cubes – the rebinned cubes – are created from the first Level 2 cubes, with the saturated data being *excluded*. Hence, any lines or continuum regions that are saturated will be replaced with NaN values, and in the rebinned cube spectra these spectral regions will effectively look like blanks in the spectra. For more on the calibration of saturation, see Sec. 8.2.6.

A second level of saturation detection was also part of the pipeline, however this one was intended as a warning for user to then check whether saturation was really present and to keep the mask if so but remove it if not – this saturation detection created a RAWSATURATION mask, which is also explained in Sec. 8.2.6. However, because of the action of tasks later in the pipeline, this mask was *also* taken into account when the rebinned cubes were created, meaning that the flagging – and excluding – of data that potentially was, in fact, *not* saturated may have occurred. For more detail, see Sec. 9.2.1.1. Hence for sources in rebinned cubes where there are clearly saturated features in one part of the observed field (e.g. a very bright star), with spectral lines or continuum regions with gaps in them, be aware that if gaps appear in the same parts of the spectrum but from other parts of the observed field where the flux is lower (e.g. the blank sky around the bright source), be aware that these gaps could be there because these data were mistakenly flagged as saturated. The only way to tell if this is the case is to inspect the Level 2 PacsCubes in HIPE. More information on this can be found in the PDRG (spec).

5.4 Spectral leakage

The order-selection filters of the PACS spectrometer have a steep but not perfectly vertical transmission profile at the cut-off wavelengths of the spectral bands. The PACS spectra near the band borders of bands R1, B3A and B2B are affected by higher- or lower-order wavelengths leaking into the spectra. Interpretation of spectral features (lines or continuum fluxes) in the spectral leakage regions should be avoided without first checking for leakage. Regions affected are

- R1: The spectrum between 190–220 μm has an unreliable (line) flux calibration, and can have superimposed spectral features from order 2 (95–110 μm). The standard products in the HSA do not contain this spectral range, but they can be downloaded as an HPDP (Sec. 10.4.4.2).
- B2B: beyond 98 μm the response is very low, and spectral features from order 3 (63–70 μm) can be superimposed on the spectrum. For example, a line can appear at 94.8 μm, being a leak from a bright [O I] 63 μm line.
- B3A: beyond 70 μm, the order 4 (52.5–54.5 μm) spectrum is added to the 70–73 μm order 3 spectrum. This leakage can be seen down to 69 μm for extremely bright (leaking) lines at 52 μm. The 51–52 μm order 3 spectrum can also have the 76–78 μm order 2 spectrum leaking in.

5.5 Wavelength calibration accuracy

The PACS wavelength calibration relates the diffraction grating position to the wavelength seen in every detector pixel (all 16 spatial pixels of each of the 25 modules). This calibration was derived from laboratory measurements of a water vapour absorption cell, and further refined in-flight based on fine-structure lines of planetary nebulae. For extended sources, the required accuracy of better than 20% of a spectral resolution element is met throughout all bands. While at band borders, due to leakage effects and lower SNR, the RMS calibration accuracy is closer to 20%, values even better than 10% are obtained in the band centres.

For point sources the wavelength calibration may be dominated by pointing accuracy, as a large amount of jitter during an observation, or a large offset, will affects the spectral line profiles: see Sec. 5.8.3 for more information.

5.6 Wavelength grid

The spectral resolution of the spectra of PACS cubes varies with wavelength, as demonstrated in Fig. 5.4. The spectral *sampling* of the wavelength grid varies with this resolution, being narrower where the resolution is higher and wider where it is lower. This was done so that the bins of the spectral grid at least Nyquist sample the instrumental resolution at all wavelengths, for all bands – important for SEDs where the wavelength coverage is long. This means that the bin size of the PACS spectral products vary across the spectral range they cover. In other words, the wavelength grid is *regular* but *not equidistant*. (Browse products, however, have an equidistant wavelength grid: Spec. 10.4.3).

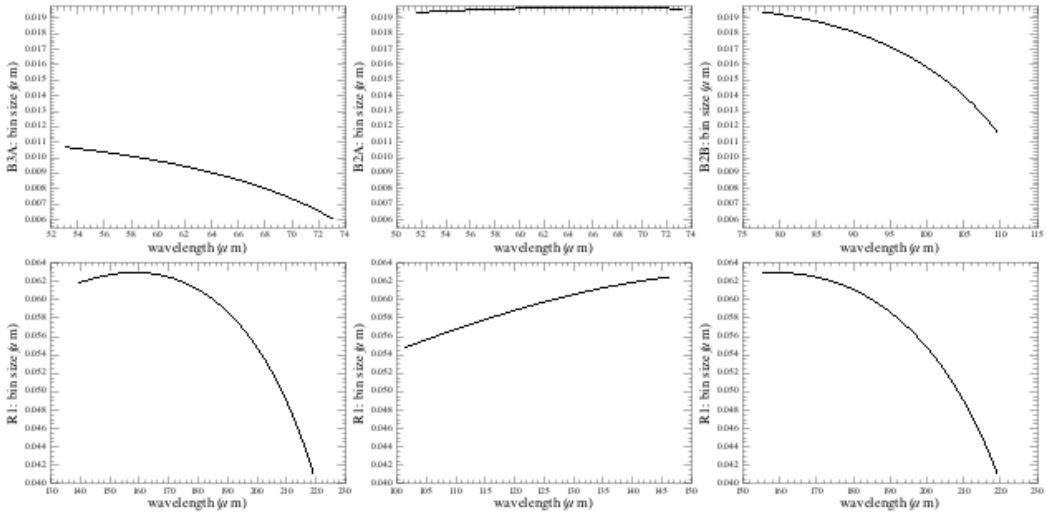

Figure 5.4: Dispersion as a function of wavelength for the various spectroscopy filters for a wavelength grid created with upsample=1 and oversample=2.

The first of the science-grade cubes (the rebinned cubes) produced by the PACS pipeline are created from preceding cubes which have data laid out on irregularly-sampled wavelength "grid". To create the rebinned cube spectra with a *regular* wavelength grid, a new grid is defined and the spectral datapoints of the preceding cubes (with their irregular grid) are averaged together where they fall in the bins of this grid. Thus the rebinned cubes are created. This is explained in Sec. 9.2.1.4 and in fuller detail in the PDRG (spec) (chp. 7). This averaging involves two important parameters: *oversample* and *upsample*. Oversample determines the fraction of the instrument resolution, at each wavelength, the bins will be, and upsample determines how many bins one shifts forward along the new grid before computing the average again. For upsample=1 each bin will begin where the previous bin ended, for upsample=2, then the second bin will begin half-way through the previous bin, and so on. This is important to know because for upsample>1, the data in adjacent bins is correlated, as there is some overlap of the data-points used to create their averages. As line scans and high density-scanning range

scans have an upsample factor of 4, and SEDs and low density-scanning range scans a factor of 2, this means that for all PACS pipeline products, the adjacent bins of the spectra are correlated – and so is their noise. A discussion of what effect this has on the spectra can be found in the PDRG (spec) (chp. 7).

5.7 Spectral profile

The instrument profile is a Gaussian with a FWHM that is only slightly dependent on the upsample and oversample factors used in the pipeline (Sec. 5.6) : the plots of 5.4 can be used to find the expected resolution at any wavelength, or a task in HIPE can be used to compute the resolution (PDRG (spec) chp. 10) for any band and wavelength. For high SNR lines (i.e. lines that have a peak over 10 times the continuum RMS, rather than lines that are intrinsically high in flux value), it is necessary to fit additional low-level wings (equal on the red and blue sides of the line centre), in which a few percent of the total flux is contained (1 to $<$10%). It will be obvious when inspecting the residuals of a Gaussian fit whether a line has these wings.

5.8 Instrumental spectral features

5.8.1 Spectral ghosts

A second pass in the optics of the PACS spectrometer can cause a ghost image on some spaxels. Fig. 5.5 shows the spaxels where a second pass ghost might appear, and the location of the corresponding spaxels where the originating, real emission is located.

If a source in one of the originating spaxels shows a strong spectral line – a typical example is an atomic fine-structure line – a weak, broadened line can be seen at an offset wavelength in the corresponding spaxel affected by $2^{\rm nd}$-pass ghosts. The peak flux of this line is typically about 5% of the peak of the originating line. The integrated line flux can be up to 14% of the integrated flux of the originating line. The ghost line will be shifted in wavelength from the originating line.

An example is shown in Fig. 5.5. The wavelength offset between the originating line and the ghost line depends on the spectral order of the band, and varies with wavelength. The strongest fine-structure lines and their ghost wavelength are given in Table 5.1, and a full list can be found in Table 5.2.

Before interpreting broad spectral lines in spaxels potentially affected by $2^{\rm nd}$-pass ghosts, use these tables and, if available, the spectra observed in the corresponding ghost source-spaxel, to check for the presence of a strong line at the originating wavelength. The central column of the PACS IFU is not affected by the ghosts. For point sources for which the point-source extracted spectrum is taken from the central spaxel only, ghosts will not be an issue, however the point-source extracted spectrum from the taken from the central 3x3 will be affected.

5.8.2 62 μm dip

In some spectra a dip–which looks much like an absorption line–can be seen around 62–63 μm. This is a filter feature, its strength and appearance depends on the angle at which light goes through the filter, and hence it depends on the source position and structure. Some examples are shown in Fig. 5.6.

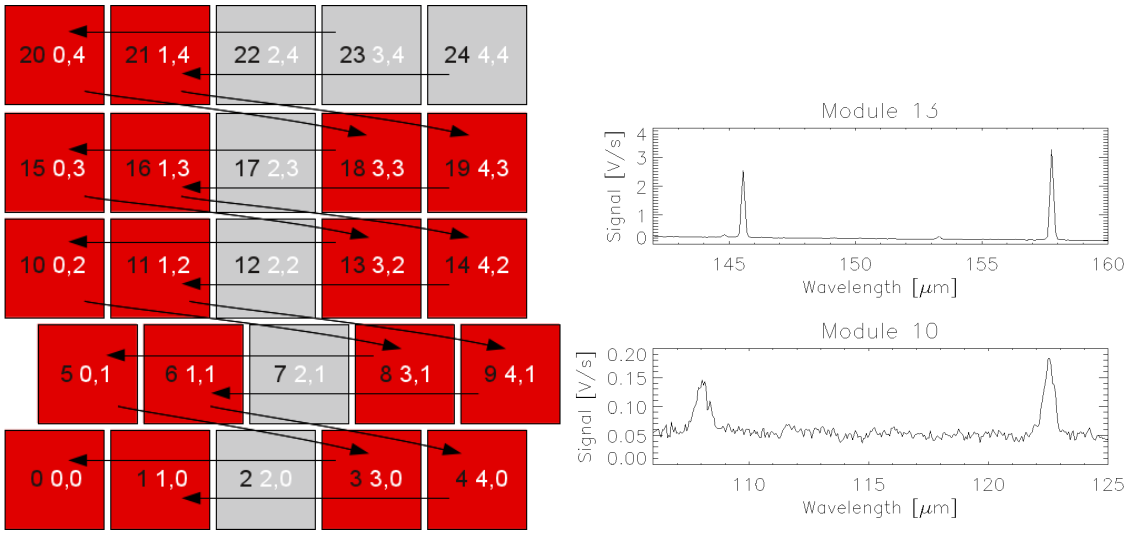

Figure 5.5: **Left**: location of the spaxels where a 2nd-pass ghost might appear. In black are the module numbers, in white the spaxel row and column numbers. The arrows indicate the direction from the originating, real emission to the ghost location. **Right**: an example of a ghost line (upper spectrum is the originator, lower is the ghost.

Table 5.1: The strongest ghosts

Band	Originating line	Ghost wavelength
B3A	O [I] 63.2 μm	54
B2B	O [III] 88.4 μm	71
R1	O [I] 145.5 μm	108
R1	C [II] 157.7 μm	122
R1	N [II] 205.3 μm	178

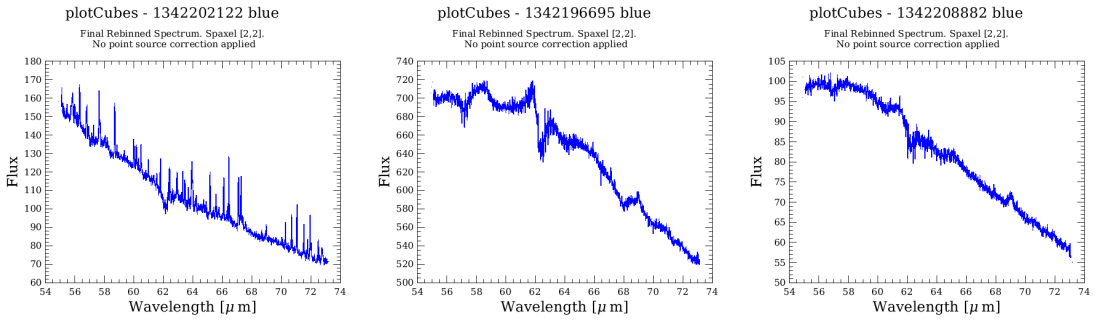

Figure 5.6: Some examples of a filter-feature at 62 μm.

5.8.3 Wavelength shifts with source position

The 5x5 spaxels of the PACS IFU are imaged onto a 1d-slit. The slit image is then dispersed by the diffraction grating. As with any diffraction grating spectrometer, moving the source centre with respect to the slit centre in the dispersion direction will result in a slight shift of the wavelengths in the resulting spectrum. Therefore, spectral lines observed from a point source with PACS will appear

Table 5.2: A list of all known ghosts

Wavelength (μm)									
Orig.	Ghost	Orig.	Ghost	Orig.	Ghost	Orig.	Ghost	Orig.	Ghost
Band R1						Band B2B		Band B3A	
140.2	102	163.3	129	186.4	156	84.6	68	59.9	50
141.1	103	164.1	130	187.2	157	85.5	69	60.7	51
141.9	104	165.0	131	188.1	158	86.3	70	61.5	52
142.8	105	165.9	132	188.9	159	87.2	71	62.4	53
143.6	106	166.7	133	189.8	160	88.0	72	63.2	54
144.5	107	167.6	134	190.6	161	88.9	73	64.0	55
145.4	108	168.4	135	191.5	162	89.7	74	64.8	56
146.2	109	169.3	136	192.3	163	90.6	75	65.6	57
147.1	110	170.1	137	193.2	164	91.4	76	66.4	58
147.9	111	171.0	138	194.0	165	92.3	77	67.2	59
148.8	112	171.8	139	194.9	166	93.1	78	68.1	60
149.6	113	172.7	140	195.8	167	94.0	79	68.9	61
150.5	114	173.5	141	196.6	168	94.8	80	69.7	62
151.3	115	174.4	142	197.5	169	95.7	81	70.5	63
152.2	116	175.3	143	198.3	170	96.5	82	71.3	64
153.0	117	176.1	144	199.2	171	97.4	83	72.1	65
153.9	118	177.0	145	200.0	172	98.2	84	73.0	66
154.8	119	177.8	146	200.9	173	99.1	85	73.8	67
155.6	120	178.7	147	201.7	174	99.9	86		
156.5	121	179.5	148	202.6	175	100.8	87		
157.3	122	180.4	149	203.4	176	101.7	88		
158.2	123	181.2	150	204.3	177	102.5	89		
159.0	124	182.1	151	205.2	178				
159.9	125	182.9	152	206.0	179				
160.7	126	183.8	153	206.9	180				
161.6	127	184.7	154						
162.4	128	185.5	155						

slightly shifted in wavelength if the source is not perfectly centred on the spaxel. This is illustrated in Fig. 5.7.

As well as a shift in the central wavelength, the line profile will be deformed from Gaussian to skewed-Gaussian. This means that point and point-like sources that are offset from the centre of a spaxel in the dispersion direction will have skewed Gaussian profiles rather than Gaussian: the line centre will be shifted in one direction and a elongation will appear on the opposite side of the line (it is "leaning over"). These features should be taken into account before interpreting wavelength shifts or line profile changes. The sign and magnitude of the shift for different wavelengths is shown in Fig. 5.8.

Note that the shifts are dependent on the location of the source in the instrument plane, not the sky plane. To most easily identify whether a source is shifted in the *dispersion* direction or perpendicular to the dispersion direction, open the rebinned cube from your observation (*not* a mosaic cube, for which it is not possible to reconstruct the instrument plane) in HIPE in the Spectrum Explorer: this tool shows the spaxel coordinates in its image display section. The relationship between spaxel coordinates (0,0 to 4,4) and spaxel number (1,2,3...24) can be found in the PDRG (spec) (chp. 10), and the relationship between spaxel number and skew is illustrated in Fig. 5.7.

If not using HIPE, then bear in mind the following: the spaxel numbers and spaxel coordinates start at 0 in HIPE, but outside HIPE that may not be true, e.g. in Saoimage the numbering starts at 1. In addition, the cube is also flipped in Saoimage with respect to its orientation in HIPE: spaxel 0 (coordinates 0,0, bottom-left) in HIPE is 1(1,1, bottom-left) in Saoimage; spaxel 1(1,0, located to the right of spaxel 0) in HIPE, in Saoimage is instead located above spaxel 1 (coordinates x=1,y=2); spaxel 5 (0,1, above spaxel 0) in HIPE, in Saoimage is located to the right of spaxel 1 (x=2,y=1). This means that the dispersion direction for a cube viewed in HIPE is up→down, but in Saoimage is right→left.

A final consideration: mosaic cubes are created by combining the spectra of the rebinned cubes onto a finer spatial grid – i.e. combining the spectra of different rebinned cube spaxels. This means that for a point or point-like source offset in the dispersion direction from the centre of a spaxel (in the rebinned cube), when their spectra are combined, their skews are also. This will also happen if you combine the spectra in a rebinned cube, e.g. summing the spectra of the spaxels around the point source or if using the "c9" or "c129" result of the point-source correction task (e.g. Sec. 11.2.1). Consider a point source located between spaxels 12 and 17 (as in Fig. 5.7). The spectrum from spaxel 12 will have lines with a skew to the red side, and that from spaxel 17 will have a skew to the blue. When you add these two spectra together, you end up with a wider line. Bear this in mind when interpreting features from point or point-like sources in mosaic cubes or resulting from the point-source correction tasks.

Pointing offsets perpendicular to the dispersion direction do not result in a wavelength shift.

5.9 Beam efficiency

5.9.1 Detector sampling and the PSF

The PACS spectrometer spaxels sample a part of the PSF delivered by the *Herschel* telescope. The telescope PSF becomes larger with wavelength, and shows substantial departure from a Gaussian profile due to the telescope wavefront errors, mainly caused by the three-point mount of the telescope dish. At different wavelengths, different fractions of the PSF structure are seen by the different spaxels. This is illustrated in Fig. 5.9.

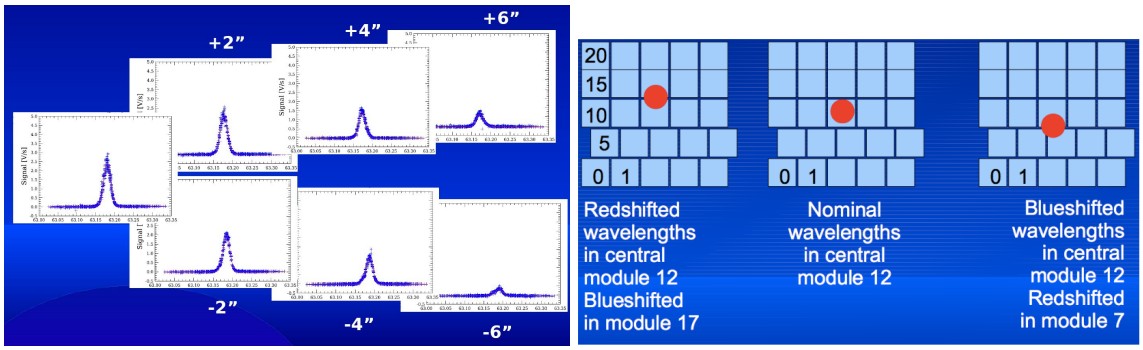

Figure 5.7: **Left**: when a point source is offset in the dispersion direction with respect to the centre of a spaxel, the observed lines show a distinct shift in the wavelength and a skew in the profile. **Right**: If a point source is offset in dispersion direction, wavelengths will be shifted to the red when moving "up", e.g. from module 12 to module 17 in the PACS IFU. When the source is offset "down", the wavelengths will be blueshifted. (Note: when you view such a rebinned cube in any viewer, you will not be able to see the offset spaxel-row as the cube will display with a regular 5×5 grid.)

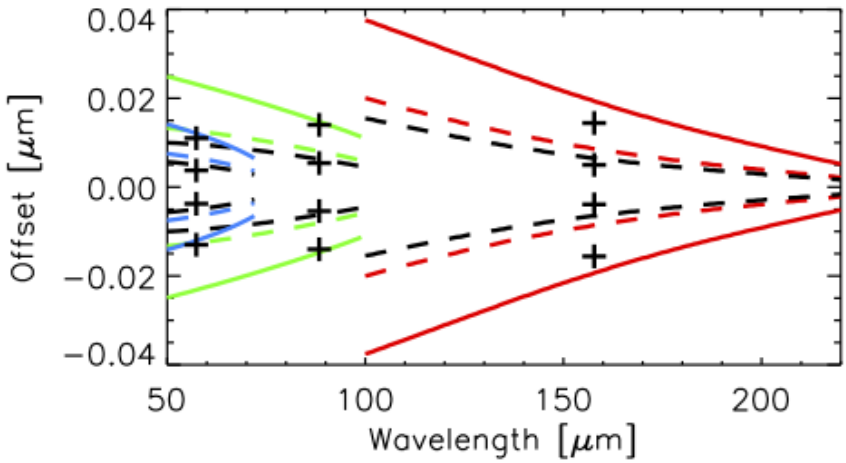

Figure 5.8: The wavelength shift, seen when a point source is not centred perfectly, depends on the observed wavelength and band, and the pointing offset. The black dashed line shows the wavelength shift seen for a point source offset by 1.5″. The blue, green and red dashed line shows the wavelength shift for a pointing offset of 2″. The solid red, green and blue line show the wavelength shift seen when the source is centred on the spaxel edge (offset 4.7″)

The fraction of the PSF falling onto the central spaxel varies depending on the source placement in the FoV, and therefore also on the pointing accuracy of the spacecraft for any observation. The correction for this fraction for point sources is unique to each observation, and the point-source correction tasks were developed in HIPE to accommodate this (the point-source correction is explained in Sec. 8.3.3 and its application in Sec. 11.2.1); this correction was used in the flux calibration work and the resulting uncertainties reflect the residual effects. This is the main limitation of the flux calibration.

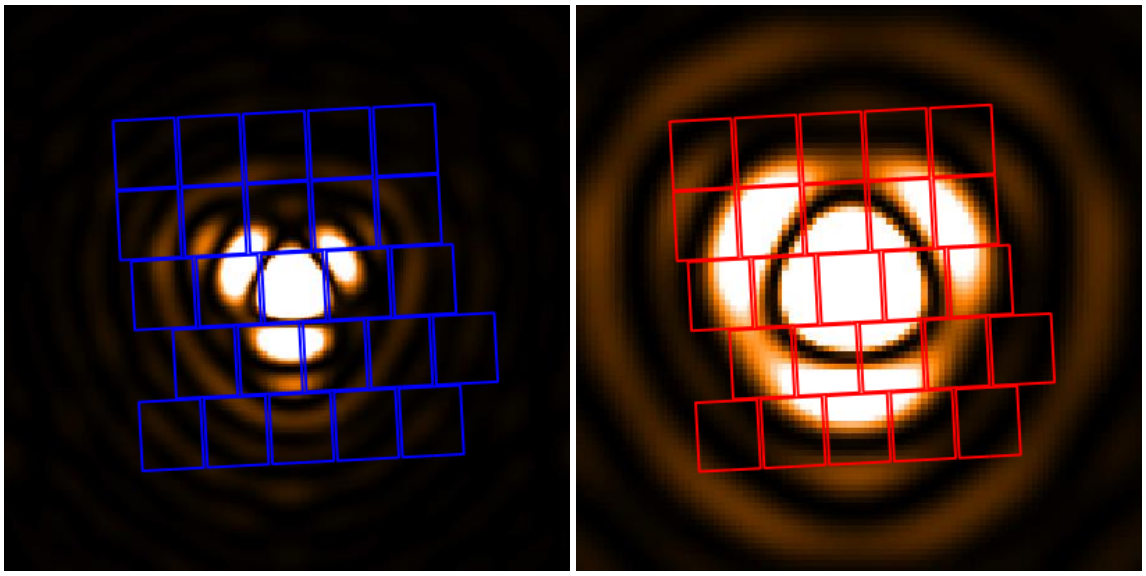

Figure 5.9: PACS spectrometer detector positions overlaid on the telescope PSF at 75 μm (**left**) and 150 μm (**right**). The colour scaling of the PSF is chosen to enhance its lobes and wings.

5.9.2 Measured beam efficiencies

The beam efficiencies have been measured via raster maps on Neptune at a few selected wavelengths. The measured beam maps measured in every spaxel are available on HELL L1and are also included as calibration products in the PACS calibration product tree (e.g. `beamsB2A` or `beamsPerSpaxelB2A` link to where discuss calfiles on disc. ToDo). A beam image is provided for each wavelength and for each of the 25 spaxels in HELL L2 ("PACS Spectrometer Beams ...."), together with explanatory notes. The beam image data are also provided in the calibration files 'PCalSpectrometer_BeamsPerSpaxel¡BAND¿_FM_v4.fits', but it is easier to use the maps provided in HELL L2. Beam data can also be downloaded from the Ancillary Data Products page: modelled beams and measured beams. In Fig. 5.10 we show the measured beam efficiencies at four wavelengths across the PACS range. The pixel size dominates the width of the beam efficiency up to 150 μm. Fig 5.11 plots the width of the measured beams as a function of wavelength.

5.9.3 Working with the beam images

The beams maps referenced above are images (one per key wavelength) with a high spatial sampling (small pixel sizes). Note that the beams are not exactly the same for each spaxel, although their difference are, in the real world, not so great. If comparing the beam images to image slices (or to a wavelength-summed image) taken from your own cube, it may help to resample the beam images to the lower pixel sizes of your images. The pixel size of images created from a cube will be the spaxel size of the cube: for mosaic cubes this is usually about 3″; for rebinned cubes it is 9.4″, however, as the spatial grid of rebinned cubes is irregular (which the footprint plotted in Fig 5.9 demonstrates), a direct comparison to the beam images (which have a regular grid) will have to take this into account.

Note that the angle of the trilobal shape of the beam is fixed to the instrument plane, and therefore observations of the same source at different dates may have these placed in a different position angle

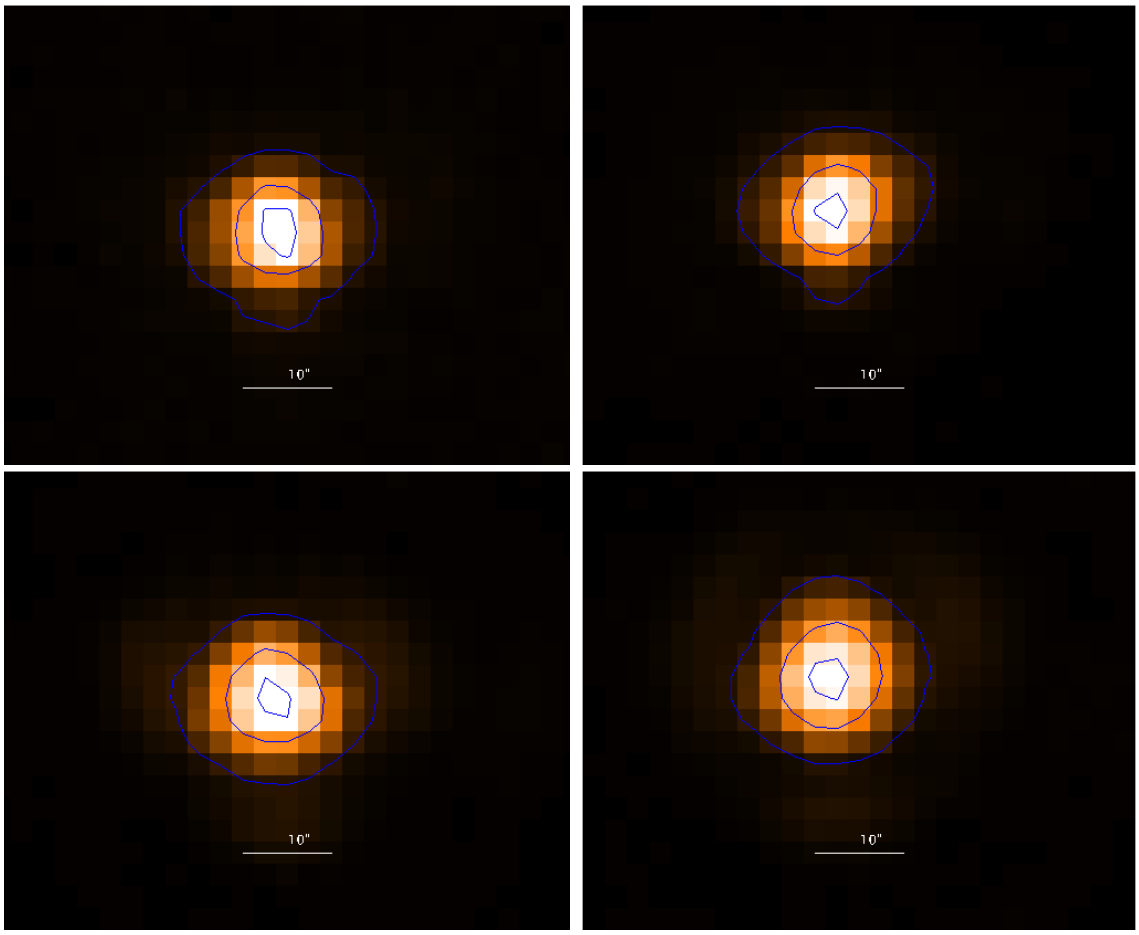

Figure 5.10: PACS spectrometer beam efficiency as measured from oversampled raster maps on Neptune. From top left, to bottom right: 62 μm, 75 μm, 125 μm, 150 μm. The contours indicate 10%, 50% and 90% of the peak response.

on the sky. In practise, however, point sources observed even with fine mapping observations do not show these lobes, rather they become part of the wing of the more-or-less Gaussian shape of the beam.

For undersampled observations – tiling or pointed observations in particular – the PSF is insufficiently sampled to map the beam profile (the spaxels are 9.4$''$ and the PSF varies from about 9$''$ to about 13$''$). Hence, point sources observed as a pointed observation will have a more top-hat like profile, where for middling and faint sources all or most of the flux in just one (usually the central) spaxel, and for bright sources flux will also fall in the immediately surrounding spaxels. Point or point-like sources that are offset from a spaxel will show additional flux in the neighbouring spaxels – which ones depends on the offset direction – and for moderately bright sources with offsets of about 3$''$ or more, you can usually see this in the rebinned cube images. If working with pointed observations of point or small sources, and looking at the interpolated cubes, please do not over-interpret the structure you see – remember that the shape is dominated by the spaxel grid of the PACS instrument.

For point or small sources which are offset from the centre of a spaxel and which consequently show skewed emission-line profiles (Sec. 5.8.3), it is necessary to take this into account also when viewing image slices of your cube. For example, let us take the example of Fig 5.7: the point (or point-like)

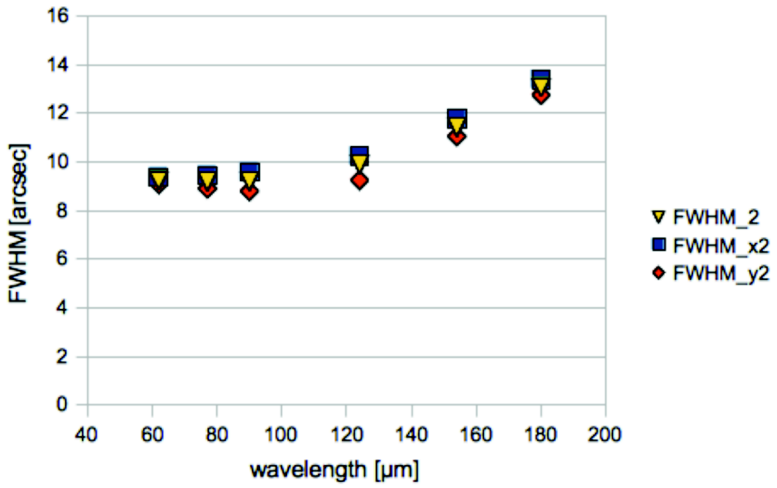

Figure 5.11: Width of the PACS spectrometer beams as a function of wavelength. The PACS spectroscopy beam is not strictly a 2d Gaussian, and these numbers are therefore not exact. We show the FWHM in the two instrument directions (blue squares, red diamonds) and the mean of the two (yellow triangles).

source is offset between spaxels 12 and 17. In spaxel 12 the line is skewed to the red and in 17 it is skewed to the blue. If you take an image cut of this cube (or of a mosaic cube created from it) on the red side of the nominal line centre, the centre of brightness of the image will be in spaxel 12. But if you take an image cut on the blue side of the nominal line centre, the source will appear to be located around spaxel 17. Do not confuse this with source motion – it may be entirely due to the skew.

Chapter 6

The Calibration Models

The detailed work on the calibration of the PACS photometer and spectrometer are addressed in the following two chapters. In this chapter, the details of the models of the astronomical calibration sources used for photometry and spectroscopy are given. Comparison of the model predictions to photometry results is given here, to indicate the quality of the modelling. The comparison of the models to the spectroscopy observations is discussed in Sec. 8.2.4.

6.1 Fiducial standards

As prime flux references, models of the photospheric emission of late-type giants were used (Dehaes et al., 2011). This type of star was also used as absolute calibrators for earlier IR space missions (e.g. IRAS: Rieke et al. 1985, ISO: Cohen 2003, Spitzer: Gordon et al. 2007). The flux regime they cover is inside the linear flux behaviour of the PACS bolometers. Ideally, stars of different stellar types would be used to prevent systematic uncertainties from the modeling; unfortunately only the late-type giants are bright enough at far infrared wavelengths to be observed at high SNR. One star, Sirius (α CMa), was the only A-type exception, but unfortunately had to be dropped from the set of primary flux calibrators. Models of the atmospheres of the giant planets Uranus and Neptune (Moreno, 2012) are equally accurate, however these sources are in the non-linear flux regime of PACS. Asteroids are about to be established as independent prime FIR flux calibrators (Müller et al., 2014). The five fiducial stellar standards αBoo, αCet, αTau, βAnd and γDra were observed repeatedly during the mission for absolute calibration and to monitor the system stability (for this γDra, which was visible during the whole mission, was observed on a monthly basis).

The photometric system was also monitored using the internal calibration blocks, for photometry and spectroscopy. For the photometer, the response of the calibration blocks were measured several times a day throughout the mission (at least one calblock per obsid), and the result shows, with a high accuracy, that the photometric system was very stable (Moór et al., 2014).

The flux calibration of the spectrograph was ultimately tied to that of the photometer, and so relied on the same calibrators. Independent work on the spectrograph's flux calibration was done using a similar set of stellar calibrators, whose theoretical spectra in the far infrared were generated using the MARCS stellar atmosphere code (Gustafsson et al., 1975, 2003) and the TURBOSPECTRUM synthetic spectrum code (Plez et al., 1992) and are presented in Dehaes et al. (2011). The stellar

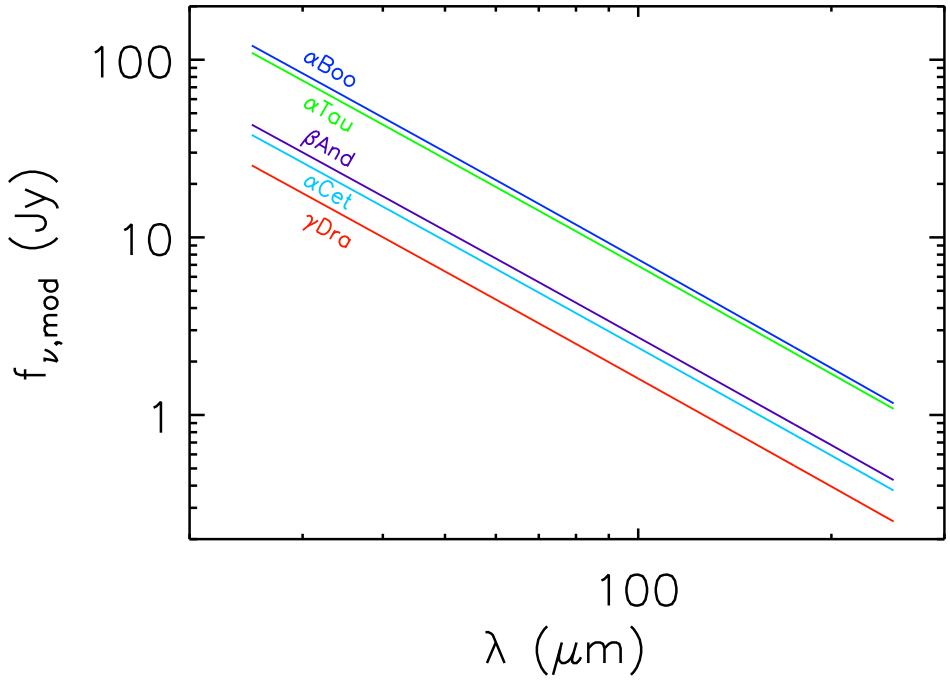

Figure 6.1: Continuum flux SEDs from 25 to 250 μm of the five fiducial stars used for the PACS photometer absolute calibration. The different stars are designated by different colors. Blue: α Boo, green: α Tau, magenta: β And, cyan: α Cet and red: γ Dra.

parameters and their uncertainties were derived by Decin et al. (2003). The line lists used in the spectrum calculations and the model uncertainties are discussed in Decin and Eriksson (2007), where it is estimated that the uncertainty of the models in the PACS wavelength range is $\sim 5\%$. The absolute flux calibration is based on Selby's (Selby et al., 1988) K-band photometry, the zero-point is determined on the basis of an ideal Vega, i.e. the K-band photometry of Vega is corrected for a flux excess of 1.29% (cf. Absil et al. 2006). The determined Selby K-band zeropoint is 4.0517×10^{-10} W/m^2/μm.

The original models of Dehaes et al. (2011) of 7 stellar calibrators from 2 to 200 μm including lines with a spectral resolution of $\frac{\lambda}{\Delta\lambda}$ = 5000 are contained in the VizieR Online Data Catalog J/A+A/533/A107/stars. For the PACS photometer calibration model, versions predicting only the pure continuum flux and covering the wavelength range 0.5 μm to 7 cm were used. Detailed information on these latter models can be found in the *Herschel* stellar calibrator models release note. The model data files can be downloaded from here. The SEDs from 25 to 250 μm of the five fiducial stars used for the PACS photometer absolute calibration as listed in Table 6.1 are shown in Fig. 6.1.

The types of stars that the calibrators are can show excess flux in the far infrared wavelengths – due to debris disks for early-type dwarfs, or chromosphere or ionised wind for late-type giants – therefore it is important to investigate whether one can rule out the existence of such excesses for the candidate calibrators. Dehaes et al. (2011) present observations in the sub-mm up to cm wavelength range for nine late type giant stars, of which seven were in the original list of candidate calibrators. These

Table 6.1: Information on the fiducial stars selected for photometry. Monochromatic flux densities at 70.0, 100.0 and 160.0 μm are given. The stellar temperatures are taken from Decin et al. (2003) and the fluxes are based on models published in Dehaes et al. (2011).

HR	HD	HIP	ID	RA (J2000)	Dec (J2000)	SpType	Temp [K]	Model flux [mJy] 70 μm	100 μm	160 μm
337	6860	5447	β And	01:09:43.9236	+35:37:14.008	M0III	3880	5594	2737	1062
911	18884	14135	α Cet	03:02:16.8	+04:05:24.0	M1.5IIIa	3740	4889	2393	928
1457	29139	21421	α Tau	04:35:55.2387	+16:30:33.485	K5III	3850	14131	6909	2677
5340	124897	69673	α Boo	14:15:39.6720	+19:10:56.677	K1.5III	4320	15434	7509	2891
6705	164058	87833	γ Dra	17:56:36.3699	+51:29:20.022	K5III	3960	3283	1604	621

observations were made in preparation of the *Herschel* mission and performed on several ground based telescopes. Sirius, an A1V star, was also studied, but it is not included in the Dehaes et al. (2011) paper, which only considered K and M giants. Although for seven out of the nine giants an excess was detected, it was found that for the eight stars, selected as prime flux calibrators for the PACS photometer, the excess only started beyond the PACS wavelength range.

Based on early analysis of *Herschel* observations of potential calibration stars it was decided to use the following five fiducial stars for the final analysis for photometry: β And, α Cet, α Tau, α Boo, γ Dra. The monochromatic continuum flux densities at 70.0, 100.0 and 160.0 μm for these five are given in Table 6.1. For spectroscopy, the following five were used: α Boo, β Peg, α Cet, γ Dra, α Tau. Price et al. (2004) showed that β Peg is variable in the mid-IR bands by about 10%, however this was not a problem for spectroscopy. Two calibrators were abandoned: for β UMi no Selby K-band photometry was available for the absolute calibration and only a less accurate ($\sim$ 10%) Johnson K band from Ducati (2002) could be used; and α CMa shows about 20% excess at 160 μm, the underlying cause of which is still unclear and is under investigation.

6.2 Planets and moons

The planets of the solar system and their satellites have surface and brightness temperatures of few hundred Kelvin and are thereby bright infrared emitters. Thanks to radiometers on space probes, such as the infrared radiometer for Mariner (Chase, 1969), IRIS on Voyager (Hanel et al., 1980), and the Photopolarimeter-Radiometer (PPR) on Galileo (Russell et al., 1992), accurate information on temperatures, thermal properties, albedo, energy balance and the infrared emission spectra have been collected, making the outer planets and their satellites suitable bright calibration standards. The inner planets were not accessible to *Herschel*, since they were inside the Sun constraint. Radio occultation data acquired with Voyager have been used to probe the vertical structure of the planetary atmospheres (Lindal, 1992).

In particular, Uranus and Neptune have been established as excellent flux standards for contemporary far-infrared space observatories, providing flux levels well adapted to the dynamic range of their instrument detectors, including the PACS photometer. Mars, Jupiter, and Saturn are too bright for sensitive instruments such as PACS. In the PACS photometer calibration scheme Uranus and Neptune and the satellites Titan, Callisto and Ganymede were used as complementary flux calibrators to the fiducial stars and the asteroid prime calibrators to cover an as large as possible flux range, to address

Table 6.2: Model flux predictions for Uranus, Neptune, Callisto, Ganymede, and Titan. In the case of Callisto, Ganymede and Titan the model fluxes are given for the epoch of observation (OD). For Uranus and Neptune the flux range encountered during the entire mission is reflected by maximum and minimum values and the epoch of observation (OD). Appropriate colour-correction factors (cc) to be applied to measured PACS fluxes for comparison with the model predictions are given. The estimated maximal uncertainty for these corrections is 2% for Titan and about 1% for the others.

Source	model source	OD	f_70 (Jy)	cc_70	f_100 (Jy)	cc_100	f_160 (Jy)	cc_160
Uranus	Orton, esa5	789	969.0	0.984	943.3	0.995	673.0	1.018
		1121	917.3	0.984	887.5	0.995	631.7	1.018
Uranus	Moreno, esa2	789	886.1	0.984	884.5	0.992	636.1	1.019
		1121	835.2	0.984	833.7	0.992	599.5	1.019
Neptune	Moreno, esa5	540	374.2	0.984	374.4	0.993	268.2	1.020
		1444	357.9	0.984	358.1	0.993	256.5	1.020
Callisto	Moreno, esa	981	1272.8	0.998	788.5	1.016	371.2	1.055
Ganymede	Moreno, esa2	981	1168.1	0.996	741.3	1.014	355.9	1.053
Titan	Moreno, esa3	1138	89.0	0.985	81.5	1.002	52.0	1.028

the issue of the non-linear detector response and to allow consistency checks in the case of overlapping fluxes of different calibrator types and reference models.

In Table 6.2 the planet and satellite models used for the calibration of PACS spectroscopy and photometry are listed together with flux predictions for certain epochs and appropriate colour correction factors for comparison with measured PACS fluxes. Detailed information on the planet models can be found in the *Herschel* planetary calibrator models release note. The model data files can be downloaded from here. The SEDs of the planets and satellites are shown in Fig. 6.2.

The predictions for Uranus are based on two models: (i) that provided by Glenn Orton (Orton et al., 2014) and (ii) the Uranus model provided by Raphael Moreno (Moreno et al. 2016, in preparation). Both models of Uranus were used to check the PACS calibration. They are connected to slightly different thermal structures. For the Moreno model the thermal profiles go back to Voyager radio-occultation measurements (Pearl et al., 1990; Lindal, 1992) , while for the Orton model measurement constraints from mid- and far-IR (Spitzer-IRS and *Herschel*/SPIRE) were considered. The radiative-transfer modelling includes continuum opacities from collision-induced absorption of H_2, He, and CH_4. The brightness-temperature differences between the models are below 5% in the PACS wavelength range. The model uncertainties are linked mainly to the input parameters and therefore reflect the absolute calibration accuracy. The model brightness temperatures were combined with Uranus' angular diameter as seen from *Herschel*, taking into account the equatorial and polar radii and the sub-observer latitude (i.e. Ob-lat in JPL/Horizon). The correspondence of the Moreno model with measured PACS fluxes is better than 4%. The Orton model predictions are too high by about 8% at 70 μm and still about 4-5% too high at 100 μm. The overall impression is that the model seems to work well from 160 μm onwards. The reason for the offset might be related to the He/H_2 ratio used in the model (Orton, priv. comm.).

The radiative-transfer modeling for Neptune includes continuum opacities from collisionially-induced

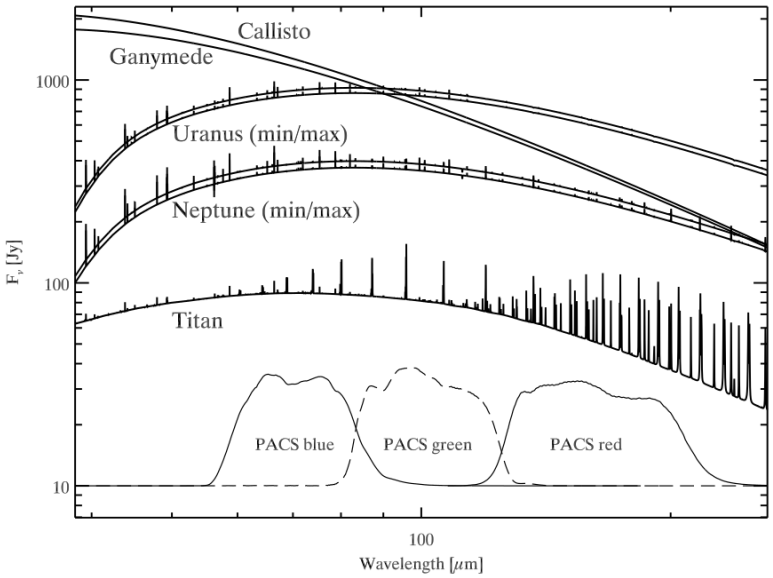

Figure 6.2: Absolute disk-integrated model flux density predictions for Callisto, Ganymede, Uranus, Neptune, and Titan in the *Herschel*-centric reference system. For the three planet satellites the predictions are for the epoch of the corresponding PACS measurements. The minimum–maximum model predictions for Uranus and Neptune refer to all available PACS measurements during the entire *Herschel* mission. The PACS band-passes are shown in arbitrary units.

absorption of H_2, He, and CH_4. The thermal profiles go back to Voyager measurements (Pearl and Conrath, 1991; Lindal, 1992) and fit the IR measurements of Akari spectra of Neptune's stratosphere (Fletcher et al., 2016). The Neptune model also fits the line-to-continuum (i.e. relative measurements) of SPIRE and PACS spectra including CO and HD lines (Moreno et al. 2016, in preparation). The model brightness temperatures were combined with Neptune's angular diameter as seen from *Herschel*, taking into account the equatorial and polar radii and the sub-observer latitude. The correspondence with measured PACS fluxes is better than 3%.

The model of Titan was computed using the radiative transfer model for a disk-averaged geometry, described in Courtin et al. (2011) and Moreno et al. (2012). This model includes continuum opacities from collision-induced absorption of N_2-CH_4 pairs and uses the thermal profile from Huygens probe measurements (Fulchignoni et al., 2005) combined with CIRS measurements (Vinatier et al., 2010). Molecular lines of CO, HCN, and CH_4 and their isotopes are included, which fit the HIFI and SPIRE observations. The final absolute accuracy is estimated to be better than 5%. The correspondence with measured PACS fluxes is better than 2%.

The disk-averaged models of Callisto and Ganymede are based on thermal models of the sub-surface computed with the Spencer et al. (1989) algorithm. The models solve the heat diffusion equation in the planetary surface material as a function of longitude, latitude, and depth. The thermal inertia used was originally derived by Spencer (1987) from two-layer models and based on 10–20 μm data from Voyager. These models also include the surface dielectric constant and roughness, which are fitted from the ground based measurements at mm-wavelength performed with the IRAM-PdBI and the SMA (Moreno et al., 2008). Model accuracies were estimated to be better than 7% for Ganymede and Callisto, however, these Callisto and Ganymede continuum models turned out to be not very accurate

in the PACS wavelength range. The Callisto model shows a 5% agreement at 70 μm and is about 10% too low at 160 μm. The Ganymede model underestimates the observed and calibrated PACS fluxes by 10 to 25%. This is probably linked to the effective albedo and different thermal inertia layers in the sub-surface, which are very difficult to constrain from disk-averaged observations.

A detailed comparison of PACS photometry of Uranus, Neptune, Titan, Callisto and Ganymede with the model predictions and the discussion of the results is given in Müller et al. (2016).

6.3 Asteroids

The idea of using asteroids for calibration purposes goes back to IRAS (Beichmann, 1985). The IRAS 12, 25 and 60 μm bands were calibrated via stellar models and in that way connected to ground-based N- and Q-band measurements. But at 100 μm neither stellar model extrapolations nor planet models were considered reliable. Asteroids solved the problem. Models for a selected sample of large main-belt asteroids were used to "transfer" the observed IRAS 60 μm fluxes out to 100 μm to calibration the IRAS 100 μm band.

The Infrared Space Observatory (ISO) (Kessler et al., 1996) also lacked reliable photometric standards at far-IR wavelengths (50–250 μm) in the flux regime between the stars and the planet calibrators Uranus and Neptune. Mueller and Lagerros (1998) provided a set of 10 asteroids, based on a previously-developed thermophysical model code by Lagerros (1996, 1997, 1998) AKARI (Murakami et al., 2007) followed the same route to calibrate the Far-Infrared Surveyor (FIS) (Kawada et al., 2007) via stars, asteroids and planets in the wavelength regime 50–200 μm. The Spitzer mission (Werner et al., 2004) considered only stars for calibration purposes in the beginning, but due to a near-IR filter leak of the MIPS (Rieke et al., 2004) 160 μm band, the calibration scientists were forced to establish and verify calibration aspects using cooler objects. The asteroids served as reference for the flux calibration of the 160 μm band as well as for testing the non-linear MIPS detector behaviour (Stansberry et al., 2007).

In preparation for *Herschel*, a dedicated asteroid programme was established (Müller et al., 2005). This led to a sample of about 50 well-known and well-characterised asteroids and their corresponding flux predictions with a thermophysical model. The asteroids fill a gap of more than two decades of flux between the sub-mm/mm calibrators Mars, Uranus and Neptune, and the mid-IR bright calibration stars (Fig. 6.3)

The applied thermophysical model (TPM) is based on the work by Lagerros (1996, 1997, 1998). It takes into account the true observing and illumination geometry for each observational data point, a crucial aspect for the interpretation of the main-belt asteroid observations which cover a wide range of phase angles and helio-/observer-centric distances, as well as different spin-axis obliquities. High-quality size and geometric albedo values are fundamental for reliable TPM predictions. The TPM allows one to specify simple or complex shape models and spin-vector properties. The one-dimensional vertical heat conduction into the surface is controlled by the thermal inertia $\Gamma = \sqrt{\kappa\rho c}$, where κ is the thermal conductivity, ρ the density, and c the heat capacity. The observed mid-/far-IR/sub-mm fluxes are connected to the hottest regions on the asteroid surface and dominated by the diurnal heat wave. The seasonal heat wave is less important and therefore not considered. Infrared beaming effects (similar to opposition effects at optical wavelengths) are calculated via a surface roughness model, described by segments of hemispherical craters. Mutual heating is included and the true crater illumination and the visibility of shadows is considered. An example of the shape

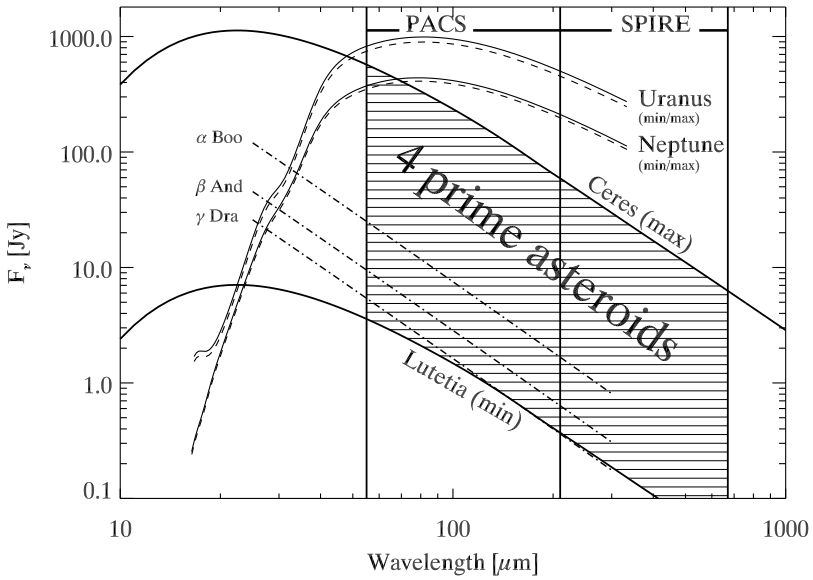

Figure 6.3: Overview with the flux densities of the different far-IR/sub-mm/mm calibrators. The Uranus and Neptune SEDs represent the minimum and maximum fluxes during Herschel visibility phases. Three fiducial stars are also shown, their flux range coverage is representative for the brightest stellar calibrators. For Ceres the maximum flux and for Lutetia the minimum flux during Herschel observations are shown.

model for asteroid (2) Pallas is shown in Fig. 6.4.

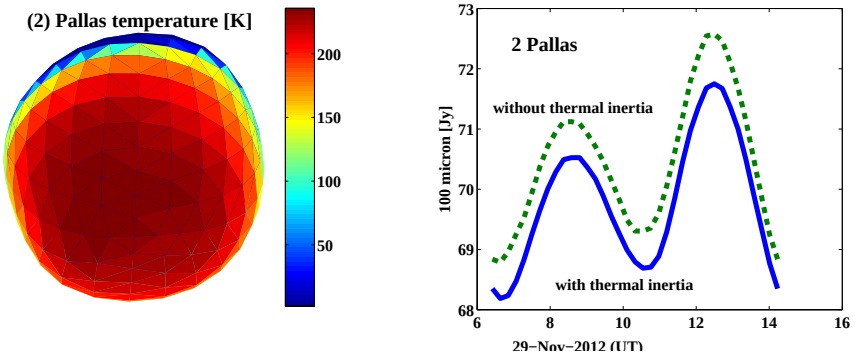

Figure 6.4: **Left**: Shape model of Pallas with the TPM temperature coding on the surface, calculated for the *Herschel* point-of-view on OD 1295, OBSID 1342256236, rotation axis is along the vertical direction. **Right**: the corresponding thermal light-curve at 100 μm with and without thermal effects included.

PACS photometry was obtained for in total 16 asteroids:

1) The four asteroids (1) Ceres, (2) Pallas, (4) Vesta, and (21) Lutetia. With newly established ther-

Table 6.3: Model flux predictions for (1) Ceres, (2) Pallas, (4) Vesta, and (21) Lutetia. The flux range encountered during the entire mission is reflected by maximum and minimum values and the epoch of observation (OD). Appropriate colour-correction factors (cc) to be applied to measured PACS fluxes for comparison with the model predictions are also given.

Source	model source	OD	f_70 (Jy)	cc_70	f_100 (Jy)	cc_100	f_160 (Jy)	cc_160
(1) Ceres	JTPM_PacsPhoto∗.tar	1244	394.2	1.00	226.6	1.02	96.8	1.07
		726	176.8	1.00	102.4	1.02	43.9	1.07
(2) Pallas	JTPM_PacsPhoto∗.tar	1295	119.1	1.00	68.8	1.02	29.3	1.07
		686	43.7	1.00	25.4	1.02	11.1	1.07
(4) Vesta	JTPM_PacsPhoto∗.tar	743	259.3	1.00	146.7	1.03	61.3	1.07
		160	88.8	1.00	51.2	1.03	21.4	1.07
(21) Lutetia	JTPM_PacsPhoto∗.tar	859	11.1	1.00	6.4	1.02	2.7	1.07
		400	2.7	1.00	1.6	1.02	0.67	1.07

mophysical models and photometric consistency verification against PACS, SPIRE and HIFI measurements, they can be considered as prime flux calibrators (Müller et al., 2014).

2) The regularly observed asteroids (10) Hygiea, (3) Juno, (52) Europa, (88) Thisbe, (704) Interamnia, (8) Flora, (6) Hebe, and (20) Massalia

3) The asteroids (47) Aglaja, (423) Diotima, (65) Cybele and (29) Amphitrite

In Table 6.3 asteroid model flux predictions of the four prime calibrator asteroids Ceres, Pallas, Vesta and Lutetia for certain epochs and appropriate colour-correction factors are listed for comparison with measured PACS fluxes. Detailed information on the asteroid thermophysical model database can be found in the *Herschel* asteroid calibrator models release note. Model data files for each individual *Herschel* OBSID can be downloaded from here.

The correspondence of the TPM models with measured PACS fluxes is better than 2% for (1) Ceres and (2) Pallas, better than 4% for (4) Vesta and better than 5% for (21) Lutetia. For further details of the photometric verification against PACS, SPIRE and HIFI measurements, see Müller et al. (2014).

6.4 Faint stars

The photometric calibration of PACS used five fiducial stars. They are still relatively bright in the FIR (in the range 1–10 Jy) so one can obtain a high SNR within reasonable measurement times. For the photometer, alongside repeated measurements of these standard stars, a set of fainter secondary standard stars was repeatedly measured as part of the calibration program. This included sources down to a few mJy (hence too faint for the spectrometer). Including fainter sources with well-known flux predictions allows one to address the following issues:

1. How does the sensitivity scale with flux and time?

2. How does the finally-achieved sensitivity compare with predictions by the PACS exposure-time calculator of the *Herschel* observation planning tool?

3. What is the impact and consistency of the applied data reduction scheme on the resulting source flux for increasingly fainter flux contributions to the telescope background level?

4. What is the impact of background confusion noise on the resulting fluxes and the sensitivity limit?

In preparation of the PACS in-flight photometric calibration, secondary standard source lists with stars described in Cohen et al. (1996) [1], Hammersley et al. (1998) [2] and Gordon et al. (2007) were prepared. Depending on the source visibility during the *Herschel* mission, a subset of sources from these lists were observed to cover the flux range from 0.5–2.5 Jy down to 4–20 mJy over the three photometer bands. The final 15 sources for which photometry was obtained (Klaas et al., 2017) are listed in Table 6.4.

From these 15 sources, Klaas et al. (2017) could establish a set of 5 primary standard candidates, namely α Ari, ε Lep, ω Cap, HD 41047, and 42 Dra, with an absolute accuracy of $<$6%. HD 152222 is a very promising candidate as faintest FIR primary standard, but the absolute accuracy is limited to $<$13% due to a lack of accurate K-band photometry. The stars θ Umi, HD 138265 and HD 159330 prove to be good primary standard candidates, but significant source confusion at 160μm limited their use beyond 100μm. These primary standard candidates with their available photometry are shown in Fig. 6.5 with regard to the relative scaling to the fiducial primary standard stars α Boo, α Tau, γ Dra and β And. δ Dra appears to be a quite reliable standard, but there is no suitable counterpart among the fiducial standard stars. Beside the modelling by Cohen et al. (1996), it was modeled by Decin et al. (2003) as *ISO*-SWS calibrator. β Gem and η Dra had to be ruled out as standards, since both exhibit an intrinsic excess caused by dust disks. HD 39608 had to be ruled out as a standard, since it is severely affected by background confusion longward of 70 μm. HD 181597 and HD 15008 were only detected at 70 μm by the available PACS measurements, so that no final judgment of their quality as standards can be made.

[1] corresponding model data can be found under http://iso.esac.esa.int/users/expl_lib/ISO/wwwcal/isoprep/cohen/extraps/
[2] corresponding model data can be found under http://iso.esac.esa.int/users/expl_lib/ISO/wwwcal/isoprep/gbpp/

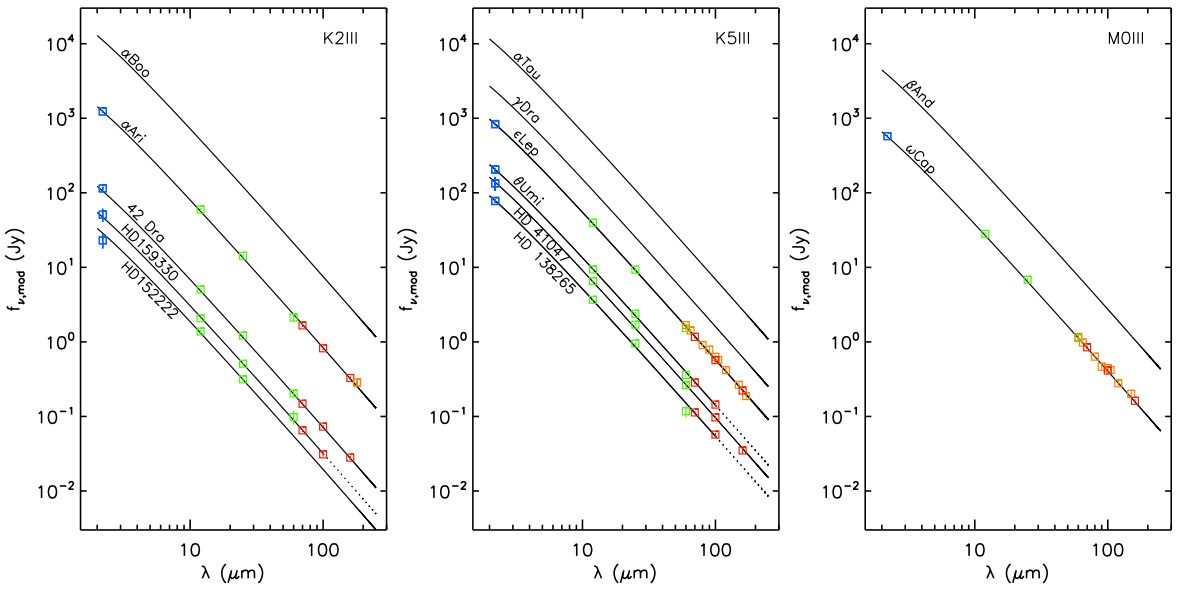

Figure 6.5: Establishment of new primary standard candidates from the faint secondary standard list in Table 6.4 for three different spectral types. Model predictions were obtained by scaling of the corresponding PACS fiducial star continuum models (black lines, cf. Fig. 6.1) to the flux level of the new primary standards with the scale factors as derived by Klaas et al. (2017). Photometry of the new standards is shown as blue squares: K-band photometry, green squares: colour-corrected IRAS FSC photometry (Moshir et al., 1993), orange squares: ISOPHOT Highly Processed Data Products (Klaas et al., 2017) and red squares: PACS photometry (Klaas et al., 2017). Dashed parts of the SEDs of HD 159330, θ Umi and HD 138265 indicate that these stars are proven reliable standards only up to 100 μm due to background confusion (cf. discussion in Klaas et al. 2017).

Table 6.4: Faint secondary standards observed by *Herschel*–PACS in chop-nod (c) and/or scan map (s) mode. Source fluxes from Gordon et al. (2007) are for an effective wavelength of 71.42 μm and have been colour corrected to the PACS central wavelength of 70 μm, by dividing by the factor 0.961 (cf. Sec. 7.5.3) for a Rayleigh-Jeans tail type SED. 100 and 160 μm fluxes for these sources are then extrapolated values for this adopted SED.

		PACS	model flux prediction (mJy)			spectral type	reference
HD	other name	obs mode	f_{70}	f_{100}	f_{160}		
62509	β Gem	c,s	2457 ($\pm$5.73%)	1190 ($\pm$5.73%)	455.9 ($\pm$5.73%)	K0IIIb	Cohen et al. (1996)
12929	α Ari	s	1707 ($\pm$5.9%)	831.4 ($\pm$5.9%)	321.0 ($\pm$5.9%)	K2III	Cohen et al. (1996)
32887	ε Lep	c,s	1182 ($\pm$5.9%)	576.2 ($\pm$5.9%)	222.7 ($\pm$5.9%)	K4III	Cohen et al. (1996)
198542	ω Cap	s	857.7 ($\pm$6.03%)	418.0 ($\pm$6.03%)	161.5 ($\pm$6.03%)	M0III	Cohen et al. (1996)
148387	η Dra	c,s	479.5 ($\pm$3.38%)	232.6 ($\pm$3.45%)	89.4 ($\pm$3.51%)	G8III	Hammersley et al. (1998)
180711	δ Dra	c,s	428.9 ($\pm$5.7%)	207.7 ($\pm$5.7%)	79.6 ($\pm$5.7%)	G9III	Cohen et al. (1996)
139669	θ Umi	c,s	286.2 ($\pm$5.67%)	139.5 ($\pm$5.67%)	53.9 ($\pm$5.67%)	K5III	Cohen et al. (1996)
41047	HR 2131	c,s	195.6 ($\pm$5.96%)	95.4 ($\pm$5.96%)	36.9 ($\pm$5.96%)	K5III	Cohen et al. (1996)
170693	42 Dra	s	153.7$\pm$4.6	75.3 ($\pm$3.0%)	29.4 ($\pm$3.0%)	K1.5III	Gordon et al. (2007)
138265	HR 5755	c,s	115.9$\pm$4.0	56.8 ($\pm$3.5%)	22.2 ($\pm$3.5%)	K5III	Gordon et al. (2007)
159330	HR 6540	c,s	64.2$\pm$2.1	31.5 ($\pm$3.3%)	12.3 ($\pm$3.3%)	K2III	Gordon et al. (2007)
152222		c,s	39.4$\pm$1.9	19.3 ($\pm$5.0%)	7.5 ($\pm$5.0%)	K2	Gordon et al. (2007)
39608		s	30.9$\pm$1.2	15.1 ($\pm$4.0%)	5.9 ($\pm$4.0%)	K5III	Gordon et al. (2007)
181597	HR 7341	c,s	28.0 ($\pm$3.29%)	13.6 ($\pm$3.34%)	5.2 ($\pm$3.42%)	K1III	Hammersley et al. (1998)
15008	δ Hyi	c,s	22.9$\pm$0.8	11.2 ($\pm$3.5%)	4.4 ($\pm$3.5%)	A1/2V	Gordon et al. (2007)

Chapter 7

The Photometer Calibration

7.1 Introduction

The calibration of the PACS photometric observing modes was addressed centrally by the Observatory. The PACS Instrument Control Centre Team in collaboration with the *Herschel* Calibration Scientists established a smooth evolution of the calibration from module characterisation, over the detailed instrument and integrated system tests on ground, to the final full system verification and calibration in-flight, as outlined in the PACS Calibration Document Klaas et al. (2014). The PACS calibration team planned, worked out, executed and analysed dedicated calibration observations on blackbody sources on ground, generating continuum emission over the full field-of-view (via integrating spheres or simulating point sources with hole masks) and computing celestial standards, to consistently and thoroughly characterise all instrumental effects of the PACS photometer while in flight.

Once in orbit, after the initial instrument check-out, there was a larger calibration block during the Performance Verification Phase verifying the in-orbit performance of the photometer observing modes, comparing against predictions and the ground performance, and tuning for optimal performance in the space environment as well as providing the baseline in-flight calibration. 528.6 h of observing time were spent on this, as outlined in detail in the PACS PV Phase Plan (Klaas and Nielbock, 2014a). Verification of the calibration stability and refinement and extension of the calibration, taking into account the growing knowledge in data processing, was then done during the Routine Science Phase of the *Herschel* mission. An additional 293.2 h were allocated to this goal, as described in detail in the PACS Routine Science Phase Plan (Klaas and Nielbock, 2014b).

The results of the calibration work that is described in this chapter were converted into calibration files which were added to the 'calibration tree' that was used for the SPG and interactive pipeline processing. Most calibration files were updated several times during the first few years of the mission, and those of the higher levels were updated even during the post-operations phase. A history of the calibration tree updates can be found as a pdf file posted on HELL L2 (Level 2). The calibration files themselves (FITS and ascii files) are provided as Ancilliary data products on this HSC repository. The calibration tree is also explained in Sec. 10.5.

Since the PACS blue photometer camera offered the best spatial resolution of all *Herschel* instruments, it was used to verify the absolute pointing accuracy of the *Herschel* telescope. The characterisation of specular straylight features generated by *Herschel* telescope parts was established in a PACS/SPIRE photometer parallel-mode calibration program. Both of these calibration aspects are described in the

Herschel Satellite Handbook. The issue of *Herschel* instrument cross-calibration is also addressed there.

In the following, the individual calibration items are shortly described and their accuracies are given. This includes also an overview on the celestial calibration standards.

7.2 Calibration achievements during CoP and PV phases

The *Herschel* Commissioning Phase (CoP) lasted for the first two months of the mission and was characterised by a not yet final and stable observing environment, the first part being executed with the cryo cover still closed and the second part with the telescope still cooling down. Nevertheless, the following results were achieved:

- The photometer was found fully functional and in its nominal operation mode.
- The smooth operation of the chopper control loop was verified and even slightly improved. The warm electronics was temperature stabilised, thus avoiding control loop gain drifts.
- The so-called "sneak preview" on OD 32 with the PACS photometer executing scan maps on M 51 provided the first light results shortly after successful opening of the cryostat cover. This verified early on that the telescope was in focus and revealed the triangular wing feature of the PSF. The measurements also gave the first feedback to a global telescope pointing improvement (SIAM update).
- A perfect tracking of the telescope on the fast moving asteroid Melpomene (67″/h) was verified.
- The bolometer bias voltages were successfully tuned during the cool-down of the telescope with no saturation effects being encountered in low gain mode, thus providing optimal start conditions for the bolometer detector set-up optimisation in the first part of the PV Phase.
- A first, already quite accurate, prescription for the ^{3}He cooler hold-time calculation was derived, which enabled efficient usage of the cold bolometer state between two cooler recyclings.

The objectives and details of the PACS photometer operations during the Commissioning Phase are explained in detail in the PACS Commissioning Phase Plan (Feuchtgruber, 2009) and the PACS Commissioning Phase Timeline (Klaas & Nielbock 2009).

The PV Phase for the PACS photometer lasted from OD 64 until OD 191, at the end overlapping with the Observatory SD Phase. Fig. 7.1 shows the logical build-up of the initial in-flight calibration of the PACS photometer during the PV Phase:

- After adjusting the dynamic range of the bolometers to the telescope background at its lower end towards the end of the Commissioning Phase, one of the first photometer calibration tasks was to find the bolometer bias for optimal detector responsivity and noise equivalent power (NEP) in the high-gain mode. The direct read-out mode was preferred to the double-differential correlated sampling mode. In the last step the low frequency noise and the signal dependence on the chopper frequency was characterised.

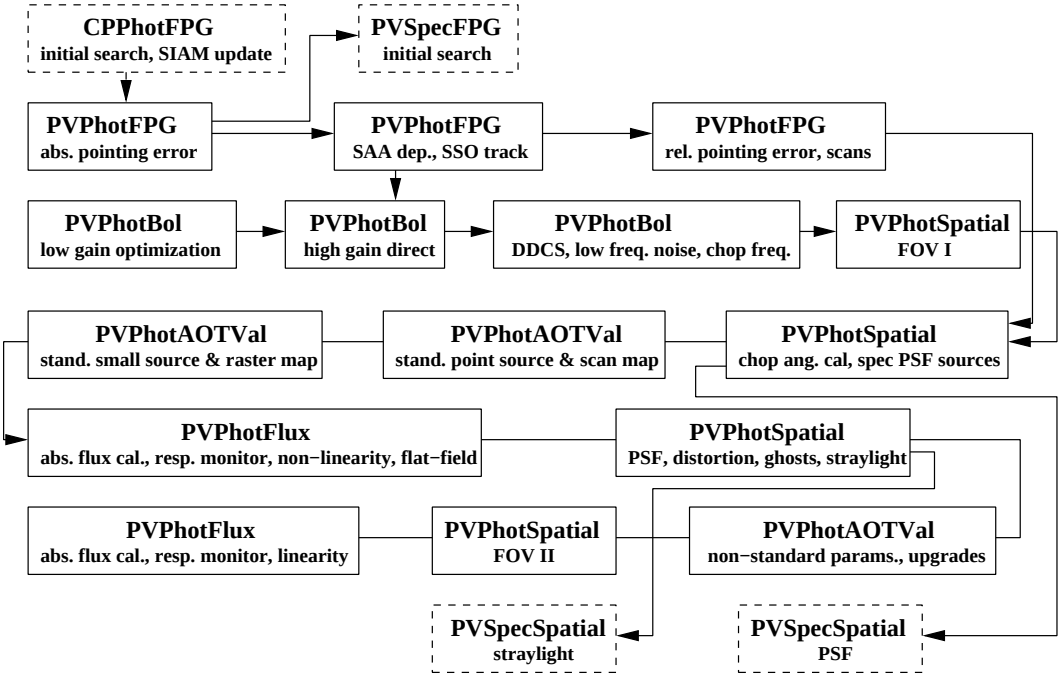

Figure 7.1: Logical flow of addressing the PACS photometer calibration items during the *Herschel* PV Phase, taking into account mutual dependencies and prerequisites. Each box includes the calibration proposal name and the list of calibration items addressed during this block.

- Parallel to the optimisation of the detector settings, the *Herschel* telescope pointing behaviour could be investigated and characterised – this did not need the final sensitivity, since the pointing calibration sources were reasonably bright.

- With the finalisation of the detector set-up, the performance of the pre-flight designed observing modes could proceed. It was rapidly obvious that the scan-map mode was more efficient and sensitive for mapping than the small-source and rastering chopped modes. This led to an early deprecation of the latter two modes. For point-source observations, dedicated mini-map scans were newly designed and optimised. A scan speed of 20 arcsec/s was found superior to the original baseline scan speed of 10 arcsec/s, so that this speed was not offered any more for scientific observations. The original chop-nod point source mode was maintained throughout the mission for pointing calibration (delivering more precise astrometry) and as an independent check of the overall photometric calibration on a subset of flux standards (Nielbock et al., 2013).

- The photometric flux calibration program, including non-linearity assessment, started in PV Phase, however some of the fiducial standard star and planet measurements had to be deferred to after the PV Phase for visibility reasons and additional measurements had to be accumulated to address the aspect of reproducibility. A consistent in-flight calibration update also needed the evaluation of the beam profiles to derive the encircled energy fractions for the apertures. Both steps were achieved only some time after the end of PV Phase.

- The first basic measurement set for the spatial calibration of the PACS photometer was acquired. This included the verification of the chopper angular scale on double sources with well known separation, the first PSF characterisation on point sources with different SED shapes and maps

on a bright source allowing its instantaneous detection in each detector frame in support of determining the photometer's field distortion. Dedicated programs around very bright sources aimed for characterising ghost and near-field straylight features generated inside the instrument and for detecting predicted specular out-of-field straylight spots by the telescope structure. The spatial extent and structure of some very bright sources selected for the spatial calibration of the spectrometer was also checked with the better spatial resolution of the photometer.

The objectives and details of the PACS photometer operations during the PV Phase are given in the PACS Performance Verification Phase Plan (Klaas and Nielbock, 2014a). A summary of the pre-flight and in-flight calibration tests for PACS can be found in the PACS Calibration Document (Klaas et al., 2014), and in the PACS Calibration Document Overview (Klaas, 2014) the document numbers for all relevant technical notes can be found.

7.3 Spatial calibration

The spatial calibration of the PACS photometer covered two main topics:

1. Mapping the focal plane to the sky. This was needed to assign sky coordinates RA, Dec to each individual flux measurement, as defined by a bolometer pixel and a time. Sky coordinates were required for the centre of a photometer pixel and/or its corners.

2. Characterising the point spread function (PSF) and related effects such a ghosts or straylight. This included the determination of encircled energy fractions.

7.3.1 Focal plane mapping and field-of-view distortion

The photometer pointing and spatial calibration was defined with reference to a "virtual aperture" at the centre of the blue array. This virtual aperture actually corresponds to a gap between the matrices constituting the bolometer. Chopped/nodded observations were set up to provide a symmetric beam pattern around this position. This were done for a large set of pointing sources with accurate positions, to ensure that *Herschel* placed this virtual aperture at the intended position. The location of the virtual aperture is captured in the `Siam` calfile.

The following coordinate systems and transformations were used to assign a sky position to photometer pixels:

- Subarray coordinates p,q: A coordinate system for the subarrays (= bolometer matrices), trivially assigning the centre of each pixel with an integer coordinate e.g. p,q=(4,5). This corresponds to the indices of each pixel in a PACS "frame".

- Array coordinates u,v: A cartesian coordinate system in the PACS focal plane, with the long "v" axis aligned with the chop direction. The `SubArrayArray` calfile captures the location of each pixel p,q in these coordinates. Here, each matrix was assumed to be an ideal grid, but the relative spacings and orientations of matrices were allowed to be imperfect. For each pixel, the positions of the centre and of the four corners of the nominally active region ($640\times640\mu$m within the full $750\times750\mu$m pixel) were provided.

- Instrument coordinates y,z: An orthogonal local coordinate system on the tangential plane of the sky. The two axes are aligned with the spacecraft Y and Z axes as projected onto the sky, and the zero point is the "virtual aperture" of the bolometer. It corresponds to the zero point of the array coordinate system for the blue array and chopper angle = 0. The `ArrayInstrument` calfile contains polynomial relations that permits the computation of y and z given u,v, and the chopper angle.

- Sky coordinates: The J2000 ICRS right ascension and declination of a measurement. Standard methods can be used to compute this from y,z, plus RA, DEC of the virtual aperture and the spacecraft position angle.

The `AubArrayArray` and `ArrayInstrument` calfiles were initially derived from instrument-level tests in the laboratory. A "punched hole" far-infrared source was rastered over a grid of positions, in front of a setup that included test optics and PACS. Such measurements were obtained for dense spatial grids and for several chopper positions, and transferred to the first on-sky versions of the calfiles via the optical model of the test optics. For that step, the optical model had to be assumed to be fully accurate.

Over much of the mission, the quality of the reconstructed *Herschel* pointing was insufficient for a fully independent re-derivation of these quantities. Instead, only the scale and rotation of the ground-based calibration were adjusted to match actual observations, but distortions were still traced back to the ground tests. When more accurate gyro-reconstructed pointing became available, detailed scans across bright (near) point sources were used to re-derive the `SubArrayArray` and `ArrayInstrument` calfiles. These observations were obtained only for the zero chopper position because they are very time consuming, hence chopper-related terms in the most recent `ArrayInstrument` calfile still make use of the ground tests. This has no practical consequences because in-orbit experience led to the overwhelming majority of PACS observations being unchopped scan maps with the chopper at the zero position.

Fig. 7.2 uses results of an R Dor observation to visualise the footprint of the blue and red photometer pixels on sky. Fits to these and other observations were used to derive the final spatial calfiles. Salient feature include:

- A several degree tilt of the photometer arrays with respect to the spacecraft y direction. In contrast, the chopper direction is close to the y direction.

- Slight deviations from a regular pattern for the relative positions of the individual matrices – most visible for the two left blue matrices in Fig. 7.2.

- Field-of-view distortions requiring nonlinear terms, most clearly visible for the red array.

More detailed information can be obtained from a number of documents in HELL: the Lutz and Contursi (2013) technical note describes the coordinate systems, the calibration files transforming between them, and their version history; Contursi and Lutz (2008) provides an overview sketch of some coordinate orientations; and Lutz and Feuchtgruber (2013) presents the most accurate evidence on mapping the pixel positions to sky, and the FOV distortion.

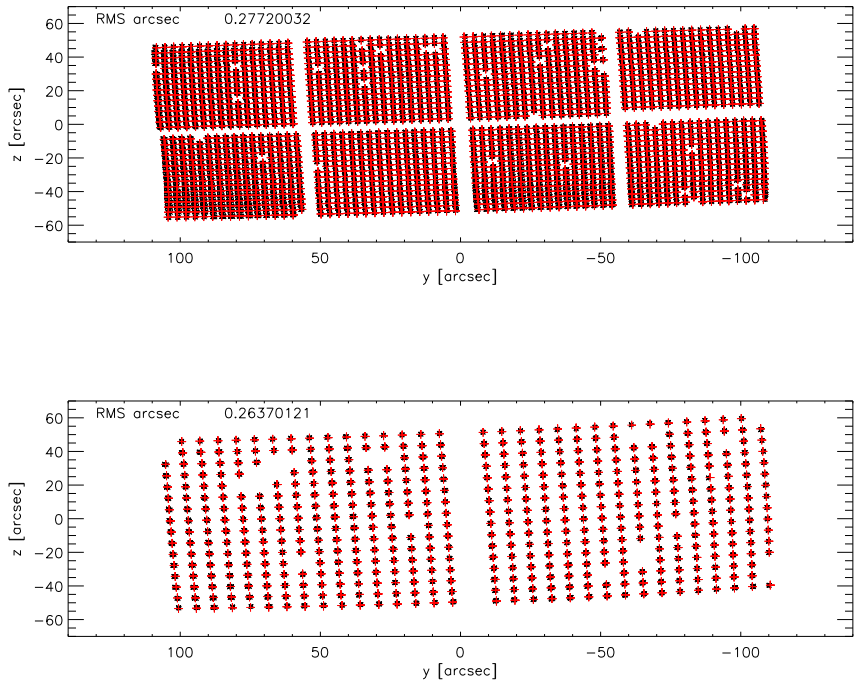

Figure 7.2: Location of PACS photometer pixels on the sky, as measured from OD1308 observations of R Dor (black symbols). **Top**: blue array, **bottom**: red array. The coordinates are defined by the photometer virtual aperture and the y and z direction of the *Herschel* spacecraft coordinate system. Bad pixels and few outliers from the preliminary fit that is shown in red are not plotted.

7.3.1.1 Non-uniform pixel size

As described below in Sec. 7.4, the photometric calibration of the PACS photometer uses units of Jy/pixel both for the individual detector timelines in the frames, and for the final sky-projected photometric maps. It is important to note that in *Frames* products, Jy/pixel refers to the instrument's physical pixels. Given the distortions just discussed, for different pixels these physical pixels project to different solid angles on sky, despite their same physical size in μm. Mappers creating final maps with regular sky pixels from the frames have to consider this, via use of the information in the `SubArrayArray` and `ArrayInstrument` calfiles. For some mappers this may need was applied via the HIPE *convertToFixedPixelSize* task.

7.3.2 PACS photometer point spread function

The PSF of the PACS photometer is mostly derived from observations of the bright point or near-point sources Vesta, Ceres, α Tau and α Boo. The bright planets Neptune and Mars were used to probe the faint PSF wings, at the expense of heavy saturation of the PSF core for Mars. In the explanatory library, *PACS photometer point spread function* (Lutz, 2015) and its associated tarball are the main references for the observed PSF.

Modeled PSFs have been made available in the technical note by (Geis and Lutz, 2010) and its associated data tarball. While these reproduce many salient features of the observed PSF, they are **not** to be used to perform PSF fitting, deconvolution, or derivation of encircled energy fractions. This is because they reflect only pre-launch knowledge of the *Herschel* mirror shape, and do not include effects inside PACS. In addition, the actual shape of the beam depends on the details of the observation and the mapper used to create the maps.

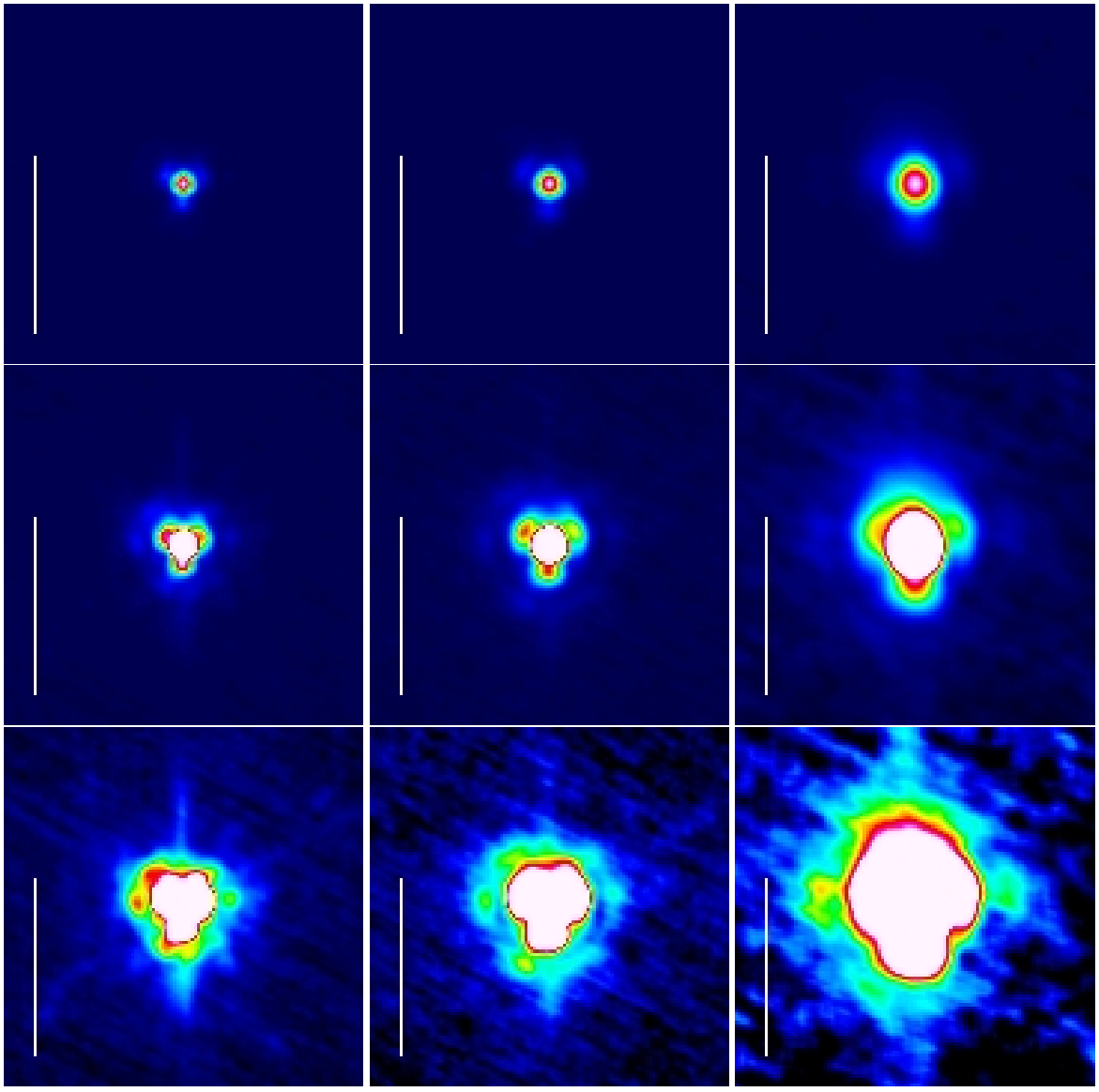

Figure 7.3: PACS photometer PSF at 70 μm (**left**), 100 μm (**centre**) and 160 μm (**right**), as derived from Vesta observations on OD160. The images use a linear stretch to 100%, 10%, and 1% of the PSF peak from top to bottom. The spacecraft Z direction is at the top, as for observations with telescope PA=0, and the scale bar indicates 60$''$.

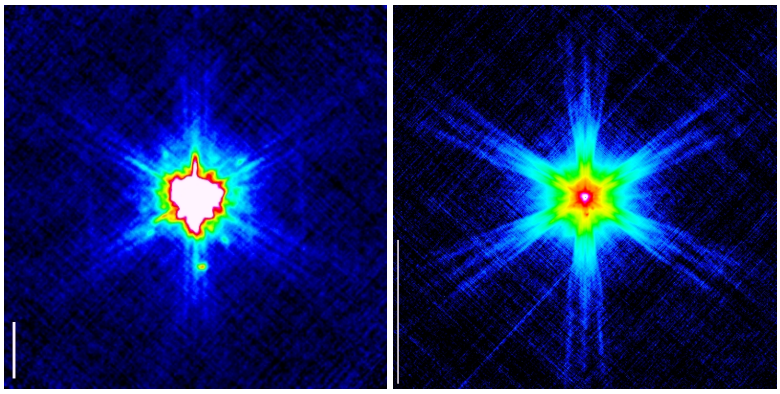

Figure 7.4: Faint structures in the PACS 70μm PSF. **Left**: Ceres with a stretch from -0.0005 to 0.001 of the PSF peak, scale bar indicates 60$''$. **Right**: Diffraction spikes from observations of Mars, scale bar indicates 600$''$.

7.3.2.1 PSF morphology

In all three PACS bands, the PSF core is surrounded by a tri-lobe pattern at the level of up to 10% (in the blue) of the PSF peak (Fig. 7.3). This basic morphology reflects the wavefront errors caused by the *Herschel* main-mirror surface imperfections. Among other factors, they reflect the 120 degree symmetry of the secondary mirror suspensions. In all three bands, the top-right of the three lobes is the weakest, this being qualitatively reproduced by models.

The next fainter level of PSF structure is a knotty pattern at the few % level and below. It is clearly seen in the blue and with less detail in the green and red. The blue data clearly show a weak spike in roughly vertical (spacecraft Z) direction that is also present in the green and red. At roughly 70$''$ towards the -Z direction, a bright spot is superposed on this spike, clearly seen at 70 μm (Fig. 7.4) and weakly at 100 μm. It is induced in PACS rather than the telescope, and is likely caused by an optical ghost. At yet fainter levels we have a knotty PSF structure, and finally the telescope secondary support diffraction spikes (Fig. 7.4).

The PSFs at the medium scan speed 20$''$/s, that was employed for almost all prime-mode PACS scan-maps, and for the rarely-used slow 10$''$/s speed are virtually identical. They are roughly round for 70 μm and 100 μm but vertically (Z direction) elongated in the red. This elongation is seen in the PSF core and is not just an effect of wings or lobes. These $\leq$20$''$/s prime mode PSFs reflect the optical properties of *Herschel*+PACS.

For fast 60$''$/s prime-mode scans, detector time constants led to a significant PSF elongation in the scanning direction. For the blue channel in PACS/SPIRE parallel mode, the smoothing into 5 Hz rather than 10 Hz frames led to an equivalent elongation that is already noticeable at 20$''$/s and is strong for the widely adopted 60$''$/s of the parallel-mode observations. Fig. 7.5 uses the example of the 70 μm band to show these elongations. Note that for a typical parallel-mode map composed from two observations with crossed scans, these elongated PSFs will superpose to a cross-like structure.

The fast scan-speed 70 and 100 μm PSFs show a region along the scan direction and directed from the PSF peak, where the flux undershoots to below zero, to a level of about -1% of the peak. This is a consequence of an undershoot in the detector timeline after a bright signal, i.e. it is not a processing artefact.

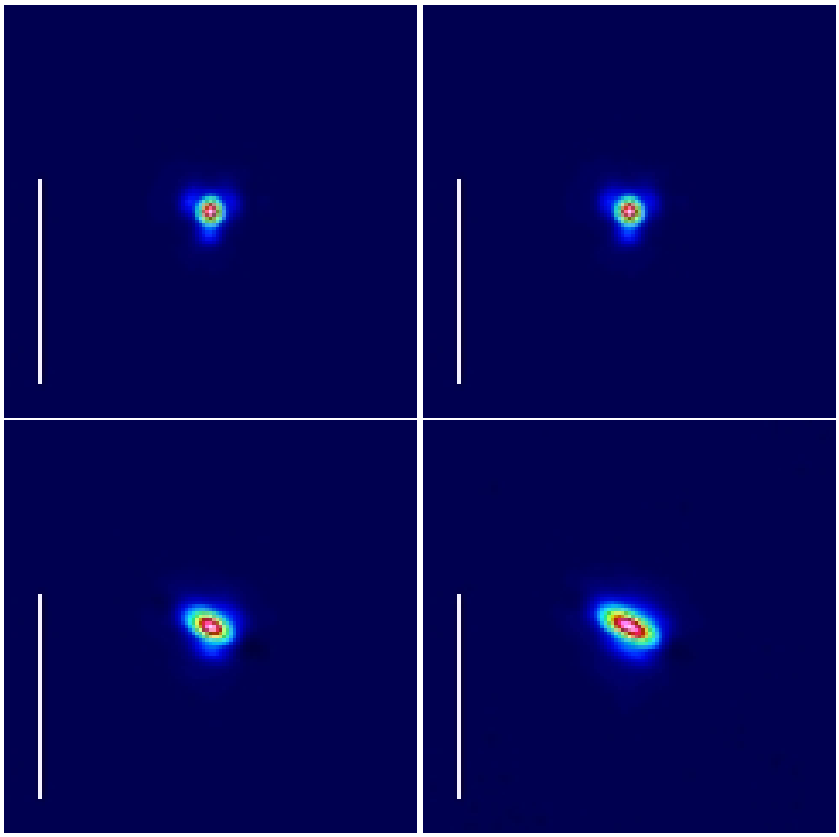

Figure 7.5: Effects of scan speed. The PACS photometer PSF at 70μm is shown for prime mode scan speeds of 10″/s (**top left**), 20″/s (**top right**), and 60″/s (**bottom left**). The additional smoothing because of the 5 Hz averaging in the blue channel for PACS/SPIRE parallel mode is indicated in the bottom right panel for speed 60″/s. The PSF images are at 70 μm, use a linear stretch to the PSF peak, and the scale bar indicates 60″.

7.3.2.2 Effects of source colour and reduction schemes

Table 7.1 lists the FWHM of the photometer PSF as obtained from a Rayleigh-Jeans source and masked highpass plus photProject mapping onto small 1″ pixels. Several influences can modify these values.

Because of the large spectral width of the PACS filters, noticeable effects of the SED slope on the width of the PSF exist. Convolving the modelled PSFs (Geis and Lutz, 2010) for different spectral slopes $F_\lambda \propto \lambda^\alpha$ with the PACS pixel size, the ratio of the PSF's FWHM for $\alpha = -4$ (as for a star or asteroid) and the FWHM for $\alpha = -1$, is 0.979, 0.971, 0.956 for the 70, 100, 160μm filters. Exactly tuning the convolution to the precise observed FHWM for the Rayleigh-Jeans $\alpha = -4$ and comparing to a specific source's α can refine such comparisons further. All stellar and asteroid bright point sources used to calibrate the PACS PSF have Rayleigh-Jeans like slopes in the far-infrared. A FWHM comparison to observations of the comparatively faint and lower S/N Blazar 3C345, which has a much redder SED, shows a consistency with the model-based estimates of the FWHM increase.

The PSF images obtained from any mapper depend on the chosen map pixel size. For the drizzle-like

Mode	AMA	blue 70μm		green 100μm		red 160μm	
		FWHM	PA	FWHM	PA	FWHM	PA
	$^\circ$	$''$	$^\circ$	$''$	$^\circ$	$''$	$^\circ$
Prime 10 $''$/s	+63	5.20× 5.56		6.54× 6.78		10.38×11.97	6.1
Prime 20 $''$/s	+63	5.41× 5.72		6.66× 6.89		10.55×12.08	9.1
Prime 60 $''$/s	+63	5.70× 9.05	61.7	6.84× 9.81	61.8	11.39×13.37	41.2
Parallel 20 $''$/s	+42	5.44× 6.51	30.8	6.62× 7.44	31.1	10.29×12.20	8.5
Parallel 20 $''$/s	−42	5.31× 6.68	-26.5	6.53× 7.56	-27.0	10.37×12.27	-3.4
Parallel 60 $''$/s	+42	5.85×12.58	43.7	6.99×13.15	43.9	10.90×14.09	27.7
Parallel 60 $''$/s	−42	5.69×12.74	-36.9	6.87×13.41	-37.1	11.01×14.53	-23.7
Parallel 20 $''$/s	+42,−42	5.74×6.26	0.4	6.98× 7.42	−2.9	10.46×12.27	3.1
Parallel 60 $''$/s	+42,−42	8.80×9.60	−4.4	9.73×10.69	−3.8	11.51×13.65	5.3

Table 7.1: FWHM of the PACS PSF for several important cases. 2-dimensional Gaussian fits were used to derive the FWHM for the small and large axis. For noticeably non-round PSF cores, the position angle east of the spacecraft Z direction is noted. The array to map angle (AMA) of the scan is also specified. The maps used to derive the FWHM were created by the mapper *photProject* with map pixel size $1''$ and pixfrac=1. Entries above the line refer to single direction scans, showing the in-scan elongation for fast scan and for parallel mode. Entries below the line refer to co-added parallel-mode crossed scans, where a cross-like PSF emerges from co-adding the two elongated PSFs.

algorithm implemented by the *photProject* task, the drop size (controlled via the pixfrac parameter) is also relevant. Lutz (2015) lists the effect for map pixel sizes ranging from $1''$ to the nominal $3.2''$ or $6.4''$ photometer pixels, and for pixfrac from 0.01 to 1. The largest increase of PSF's FWHM over that range is 18%, 10%, 17% for 70, 100, 160 μm. For PSF fitting or similar tasks, it is strongly recommended to extract PSFs from the map proper, or from point source data that were reduced in a fully equivalent way.

Other effects on the PSF are more specific to the mapper. In the simple masked highpass filter and photProject scheme, the PSF is sensitive to the mask that is applied to a given source. In particular, unmasked sources that may e.g. later be retrieved via stacking will show negative filter residues in the scan direction. This is related to the slight fluxes losses in such reductions that are discussed by Popesso et al. (2012). Other mappers have occasionally produced enhanced flux in the PSF wings or artefacts near very bright point sources (see Sec. 9.1.1.7).

7.3.2.3 Effects of nonlinearity, saturation, crosstalk, ghosts, straylight on observed PSF

A number of effects can influence the PSF, in particular for very bright sources, and these may need to be considered when e.g. probing the the reality of faint companion structures. More detail is provided in Lutz (2015), but a brief summary is:

- **Nonlinearity**. The PACS bolometers respond in a nonlinear way to very bright sources. For point sources in the $\geq$ 100 Jy regime, this would lead to a flattening of the PSF peak. All reductions invoking the *photNonLinearityCorrection* task (i.e. the products in the HSA) are already corrected for this.
- **Saturation after effects**. After passing by very bright and saturated sources such as Mars, the signal did not instantaneously return to its stable pre-saturation value, since the detector

response changes. This can cause trails that are not an artefact of the mapmaker that was used.

- **Detector crosstalk**. An electrical crosstalk is observed between columns 15 and 0 in the same row of each bolometer matrix. The *photMaskCrosstalk* task excludes the affected column 0 from the final maps. If this task is not used and column 0 included, a faint negative signal may be seen about 50″ (70 or 100 μm) or 100″ (160 μm) offset in spacecraft Y direction from a very bright source. Its strength depends on processing details, e.g. the method of deglitching.

- **Ghosts, reflections, straylight**. A number of weak effects have been characterised for a situation where a very bright source falls onto certain spots in the focal plane. These can be safely ignored for all cases except for testing the reality of very faint structures near very bright sources. More detail can be found in two technical notes: Lutz (2015), Okumura (2010).

7.3.2.4 Encircled energy fraction

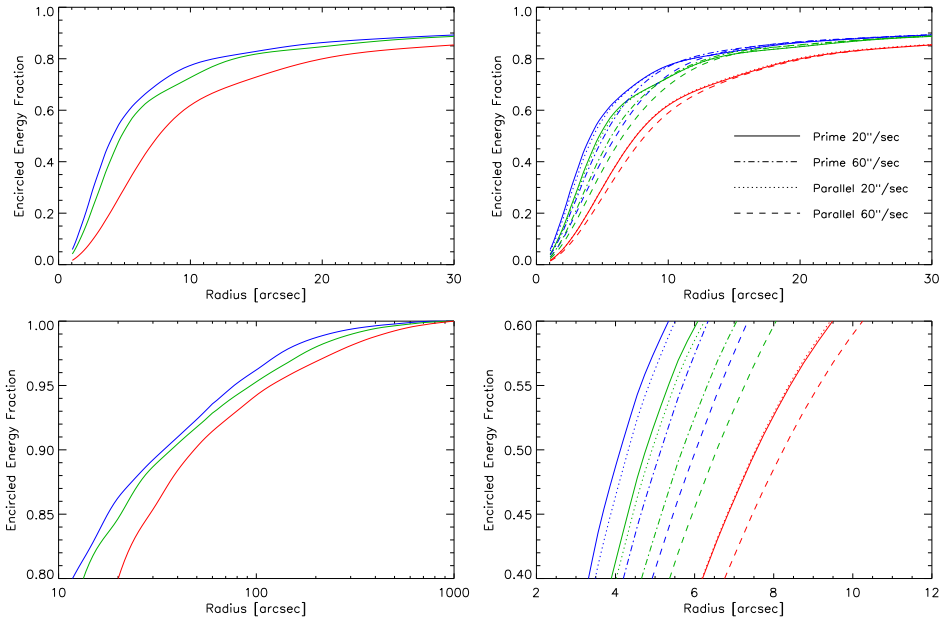

Figure 7.6: Fraction of energy from a point source contained within a circular aperture of given radius. **Left**: For the standard case of prime mode and slow or medium scan speed. The three PACS bands are shown in blue, green, red for 70, 100, 160 μm. **Right**: Repeat of the same curves, plus additional ones showing the smoothing effect of fast scan and/or parallel mode.

The radial profile of the PSF, or equivalently the fraction of energy from a point source contained in a given aperture (encircled energy fraction EEF), are the link between point-spread function and flux calibration. To achieve sufficient dynamic range, the PACS EEFs were derived from a combination of Vesta data (for the inner part of the profile) and Mars data (for the faint wings, but heavily saturated in the centre, and far from being a point source). Fig. 7.6 shows the EEF for the three bands and the default case of slow or medium scan speed in prime mode. This EEF underlies the PACS flux calibration. As discussed above, fast scan and/or PACS/SPIRE parallel mode lead to elongated PSFs. Fig. 7.6 also shows the resulting EEF curves.

7.3.2.4.1 EEFs for extended sources

The PACS photometry EEFs were derived from and applicable to point sources. If the target is a slightly extended source and an aperture large enough to encompass the entire source can be used, it will usually be sufficiently accurate to apply the point-source EEFs to the resulting photometry. However, bearing in mind that the observed source is a convolution of the PSF with the true source, a dedicated treatment will be needed for apertures similar to the source size, or if aiming for very high accuracy. Given that EEFs for this case depend, in addition to aperture size, on the parameters of the source itself (e.g. profile and shape), no such values are provided as part of the standard PACS photometry calibration. EEFs for such cases have to be derived by the user from a convolution of PSF and a source model. But, as already noted, these will be close to the point-source EEF for sources clearly smaller than the adopted aperture size.

7.4 Flux calibration

7.4.1 Flat-field

The flat-field describes the pixel-to-pixel response variation of the bolometer cameras under a homogeneous illumination. Each pixel had a slightly different gain from its neighbor (detector flat-field: the gain specification was 8% RMS over a whole 16×16 pixel detector matrix), and the transmission of the optical system was not spatially homogeneous (optical flat-field).

A homogeneous illumination was practically fulfilled during the instrument ground-level tests, when two blackbody sources were imaged via integrating spheres onto the photometer detectors, thus illuminating the whole arrays. The flat-field was constructed from the difference of pairs of measurements with small illumination power differences and appropriate normalisation over a selected pixel area. This established the first version of a flat-field used in the PACS data reduction. However, one deficit of this pre-flight generated flat-field was that the operational bias voltages applied to the detectors were different from the final ones in-flight. The flat-field in the green filter was not measured in this way but assumed to be the same as in the blue filter, since the detector was the same.

The use of the PACS internal calibration sources – which were relatively homogeneous sources illuminating the whole array – for construction of a flat-field could in the end not be realised. The optical field distortion at the chopper deflection pointing to the internal calibration sources (at about ± 6 arcmin from the optical zero position) was different from the field distortion inside the sky field-of-view and was not independently measurable. This would have been a significant drawback for the quality of the flat-field.

A determination of a sky flat-field had the difficulty that there is no real flat extended celestial source. This was overcome by performing scan maps on bright point and compact sources. The scan maps were performed with the slow scan speed ($10''$/s) and with 90^o orientation with regard to the instrument reference system (along the S/C Y-axis) to minimise the scan area and to illuminate each pixel by the source. Very small scan leg separations were selected ($2''$ or $3''$ with 2 maps shifted relatively by $1.5''$) to achieve a very high coverage.

Two reduction methods were applied:

1) The signal time-line for each pixel was used. After removing glitches, the time-line data were filtered to remove low-frequency noise. For each pixel, the value of the maximum minus the

median of the time-line signals was computed. The variation of this value over all pixels is the flat-field.

2) For each pixel, an independent map of the object was generated with the PhotProject projection algorithm (cf. Sec. 9.1.1.3). This included glitch removal and high-pass filtering to reduce the low-frequency noise. The flux of the source was then measured for each pixel by aperture photometry on the map generated from the single pixel. The variation of the fluxes over all pixels is the flat-field.

There is one significant difference in reduction philosophy between the pre-flight flat-field and the sky flat-fields: the treatment of electrical cross-talk. While for the pre-flight flat-field, which was generated by extended illumination, it was assumed that the cross-talk is part of the flat-field, for the sky flat-field, which was generated by scanning a compact source over the array, pixels affected by cross-talk were discarded.

The resulting sky flat-fields were ratioed to the ground-level flat-field. This allowed the identification of spurious features introduced by the processing. One of these features was a fringe pattern resulting from using a point source. It was caused by the interference of the map pixel grid and the telescope scanning pattern, which moved in the horizontal direction of the bolometer array. It was most visible for the blue filter, due to its sharp(est) PSF causing the flux falling onto one pixel to vary quickly with the position of the source within the pixel. Using a slightly extended source reduced this flux variation.

The final sky flat-field was constructed with the mapping method from special calibration measurements taken on OD 780 on the compact planetary nebula NGC 6543. This flat-field is most up-to-date with respect to the instrument settings in-flight and most consistent with the overall data-reduction strategy which includes the removal of cross-talk and optical distortion corrections. A more detailed description of the reduction is given in Okumura and Klaas (2016). Fig. 7.7 shows the photometer flat-field for each filter.

7.4.2 Responsivity calibration

The physical quantity which determines the bolometer's absolute photometric calibration is its responsivity, R, in units [V/W]. It is the ratio of the measured output signal, $U_{\rm sig}$ [V], and the infalling far-infrared radiation power, $F_{\rm photband}$ [W], in the photometric band, hence

$$U_{\rm sig} = R \times F_{\rm photband} \tag{7.1}$$

With a source SED, conventionally expressed as $f_{\nu,s}(\lambda)$ [Jy] in the FIR, and the relation $f_\lambda = \frac{c}{\lambda^2}\, f_\nu$, the flux in a PACS photometer band can be expressed as

$$F_{\rm photband}\ [W] = T\ A_{\rm eff} \int_{\lambda_1}^{\lambda_2} \frac{c}{\lambda^2}\, f_{\nu,s}(\lambda)\, S(\lambda)\, d\lambda \tag{7.2}$$

with T being the product of reflection losses by the optical mirrors, $A_{\rm eff}$ being the effective telescope area, and $S(\lambda)$ being the system response of the PACS photometer band.

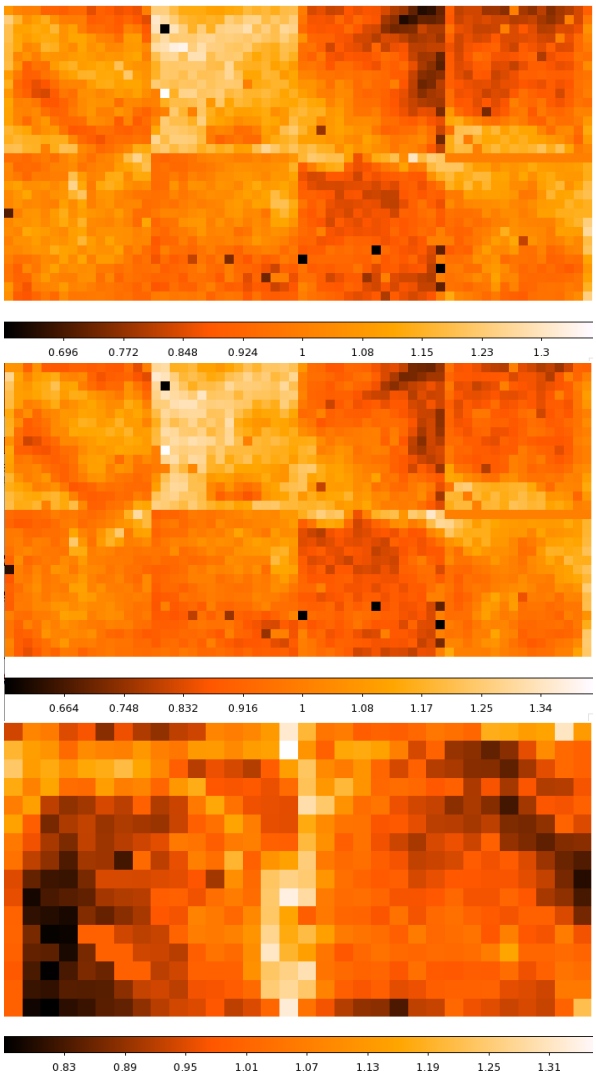

Figure 7.7: Photometer flat-fields for the three filter bands: blue (top), green (middle) and red (bottom). Individual detector matrices making up the camera field-of-view can be recognised. The scales indicate the amplitude of variation over the field-of-view.

For the PACS photometer, the convention is that the flux density at the reference wavelength $\mathrm{f}_{\nu,s}(\lambda_0)$ is determined for the reference SED $\mathrm{f}_{\nu,1} = \nu^{-1}$, i.e. $f_{\nu,1}(\lambda) = \frac{\nu_0}{\nu}\ f_{\nu,1}(\lambda_0) = \frac{\lambda}{\lambda_0}\ f_{\nu,1}(\lambda_0)$, hence

$$F_{\mathrm{photband}}\ \ [W] = T\ A_{\mathrm{eff}}\ f_{\nu,1}(\lambda_0)\ \frac{c}{\lambda_0} \int_{\lambda_1}^{\lambda_2} \frac{1}{\lambda}\ S(\lambda)\ d\lambda \tag{7.3}$$

$$f_{\nu,1}(\lambda_0)\ \ [Jy] = \frac{F_{\mathrm{photband}}}{T\ A_{\mathrm{eff}}\ \frac{c}{\lambda_0} \int_{\lambda_1}^{\lambda_2} \frac{1}{\lambda}\ S(\lambda)\ d\lambda} = F_{\mathrm{photband}}\ C_{\mathrm{conv}} \tag{7.4}$$

with conversion factor

$$C_{\rm conv}\ \ [m^{-2}\,Hz^{-1}] = \frac{1}{T\ A_{\rm eff}\ \frac{c}{\lambda_0}\int_{\lambda_1}^{\lambda_2}\frac{1}{\lambda}\ S(\lambda)\ d\lambda} = \frac{1}{T\ A\ \Delta\nu_0} \tag{7.5}$$

and effective bandwidth

$$\Delta\nu_0\ \ [Hz] = \frac{c}{\lambda_0}\int_{\lambda_1}^{\lambda_2}\frac{1}{\lambda}\ S(\lambda)\ d\lambda \tag{7.6}$$

The monochromatic flux density for the reference SED at the reference wavelength, $f_{\nu,1}(\lambda_0)$, can therefore be directly related to the measured output signal, $U_{\rm sig}$, as

$$f_{\nu,1}(\lambda_0)\ [Jy] = \frac{U_{\rm sig}\ C_{\rm conv}}{R} = \frac{U_{\rm sig}}{R_{\nu,1}} \tag{7.7}$$

with

$$R_{\nu,1}\ \ [V/Jy] = \frac{R}{C_{\rm conv}} \tag{7.8}$$

Note, that the nominal responsivity $R^{\rm nom}_{\nu,1}$ used in the calibration processing of PACS standard data products and as listed in Table 7.2, is a global value for the whole detector array. Individual pixel-to-pixels variations are accounted for by the flat-field ff_{pix}.

$R_{\nu,1}$ is actually not a constant. It depends on the operational temperature of the bolometers and their total flux load, hence $R_{\nu,1}$ = f(T, $B_{totalflux}$). These dependencies are treated as corrections to the nominal value $R^{\rm nom}_{\nu,1}$, as described in Sections 7.4.2.4.

Table 7.2 also lists the effective bandwidth $\Delta\,\nu_0$ and conversion factor $C_{\rm conv}$ for each band.

Table 7.2: Nominal responsivity $R^{\rm nom}_{\nu,1}$ and related $R^{\rm nom} = C_{\rm conv}\,R^{\rm nom}_{\nu,1}$ of the three photometer bandpasses. For the calculation of $C_{\rm conv}$, an effective telescope area $A_{eff} = \pi\,(\frac{3.33}{2.})^2 = 8.709\,m^2$ and a constant transmission factor T = $0.9315 \cdot 0.99^{16}$ = 0.7931 have been used. The effective bandwidth $\Delta\,\nu_0$ has been calculated for a constant in the flux per logarithmic frequency interval SED as defined in Eq. 7.6. $\Delta\,\lambda_0 = \frac{\lambda_0^2}{c}\,\Delta\,\nu_0$ is the corresponding bandwidth in wavelength.

λ_0 (μm)	$R^{\rm nom}_{\nu,1}$ (10^{-3} V/Jy)	$C_{\rm conv}$ (Jy/pW)	$R^{\rm nom}$ (10^{10} V/W)	$\Delta\,\nu_0$ (10^{11} Hz)	$\Delta\,\lambda_0$ (μm)
70	1.153	22.338	2.575	6.48	10.6
100	1.161	28.439	3.302	5.09	17.0
160	0.995	40.892	4.069	3.54	30.2

If the source SED $f_{\nu,s}(\lambda)$ is known, the true photometer source flux is determined as

$$f_{\nu,s}(\lambda_0) = \frac{f_{\nu,1}(\lambda_0)}{K_{cc,s}} \tag{7.9}$$

with $K_{cc,s}$ being the appropriate colour correction factor as described in section 7.5.3.

The value of R was thoroughly characterised in the lab (cf. Billot et al. 2006) with regard to its dependence on bias voltage setting, operational temperature, and optical load. The ground-based calibration was used to estimate the initial in-flight responsivity at the beginning of the mission once the telescope foreground emission had stabilised. For in-flight calibration only a relative update in the form of

$$\frac{R_{\nu,1}^{new}}{R_{\nu,1}^{old}} = \frac{f_{\nu,s}(\lambda_0)}{f_{\nu,standardmodel}(\lambda_0)} \tag{7.10}$$

was necessary, using the ratio of the measured flux to the celestial standard-star model flux, when calibrating $f_{\nu,s}(\lambda_0)$ with $\mathrm{R}_{\nu,1}^{old}$.

In practice, the update of R did not rely on one single flux measurement alone, but on a set of measurements on several standards, done to minimise systematic effects

$$\frac{R_{\nu,1}^{new}}{R_{\nu,1}^{old}} = \frac{1}{n}\sum_{i=1}^{n}\frac{f_{\nu,s,i}(\lambda_0)}{f_{\nu,standardmodel,i}(\lambda_0)} \tag{7.11}$$

so that $\frac{1}{n}\sum_{i=1}^{n}\frac{f_{\nu,s,i}(\lambda_0)}{f_{\nu,standardmodel,i}(\lambda_0)} = 1$ by applying $\mathrm{R}_{\nu,1}^{new}$.

This scheme was applied as and when more standard star measurements became available, when additional systematic instrument effects altering the signal level were corrected for, when changes in the encircled energy fraction altered the resulting flux (see below), or when new standard-star models became available.

The standard evaluation procedure for flux calibration measurements is aperture photometry. Hence, it is not the the total source flux that is measured, but only the fraction inside an aperture. For the derivation of the total measured source flux, a correction for the encircled energy fraction (EEF, see Figure 7.6 and Table 7.4) inside the aperture was performed:

$$f_{\nu,1}(\lambda_0) = \frac{f_{\nu,1}^{aperture}(\lambda_0)}{f_{EEF}} \tag{7.12}$$

7.4.2.1 Zero-magnitude conversion

In continuation of the flux-to-magnitude conversion information provided by previous FIR space missions, e.g. in IRAS Explanatory Supplement (Beichmann, 1985), (section VI C.2.a) and in the ISOPHOT Handbook (Laureijs et al., 2003), (appendix D), and in support of filter standardisation work for the Virtual Observatory (see e.g. this link), zero-magnitude flux densities have been determined for the central wavelengths of the three PACS photometer filters by use of an absolutely-calibrated theoretical photospheric model spectrum of Vega extrapolated to 300 μm (see this website; Cohen et al. 1992, 1995). Details are given in Nielbock and Klaas (2013). The interpolated zero-magnitude flux densities per unit wavelength, $\mathrm{f}_{\lambda,\mathrm{Vega}}^{0\,\mathrm{mag}}(\lambda_0)$, and converted flux densities per unit frequency, $\mathrm{f}_{\nu,\mathrm{Vega}}^{0\,\mathrm{mag}}(\lambda_0)$, for the PACS reference wavelengths λ_0 are listed in Table 7.3.

Table 7.3 also gives the zero-magnitude flux density for the PACS reference SED flux density $f_{\nu,1}^{0\,\mathrm{mag}}(\lambda_0) = K_{\mathrm{cc,BB10000}} \times f_{\nu,\mathrm{Vega}}^{0\,\mathrm{mag}}(\lambda_0)$. Zero-magnitude flux densities for any source SED can

then be computed by appropriate colour correction (see Section 7.5.3) of this reference SED zero-magnitude flux density. The magnitude of an observed source flux (if not colour-corrected, then as $f_{\nu,1}$) can then be calculated as

$$m_{\lambda_0}(mag) = -2.5\, log_{10} \frac{f_{\nu,\mathrm{S}}(\lambda_0)}{f_{\nu,\mathrm{S}}^{0\,\mathrm{mag}}(\lambda_0)} \tag{7.13}$$

The monochromatic AB magnitude (Oke and Gunn, 1983) is defined as

$$m_{\mathrm{AB},\lambda_0}(mag) = -2.5\, log_{10} \frac{f_{\nu,\mathrm{S}}(\lambda_0)}{3631\, Jy} = -2.5\, log_{10}(f_{\nu,\mathrm{S}}(\lambda_0)) + 8.90 \tag{7.14}$$

relative to a constant source SED with flux density 3 631 Jy. Note that the AB magnitude system and the Vega-based magnitude system are practically identical for the optical V band, but in the FIR the two magnitude systems differ quite significantly due to the Rayleigh Jeans behaviour of the Vega SED for FIR wavelengths. Table 7.3 gives the magnitude relation between AB magnitudes and the magnitudes based on the Vega SED.

Table 7.3: Zero magnitude flux densities for the three PACS photometer central wavelengths derived from an absolutely-calibrated theoretical photospheric model spectrum of Vega extrapolated to 300 μm. Also given are the colour-correction factors $K_{\mathrm{cc,BB10000}}$ for a 10 000 K blackbody (approximation of the Vega FIR spectrum with T_{eff} = 9 400 K) to convert $f_{\nu,\mathrm{Vega}}$ to the reference SED flux density $f_{\nu,1}$. The last column gives the magnitude relation between AB magnitudes and the magnitudes based on the Vega SED (using $f_{\nu,1}^{0\,\mathrm{mag}}$).

λ_0 (μm)	$f_{\lambda,\mathrm{Vega}}^{0\,\mathrm{mag}}$ (W m^{-2} μm^{-1})	$f_{\nu,\mathrm{Vega}}^{0\,\mathrm{mag}}$ (Jy)	$K_{\mathrm{cc,BB10000}}$	$f_{\nu,1}^{0\,\mathrm{mag}}$ (Jy)	$m_{\mathrm{AB},\lambda_0} = m_{\mathrm{Vega},\lambda_0} +$ (mag)
70	4.871×10^{-16}	0.7961	1.016	0.8088	9.13
100	1.160×10^{-16}	0.3868	1.034	0.4000	9.89
160	1.745×10^{-17}	0.1500	1.074	0.1611	10.88

7.4.2.2 Internal calibration sources

As described in Section 2.3.2, the PACS internal calibration sources were grey body radiators with emissivity of about 4–8%. The two sources were operated at 55 K (CS1, corresponding to a resistance of 48Ω) and 60 K (CS2, corresponding to 58Ω). The observed resistance values were 48.0040 ± 0.0015 Ω (13 mΩ peak-to-peak) for CS1 and 58.0000 ± 0.0019 Ω (14 mΩ peak-to-peak) for CS2. A 20 mΩ resistance variation corresponded roughly to a 10 mK temperature variation in the selected temperature range, which was about 0.05% flux or surface brightness variation, well below the bolometer measurement accuracy.

Each PACS photometric observation includes at least one calibration block (CB) measurement which consists of chopped observations between the two internal calibration sources. It preceded the sky observation and was performed during the target acquisition slew. In the end, the scientific measurements did not need to be flux calibrated with the help of the calibration-block measurements thanks to the

fantastic stability of the bolometer response over the whole mission (0.5% standard deviation); a fixed detector responsivity in the first order (cf. Eqn. 7.7) was applied, with a small dedicated second-order correction for time-dependent variations.

7.4.2.2.1 Calibration block observation database

The *Herschel* archive includes in total 22000 calibration-block observations from 20795 PACS photometric observations which cover both scientific and celestial calibration observations. All were taken with the identical CS set-up, in the blue/red or the green/red filter combination. This homogeneous database covering the photometer operational period with the densest time grid allows for a study of a number of subtle instrumental flux-calibration effects.

1) A correlation of the differential CS signal, i.e. the detector responsivity, with the ^{3}He cooler evaporator temperature: Sec. 7.4.2.4.

2) A correlation of the differential CS signal, i.e. the detector responsivity, with the temperature of the focal plane unit. This effect is weaker than the trend with evaporator temperature.

3) A signal drift of few percent for the first half hour after the end of the orbit prologue (photometer instrument set-up prior to a photometer observation block) following a recycling of the ^{3}He cooler.

Details of the photometer calibration block trend analysis are given in Moór et al. (2014).

7.4.2.3 Calibration models

Details of the celestial models used in the flux of the photometer and spectrometer can be found in Chp. 6. There, tables showing the comparison of the photometer fluxes to the model predictions for various sources and ODs can be found.

Five late-type giants (β And, α Cet, α Tau, α Boo, and γ Dra) were used as fiducial standards, and five SSO targets (Uranus, Neptune, Titan, Callisto, and Ganymede) were taken to cover the higher flux regime. Callisto and Ganymede continuum models turned out to be not very accurate in the PACS regime; for the other three the agreement with PACS photometry fluxes is better than 4%. A detailed comparison of PACS photometry of Uranus, Neptune, Titan, Callisto and Ganymede with the model predictions and the discussion of the results is given in Müller et al. (2016). A total of 16 asteroids were also used as calibrators, and overall the agreement with PACS fluxes is better than 5%.

7.4.2.4 Evaporator temperature correction

Each PACS photometric observation includes at least one calibration block measurement taken by chopping between the two PACS internal calibration sources. Calibration block observations – contrary to science measurements – were always performed in a standard, identical manner. This homogeneous data set allowed for a monitoring for the short- and long-term evolution of bolometer response during the full mission lifetime.

A ^{3}He cooler was used during the mission to ensure sub-Kelvin temperatures for the operation of the PACS photometer. The evaporation of ^{3}He provided a very stable temperature environment at

$\sim$300mK. After each cooler recycling procedure, which took about 2.5 h, about 2.5 ODs of PACS photometer observations were possible. The evaporator temperature (T_{EV}) rose towards the end of these cooling cycles (Sauvage et al., 2014). By investigating the behaviour of calibration blocks' differential signals (S_{diff}) as a function of T_{EV}, we found a clear correlation between the two parameters for both the blue and the red arrays. The observed trend can be well fitted by a linear relationship, enabling a correction for this effect. It is important to note that the measured flux densities of the standard stars extracted from PACS calibration observations showed a similar trend with evaporator temperature, and their photometry was improved by applying our pixel-based T_{EV} correction for their observations (Balog et al., 2014). This improvement was adopted in the SPG pipeline.

The correlation with T_{EV} is very clear, although the related corrections are typically well below 1%, varing slightly from pixel to pixel. It is only $\sim$1.2% of all measurements for which this correction is larger than 1%.

7.5 Photometry corrections

7.5.1 Non-linearity corrections

Bolometers are thermal detectors where a thermistor converts the infrared heat radiation into an electrical signal. The impedance of the thermistor depends strongly on its temperature, and hence the relation between the incoming flux and the output voltage is non-linear.

During the ground-level tests of PACS, this non-linear behaviour of the bolometers was characterised with the help of blackbody sources in the ground calibration facility for a wide illumination range – from zero to an illumination power of at least 7 pW per pixel in each filter band (which corresponds approximately to 125, 160, and 230 Jy/pixel in the blue, green and red filters). The voltage measured across the thermistor increases relatively less the larger the illumination power is, which means that the responsivity of the bolometers decreases with an increase of the infalling flux.

7.5.1.1 Establishment of the non-linearity correction

There is no physical model available for the PACS bolometer arrays. The impedance of the thermistors was found to vary exponentially with the detector temperature, and a logarithmic behaviour proved to be appropriate empirical model.

The fitting of the calibration curves was done with a monotonic function of the form

$$Sig(F)[Jy/pix] = a \times ln(b \times F[W] + 1) \tag{7.15}$$

with S being the output signal converted to Jy/pix as described below and F being an illumination power of the applied range during the ground-level test.

Before the fitting, the following steps were applied:

- The originally-measured voltages across the thermistors for the nominal in-flight bolometer biases were transformed into Jy/pixels using the transfer function of the bolometer read-out electronics and applying the nominal responsivity and flat-field calibration.

- The non-linearity is derived relative to the permanent telescope background level, which absolute value becomes the zero point on the calibration curve. The values used were 1.8 pW (30 Jy/pix), 1.3 pW (30 Jy/pix) and 4 pW (130 Jy/pix) for the blue, green, and red filter band, respectively.

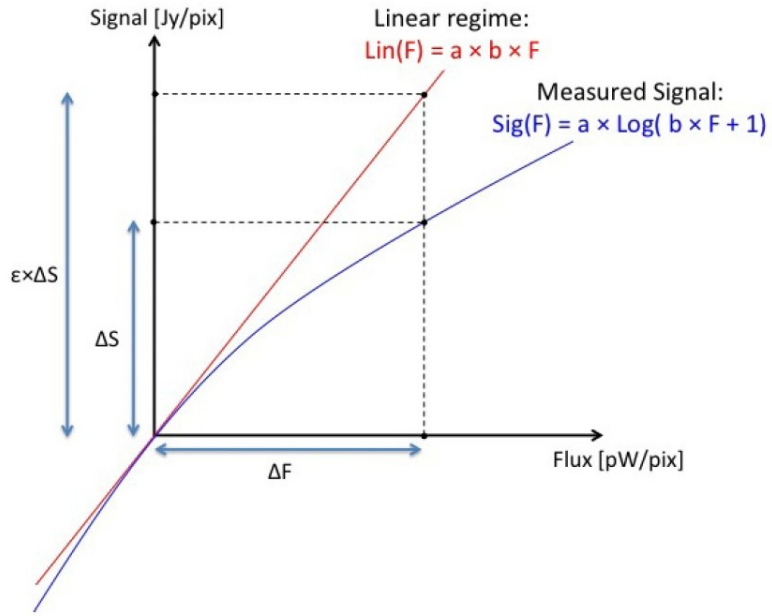

Figure 7.8: Calibration scheme of the non-linearity correction: The measured signal difference above telescope background ΔS is related to a linearised signal difference via the correction factor ε which is dependent on the corresponding true flux difference ΔF.

The establishment of the calibration correction is sketched in Fig. 7.8. The measured signals were fitted with the function of Eq. 7.15. The linearised reference signal is given by the tangent of the logarithmic function at $F = 0$, which is given by the function

$$Lin(F)[Jy/pix] = a \times b \times F[W] \tag{7.16}$$

For a difference flux, ΔF, with respect to the zero point, the measured signal difference is

$$Sig(\Delta F) = a \times ln(b \times \Delta F + 1) = \Delta S \tag{7.17}$$

The linearised signal difference is

$$Lin(\Delta F) = a \times b \times \Delta F = \varepsilon \times \Delta S \tag{7.18}$$

The correction factor, ε, can be expressed as a function of the measured signal above zero ΔS by solving Eq. 7.17 for $\Delta F = \frac{1}{b} \times (e^{\frac{\Delta S}{a}} - 1)$ and inserting into Eq. 7.18

$$\varepsilon = a \times b \times \frac{\Delta F}{\Delta S} = a \times \frac{(e^{\frac{\Delta S}{a}} - 1)}{\Delta S} \tag{7.19}$$

The correction factor was determined individually for each pixel of a detector. Fig. 7.9 shows typical values of the correction factor for each filter band depending on the difference signal above the telescope background, which has always to be subtracted and hence set to zero in the data-reduction chain before applying the non-linearity correction. In practice, the correction was only applied above a threshold of 1.5%, corresponding to a differential source flux of about 10 Jy/pixel (cf. 7.9). One reason for restricting the correction to above this threshold is that the correction task was quite memory intensive where a correction for all pixels in all frames were required, and because the correction was anyway negligible for a large fraction of the data. Furthermore, the correction is quite sensitive to the background subtraction and the correction of negative differential fluxes is not supported (due to the logarithmic function). The threshold approach avoided processing complications. Another aspect is that the correction introduces extra noise into the flux time-lines. This is not problematic for bright sources with a significant correction, but it would raise the detection limit for faint sources with an, in principle negligible, correction.

Note that this correction factor has to be applied to individual pixel signals during the Level 0.5 to Level 1 processing and is not directly applicable to correct the total flux of a source. The source flux is distributed over several pixels with different signal levels above the background involving quite different values of the correction. For a rough estimate of what the correction means in terms of absolute source flux, assume that the FWHM of the source containing about 40% of the flux is 2×2 pixels: for a 400 Jy source, this is a non-linearity correction of about 5%, and for a 1000 Jy source the non-linearity correction is 15–20%.

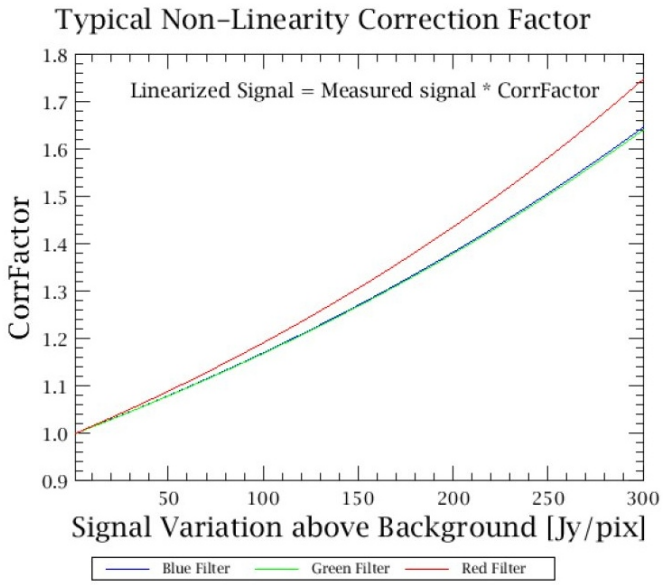

Figure 7.9: Typical curves for the non-linearity correction factor ε per filter band as a function of the signal variation above the telescope background. The signal has been converted to the flux unit Jy/pixel.

Uncertainties for this calibration arise from the following:

- The applied absolute telescope background levels are an approximation. The telescope background was not constant, but varied over the mission due to the seasonal solar illumination

variation and a slight increase of the mirror emissivity. The variation of the telescope background power was about 9% at 70 μm, 5% at 100 μm, and 3% at 160 μm, as derived from the *Herschel* telescope background model for the PACS photometer (Klaas, 2016). It was verified that a change of 10% in the telescope background has a minor impact on the non-linearity coefficients.

- Part of the calibrated range is covered by extrapolating the fitting function. Since for the red channel the fitting could be verified up to 32 pW, there is confidence that the extrapolations for the blue and green channel are reliable.

A detailed description of the original calibration analysis, and including the reduction scripts, is given in Billot (2011).

7.5.1.2 Verification with celestial standards

The non-linearity correction was verified in-flight with the help of flux standards covering nearly the whole accessible flux range of PACS (cf. Chp. 6). This is shown in Fig. 7.10 for the flux standards best characterised in measurement and model accuracy. From the statistics of this sample, no deviation of $>$3% on average from linearity over more than five orders in flux can be found. There are also no offsets between low- and high-gain observations, fixed or solar system tracked targets, and measurements taken in chop-nod or in scan-map mode. In particular, the results for Neptune, Uranus, and Callisto show the reliability of PACS fluxes in the high flux regime, where the bolometer responsivity is noticeably in a non-linear regime. The rare cases of even brighter sources – up to the saturation limit – where non-linearity corrections of $>$20% are needed, are formally not verified. The residual uncertainty for these sources is estimated to be $\leq$10% (Müller et al., 2016).

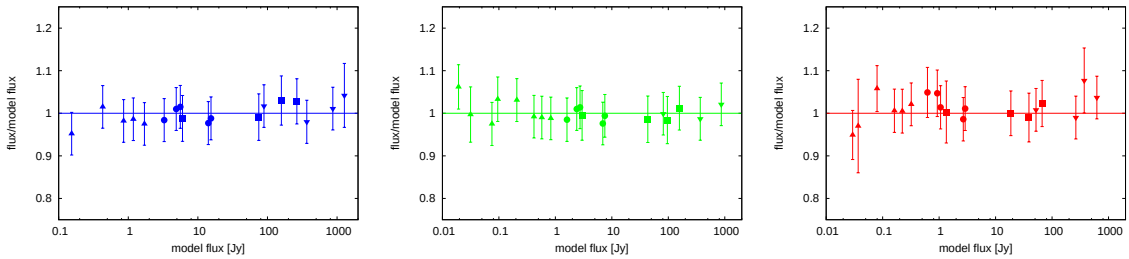

Figure 7.10: In-flight verification of the non-linearity correction with flux standards over nearly the whole accessible flux range of PACS. For the blue (**left**), green (**middle**) and red (**right**) bands, the measured flux to model flux ratio for the most reliable flux standards is shown. Triangles represent faint secondary standard stars, circles the fiducial prime standard stars, boxes prime asteroid calibration standards and reverse triangles planets (Neptune & Uranus) and planet satellites Callisto & Titan.

7.5.2 Aperture corrections

Aperture photometry measures the flux within a finite, relatively small aperture. The total flux, however, is distributed in a much larger area. This is represented by the Encircled Energy Function (EEF)

which is described in Sec. 7.3.2.4. To account for this missing flux one needs to apply the EEF correction factor to the aperture-measured flux values. These correction factors are available as calibration files in HIPE, with the final update including the correction factors for the fast scan speed. More information about the EEFS for different scan speeds and observing modes can be found in the PACS overview page linked from the HSC pages (here), data and reports can be found on the PACS phot PSF Ancillary data pages. On HELL L2 more documentation on the PSF and on the EEFs and colour corrections can be found.

Table 7.4: Encircled Energy Fraction (EEF) as a function of circular aperture radius for the three PACS filter bands for the 20″/s scan speed. Valid for `Responsivity` calibration file version FM, 7. See Sec. 7.3.2 for the description of the PACS PSF and the calculation of the encircled energy fractions

radius	Encircled Energy Fraction			radius	Encircled Energy Fraction		
[″]	blue	green	red	[″]	blue	green	red
2	0.192	0.141	0.060	32	0.896	0.891	0.861
3	0.353	0.278	0.127	33	0.898	0.893	0.864
4	0.487	0.413	0.209	34	0.900	0.895	0.867
5	0.577	0.521	0.298	35	0.902	0.896	0.870
6	0.637	0.595	0.384	36	0.904	0.898	0.873
7	0.681	0.641	0.461	37	0.905	0.900	0.876
8	0.719	0.673	0.527	38	0.907	0.902	0.879
9	0.751	0.700	0.579	39	0.908	0.903	0.882
10	0.774	0.727	0.619	40	0.910	0.905	0.884
11	0.791	0.753	0.649	41	0.911	0.906	0.886
12	0.802	0.776	0.673	42	0.913	0.908	0.888
13	0.812	0.795	0.694	43	0.914	0.909	0.890
14	0.820	0.808	0.712	44	0.916	0.910	0.892
15	0.829	0.818	0.729	45	0.917	0.912	0.894
16	0.837	0.826	0.746	46	0.919	0.913	0.896
17	0.845	0.832	0.761	47	0.920	0.914	0.897
18	0.852	0.837	0.776	48	0.921	0.915	0.899
19	0.858	0.842	0.789	49	0.922	0.917	0.901
20	0.863	0.847	0.800	50	0.924	0.918	0.902
21	0.867	0.852	0.809	51	0.925	0.919	0.904
22	0.870	0.857	0.817	52	0.926	0.920	0.905
23	0.874	0.863	0.824	53	0.927	0.921	0.906
24	0.877	0.867	0.830	54	0.929	0.922	0.908
25	0.880	0.872	0.835	55	0.930	0.923	0.909
26	0.883	0.876	0.839	56	0.931	0.924	0.910
27	0.885	0.879	0.843	57	0.932	0.925	0.911
28	0.888	0.882	0.847	58	0.933	0.926	0.912
29	0.890	0.885	0.850	59	0.935	0.928	0.913
30	0.892	0.887	0.854	60	0.936	0.929	0.914
31	0.894	0.889	0.857	61	0.937	0.929	0.915

7.5.3 Colour corrections

In the description of the basic photometric flux calibration strategy in Sec. 7.4.2 the concept of colour correction was introduced in Eq. 7.9. This is necessary because the contribution of the monochromatic flux density $f_{\nu,s}(\lambda_0)$ at the reference wavelength, λ_0, to the total flux inside the broad photometric bands ($\frac{\lambda}{\Delta\lambda}$ = 6.6, 5.9 and 5.3 for the blue, green, and red band, respectively) depends on the shape of the source SED within the bandpass. In other words, the effective bandwidth depends on the source SED. The PACS photometer standard data products are calibrated in Jy/pixel, for the filter's reference wavelength and an input energy distribution which is constant in the flux per logarithmic frequency interval (flux per octave). The flux density with frequency ν goes as $f_{\nu,1} \propto \nu^{-1}$ or the flux density with wavelength λ goes with $f_{\lambda,1} \propto \lambda^{-1}$. This is in accordance with the flux-calibration schemes used for IRAS, ISO and Akari.

The colour-correction factor $K_{cc,s}$ is therefore the ratio $\frac{\Delta\,\nu_s}{\Delta\,\nu_0}$, with $\Delta\,\nu_0$ being the effective bandwidth for the constant-in-flux per logarithmic frequency interval SED that is used in Eq. 7.5, and as defined in Eq. 7.6 and tabulated in Table 7.2. $\Delta\,\nu_s$ can be derived starting from the general description in Eqn. 7.2 and solving this equation for $f_{\nu,s}(\lambda_0)$ in analogy to Eqn. 7.4:

$$K_{cc,s} = \frac{\Delta\,\nu_s}{\Delta\,\nu_0} = \frac{\frac{c}{\lambda_0^2}\,\int_{\lambda_1}^{\lambda_2} \frac{f_{\nu,s}(\lambda)}{f_{\nu,s}(\lambda_0)}\,S(\lambda)\,d\lambda}{\frac{c}{\lambda_0}\,\int_{\lambda_1}^{\lambda_2} \frac{1}{\lambda}\,S(\lambda)\,d\lambda} \tag{7.20}$$

$\frac{f_{\nu,s}(\lambda)}{f_{\nu,s}(\lambda_0)}$ is the normalised function of the source SED and $S(\lambda)$ is the photometer spectral response $S(\lambda)$, i.e. the convolution of the filter transmission curves and the bolometer responses (see Section 2.4.1.1).

In Tables 7.5 to 7.7 the colour-correction factors $K_{cc,s}$ for representative source SED models such as blackbodies ($f_{\nu,s}(\lambda) \sim B(\lambda,T)$), modified blackbodies ($f_{\nu,s}(\lambda) \propto \lambda^{\alpha}\,B(\lambda,T)$), or power laws ($f_{\nu,s}(\lambda) \propto \lambda^{\alpha}$) are tabulated for the PACS reference wavelengths 70, 100, 160 μm (**Note:** Due to the usage of the unit Jy for the PACS fluxes, i.e. per unit frequency flux, one has to consider the correct conversion between f_ν and f_λ, which is given by the relation $\nu\ f_\nu = \lambda\ f_\lambda$). The correction factors are usually small; only for sources with temperatures below 20 K they can become significant, in particular at 70 μm. The PACS bandpasses have been measured at cold (operational) temperatures and are well known. Nevertheless, large colour-correction factors above 1.5 or below 0.5 (mainly for very cold sources) have to be taken with care, and they may even dominate the final flux accuracy.

The fluxes derived from the PACS photometer standard data products $f_{\nu,1}(\lambda_0)$ have to be divided by the appropriate colour correction factor[1] to derive the source flux for the proper source SED:

$$f_{\nu,s}(\lambda_0) = \frac{f_{\nu,1}(\lambda_0)}{K_{cc,s}}$$

7.5.3.1 Comparison with similar bands from other missions

In addition to the colour-correction terms, we provide corrections factors $K_{lc,s}$ in Tables 7.5 to 7.7 which can allow one to perform a direct comparison with published monochromatic colour-corrected flux densities derived from other projects.

[1] In the technical literature, this term is traditionally called a "factor". To avoid confusion, we emphasise here again that the raw flux density values have to be *divided by*, and **not** multiplied with, the correction term.

- For a comparison of a PACS photometer blue band measurement with monochromatic flux densities derived from the IRAS_60-band or the ISOPHOT P3_60-band: Use the values in column IRAS 60.0 μm
- For a comparison of a PACS photometer blue band measurement with monochromatic flux densities derived from the Spitzer/MIPS 70 μm band: Use the values in column MIPS 71.42 μm
- For a comparison of a PACS photometer green band measurement with monochromatic flux densities derived from Akari/FIS Wide-S or the ISOPHOT C100_C90 band: Use the values in column ISOPHOT 90.0 μm
- For a comparison of a PACS photometer green band measurement with monochromatic flux densities derived from ISOPHOT C100_C105 band: Use the values in column ISOPHOT 105.0 μm
- For a comparison of a PACS photometer red band measurement with monochromatic flux densities derived from the Akari/FIS Wide-L band: Use the values in column FIS 140.0 μm
- For a comparison of a PACS photometer red band measurement with monochromatic flux densities derived from Spitzer/MIPS 160 μm band: Use the values in column MIPS 155.9 μm
- For a comparison of a PACS photometer red band measurement with monochromatic flux densities derived from the ISOPHOT C200_C160 band: Use the values in column ISOPHOT 170.0 μm

These correction factors $K_{lc,s}$ (wavelength corrections "lc") have been determined for the assumed object SED by simply moving along the SED curve from the PACS key wavelength to the new wavelength and determining the ratio of the flux densities. They have to be applied in the following way:

1. Determine the monochromatic colour-corrected flux density at the PACS reference wavelength: $f_{\nu,s}(\lambda_0) = \frac{f_{\nu,1}(\lambda_0)}{K_{cc,s}}$
2. "Transport" the monochromatic colour-corrected flux density at the PACS reference wavelength to a neighbouring wavelength along the given object SED: $f_{\nu,s}(\lambda_{lc}) = f_{\nu,s}(\lambda_0) \cdot K_{lc,s}$

7.5.3.2 Colour-correction factor tabulation

The correction factors listed in Tables 7.5 to 7.7 are taken from Müller et al. (2011).

Table 7.5: Photometric colour corrections for a range of different blackbody temperatures from 5 K to 10 000 K. Bold values in columns 2 to 4 are the $K_{cc,BB}$ factors for the PACS bands. Columns 5 to 11 contain the $K_{lc,BB}$ factors needed to obtain a monochromatic flux density at neighbouring key wavelengths used by other missions.

PACS	blue	green	red	PACS blue band from 70.0 μm to		PACS green band from 100.0 μm to		PACS red band from 160.0 μm to		
	CC_70	CC_100	CC_160	IRAS	MIPS	ISOPHOT		FIS	MIPS	ISOPHOT
λ_{ref} [μm]	70.0	100.0	160.0	60.0	71.42	90.0	105.0	140.0	155.9	170.0
10 000 K	**1.016**	**1.034**	**1.074**	1.359	0.961	1.234	0.907	1.305	1.053	0.886
5 000 K	**1.016**	**1.033**	**1.074**	1.356	0.962	1.233	0.908	1.304	1.053	0.886
1 000 K	**1.013**	**1.031**	**1.072**	1.337	0.963	1.224	0.910	1.298	1.052	0.888
500 K	**1.011**	**1.029**	**1.068**	1.312	0.965	1.214	0.914	1.289	1.051	0.891
250 K	**1.005**	**1.023**	**1.062**	1.258	0.970	1.192	0.921	1.271	1.048	0.896
100 K	**0.989**	**1.007**	**1.042**	1.081	0.987	1.118	0.946	1.212	1.039	0.913
50 K	**0.982**	**0.985**	**1.010**	0.794	1.023	0.980	0.999	1.105	1.022	0.948
40 K	**0.992**	**0.980**	**0.995**	0.672	1.043	0.911	1.031	1.049	1.012	0.968
30 K	**1.034**	**0.982**	**0.976**	0.507	1.078	0.802	1.088	0.955	0.995	1.005
20 K	**1.224**	**1.036**	**0.963**	0.286	1.153	0.617	1.217	0.781	0.959	1.090
19 K	**1.269**	**1.051**	**0.964**	0.262	1.165	0.591	1.239	0.756	0.953	1.104
18 K	**1.325**	**1.069**	**0.967**	0.237	1.179	0.564	1.264	0.729	0.947	1.121
17 K	**1.396**	**1.093**	**0.972**	0.212	1.194	0.536	1.293	0.699	0.940	1.140
16 K	**1.488**	**1.123**	**0.979**	0.187	1.212	0.505	1.326	0.667	0.932	1.162
15 K	**1.607**	**1.162**	**0.990**	0.162	1.233	0.473	1.364	0.633	0.923	1.187
14 K	**1.768**	**1.213**	**1.005**	0.137	1.257	0.438	1.409	0.596	0.913	1.217
13 K	**1.992**	**1.282**	**1.028**	0.114	1.285	0.401	1.463	0.555	0.901	1.253
12 K	**2.317**	**1.377**	**1.061**	0.091	1.318	0.362	1.529	0.512	0.888	1.296
11 K	**2.816**	**1.512**	**1.110**	0.071	1.359	0.321	1.610	0.464	0.872	1.349
10 K	**3.645**	**1.711**	**1.184**	0.052	1.410	0.277	1.714	0.413	0.853	1.415
9 K	**5.175**	**2.024**	**1.300**	0.035	1.475	0.232	1.849	0.358	0.831	1.501
8 K	**8.497**	**2.554**	**1.491**	0.022	1.559	0.186	2.034	0.300	0.804	1.615
7 K	**17.815**	**3.552**	**1.833**	0.012	1.676	0.140	2.299	0.238	0.771	1.775
6 K	**58.391**	**5.774**	**2.528**	0.005	1.845	0.096	2.706	0.175	0.729	2.013
5 K	**456.837**	**12.259**	**4.278**	0.002	2.110	0.056	3.400	0.114	0.674	2.401

Table 7.6: Photometric colour corrections for different modified black-bodies ($F_\nu^{modified} = \nu^\beta B_\nu(\nu, T)$). Bold values in columns 2 to 4 are the $K_{cc,mBB}$ factors for the PACS bands. Columns 5 to 11 contain the $K_{lc,mBB}$ factors needed to obtain a monochromatic flux density at neighbouring key wavelengths used by other missions.

PACS	blue	green	red	PACS blue band		PACS green band		PACS red band		
	CC_70	CC_100	CC_160	from 70.0 μm to		from 100.0 μm to		from 160.0 μm to		
				IRAS	MIPS	ISOPHOT		FIS	MIPS	ISOPHOT
λ_{ref} [μm]	70.0	100.0	160.0	60.0	71.42	90.0	105.0	140.0	155.9	170.0
$\nu^{-2}B_\nu(10\,K)$	**5.150**	**2.162**	**1.495**	0.038	1.466	0.225	1.890	0.316	0.810	1.597
$\nu^{-2}B_\nu(15\,K)$	**2.013**	**1.356**	**1.126**	0.119	1.282	0.383	1.504	0.485	0.876	1.341
$\nu^{-2}B_\nu(20\,K)$	**1.442**	**1.152**	**1.035**	0.210	1.199	0.499	1.342	0.598	0.911	1.230
$\nu^{-2}B_\nu(30\,K)$	**1.141**	**1.037**	**0.993**	0.372	1.121	0.650	1.199	0.731	0.945	1.134
$\nu^{-2}B_\nu(40\,K)$	**1.058**	**1.008**	**0.987**	0.494	1.085	0.738	1.136	0.803	0.961	1.092
$\nu^{-2}B_\nu(50\,K)$	**1.026**	**0.998**	**0.987**	0.583	1.064	0.794	1.102	0.846	0.970	1.070
$\nu^{-2}B_\nu(75\,K)$	**1.001**	**0.993**	**0.991**	0.721	1.038	0.869	1.061	0.902	0.981	1.043
$\nu^{-2}B_\nu(100\,K)$	**0.996**	**0.993**	**0.994**	0.794	1.027	0.905	1.043	0.928	0.986	1.031
$\nu^{-1}B_\nu(10\,K)$	**4.307**	**1.916**	**1.319**	0.044	1.438	0.250	1.800	0.361	0.831	1.503
$\nu^{-1}B_\nu(15\,K)$	**1.790**	**1.249**	**1.045**	0.139	1.257	0.425	1.432	0.554	0.899	1.262
$\nu^{-1}B_\nu(20\,K)$	**1.322**	**1.086**	**0.988**	0.245	1.175	0.555	1.278	0.683	0.935	1.158
$\nu^{-1}B_\nu(30\,K)$	**1.081**	**1.003**	**0.974**	0.434	1.099	0.722	1.142	0.836	0.970	1.067
$\nu^{-1}B_\nu(40\,K)$	**1.019**	**0.988**	**0.981**	0.576	1.064	0.820	1.082	0.918	0.986	1.028
$\nu^{-1}B_\nu(50\,K)$	**0.998**	**0.986**	**0.988**	0.680	1.043	0.882	1.049	0.967	0.996	1.007
$\nu^{-1}B_\nu(75\,K)$	**0.987**	**0.990**	**1.001**	0.841	1.018	0.966	1.010	1.030	1.007	0.982
$\nu^{-1}B_\nu(100\,K)$	**0.987**	**0.994**	**1.008**	0.927	1.007	1.006	0.993	1.061	1.012	0.970
$\nu^{+1}B_\nu(10\,K)$	**3.116**	**1.541**	**1.083**	0.060	1.382	0.308	1.632	0.472	0.876	1.332
$\nu^{+1}B_\nu(15\,K)$	**1.456**	**1.092**	**0.956**	0.189	1.208	0.525	1.299	0.723	0.947	1.118
$\nu^{+1}B_\nu(20\,K)$	**1.144**	**0.999**	**0.957**	0.334	1.130	0.685	1.159	0.893	0.984	1.026
$\nu^{+1}B_\nu(30\,K)$	**1.000**	**0.973**	**0.997**	0.591	1.057	0.891	1.036	1.092	1.021	0.946
$\nu^{+1}B_\nu(40\,K)$	**0.976**	**0.983**	**1.029**	0.784	1.022	1.013	0.982	1.198	1.039	0.911
$\nu^{+1}B_\nu(50\,K)$	**0.975**	**0.995**	**1.051**	0.926	1.003	1.089	0.952	1.263	1.049	0.892
$\nu^{+1}B_\nu(75\,K)$	**0.989**	**1.018**	**1.082**	1.144	0.979	1.192	0.916	1.346	1.061	0.869
$\nu^{+1}B_\nu(100\,K)$	**1.001**	**1.031**	**1.098**	1.262	0.968	1.242	0.901	1.386	1.066	0.859

Table 7.6: Photometric colour corrections for different modified black-bodies ($F_\nu^{modified} = \nu^\beta B_\nu(\nu, T)$) continued. Bold values in columns 2 to 4 are the $K_{cc,mBB}$ factors for the PACS bands. Columns 5 to 11 contain the $K_{lc,mBB}$ factors needed to obtain a monochromatic flux density at neighbouring key wavelengths used by other missions.

PACS	blue	green	red	PACS blue band		PACS green band		PACS red band		
	CC_70	CC_100	CC_160	from 70.0 μm to		from 100.0 μm to		from 160.0 μm to		
				IRAS	MIPS	ISOPHOT		FIS	MIPS	ISOPHOT
λ_{ref} [μm]	70.0	100.0	160.0	60.0	71.42	90.0	105.0	140.0	155.9	170.0
$\nu^{+2}B_\nu(10\,K)$	**2.691**	**1.399**	**1.009**	0.070	1.355	0.342	1.555	0.540	0.899	1.253
$\nu^{+2}B_\nu(15\,K)$	**1.333**	**1.038**	**0.943**	0.220	1.185	0.583	1.237	0.827	0.972	1.052
$\nu^{+2}B_\nu(20\,K)$	**1.080**	**0.974**	**0.971**	0.390	1.108	0.761	1.104	1.020	1.010	0.965
$\nu^{+2}B_\nu(30\,K)$	**0.977**	**0.974**	**1.037**	0.689	1.036	0.991	0.987	1.248	1.048	0.890
$\nu^{+2}B_\nu(40\,K)$	**0.970**	**0.997**	**1.083**	0.915	1.002	1.125	0.935	1.370	1.066	0.857
$\nu^{+2}B_\nu(50\,K)$	**0.979**	**1.017**	**1.113**	1.080	0.983	1.210	0.907	1.443	1.076	0.840
$\nu^{+2}B_\nu(75\,K)$	**1.005**	**1.049**	**1.155**	1.335	0.959	1.325	0.873	1.538	1.089	0.818
$\nu^{+2}B_\nu(100\,K)$	**1.023**	**1.067**	**1.175**	1.472	0.949	1.380	0.858	1.584	1.094	0.809

Table 7.7: Photometric colour corrections for a range of different power-law spectra ($F_\nu \sim \nu^\beta$). Bold values in columns 2 to 4 are the $K_{cc,\beta}$ factors for the PACS bands. Columns 5 to 11 contain the $K_{lc,\beta}$ factors needed to obtain a monochromatic flux density at neighbouring key wavelengths used by other missions.

PACS	blue	green	red	PACS blue band from 70.0 μm to		PACS green band from 100.0 μm to		PACS red band from 160.0 μm to		
	CC_70	CC_100	CC_160	IRAS	MIPS	ISOPHOT		FIS	MIPS	ISOPHOT
λ_{ref} [μm]	70.0	100.0	160.0	60.0	71.42	90.0	105.0	140.0	155.9	170.0
β=-3.0	**1.043**	**1.037**	**1.056**	0.630	1.061	0.729	1.158	0.670	0.925	1.199
β=-2.0	**1.016**	**1.012**	**1.017**	0.735	1.040	0.810	1.103	0.766	0.949	1.129
β=-1.0	**1.000**	**1.000**	**1.000**	0.857	1.020	0.900	1.050	0.875	0.974	1.062
β= 0.0	**0.995**	**1.000**	**1.004**	1.000	1.000	1.000	1.000	1.000	1.000	1.000
β= 1.0	**1.000**	**1.011**	**1.029**	1.167	0.980	1.111	0.952	1.143	1.026	0.941
β= 2.0	**1.016**	**1.034**	**1.075**	1.361	0.961	1.235	0.907	1.306	1.053	0.886
β= 3.0	**1.043**	**1.069**	**1.142**	1.588	0.942	1.372	0.864	1.493	1.081	0.833

Chapter 8

The Spectrometer Calibration

8.1 Early in-flight calibration achievements

The calibration of the PACS observing modes was addressed centrally by the Observatory. The PACS Instrument Control Centre Team in collaboration with the *Herschel* calibration scientists established a smooth evolution of the calibration from module characterisation over the detailed instrument and integrated system tests on ground to the final full system verification and calibration in-flight, as outlined in the PACS Calibration Document (Klaas et al., 2014). The PACS calibration team planned, worked out, executed and analysed dedicated calibration observations on blackbody sources on-ground, simulating line emission, generating continuum emission over the full field-of-view via integrating spheres or simulating point sources with hole masks in front, and on celestial standards, to consistently and thoroughly characterise all instrumental effects of PACS while in-flight.

Once in orbit, after the initial instrument check-out, there were large calibration block observations during the Commissioning Phase (CoP) and Performance Verification (PV) Phase, verifying the in-orbit performance of the spectrometer instrument settings and the observing modes, comparing against predictions and the ground performance, and tuning for optimal performance in the space environment as well as providing the baseline in-flight calibration: this is outlined in detail in the PACS PV Phase Plan (Klaas and Nielbock, 2014a). Verification of the calibration stability (in particular repeatability measurements) and refinement and extension of the calibration, taking into account the growing knowledge in data processing, was then done during the Routine Science Phase of the *Herschel* mission: this is described in the PACS Routine Science Phase Plan (Klaas and Nielbock, 2014b).

The results of the calibration work that is described in this chapter were converted into calibration files which were added to the 'calibration tree' that was used for the SPG and interactive pipeline processing. The calibration files for the lowest levels of the pipeline processing were updated during the first few years of the mission, but only those of the intermediate and higher levels were updated up until the very last processing done on the PACS spectroscopy data (SPG 14), which took place near the end of the post-operations phase (2016). A history of the calibration tree updates can be found as a pdf file posted on HELL L2 (Level 2). The calibration files themselves (FITS and ascii files) are provided as Ancilliary data products on this HSC repository. The calibration tree is also explained in Sec. 10.5.

8.1.1 Highlights

The *Herschel* Commissioning Phase (CoP) lasted for the first two months of the mission and was characterised by a not yet final and stable observing environment, the first part being executed with the cryo cover still closed and the second part with the telescope still cooling down. The Performance Verification (PV) Phase for PACS lasted from OD 64 until OD 200, at the end overlapping with the Observatory SD Phase. Much of the calibration work started in CoP and continued through PV phase and for some, also through the Routine Phase.

Some noteworthy results for PACS spectroscopy are:

- The 'first-light' observation on OD 41 was of the planetary nebula NGC 6543. Recognisable spectral images in the light of two emission lines could be made – confirmation that the PACS integral field spectrograph worked!

- A full range of tests were run to establish the detector settings (bias, capacitance, ramp-length) that gave the best NEP levels for the two detectors (see the Royer et al. 2009 report). Highlights:

  - The detector response in-flight was much higher than in the laboratory, due to the higher flux of cosmic rays. The optimal settings included a shorter ramp-length and significantly lower bias level than had resulted from the pre-flight tests.
  - It was established that after switch-on, the blue detector required six to seven hours to stabilise, with a long term response drift of 20% over that period of time. It was therefore decided that when the spectrograph was to be used, the detectors should be switched on as soon as possible – during the DTCP in fact. To speed up the process of stabilisation, after switch-on the detectors stared for at one of the calibration sources for 45 mins. In this way it was possible to reach near to the end of the exponential decay end of the response drift before astronomical observations began.

- The AOT logic was investigated (some of this continuing during the PV phase). Two AOTs ('wavelength switching' and 'pointed with dither') were abandoned in favour of other existing AOTs for performance reasons. The chopping pattern on-off-off-on rather than on-off-on-off was selected, being more stable against transients. The grating steps sizes were optimised, paying especial attention to the SED mode which has a lower sampling density. A spectral dithering was implemented for SEDs and Nyquist-density ranges with repetition factors > 1 on the grating scan, as this improved the spectral sampling, and a default of two grating scans (up-down twice) was set as the quantum for the unchopped line-scan AOTs. It was decided to offer band B2A in addition to the other two blue bands, and to give access to wavelengths $< 55\,\mu$m using band B2A.

- The FPG was investigated, to refine the location of the spectrometer aperture and its sky coordinates from pre-flight determinations. Via the spatial characterisation programme, the relative sky coordinates for all spectral pixels of each module of the detector were checked and refined. As with the pre-flight tests, this was done for all chopper positions, to account for all of its angular displacements. The first versions of the spectrometer beams (provided for the key wavelengths; and later updated during the Routine Phase) were created. Straylight from bright external sources was investigated.

- The first astronomical calibration sources were observed during the CoP, and during the PV phase this continued with the spectrometer flux calibration programme. The absolute calibration was checked against the calibrators. Later, during the Routine phase, the flux calibration programme continued with repeatability studies on the fiducial sources and the internal calibration sources, and a determination of the telescope background.
- The absolute wavelength scale and the spectral profile measured pre-flight were checked from observations of unresolved emission lines. The location of spectral 'ghosts' was established (bright spectral lines echoing from one detector module to another).

The objectives and details of the PACS photometer operations during the Commissioning Phase are explained in detail in the PACS Commissioning Phase Plan (Feuchtgruber, 2009) and the PACS Commissioning Phase Timeline (Klaas & Nielbock 2009). The reference document for the PV Phase is the PACS Performance Verification Phase Plan (Klaas and Nielbock, 2014a). A summary of the pre-flight and in-flight calibration tests for PACS can be found in the PACS Calibration Document (Klaas et al., 2014), and in the PACS Calibration Document Overview (Klaas, 2014) the document numbers for all relevant technical notes can be found.

In the rest of this chapter the spectral and spatial calibration of the PACS spectrometer is described. All supporting documents, mostly in the form of technical notes, can be found on HELL L2 and HELL L3.

8.2 The spectrophotometric calibration

Two calibration schemes were used for PACS spectroscopy.

- The internal calibration sources and the RSRF was originally used to compute the fluxes in Jy for all observations. However eventually (and for all products that are now in the HSA) this was only used for unchopped observations, and for wavelengths $> 190\,\mu$m for all observations (these "red leak" products being provided as HPDPs in the HSA).
- The default calibration scheme for chop-nod observations uses the telescope. The flux of the target is related to that of the telescope, and the target flux is first expressed in units of "telescopes". The flux of the telescope Jy is calibrated independently, in wavelength and date, and this is used to convert the target flux from "telescopes" to Jy.

In this section we explain the concept of the absolute flux calibration of these two schemes, as well as the calibration of the telescope itself.

8.2.1 The calibration sources and models

Details of the celestial models used in the flux of the photometer and spectrometer can be found in Chp. 6. Five stellar calibrators (α Boo, β Peg, α Cet, γ Dra, α Tau) were used as fiducial standards, and eleven SSO targets (Ceres, Europa, Hebe, Juno, Neptune, Thisbe, Vesta, Callisto, Hygiea, Pallas, Uranus). In addition to these, repeatability sources were used (primarily HD 161796). Tables showing the comparison of the photometer fluxes to the model predictions for various sources and ODs are given in Chp. 6. The same set of models were developed for photometry and spectroscopy, although

not all of the same sources were used for the calibration of the two instruments of PACS. Details about the comparison of the models to the spectroscopy observations are given in Sec. 8.2.4.

8.2.2 Chopped observations: telescope background normalisation

8.2.2.1 Absolute flux calibration concept

When the parameter "normalize" is activated in the pipeline task *SpecDiffChop*, the RSRF is not used for the flux calibration, but rather the telescope itself. This was the calibration scheme used for chop-nod observations. The uncalibrated signals are processed in *SpecDiffChop* in the following way:

$$norm = 1/2\left[\underbrace{\frac{A-B}{(A+B)/2}}_{\text{Nod A}} + \underbrace{\frac{B'-A'}{(A'+B')/2}}_{\text{Nod B}}\right] \tag{8.1}$$

where A and B are the sfignals detected in the two chopper positions (on- and off-source) in Nod A and A' and B' are the signals detected in the two chopper positions (off- and on-source: note the swapped order) in Nod B. (The combination of nods is performed near the end of the pipeline, in 'specAddNod'.) $norm$ is calculated by the task, and at this point can be considered to have units of "telescopes".

The idea behind normalising every measurement (every readout) to the telescope background is the elimination of drifts with time in the system response (mostly those from the detectors). The response is expressed in [V/s/Jy] and relates the flux [Jy] to the slope (fitted ramps, i.e. the downlinked signal) [V/s] measured by the detectors (e.g. Sec. 2.6.2.2 or Sec 2.5.5).

Next, we express the observed signals as fluxes T_A and T_B from the telescope in the two chopper positions, and the flux from the source as s, all converted to fitted ramps by the gain factor g. This gain, or response, is not necessarily constant with time, but it is here assumed constant for the duration of a complete chop cycle ($\sim$ 2 seconds). We can then write the normalised result as:

$$norm = \frac{(T_A+s)*g - T_B*g}{(T_A+s+T_B)*g} + \frac{(T_B+s)*g' - T_A*g'}{(T_A+s+T_B)*g'} \tag{8.2}$$

$$= \frac{2s}{T_A+T_B+s} \tag{8.3}$$

$$= \frac{s}{(T_A+T_B+s)/2} \tag{8.4}$$

Note that $norm$, T_A, T_B, s, and g are all as a function of wavelength. For signals $s << T_A+T_B$, this expresses the source flux as a fraction of the mean telescope flux (per spectral pixel), and it eliminates any time evolution of the responsivity between nods (or even within nods, as it is done on individual chop cycles). In addition, and implicitly contained in g (which, as with the other parameters, is a function of wavelength), the system response variations as a function of wavelength are eliminated. But the main purpose is to make the offset signals[1] in Nod A and Nod B cancel each other even when there is a detector response drift.

If the source flux is not negligible then we have:

$$x = \frac{s}{(T_A+T_B)/2} \tag{8.5}$$

[1]The signal detected in the two telescope positions, which differ only by the telescope flux at the two chop positions.

where x is the source flux as a fraction of the telescope flux. We now have:

$$norm = \frac{s}{(T_A + T_B + s)/2} \tag{8.6}$$

$$= \frac{\frac{s}{(T_A+T_B)/2}}{1 + \frac{s/2}{(T_A+T_B)/2}} \tag{8.7}$$

$$= \frac{x}{1 + x/2} \tag{8.8}$$

so that:

$$norm + norm\frac{x}{2} = x \tag{8.9}$$

$$x = \frac{norm}{1 - norm/2} \tag{8.10}$$

For signals $s >> T_A + T_B$ (which is rare, but there are some observations in this regime), $norm$ approaches a constant value of 2 asymptotically, and the sensitivity of norm to the infalling flux progressively decreases.

What we measure from the data is the signal in Nod A and Nod B, being a combination of the target signal and the differential telescope signals. We compute $norm$ from that, but it is x we require to later convert the signal into Jy. The conversion factor between x and the final spectrum expressed in actual flux units is simply the telescope spectrum, expressed in [Jy]. Its derivation is detailed in the next section.

The technical note reference for this section can be found in here in HELL L2.

8.2.2.2 Telescope spectrum model

When the telescope background normalisation method was established as the default scheme for the flux calibration of chopped observations, there was the initial assumption that the emission of "the telescope" could be described by a physical model, as a function of wavelength and time. As it turned out, the light illuminating the detectors could not be consistently explained as originating from the telescope proper: the spectral shape and its time evolution clearly indicated more than one source of background light, and there was no plausible basis for a "physical" model of the additional light source(s).

Therefore, what is referred to as the "telescope" could only be empirically derived from trusted, celestial sources as absolute flux calibrators and as references to trace the (relative) time-variability of the "telescope". In fact, both types of sources and different types of observations had to be employed to define the SED of the "telescope" and its evolution with time, with sufficient resolution in wavelength and time.

It should be further noted that the measurement of the telescope was done with chopping – we have an "AC" measurement, and we do not measure *the* "telescope", but rather *a* "telescope". For example, the detectors (and differently so between the red and blue detector arrays) have some electrical low-pass filter characteristics which are not calibrated out in the "telescope". This means that the "telescope" SED is only suited for calibration of chop-nod observations and cannot be used to derive any direct conclusions about the properties of the telescope itself.

Source selection: After an inventory of available calibration observations, their suitability in terms of source flux compared to telescope background flux and the estimated error in celestial source flux models, three sources emerged, two for absolute SED calibration and one for relative monitoring of time evolution of the telescope background with sufficient sampling and full coverage of the mission duration. The absolute SED calibration is now linked to a combination of two asteroids, Ceres and Pallas, while the frequent sampling at key wavelengths is taken from observations of HD 161796. The latter was selected as being bright, constant in the FIR, unresolved, and always observable by *Herschel*. Model fluxes of the asteroids on each day of their observations were provided by Müller et al. (2014), and the obsids are given in Table 8.2.2.2.

Table 8.1: OD and obsids of the asteriod observations for spectroscopy

Target	OD	Obsids
Ceres	286	1342191138–40
	485	1342204332–4
	782	1342223711–13
	947	1342234477–79
	1237	1342252074–76
	1420	1342269291–93
Pallas	245	1342189271–73
	460	1342203135–37
	720	1342220595–97
	889	1342231274–76
	1139	1342247443-45
	1295	1342256243–45

HD 161796 was visited regularly on 120 ODs between OD169 and OD1442 and observed at the key wavelengths of 60 μm, 75 μm, 120 μm, 150 μm and 180 μm in line spectroscopy mode with standard chopping/nodding.

Data analysis: All data were processed in HIPE with a special script which exported the intermediate quantity x as specified in eqn 8.5. For the asteroid observations, the SED-mode observations were processed in individual chunks of 2 μm width with the range spectroscopy script and then the average was formed as the representative value for that wavelength interval. For the HD 161796 observations, which were taken in line spectroscopy mode, a default processing was applied.

Construction of the "telescope" SED: The procedure involves two main steps:

A. Derive a robust mean SED, formally valid on one OD roughly in the middle of the mission

B. Derive a daily correction of this SED to reflect the evolution of the SED with time, as a function of wavelength

A. The first step consists of two parts:

1. Define a reference SED with high S/N ratio and high fidelity in the spectral features (Fig. 8.1)
2. Analyse the effect of potential detector non-linearities, which a comparison of the Ceres-based and Pallas-based mean SEDs suggests could exist (see caption of Fig. 8.2)

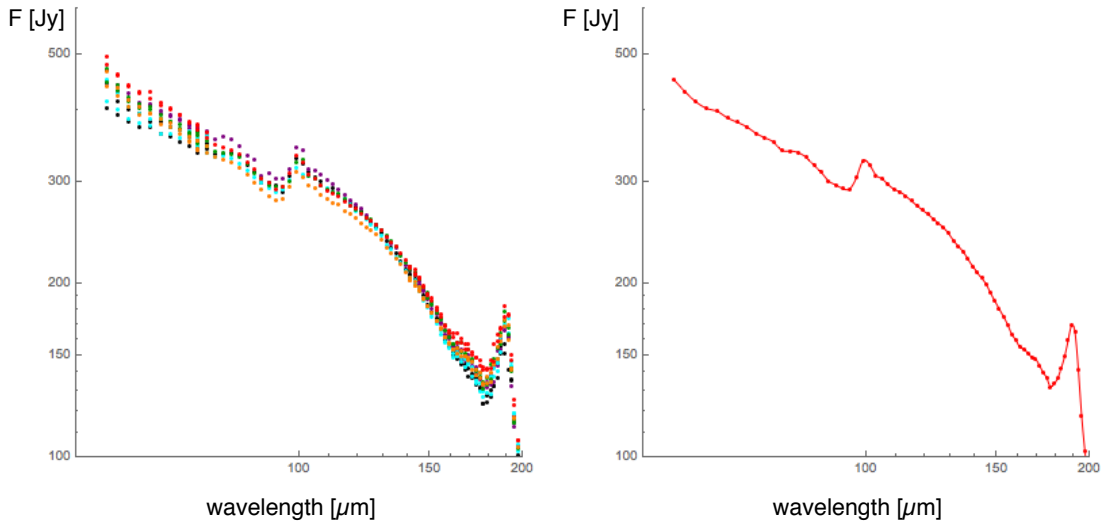

Figure 8.1: **Left**: telescope background SED derived from several Ceres observations over the *Herschel* mission, showing the general shape of the "telescope" emission and also its evolution with time: this is strongest at the short-wavelength end, shows a minimum near 130μm, and increases toward longer wavelengths, indicating at least two contributions of different colour temperature and different evolution. **Right**: mean telescope background SED, which has a sufficiently high S/N ratio to be a calibration data-set.

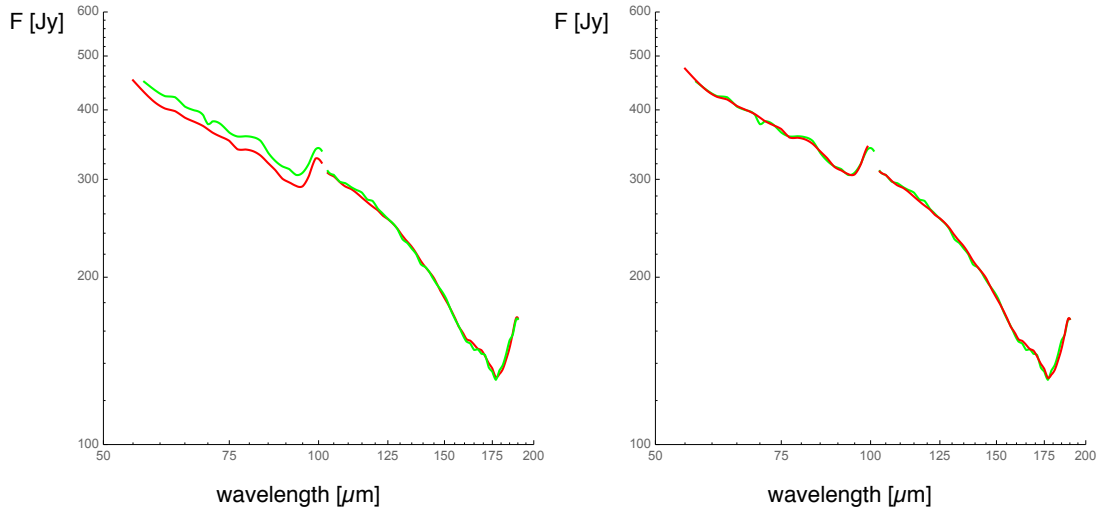

Figure 8.2: **Left**: mean telescope background SED as derived from Ceres (red) and from Pallas (green) observations. The agreement is impressive in the red band, where both sources are fainter than the telescope, but the discrepancy in the blue band, where Ceres becomes brighter than the telescope, could indicate non-linearity in the detector response. **Right**: Ceres-based mean telescope background SED (red), adjusted to the Pallas-based SED (green), by a linear correction function for each detector band (see text). This way, we benefit from the higher S/N ratio of the Ceres-based SED while avoiding detector saturation issues thanks to the lower flux levels of Pallas.

Part 1 is straightforward: since the selected asteroid observations are roughly evenly distributed over the mission, a simple arithmetic mean is sufficient to define the reference SEDs based on Ceres and on Pallas observations. Both asteroids are relatively blue compared to the telescope SED: Ceres, at the short-wavelength end, becomes as bright as the telescope, introducing a very strong signal modulation (compared to many science targets), while Pallas as the fainter source does not raise such concerns. In the red band, both sources are sufficiently fainter than the telescope – the spectrum shown in Fig. 8.2 (left panel) is suggestive of this view, since in the red (the faint end of the asteroid spectra) both asteroids produce the same telescope SED (with a higher noise level on the Pallas-based SED), but in the blue the Ceres-based SED appears slightly suppressed compared to the Pallas-based SED, which is what one would expect if the high flux of Ceres caused some detector "self-curing" (Sec. 8.2.8).

For Part 2 we fitted the ratio of $SED_{\mathrm{Ceres-based}}/SED_{\mathrm{Pallas-based}}$ with a first-order polynomial, separately for each band, and corrected the Ceres-based telescope SED. The result is shown in the right panel of Fig. 8.2. The red curve represents the reference telescope SED on the reference OD, i.e. OD 791, which is the centre-of-gravity of the asteroid observations.

B. The second main step is the recipe for the time evolution of the telescope SED, and this, again, has two components:

1. An ageing effect, causing a continuous increase of the telescope background
2. A periodic/seasonal modulation in telescope/satellite temperature, caused by the orbital modulation of the distance to the Sun

The time sampling of the asteroid observations is not sufficient to clearly show the periodic part, but it is quite visible in the many data points we have from our reproducibility source, HD 16179.

Fig. 8.3 (left) shows all observations without quality issues at the five key wavelengths. Note that the 60 μm trace (blue) actually represents two sets of measurements, in the second and third grating order and with very good agreement between the two sets. We plot the quantity $1/x$, as x is defined as source/telescope; so, for a non-variable source, $1/x$ is strictly proportional to the telescope background, of which we only want to monitor *changes* (not absolute fluxes) here.

The 60 μm trace clearly shows not only the increasing trend, but also the periodic modulation, whose amplitude is noticeably reduced at 75 μm, and is undetectable in the red band. The (linear) growth with time is also wavelength-dependent. The central panel shows how we fit that wavelength dependency with a second-order polynomial, in the absence of any physical explanation or more detailed empirical information. The correction factor, as a function of wavelength and OD, is then described by the following definitions:

$$\Delta_\lambda(\lambda) = b_0 + b_1\lambda + b_2\lambda^2 \tag{8.11}$$

$$\Delta_t(\lambda, OD) = \frac{OD - OD_{\mathrm{ref}}}{1000}\,\Delta_\lambda(\lambda) \tag{8.12}$$

$$corr_{\mathrm{red}}(\lambda, OD) = 1 + \Delta_t(\lambda, OD) \tag{8.13}$$

$$corr_{\mathrm{blue}}(\lambda, OD) = 1 - \frac{100-\lambda}{100-60}\,k_1[\sin(\frac{2\pi}{365}\,OD + k_2) - \sin(\frac{2\pi}{365}\,OD_{\mathrm{ref}} + k_2)] + \Delta_t(\lambda, OD) \tag{8.14}$$

where λ is in units of microns and OD in units of days. The fit parameters are compiled in Table 8.2.

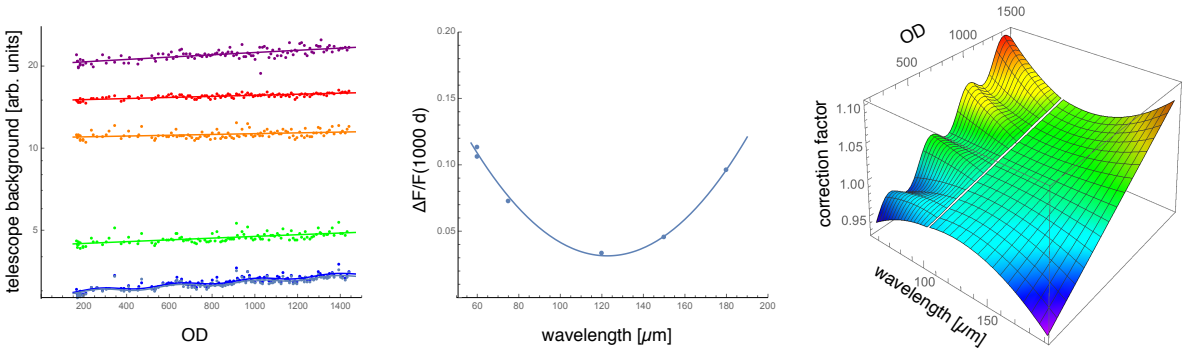

Figure 8.3: **Left**: Telescope background monitored vs. OD against the reproducibility source HD 16179. The vertical axis shows 1/x (in telescope normalisation speak), on a logarithmic scale, such that slopes are representative of $\Delta F_{\rm telescope}/F_{\rm telescope}$, at key wavelengths of 60 μm (blue), 75 μm (green), 120 μm (orange), 150 μm (red) and 180 μm (purple). The periodic (seasonal) modulation is clearly visible in the blue, but not significant in the red. **Centre**: Evolution of $\Delta F_{\rm telescope}/F_{\rm telescope}$ over 1000 ODs, without the periodic part. The fitted "bowl" is a second-order polynomial. **Right**: Evolution of the total telescope flux correction function, used to calculate a telescope background for each OD from the reference SED valid on OD 791. At each wavelength, a linear evolution is applied, with the slope taken from the "bowl" in the centre panel. In the blue band, the periodic modulation from the fit at 60 μm (left panel) is then applied, with the amplitude pinned to the value fitted at 60 μm, and a linear wavelength dependence with a slope to reach zero amplitude at the long-wavelength end of the blue band.

Table 8.2: Parameters of the telescope flux correction function

b_0	b_1	b_2	$OD_{\rm ref}$	k_1	k_2
0.328015	-0.00483656	0.0000197192	791	0.01497	0.01511

In a nutshell, we can summarise the telescope model derivation above by saying that the shape of the telescope model is derived from Ceres, which allows for a very high SNR, while its absolute level is derived from Pallas, allowing for more robustness against short-term transients in the detectors due to the high flux levels of Ceres.

In order to reduce the effects of any systematic errors on the model of Pallas, we applied an extra correction to the absolute scaling of the telescope background model. The goal of this correction is to tie the absolute flux calibration to the average of our set of calibration observations instead of Pallas only.

To this aim, we derived the flux of the celestial calibrators at all key wavelengths in all calibration observations. We then compared those to their respective models, and (excluding Neptune and Uranus, at the bright end) found the following averages: 60 & 75 μm=1.04, 150 μm=0.98. This indicates that, on average and in comparison with all other models, calibrating on Pallas only leads to a slight overestimate of the flux in our blue bands, and a slight underestimate in the red. Consequently, we rescaled the telescope model by the inverse of these averages, ensuring the final calibration is linked to the entire set of calibrators and consistent with the calibration of the unchopped observations.

Various technical notes describing the derivation of the telescope background and its evolution with time can be found on HELL L2. A script that can be imported into HIPE to create the telescope

spectrum for any is described in a technical note that is in HELL L2.

8.2.3 Unchopped observations and leak regions: using the internal calibration sources and the RSRF

In the unchopped observing mode and in the wavelength ranges affected by light leaks (from unchopped and chop-nod observations), we cannot assess the detector response via the telescope background: because we do not measure it (unchopped), or because it is not reliable (leak regions). In these cases the internal calibration sources (CSs) were used as flux reference instead. The flux of these sources was calibrated independently, and was assumed to be constant throughout the mission (this was verified via regular observations of constant celestial sources). The detector response was measured during a dedicated "calibration block" which took place at the beginning of every observation and used the calibration sources as a light source.

This is described in this section.

8.2.3.1 Absolute flux calibration concept: unchopped

The principle is here the same as in previous section and absolute response is derived in an identical way. For the unchopped mode there is no chopping and telescope nodding, rather the observations were done at a single chopper position and the telescope slewed between the on-source and off-source positions after the entire requested spectral range had been covered. This means that the on- and off-source measurements are further apart in time, and that they contain the same telescope background (as they look at the same sky position). The measured signal is then simply:

$$unchopped = [ON - OFF] \tag{8.15}$$
$$= (T + s) * g - T * g' \tag{8.16}$$
$$= s * g + T * (g - g') \tag{8.17}$$

where ON and OFF are the on- and off-source signals respectively; $T = T_{ON} = T_{OFF}$ is the telescope background, and g and g' are the absolute instrument response during the on- and off-source measurements.

For unchopped line-scan observations, we assume the measurement is short enough so that response drifts between the on- and off-source measurements are negligible, i.e. $g \sim g'$. In this case, eqn 8.17 simplifies to:

$$unchopped\_line \sim s * g \tag{8.18}$$

For unchopped range-scans, the duration of the observation is sometimes much larger, and the general assumption that there is no drift between on- and off-source acquisition is no longer valid. For this reason, the AOT for range-scan did not include the on- and the off-source measurements in the same observation as for line-scans, rather they were taken as different obsids, each having their calibration block, allowing for an independent determination of g and g'.

This leaves nevertheless a fraction $(g - g')$ of the telescope background appearing as an additive term in the final signal, as expressed in eqn 8.17. The telescope background is a very smooth continuum, hence this term does not affect spectral lines or narrow spectral features. It does nevertheless impact the continuum level: the continuum level of the background-subtracted final products for the

unchopped AOTs is therefore very uncertain, and may even be negative or appear to vary from one side of a mapping sequence to the other, simply because the response happened to be higher during the off-source measurement than it was on-source (e.g. due to self-curing, see Sec 8.2.8).

The instrument response is expressed in [V/s/Jy] and relates the flux [Jy] to the slope measured by the detectors [V/s]. The function describing the absolute response of the instrument at all wavelengths is the ASRF, for Absolute Spectral Response Function.

In flight, it was impossible, and anyway unnecessary, to recalibrate this function for every observation. Instead, we distinguish its two main components:

$$g = ASRF(\lambda) = absResp|_{\lambda_{key}} * RSRF(\lambda) \tag{8.19}$$

where

- $absResp|_{\lambda_{key}}$ is the absolute response of the instrument at a key wavelength, taken as a reference for the calibration in that spectral band. It is expressed in [V/s/Jy]
- RSRF is the Relative Spectral Response Function. It is normalised at the key wavelength of each spectral band, and relates the instrument response at that wavelength with the response at any other wavelength in the band (see Sec. 8.2.3.4)

The RSRF was measured on the ground with very high precision, and verified in flight. The ground calibration was used throughout the mission.

The $absResp|_{\lambda_{key}}$ is established via the calibration block. During the execution of the calibration block, the grating wass fixed (on λ_{key}), but the chopper moved back and forth from one internal calibration source (CS1) to the other (CS2). These sources have different temperatures, hence different signal. We compute the average of the signal of pairwise differences between the two calibration sources (i.e. first we compute CS1-CS2 for each readout, and then average that over the calibration block). By dividing this average, expressed in [V/s], by the difference of the (known) spectral flux densities of the calibration sources (by task *specDiffCs*, Sec. 8.2.3.3.6), expressed in [Jy], we get the absolute pixel response, in [V/s/Jy]:

$$absResp|_{\lambda_{key}} = \left.\frac{CS_1 - CS_2}{DiffCS}\right|_{\lambda_{key}} \tag{8.20}$$

which can be used with eqns 8.19 and 8.17 to derive the source's flux.

8.2.3.2 Absolute flux calibration concept for chop-nod above 190 μm

The same calibration block+RSRF scheme is used for the calibration of spectral ranges affected by the "red leak", at $\lambda > 190\,\mu$m for any AOT. For the unchopped AOTs, the details are as given in the previous section. For the chop-nod AOTs there are some differences because of the chopping and nodding that takes place for these observations. Here, the uncalibrated signals are processed in the following way:

$$chopnod = 1/2\left[\underbrace{A - B}_{\text{Nod A}} + \underbrace{B' - A'}_{\text{Nod B}}\right] \tag{8.21}$$

$$\tag{8.22}$$

where A and B are the signals detected in the two chopper positions (on- and off-source) in Nod A and A' and B' are the signals detected in the two chopper positions (off- and on-source) in Nod B. All signals are expressed in [V/s].

Next we express the observed signals as fluxes T_A and T_B from the telescope in the two chopper positions, and the flux from the source as s, all converted to fitted ramps by the gain factor g. This gain is here assumed constant for the duration of a complete observation. The combination of nods is performed near the end of the pipeline, in *specAddNod*, and can be expressed as:

$$chopnod = 1/2 * \Big((T_A + s) * g - T_B * g + (T_B + s) * g' - T_A * g' \Big) \tag{8.23}$$

$$= 1/2 * \Big(s * (g + g') + (T_A - T_B) * (g - g') \Big) \tag{8.24}$$

$$\sim \; s * g \tag{8.25}$$

Note that all parameters are wavelength dependent. Given that we assume $g \sim g'$, i.e. we neglect any response drift occurring between the nods, and that $T_A \sim T_B$, i.e. the difference in telescope background between the two chopper positions is small, the last term in eqn 8.24 is of the second order.

8.2.3.3 Calibration source fluxes

Each spectrometer observation was preceded by a staring at the calibration sources: the calibration "block". In this section, we describe the derivation of the calibration files that were used to establish the instrument response via this part of the observation.

During the calibration block, the grating did not move at all while the chopper alternated between the two internal calibration sources (CS) at a frequency of 1 Hz. The CSs were at different temperatures, and hence delivered different signal levels.

A chopping cycle contains 17 integrating ramps (each ramp lasts for $\frac{1}{8}$ second): 4 visits on each of the two internal calibration sources, each counting 4 ramps, plus one extra ramp per cycle on CS1. A calibration block contains 40 such cycles. For each of the 400 detectors and for each camera, this leads to 360 measures of CS1 and 320 of CS2. To alleviate any effect from a possible transient behaviour at the start of the calibration block, we systematically exclude the first 30 seconds, leaving 234 measures/detector for CS1 and 208 for CS2. For practical reasons, we also disregard the extra measurements on CS1, hence leaving to 208 measurements from each source.

Each and every measurement performed by the PACS spectrometer included a high level of redundancy. All equations below describe the concept of the calibration as if the measurements were 'unique'. In reality, every mention of a measure of the CS refers to the average over all (208) frames described above. This is also true for the on-sky part of any measurements performed by the spectrometer: every measurement includes a high level of redundancy, so that the final rebinned spectrum involves averaging over a number of integration ramps at every grating position, and a number of detectors (i.e. spectral pixels) visiting every wavelength bin.

Except for the SEDs, all calibration observations were obtained with a high spectral sampling, so that all spectral pixels actually visited every spectral bin of the rebinned spectrum.

8.2.3.3.1 Key wavelengths, RSRF and master flatfield

The flow of our flux calibration as described below is based on point sources (e.g. Ceres) observed in the central spaxel, at one key wavelength in each spectral band. Most of the flux calibration observations were performed at those key wavelengths exclusively. A series of SED observations were also used for flux calibration, but in this case a very small wavelength range was selected around the key wavelength, rather than the entire, continuous spectral range. Consequently, all observations considered here can be regarded "at the key wavelength". One primary key wavelength was defined in every spectral band. They are listed in Table 8.3.

Blue	Red
B2A – 60 μm	R1 – 120 μm
B3A – 60 μm	R1 – 180 μm
B2B – 75 μm	R1 – 150 μm

Table 8.3: Key wavelengths used for the observations of celestial flux calibrators. The rows correspond to the three bands.

Below, we will show how to establish the detector response at the key wavelengths and in the central spaxel and the central 3×3 spaxels (which sky area encompasses a larger fraction of the PSF than the central spaxel alone). Once known at the key wavelengths, the response ws transferred to the other wavelengths via the RSRF (Sec. 8.2.3.4). In the spatial domain, the transfer to the other spaxels is performed via the flatfield.

The master flatfield was derived while processing all of the calibration observations by selecting their off-source measurements, i.e. all visits to the telescope background during the on-sky part of the observation. We get:

$$\overline{FF}_{d,s} = \frac{1}{N}\sum_{i=1}^{N} \left. \frac{m^i_{Ceres,d,s}}{\frac{1}{9\times 16}\sum_{s\in 3\times 3}\sum_{d=1}^{16} m^i_{Ceres,d,s}} \right|_{OFF} \tag{8.26}$$

$$= \frac{1}{N}\sum_{i=1}^{N} \left. \frac{m^i_{Ceres,d,s}}{\overline{m}^i_{Ceres,3\times 3}} \right|_{OFF} \tag{8.27}$$

where N is the number of observations of celestial calibrators. The "OFF" indicates that only the samples obtained on the OFF-source positions, i.e. on the telescope background, are taken into account. Here, and throughout the rest of this section, we use:

- s for spaxel ($s \in [5\times 5]$) and d for "spectral pixel (detector) within the spaxel" ($d \in [1, 16]$)
- m for a measurement in [V/s], f for a flux in [Jy], and $\Re$ for a detector response, in [V/s/Jy]
- The notation 3×3 refers to the central 3×3 spaxels of the IFU
- We use $Ceres$ as archetypal name for any measurement of a given celestial calibrator. In reality, we used more than one celestial calibrator, but this has no impact on the developments below. We will nevertheless generalise the expression when relevant.

Eqn 8.27 shows that the flatfield is renormalised to the average of the central 3×3 spaxels.

Although obtained in one step via eqn 8.27, the flatfield can be regarded as organised along two dimensions: a spatial flatfield, describing the variations between the spaxels, and a spectral flatfield, to account for response variations between the 16 spatial pixels belonging to a given spaxel. Whereas the spatial flatfield will drive the accuracy of spectral maps, a proper spectral flatfield is also crucial in order to avoid spurious features dominating the final noise in the spectrum. For example, with the Nyquist sampling of SED observations, only a few spectral pixels contribute to each wavelength bin. Hence if a pixel has a badly calibrated response, it will introduce a spike in the spectrum in every bin it contributes to, and the regular appearance of bins with an abnormal value mimics fringes in the rebinned spectrum[2]. Similarly, when several pixels are affected, the continuum RMS after rebinning may be severely increased. The spectral flatfield is therefore essential and all pipelines contain a specific task to refine it, i.e. to rescale the response from individual detectors at the time of the observation to the spaxel-average, which is calibrated during the calibration block and used as a reference at this level. The pipeline task that does the spectral flatfielding is described in Sec. 9.2.1.4. The equations of this section only concern the spatial flatfielding.

8.2.3.3.2 Instrument response during calibration observations

After observing a celestial calibrator and processing the data, we obtain a rebinned spectrum in every spaxel, i.e. taking all 16 spectral pixels into account:

$$m^i_{Ceres,s} = \frac{1}{16}\sum_{d=1}^{16} m^i_{Ceres,d,s} \tag{8.28}$$

For the flux calibration, and to be more robust against slight telescope mis-pointings, we performed the calibration on a "meta-spaxel", which is the central 3×3 spaxels instead of just the central spaxel. Although the central spaxel receives most of the flux from the source, the combined beam of the central 3×3 spaxels is wider, and so the amount of flux gathered from the point source (which is always assumed to be centrally-located in the central spaxel) is less sensitive to slight (typical) mispointings of the point source from that central location.

The final rebinned spectrum, summed up over these nine spaxels, and corrected for the fraction of the PSF falling out of their common area can be written as:

$$m^i_{Ceres} = \frac{\sum_{s\in3\times3} m^i_{Ceres,s}}{PSCF_{3\times3/\mathrm{tot}}} \tag{8.29}$$

where $PSCF_{3\times3/\mathrm{tot}}$ stands for "Point Source Correction Function" and represents the fraction of the PSF falling out of the central 3×3 spaxels. It is described in more details in section 8.3.4.

Finally, the instrument response can be derived, assuming we know the flux from the celestial calibrator:

$$\Re^i_{Ceres} = \frac{m^i_{Ceres}}{f^{model}_{Ceres}} \tag{8.30}$$

[2] A "rebinned" spectrum is a spectrum from a rebinned cube. The first cube of the pipeline, from which the rebinned cubes are created, contains, in each spaxel, a collection of all of the individual spectra gathered by each of its 16 spectral pixels. These are then spectrally-rebinned (consider this an averaging) along a regular wavelength grid, to create these rebinned cubes.

8.2.3.3.3 Average instrument response over the mission

The average instrument response, computed from all flux calibration measurements is simply

$$\overline{\Re} = \frac{1}{N} \sum_{i=1}^{N} \Re^{i}_{Ceres} \tag{8.31}$$

As shown by eqn 8.30, the response is a relative measurement, and provided its model is correct, the target itself has no effect on it. Consequently, the use of a list of calibrators in addition to Ceres has no impact on eqn 8.31. Adopting N_{cc} for the number of different celestial calibrators and $N_m(cc)$ for the number of observations of each of them, we could indeed rewrite eqn 8.31 in a heavier, though equivalent form:

$$\overline{\Re} = \frac{1}{N_{cc}} \sum_{cc=1}^{N_{cc}} \frac{\sum_{i=1}^{N_m(cc)} \Re^{i}_{cc}}{N_m(cc)} \tag{8.32}$$

where this formulation actually gives equal weight to all calibrators, while in the facts we adopt that of eqn 8.31, giving equal weight to all observations.

This average response, multiplied by the variations between spectral pixels, is stored in the calibration file `observedResponse3x3`

$$\overline{\Re}^{OBS}_{d,s} = \overline{\Re} \times \overline{FF}_{d,s} \tag{8.33}$$

The celestial calibrators were observed at all key wavelengths listed in Table 8.3.

8.2.3.3.4 Flux from the internal calibration sources

For each of the two internal calibration sources, we get a measurement in each spaxel during the calibration block:

$$m^{i}_{CS,s} = \frac{1}{16} \sum_{d=1}^{16} m^{i}_{CS,d,s} \tag{8.34}$$

Averaging it up over the 9 central spaxels:

$$m^{i}_{CS} = \frac{1}{9} \sum_{s \in 3\times3} m^{i}_{CS,s} \tag{8.35}$$

Multiplying with the response just established from the celestial part of the observation then provides the flux from the calibration source during this observation:

$$f^{i}_{CS} = \frac{m^{i}_{CS}}{\Re^{i}_{Ceres}} \tag{8.36}$$

We can now compute the mission-average flux from the internal calibration sources over the central 9 spaxels. We use a geometric average to ensure the overall self-consistency of the calibration concept, as will become clear with eqn 8.45 and subsequent equations.

$$\overline{f}_{CS} = \frac{1}{\frac{1}{N}\sum_{i=1}^{N}\frac{1}{f_{CS}^{i}}} \tag{8.37}$$

Finally, we build the calibration file `calSourceFlux` by injecting the flatfield in $\overline{f}_{CS}$:

$$\overline{f}_{CS,d,s} = \frac{\overline{f}_{CS}}{\overline{FF}_{d,s}} \tag{8.38}$$

The calibration block was limited to one single setup for each filter: when observing with filter B, i.e. in second order, the calibration block was measured at $75\,\mu m$ (band B2B) and $150\,\mu m$ (band R1) . In filter A, i.e. 3^{rd} order, it was always measured at $60\,\mu m$ (B3A) and $180\,\mu m$ (R1). In other words, the calibration block always happened in one of the last two settings as described in Table 8.3. Consequently, the flux of the calibration source was only measured at these four wavelength, and the calibration file filled accordingly. The consequence of this is explained in the next section (eqn 8.40).

8.2.3.3.5 Instrument response during scientific measurement

During a scientific measurement, the instrument response is estimated from the differential measurement performed on the calibration sources during that observation's calibration block,

$$\Re_{CS,d,s}^{i} = \frac{\frac{1}{9\times 16}\sum_{s\in 3\times 3}\sum_{d=1}^{16}(m_{CS2,d,s} - m_{CS1,d,s})}{(f_{CS2,d,s} - f_{CS1,d,s})} = \frac{m_{CS}^{i}}{\overline{f}_{CS,d,s}} \tag{8.39}$$

The first expression gives more detail on the differential signal that is actually computed. The second expression, simplified, corresponds to the notation used throughout this section (e.g. eqns 8.28 and 8.29). The absence of the PSCF in eqn 8.39 is explained by the extended nature of the internal calibration sources.

Band B2A at 60 μm constitutes a special case. As seen above, the flux of the internal calibration sources at this wavelength was exclusively calibrated in band B3A, i.e. the calibration block of all observations performed with filter A were performed in band B3A, regardless of whether they occurred in band B2A or B3A. Consequently, the instrument response in this band was derived via:

$$\Re_{CS,d,s}^{i}\big|_{B2A\_60} = \left(\Re_{d,s}^{OBS}|_{B2A\_60}\right) \times \left(\frac{\Re_{CS,d,s}^{i}\big|_{B3A\_60}}{\Re_{d,s}^{OBS}|_{B3A\_60}}\right) \tag{8.40}$$

With eqns 8.39 and 8.40 at hand, the instrument response was calibrated and the flux from the target was retrieved from:

$$f_{source,s}(\lambda) = \frac{1}{16}\sum_{d=1}^{16}\left(\frac{m_{source,d,s}(\lambda)}{\Re_{CS,d,s}(\lambda_{key})\times RSRF(\lambda)}\right) \tag{8.41}$$

where the average over the 16 detectors is actually a rebinning in wavelength. The flatfield is included in $\Re_{CS}$ and the response was transferred from the key wavelength to all wavelengths via the RSRF, as described above.

The last relation describes the celestial flux as measured in spaxel s, i.e. $f_{source,s}(\lambda)$ is expressed in [Jy/beam].

For some types of sources it iwas necessary to carry out an additional correction:

- For point sources, we needed to account for the fraction of the PSF falling outside of the central spaxel(s). For this, a task was provided to apply a dedicated point source correction function ($PSCF$). To be robust against small (but typical) mispointings, it is recommended to sum up the central 9 spaxels, and apply the corresponding $PSCF_{3\times3/tot}$ (the task gives a choice between the central spaxel only or the central 3×3).

- For extended sources, it is necessary to correct for the uneven nature of the illumination of the focal plane, i.e. our imperfect knowledge of the combined beam shapes of the 5×5 spaxel grid. For this we want to convert the [Jy/beam] units into a surface brightness. The Extended Source Correction (ESC) is dedicated to this task. It takes care of the difference between our best knowledge of the beam shapes and a perfectly uniform instrument response.

The $PSCF$ and the ESC are described in detail in Sec. 8.3.4.

8.2.3.3.6 Mission-average flux from the celestial calibrators

Restricting ourselves to a key wavelength ($RSRF(\lambda_{key}) = 1$), including the necessary point-source correction and adopting the notation introduced in eqn 8.29, we can rewrite eqn 8.41 to describe an observation of a celestial flux calibrator:

$$f_{Ceres}^{OBS,i} = \frac{m_{Ceres}^{i}}{\Re_{CS}^{i}} \tag{8.42}$$

Or, given eqns 8.39 and 8.37,

$$f_{Ceres}^{OBS,i} = \frac{m_{Ceres}^{i}}{m_{CS}^{i}} \times \overline{f}_{CS} \tag{8.43}$$

$$= \frac{m_{Ceres}^{i}}{m_{CS}^{i}} \times \frac{1}{\frac{1}{N}\sum_{i=1}^{N}\frac{1}{f_{CS}^{i}}} \tag{8.44}$$

We can now check the overall self-consistency of the our calibration concept by computing the average flux resulting from all measurements of celestial flux calibrators. Given that $\overline{f}_{CS}$ is unique for all measurements, and using 8.36 and 8.30 subsequently:

$$\overline{f}^{OBS}_{Ceres} = \frac{1}{N}\sum_{i=1}^{N} f^{OBS,i}_{Ceres} \tag{8.45}$$

$$= \left(\frac{1}{N}\sum_{i=1}^{N}\frac{m^i_{Ceres}}{m^i_{CS}}\right) \times \left(\frac{1}{\frac{1}{N}\sum_{i=1}^{N}\frac{1}{f^i_{CS}}}\right) \tag{8.46}$$

$$= \left(\sum_{i=1}^{N}\frac{m^i_{Ceres}}{m^i_{CS}}\right) \times \left(\frac{1}{\sum_{i=1}^{N}\frac{\Re^i_{Ceres}}{m^i_{CS}}}\right) \tag{8.47}$$

$$= \left(\sum_{i=1}^{N}\frac{m^i_{Ceres}}{m^i_{CS}}\right) \times \left(\frac{f^{model}_{Ceres}}{\sum_{i=1}^{N}\frac{m^i_{Ceres}}{m^i_{CS}}}\right) \tag{8.48}$$

$$= f^{model}_{Ceres} \tag{8.49}$$

These equations could be rewritten to differentiate the sum over N to take into account a set of N_{cc} celestial calibrators, as in eqn 8.32. However, this would not impact the final result.

8.2.3.4 Relative spectral response function (RSRF)

The main reference document for this section is PICC-ME-TR-006.

The Relative Spectral Response Function (RSRF) of the PACS spectrometer is the response of every spectral pixel as a function of the wavelength of the infalling far-infrared radiation. This relative spectral response function is the combination of the response functions corresponding to the detector, grating, filters, PACS optics and telescope optics. However, as some effects are highly dependent on system characteristics (e.g. filter transmission depending on the angle of incidence) its accurate characterisation is only possible at the entire system level.

The RSRF was determined during ILT based on very detailed spectral scans of a cryogenic blackbody over the entire wavelength range covered by the spectrometer in the different spectral orders (see this technical note). These measurements were obtained to sample different source temperature, chopper position and integrating capacitance. For in-flight reference, the same detailed scans were performed on the two internal calibration sources.

In the course of the FMILT the instrument was warmed up and opened up twice to perform re-alignment of important optical components. During ILT-II the RSRF characterisation at the seven chopper positions and the two internal calibration sources were obtained at full (high) spectral resolution, while in ILT-III only the characterisation at the optical zero and one of the internal calibration sources were performed at this high resolution. Time constraints during FM-ILT-III imposed that the broadband shape at the different standard AOR chopping positions was verified using a coarse spectral scan (low resolution). Hence, chopper position and integrating capacitance were analysed using ILT-II measurements, while the higher order leakage analysis made use mostly of ILT-III data.

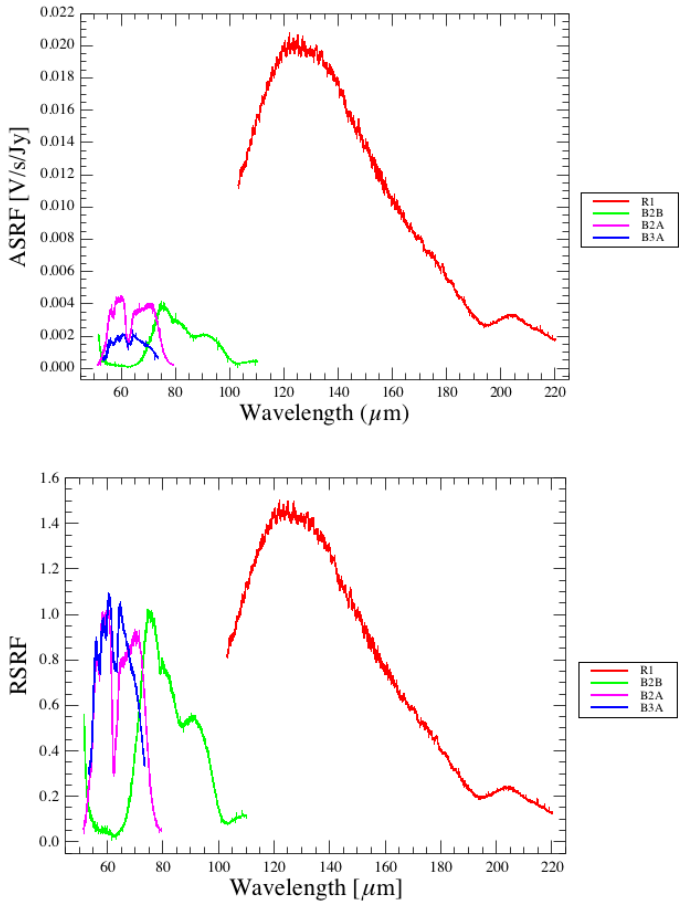

Figure 8.4: **Left**: PACS Spectrometer absolute spectral response function for spectral pixel 8 and module 12 in the four bands. **Right**: PACS Spectrometer relative spectral response function for spectral pixel 8 and module 12 in the four bands. Key wavelengths for normalisation are 60 μm for bands B2A and B3A, 75 μm for B2B and 150 μm for R1.

The measurements of the detector signals under dark conditions were obtained observing a cold blackbody (T_{bb} =5.9 K) over the entire PACS spectral range. These revealed that: (i) the signal under dark conditions is significant in the red detectors, (ii) the signal is stable within a few percent at different grating positions, indicating that the root cause of this signal is dark current, amplifier offsets or internal straylight (see here). Construction of a dark signal map was made by taking a median of the signals in the entire measurement for every detector. This dark signal map was scaled by a factor depending on the capacitance used. The scaling factor is based on the nominal capacitance ratios: 1 for capacitance 0, 1.71 for capacitance 8, 3.21 for capacitance 4, and 8.21 for capacitance 12. A little more on the dark current can be found in Sec. 8.2.5.

The data processing steps consisted of:

- noise filtering on separate up- and down-scans followed by rebinning onto same grid
- signal conversion to [V/s]

- wavelength calibration
- pixel-specific dark offset subtraction, once scaled by the integrator capacitance
- division by blackbody flux density at that wavelength

The final product is the absolute response of the instrument ASRF, per detector element, expressed in units of [V/s/Jy] (see Fig. 8.4). The final relative spectral response function was obtained by normalisation of the ASRF at the band key wavelength indicated in Table 8.3. These calibrations are stored in the calibration files `rsrfR1`, `rsrfB2B`, `rsrfB3A`, `rsrfB2A`. The RSRFs derived for the four bands are shown in Fig. 8.4. The R1 bump longward of 190 μm is due to light leakage and is addressed in the next section.

8.2.3.4.1 Line flux calibration in R1 order-leak regions

The relative spectral response is affected by spectral leakage (order overlap due to the finite steepness of order-sorting filter cut-off edges) from grating order n+1 into grating order n. At wavelengths of 70–73 μm, 98–105 μm and 190–220 μm, the next higher grating order wavelengths of 52.5–54.5 μm, 65–70 μm and 95–110 μm overlap. Continuum shapes and flux densities in these border ranges are therefore incorrect. The contaminated continuum level is irremediably lost, but a correct RSRF could solve the problem for the flux pertaining to only one order, i.e. spectral lines.

To disentangle order leakage for the R1 band, RSRF measurements during ILT-III were obtained with two blackbody temperatures. The measured flux for every wavelength at a given temperature can be expressed as

$$S(\lambda;T_1) = B(\lambda;T_1)\cdot RSRF_1(\lambda) + B(\lambda/2;T_1)\cdot RSRF_2(\lambda/2) \tag{8.50}$$

$$S(\lambda;T_2) = B(\lambda;T_2)\cdot RSRF_1(\lambda) + B(\lambda/2;T_2)\cdot RSRF_2(\lambda/2) \tag{8.51}$$

where S is the measured signal, B represents the cryogenic blackbody flux density, and $RSRF_1$ and $RSRF_2$ are the relative system responses in orders 1 and 2 at a wavelength λ. Solving for $RSRF_1$ and $RSRF_2$, we obtain:

$$RSRF_1(\lambda) = \frac{S(\lambda:T_1)\cdot B(\lambda/2;T_2) - B(\lambda/2;T_1)\cdot S(\lambda:T_1)}{B(\lambda;T_1)\cdot B(\lambda/2;T_2) - B(\lambda/2;T_1)\cdot B(\lambda;T_2)} \tag{8.52}$$

$$RSRF_2(\lambda/2) = \frac{S(\lambda:T_2)\cdot B(\lambda;T_1) - B(\lambda;T_2)\cdot S(\lambda:T_1)}{B(\lambda/2;T_2)\cdot B(\lambda;T_1) - B(\lambda;T_2)\cdot B(\lambda/2;T_1)} \tag{8.53}$$

The measurements at the two blackbody temperatures (42 K and 35.4 K) were obtained at different spectral resolutions. Hence the R1 de-leaked RSRF was constructed with the global shape of a low resolution RSRF, coupled with the high-frequency structure of the ILT high-resolution RSRF. Since the response is extremely low in the leak spectral region (>190 μm), no dark current subtraction was performed (to avoid negative response, and hence cusps in the final spectra). The final calibration R1 file is a hybrid RSRF constructed by stitching together the standard ASRF for wavelengths shortward of 185 μm and the de-leaked ASRF at longer wavelengths. A scaling factor of $\sim$ 10% was derived from the overlap region 185–188 μm and applied to the intermediate de-leaked ASRF. This final product was then normalised at the key wavelengths to obtain the final RSRF.

The order 1 relative response corrected for leakage is shown in Fig. 8.5. Note that (i) it decreases steadily up to $\sim$ 205–207 μm, (ii) it is very low longward of 205 μm, and (iii) it is unreliable beyond

217 μm. The recommendation is to use it to a maximum wavelength of 206 μm, and exclusively for line emission.

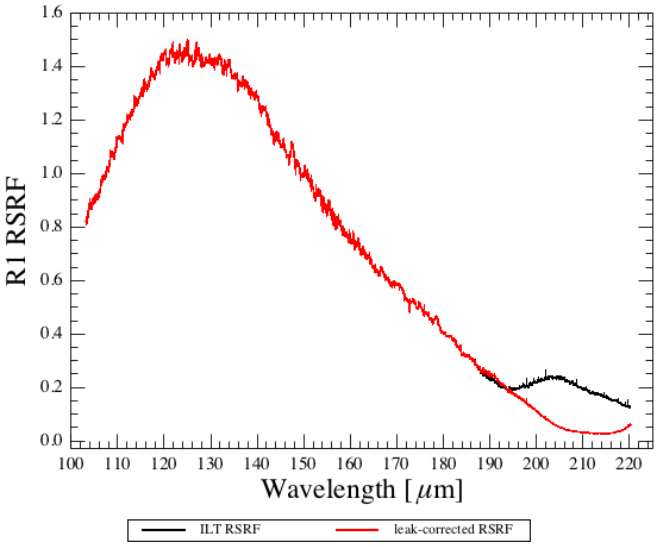

Figure 8.5: PACS Spectrometer relative spectral response function for detector 8 and module 12 in the R1 band before and after leakage correction longward of 190 μm.

8.2.4 Absolute Flux Calibration Error Budget

As explained previously, the absolute flux calibration can be performed using the telescope background (the standard for chop-nod observations) or the internal calibration sources (the standard for unchopped observations and for spectral regions $>$ 190 μm). The error budget for both of these is detailed in this section.

8.2.4.1 Telescope Background Normalisation

8.2.4.1.1 Absolute flux at the key wavelengths

A whole set of celestial calibrators have been used to establish the absolute flux calibration, covering a large domain in flux and surface temperature. These are discussed in Chp. 6. The models themselves can be found on the ESA archive and this ESA repository. Table 8.4 summarises the targets and the number of visits to each in the various observing modes. The flux calibration observations were performed in all bands, so one visit in the table typically corresponds to three obsids. All in all, we have 143 visits of celestial flux calibrators; 109 excluding Neptune and Uranus (see below).

To get an estimate of the reproducibility of the measurements, a given target was observed at the key wavelengths at very regular intervals. HD 161796 was selected. Although variable at optical wavelengths, it is constant in the far infrared. It is not an absolute flux calibrator, and its observations were therefore flux calibrated using the PACS calibration scheme. The fact that its model slightly overestimates the flux observed at PACS wavelengths is not important, since it was only used as a reproducibility source.

Table 8.4: Census of flux calibration observations, per target and per observing mode

Target	λ_{key}		**SED**	
	ChopNod	Unchopped	ChopNod	Unchopped
Solar System				
Callisto	1		1	
Uranus	8	5	6	5
Neptune	9	4	10	5
Ceres	10	2	7	4
Vesta	8		5	2
Pallas	6		6	
Europa	5		4	
Juno	4		4	
Hebe	5		3	
Hygiea	7		4	
Thisbe	6			
Fiducial Stars				
$alpha$Boo	8	4		
αCet	3			
αTau	6			
βPeg	2	1		
γDra	4			
Reproducibility Source				
HD 161796	120	5		

The overall accuracy on the absolute flux calibration is presented in Table 8.5. Neptune and Uranus were not included in the derivation of the final scaling of the telescope background model: they are slight outliers in all the calibration results, and it is suspected that this is due to non-linearity in the detector response caused by their significant flux levels. Including them would result in a 2% higher flux calibration. Figure 8.6 displays the entire set of measurements in band B3A at 60 μm and R1 at 150 μm.

Table 8.5: Flux calibration error budget. All celestial absolute flux calibrators, except Neptune and Uranus.

Band	**Std. Dev.**	**Min**	**Max**	**Peak-to-Peak**
B3A 60	**0.06**	0.75	1.19	0.44
B2A 60	**0.06**	0.76	1.12	0.36
B2B 75	**0.07**	0.77	1.14	0.37
R1 120	**0.06**	0.88	1.20	0.32
R1 150	**0.06**	0.86	1.28	0.43
R1 180	**0.12**	0.15	1.32	1.16

The scatter in Fig. 8.6 and in Table 8.5 not only reflects the repeatability of the measurements, but also includes the systematic error resulting from uncertainty on the models used for our calibrators. A typical uncertainty on a model is 5–10%. Assuming the worst case of 10% identical for all sources and given that we used 13 sources, the final systematic error resulting from the model uncertainty can

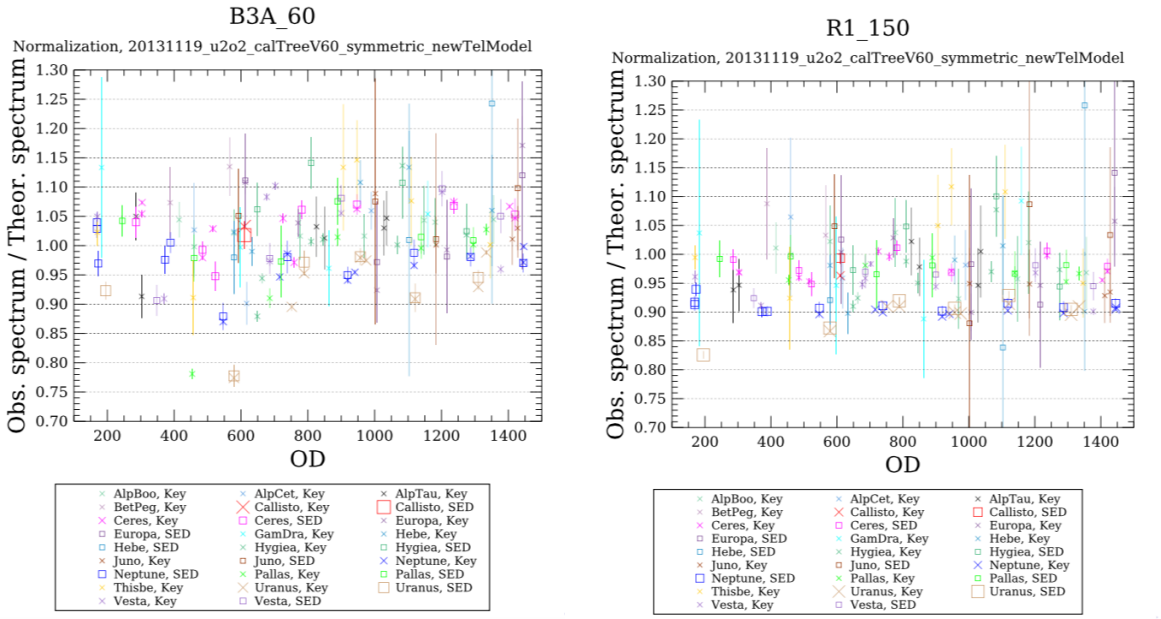

Figure 8.6: Complete set of celestial calibrators observations reduced with telescope background normalisation pipeline, at the prime key wavelengths in bands B3A (60 μm) and R1 (150 μm).

be derived from standard deviation of the measurements as indicated in Table 8.5, with $\sim$ 2% in all bands, and $\sim$ 3% around 180 μm.

Table 8.6: Flux calibration error budget. Repeatability source HD 161796 (120 visits). This source's model is slightly over-estimated (see text). Consequently on average the observations remain below the model.

Band	Std. Dev.	Min	Max	Peak-to-Peak
B3A 60	**0.02**	0.84	0.99	**0.15**
B2A 60	**0.02**	0.85	1.00	**0.15**
B2B 75	**0.03**	0.78	0.92	**0.14**
R1 120	**0.03**	0.88	1.02	**0.14**
R1 150	**0.01**	0.93	1.00	**0.07**
R1 180	**0.03**	0.81	1.01	**0.20**

8.2.4.1.2 Repeatability

The scatter in Fig. 8.7 and in Table 8.6 reflects the repeatability of the measurements at the key wavelengths. The left panel in Fig. 8.7 illustrates that the distribution of errors does not follow a Gaussian distribution. The occasional measures with a low flux correspond to occurrences of larger pointing errors. It was consequently recommended to consider the peak-to-peak variation, i.e. $\sim$15% as representative for the repeatability error rather than the standard deviation of the distribution. In this way, slight pointing mishaps during any PACS spectroscopy observation (and the effect this has on the data) are covered by the quoted calibration uncertainty.

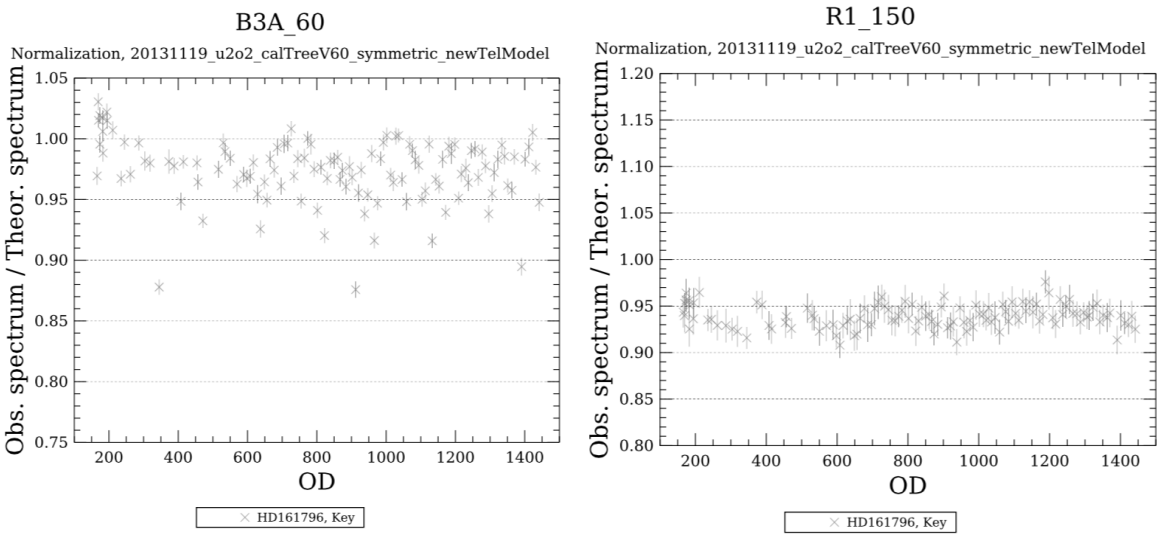

Figure 8.7: Complete set of observations of HD 161796 reduced with telescope background normalisation pipeline, at the prime key wavelengths in bands B3A (60 μm) and R1 (150 μm), illustrating the repeatability of the measurements.

8.2.4.1.3 In-band flux accuracy

As described in the previous section, the absolute flux calibration is established at the key wavelength in every band. The relative accuracy of the telescope model shape within each band then translates into an additional uncertainty for spectral regions distant from the key wavelength in the given band. This translates into an additional in-band uncertainty of 5%. The situation is slightly worse beyond 150 μm, where the in-band relative accuracy is not better than 10%.

Fig. 8.8 gives the example of Pallas. In the top panels, all Pallas SED measurements are compared with their model, showing a residual scatter of repeatability and model uncertainty of about 10%. The bottom panel, on the left, displays more specifically the remaining in-band scatter after normalisation of all observations at the key wavelengths in every band, hence eliminating the sources of error just mentioned.

8.2.4.1.4 Line flux repeatability

The line flux repeatability was checked by a series of repeated observations of HIP 21479. The observations were single pointings, but one 5×5 raster was included on OD 1113, with a step of 2.5″ in both directions. All observations targeted the same water line, at 66.43 μm. The overall resulting line flux reproducibility had a standard deviation of 4% when integrating over the central nine spaxels.

8.2.4.2 Calibration block

Tables 8.7 and 8.8 gather the same information for the calibration via the calibration block as Tables 8.5 and 8.6 for the calibration via the telescope background.

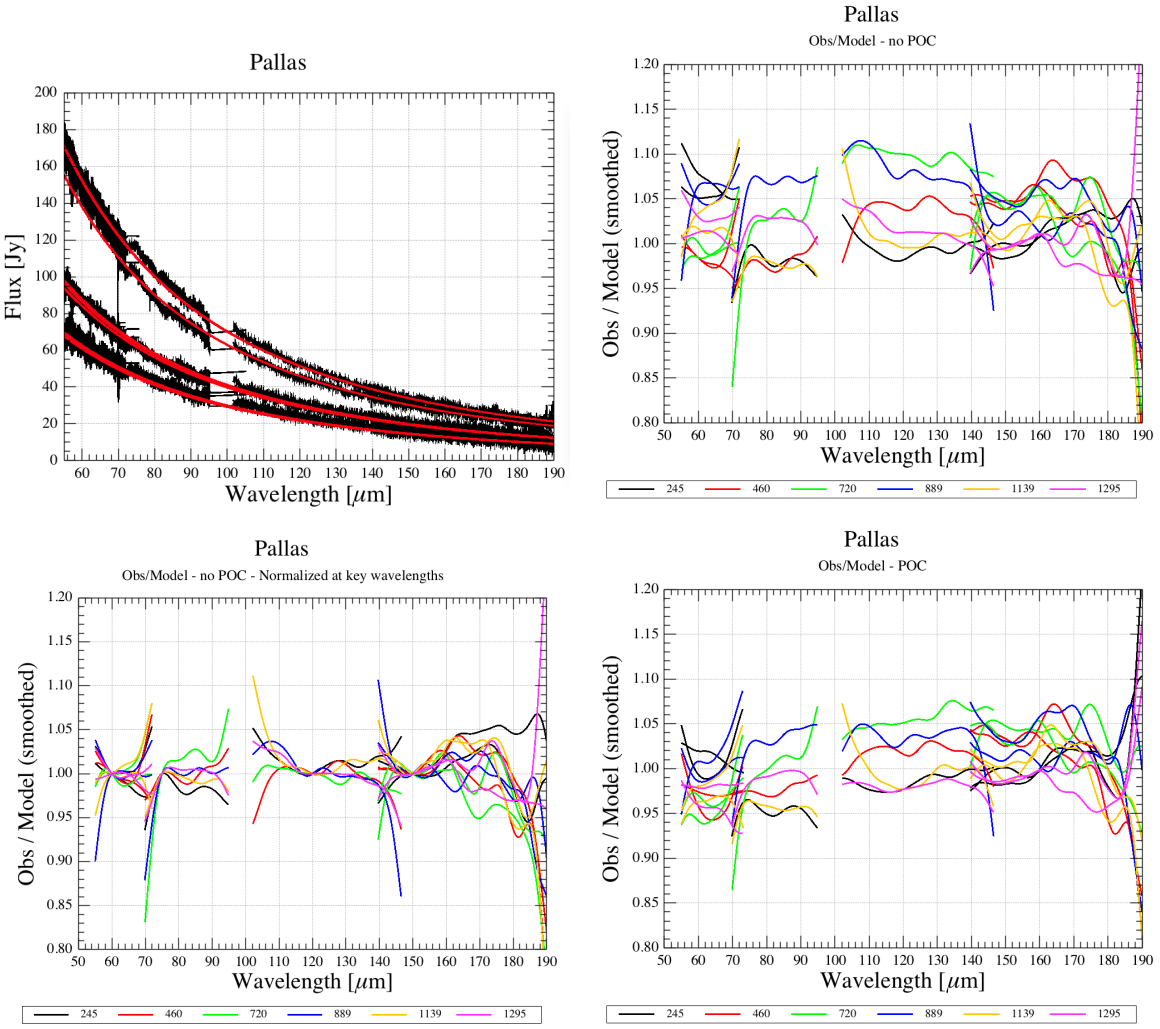

Figure 8.8: In band relative accuracy. **Top left:** the six full SED measurements obtained for Pallas are displayed in black. The Pallas models adapted to each of the observing dates are overplotted in red. **Top right:** the ratio of each observation divided by its model, for the same observations. Each visit is displayed in a different colour. The legend displays the operational days of all visits. The spectra have been smoothed with a Gaussian kernel for the sake of readability, resulting in some artifacts at the band-edges. The $\sim$10% scatter results from the intrinsic repeatability of the measurements as well as from the model uncertainty. **Bottom left:** here the spectra were normalised at the wavelengths in every spectral band, leaving only the in-band inaccuracy. **Bottom right:** same as in the top-left, except that this time the Pointing Offset Correction pipeline script was used. The flux calibration is consistent. Although marginal, a slight improvement of the spectral shape compared to that of the standard data reduction can be seen.

Calibration in flux via the calibration blocks is mandatory for the unchopped observations, where the telescope background is not visited during the observation.

Unchopped observation were mainly designed to observe spectral lines in regions of extended or confused background where no proper background could be found within the normal range accessible in

the standard chopping-nodding scheme (3 arcmin). In these observations, the background is sampled after the on-source observation, within the same obsid in line-scan mode, or in a separate obsid in range- and SED-mode (see Sec. 3.3.1).

The continuum flux derived for the source then results from the subtraction the telescope+source on the on-source position and the telescope alone on the off-source. These are usually large quantities relative to the source's continuum, and any drift in detector response – more likely to happen given the longer timescale between the on- and off-source measurements – impacts the result, as outlined in eqn 8.17.

Since spectral lines are (ideally) not present off-source, they are only marginally affected by the response drifts. However, the continuum level cannot be guaranteed to better than ~ 20 Jy (/spaxel) for any unchopped observation.

Given this limitation, and given that the calibration block was the flux calibration scheme applied to all observing modes for most of the mission (the telescope background normalisation became the standard for chop-nod observations only in the final years), the calibration of calibration sources was performed via chop-nod observations of the celestial calibrators. When combined with the model uncertainties, the scatter between all observations of celestial calibrators leads to a systematic uncertainty of $\sim 2\%$, which is the same as with the telescope background normalisation scheme.

The measurements of HD 161796 demonstrated a repeatability of 4%, following a non-gaussian distribution (mostly linked to pointing offsets), leading to the conservative recommendation to quote the peak-to-peak deviation in the distribution instead of its standard deviation, i.e. 20%.

When the instrument response is established via the calibration block, it is measured at the start of the observation, and not tracked during the observation as is done with telescope background normalisation method, i.e. any response drifts occurring during the observation are not accounted for with the same accuracy. Although the observing strategy (based on symmetric wavelength scans[3]) was aimed at reducing the effect of such drifts on the final spectrum, the relative in-band accuracy in this calibration scheme is limited to 10%.

Table 8.7: Flux calibration error budget. Calibration via the internal calibration sources and the RSRF. All celestial absolute flux calibrators.

Band	Std. Dev.	Min	Max	Peak-to-Peak
B3A 60	**0.07**	0.76	1.22	0.46
B2A 60	**0.07**	0.77	1.15	0.39
B2B 75	**0.08**	0.77	1.18	0.41
R1 120	**0.08**	0.81	1.27	0.45
R1 150	**0.07**	0.79	1.19	0.39
R1 180	**0.14**	0.15	1.66	1.51

8.2.5 Straylight and the dark current

The dark current was discussed in Sec. refChp:speccal:rsrf. Full SED scans were taken of the calibration sources with the telescope cryo-cover closed (during the commissioning phase), and so with no external light source. The resulting data showed the shape of the RSRF, indicating that a low level

[3]Symmetric grating scans: up followed by down the grating range.

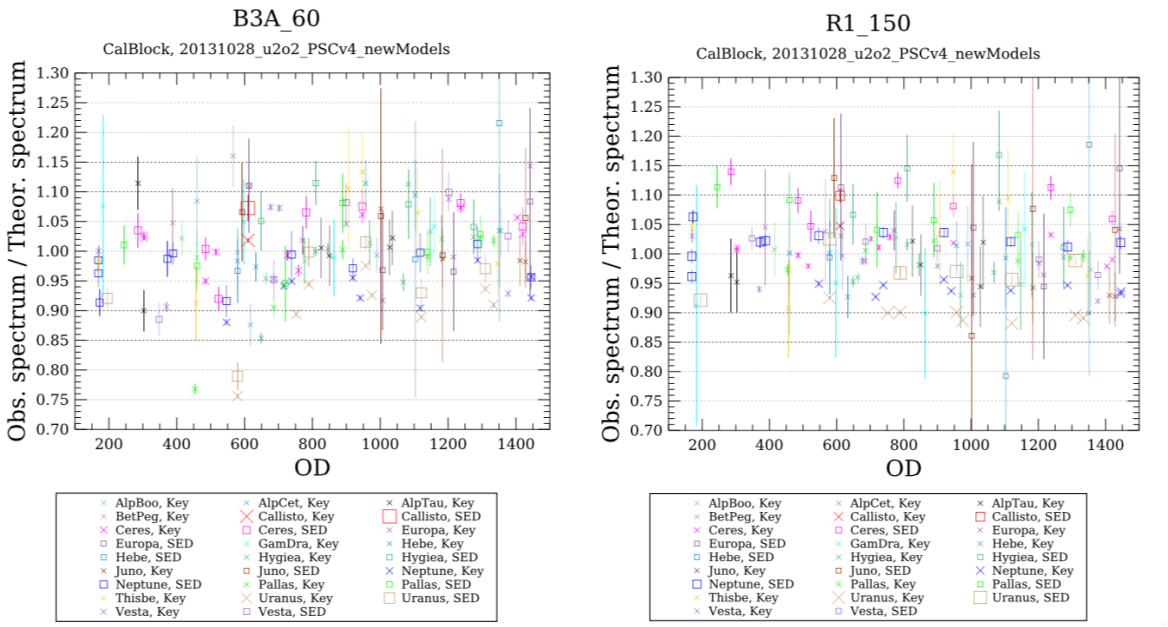

Figure 8.9: Complete set of celestial calibrators observations reduced with the calibration blocks, at the prime key wavelengths in bands B3A (60 μm) and R1 (150 μm).

Table 8.8: Flux calibration error budget. Calibration via the internal calibration sources and the RSRF. Repeatability source HD 161796.

Band	Std. Dev.	Min	Max	Peak-to-Peak
B3A 60	**0.03**	0.87	1.02	**0.15**
B2A 60	**0.04**	0.80	1.04	**0.24**
B2B 75	**0.03**	0.78	0.96	**0.17**
R1 120	**0.04**	0.80	1.01	**0.21**
R1 150	**0.02**	0.96	1.05	**0.09**
R1 180	**0.04**	0.90	1.14	**0.24**

of straylight was nonetheless present. An additional study, again looking at the calibration sources but while also pointing at a dark field, can be found in HELL L3, and here the presence of a low level of straylight is also detected. This straylight was found to have a a different level in the red and blue and between the two calibration source chopper positions. Bear in mind that the chopper positions that point to the calibration sources are not the chopper positions that astronomical observations were performed at, and there is no data that can measure any straylight at these astronomical chopper positions.

The dark current + detected straylight levels are very low compared to the flux levels from the telescope itself. For chop-nod observation, the subtraction that these data are processed through in the pipeline removes the dark current and could also remove much of any straylight present. For unchopped observations the dark current as measured pre-flight was subtracted from the signal, while any straylight equally present in the on-source and off-source positions would also have been removed when the data from these two positions were subtracted. However, for reasons discussed in the report,

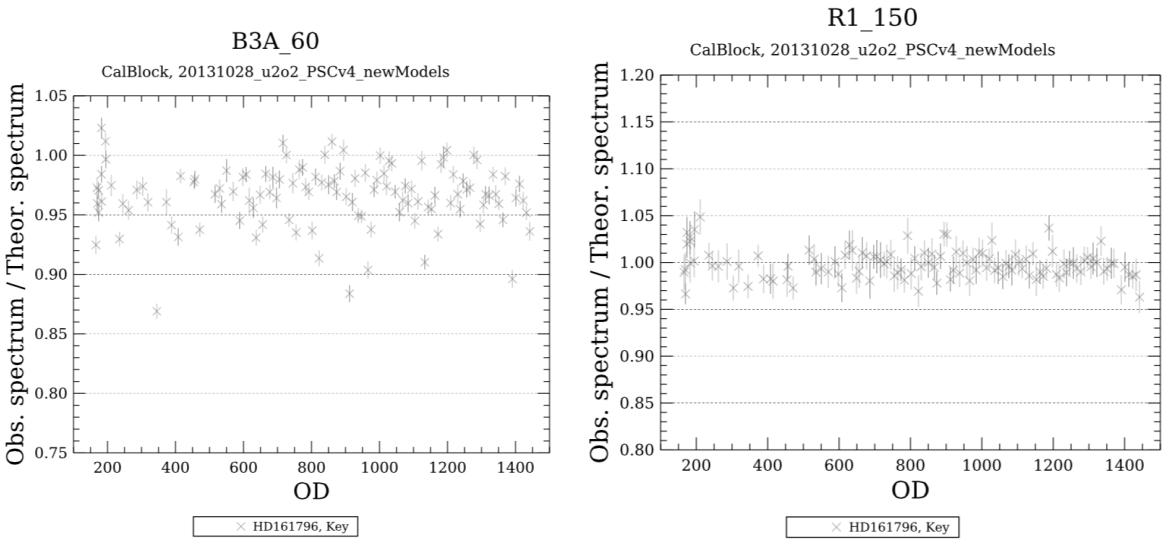

Figure 8.10: Complete set of observations of HD 161796 reduced with the calibration blocks, at the prime key wavelengths in bands B3A (60 μm) and R1 (150 μm), illustrating the repeatability of the measurements.

this straylight could nonetheless have a slight effect on the flux calibration of astronomical observations (mainly of faint sources and more so in the red band than the blue bands). Eventually, it was decided that the effect was too small to warrant further investigation.

8.2.6 Saturation

The behaviour of the signal obtained from the detectors when exposed to very high fluxes was studied in ground-based tests during FMILT (these can be found in HELL L3 "Pre-Flight testing→Laboratory testing (detectors)"; most relevant here is PICC-MA-TR-043). Two calibration files containing saturation limits resulted from these studies: `RampSatLimits`, in units of digits and to be applied to raw ramp readouts; and `SignalSatLimits`, in units of digits/s scaled to a 1-second ramp reset, and to be applied to fit-ramps readouts. Both include data for all four of the capacitance levels that could be used in-flight, and for the red and blue detector arrays separately.

To remind the reader: the PACS spectroscopy detectors were read-out non-destructively at a frequency of 256 Hz for $\frac{1}{8}$ s before a destructive readout (a reset). Each successive readout until the reset was an integration, and the shape of these "ramps" was therefore a slope; note that the PACS "ramps" have a negative slope. This slope was fitted on-board to produce a signal of units digits/s (Sec. 2.6.2.3), and this was the signal that was downlinked from *Herschel*. Some examples are given in Fig. 8.11. The effect of saturation on the raw data – the ramps – is demonstrated in these figures: the slope flattens, and some even show a turn-over. The ramps were fit on-board and it was their slope that was downlinked: as the signal increases the slope does also, however once a turn-over occurred the fitted slope was flattened. The effect of saturation for these turn-over ramps was therefore to decrease the downlinked signal: in the final data, very bright spectral lines with saturated peaks can therefore manifest with a peak that is actually too low in flux (once the saturation point has been reached), rather than a peak with a flat or increasing top (e.g. as is found for optical detectors).

The pipeline task *specFlagSaturationFrames* checked the fitted ramps data and compared the V/s readouts to the limits in the calibration file `SignalSatLimits`, flagging those detected as saturated in the mask SATURATION. This task also checked for saturation in the raw ramps data, which were also downlinked from *Herschel*. It was not possible to downlink the raw ramps for all 16×25 spectral pixels of each detector array, however it was possible to do so for one spectral pixel from each – [5,12] for the red and [10,12] for the blue, these being the most responsive spectral pixels from the central module (it was also assumed that the science source was most likely to be located in the centre of the FoV). From these data it is possible to have a more direct measure of saturation in any observation – in principle these ramps could be checked directly (by the astronomer). *SpecFlagSaturationFrames* checked the data from these pixels, and readouts that exceeded the limits in the calibration file `RawSatLimits` were flagged as saturated in the mask RAWSATURATION. See Sec. 9.2.1.1 for details of how these two masks were used in the pipeline. Note that any signal flagged as saturated was not passed on to the final cubes – saturation manifests as gaps in the spectra.

The saturation limits determined from the laboratory tests were checked – and confirmed as good – during CoP (Royer et al. 2009) and PV phase programmes (PICC-KL-TR-028). It was also confirmed that saturation in the blue detector is rare. Some plots are included in the PV phase report, showing that the effect of saturation on the ramps was as found previously.

Non-linearity in the detector response was found not to be a problem at the ramp level. Non-linearity in the sense of the detector response being affected by light ("self-curing") and cosmic irradiation ("glitches") is discussed in the following sections.

8.2.7 Glitches

The PACS spectroscopy detectors were sensitive to ionising radiation as well as to light. Both could cause a change to the response of the detectors, which in turn would cause a change to the output signal. The effect of light on the detectors is discussed in Sec. 8.2.8, here we concentrate on cosmic impacts on the detectors – aka. glitches.

Glitches induced a discontinuity in the detector response. It was expected – and found – that this caused a response increase (although – unexpectedly – glitches resulting in a response decrease were also found: PICC-KL-TN-022).

Since the output of the detectors are *integration* ramps, a jump in one non-destructive readout affects all the successive readouts, and the subsequent signal train is shifted (has a larger negative value). The effect of this on the downlinked signal can be seen in the examples in Fig. 8.11. In these fitted ramps this manifests as sudden jumps in the signal which may be followed by a signal drift for the immediately successive readouts. As a result, the wavelengths sampled *after* a glitch may also be affected by that glitch. This was more of a problem for the red detector array than the blue, as can be seen Fig. 8.11 (the glitches do not break the general trend of the signal from the blue detector, but for the red detector a step-like effect can be seen in the signal).

The spectroscopy detectors were tested under proton irradiation at the cyclotron of Louvain-la-Neuve in Belgium (UCL) in a series of tests carried out between 2004 and 2006. The test reports can be found on HELL L3 ("Pre-Flight testing→Laboratory testing (detectors)"). These laboratory tests were to establish the optimal settings of the detector to be used in flight, to look at the ways to "cure" the detector (cf. Sec. 8.2.8), to look at how to fit the detector readout ramps, and to study the effect of glitches on the ramps: changes to the shape, the slope, and to the subsequent ramps were studied.

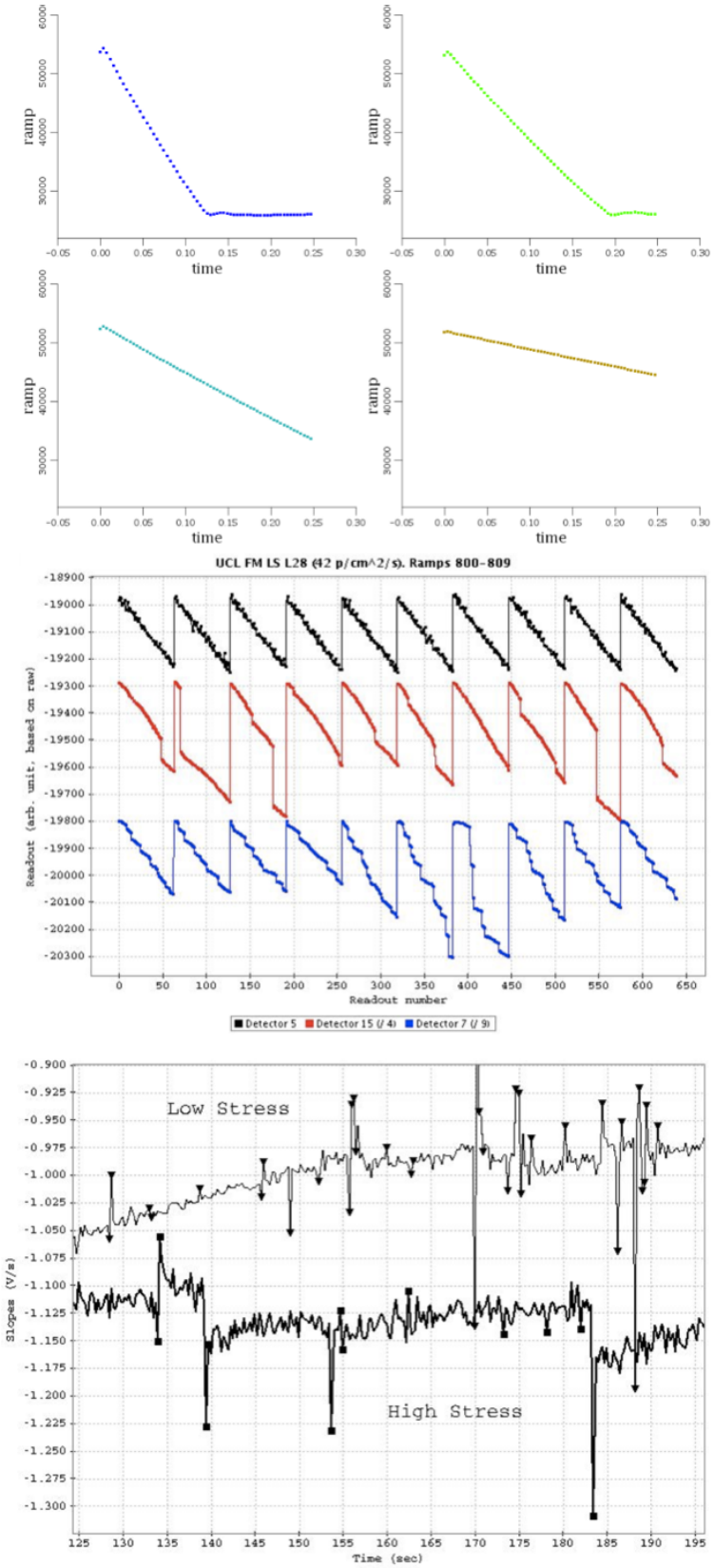

Figure 8.11: Some examples of the shape of the raw ramps from the PACS spectroscopy detector. Note that signal increases downwards. **Top**: raw ramps showing saturation (taken from PICC-MA-TR-043). **Centre** raw ramps showing glitches (taken from Royer et al. 2009). **Bottom**: fitted ramps for the red (high stress) and blue 9 (low stress) detectors, showing glitches (taken from Royer et al. 2009).

The rate of detected glitches was found to be proportional to the detector's response, and inversely proportional to the ramp-length.

A few glitch-detection routines were tested to establish the most reliable method to detect and to flag out (but not to correct) glitches in the fitted ramps. The best (a Q-test: e.g. PICC-KL-TN-022) was later adopted for the pipeline processing. Data taken during CoP gave a first look at glitches arising from the in-flight environment (see Royer et al. 2009); the effect on the ramps was similar to that studied in the laboratory and the same Q-test could be used to flag out glitches efficiently in the fitted slope signal. It was found that where a glitch produced a long response-change "tail", the Q-test would sometimes flag the glitch itself and the two or three subsequent ramps.

8.2.8 Self-curing

The detectors of the PACS spectrometer were Ge:Ga extrinsic photoconductors. This type of detector is extremely sensitive to both cosmic and (luckily) FIR radiation. Cosmic ray impacts on the detectors increased their response: for a given bias level, the response of the detectors would typically increase by a factor 4 to 5 in flight with respect to laboratory conditions (the bias levels used in flight were much lower than they were on the ground, to avoid the risk of spiking).

In contrast to this, FIR light – or more precisely the number of charges flowing through the detectors (expressed in V/s, for the slope of the resulting integration ramp) – induced a reduction of the detectors' response. We called this effect 'self-curing'.

Despite the fact that specific hardware (heaters and flashers) was integrated to cure the detectors to counteract this self-curing, no specific operation was ever performed to cure the spectrometer detectors: it was shown, both before flight and confirmed in-flight, that the specifications for noise and sensitivity of the instrument could be met with proper tuning of the operational parameters (especially bias level, length of the integration ramp, and the particular chopping scheme), and that the operational concept would be made more efficient without curing.

Consequently, the response of the detectors in flight resulted from a constant equilibrium between the level of radiation and the signal level. The signal from a detector is the product of the FIR flux with the absolute spectral response function of the instrument at the wavelength being observed. In normal conditions, the sky-induced signal is small compared to that of the telescope background, so that this equilibrium, hence the average response of the instrument over the observation, is not strongly impacted by self-curing.

When using the telescope background normalisation calibration method – which is the standard for chop-nod observations – the response of the instrument is established at every grating position, hence response drifts – including self-curing – do not impact the final spectrum. However, this is not the case in unchopped mode, where the response cannot be traced after the initial calibration block (which is the only source of absolute calibration for the observation). In this case there are two situations where the self-curing can have a significant impact on the spectrum, in terms of absolute flux calibration and spectral slope (in each band separately):

Very high continuum flux When the flux of the source is significantly higher than that of the telescope, the equilibrium described above is progressively modified, leading to a reduction of the instrument response. In extreme cases (> 1000 Jy), this can lead to real issues with respect to the absolute flux calibration.

Between 100 and 140 μm This is where the instrument response is the highest. For line-scan observations and single-scan SEDs or ranges, the observation is sufficiently fast that the effect of self-curing remains small. However, for SEDs with multiple scan repetition, self-curing induces a drop of the response between the first scan and the following ones. The main effects are **a.** an erroneous slope of the continuum, from 100 towards 140 μm and **b.** a clear mismatch between the continuum at the red-edge of the observation and the blue-edge of its SED-B2B complement (i.e. around 145 μm).

The pipeline task used for spectral flatfielding of spectral ranges (*specFlatFieldRange*) accepts a parameter "referenceScan" which is "all" by default, but can be set to "first" or "last" to experiment on self-curing, with the drawback that 'first' will improve upon the absolute flux calibration (better around 100 μm than around 145 μm in this case), while maximising the effect on the spectral slope, while 'last' will improve upon the spectral slope, but corresponds to the worst-case scenario with respect to flux calibration. The default value was that adopted for the SPG processing of these data.

8.3 Spatial calibration

8.3.1 Focal-plane geometry

The reference documents for this section are PICC-ME-TN-027 and PICC-ME-TN-019.

In this section we explains the derivation of the the spatial calibration for every spaxel of the PACS spectrometer and the procedures used to apply it to science observations.

The PACS IFU FoV is a slightly irregular 5×5 grid of spaxels of $9.4'' \times 9.4''$ projected angular size, not perfectly contiguous. The spaxels correspond to detector columns in the detector array, also known as modules with numbers from 0 to 24, with the row containing modules 5 to 9 is displaced to the right (see Fig. 8.12).

Sky coordinates are assigned to every PACS spectrometer spaxel by the data processing pipeline. This is performed in two steps:

- Addition of spacecraft coordinates (R.A., Dec, roll) to every frame[4], containing the attitude of a reference position in the PACS spectrometer focal plane (this virtual aperture is defined as the central spaxel for the blue band at the central chopper position). This attitude is calculated from the spacecraft boresight attitude in the Attitude History product, rotated with the SIAM (Spacecraft-Instrument Alignment Matrix). This step is performed by the pipeline task *addInstantPointing*

- Calculation of the offset of every spaxel with respect to the reference position assigning the correspondent R.A., Dec information. This is done via the pipeline task *specAssignRaDec*.

The coordinate systems that are used in the spatial calibration of the PACS spectrometer spaxels are:

[4] A Frame is the terminology used for the data product at the early stages of the pipeline. Inside these Frames are datasets (signal, coordinate, etc). A single "frame" is the entire dataset of the Frame for the entire detector array (16×25) for a single readout.

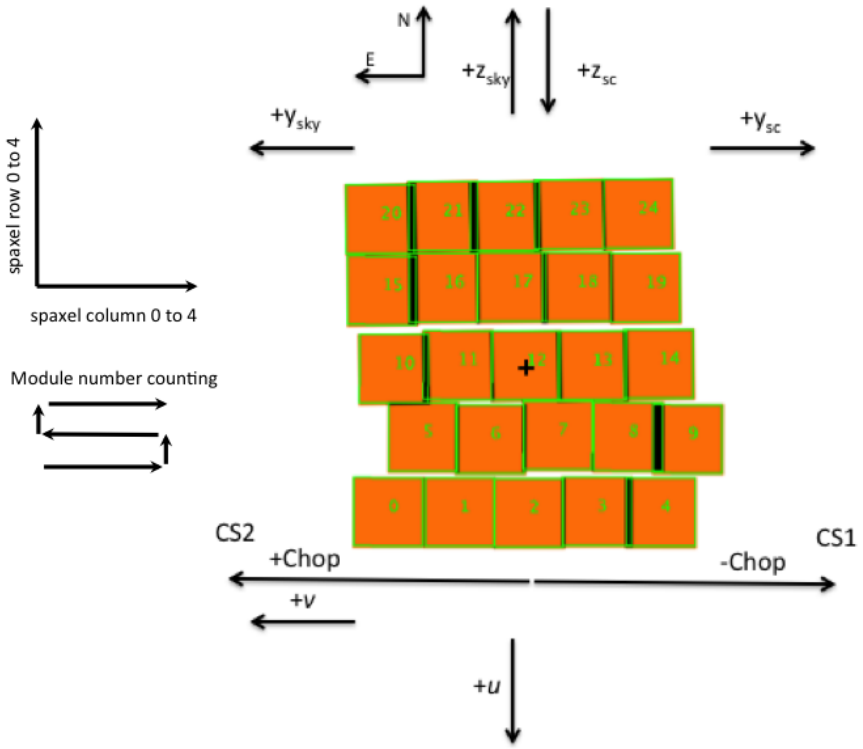

Figure 8.12: PACS IFU footprint with various coordinates indicated. The cross indicates the position of the virtual aperture, while the numbers in the spaxels indicate the module numbers.

***u,v* Array Coordinates** angular coordinate system measured in arcseconds, with the *v* axis roughly aligned with the chopping direction. This coordinate system is based on the alignment of the laboratory XY stage[5], used for the initial measurements of the spatial calibration. The zero point of this coordinate system is placed at the center of each array (blue/red), defined by the centre of gravity of all spectral pixels of the array. The signs are chosen such that a fixed source will apparently move in the positive *v* direction over the array when the chopper is commanded to more positive chopper position readback (CPR) values. This is a left-handed reference frame.

y,z Instrument Coordinates An orthogonal local coordinate system on the tangential plane of the sky. The two axes are aligned with the spacecraft Y and Z axes as projected onto the sky, with the zero point at the centre of the blue photoconductor array and chopper angle $\alpha = 0$.

y_{sc}, z_{sc} Spacecraft coordinates are coordinates in the *Herschel* focal plane, as measured by the spacecraft xyz coordinate system (right-handed orthogonal system with x along the *Herschel* optical axis, towards the *Herschel* target source/boresight, z pointing at the sun, and y completing the right-handed orthogonal system).

[5] which is a bench

y_{sky}, z_{sky} Sky coordinates describe the J2000 ICRS right ascension and declination of the position of the source on the sky relative to the projected yz directions of the spacecraft xyz coordinate system. If the telescope position angle is 0, positive z_{sky} points north.

Fig. 8.12 illustrates the orientation of the different coordinate systems with respect to the telescope's focal plane (i.e. the IFU).

The calculation of the offset for every spaxel with respect to the reference position requires two transformations, which are discussed next.

8.3.1.0.1 Module to array coordinates

The *u,v* array coordinates for every spaxel are contained in the calibration file `ModuleArray`. This was derived from laboratory measurements by moving a point source along the XY stage so it went over all spaxels, and fitting the measured xy positions. This calibration table has uv coordinates in arcseconds for the 25 modules/spaxels for the different standard chopping angles (small, medium and large) for each band. This information is tabulated in the following datasets:

- Tables *ubluesmall*, *vbluesmall*, *uredsmall*, *vredsmall* are used for the centre chopper position (unchopped measurements) and the chop/nod measurements with small chopping angle.
- Tables *ubluemedium*, *vbluemedium*, *uredmedium*, *vredmedium* are used for chop/nod measurements with medium chopping angle.
- Tables *ubluelarge*, *vbluelarge*, *uredlarge*, *vredlarge* are used for chop/nod measurements with large chopping angle.

8.3.1.0.2 Array to instrument coordinates

The array to instrument coordinate conversion, with origin at the spectrometer's reference position, is contained in the calibration file `ArrayInstrument`. The chopper describes a curved trajectory on the sky at different chopper positions and different distortions affect the spectrometer FoV. The *u,v* to *yz* conversion is described as a polynomial function of *u,v* and chopper angle α:

$$y = \sum_{i=0}^{N}\sum_{j=0}^{M}\sum_{k=0}^{O} a_{ijk} u^i v^j \alpha^k \tag{8.54}$$

$$z = \sum_{i=0}^{N}\sum_{j=0}^{M}\sum_{k=0}^{O} b_{ijk} u^i v^j \alpha^k \tag{8.55}$$

The calibration data-set was constructed using oversampled raster maps of Neptune, observed at the different chopper positions (0,$\pm small$=$\pm 0.5'$, $\pm medium$=$\pm 1.5'$, $\pm large$=$\pm 3'$). A list of the observations used to construct the file is given in Table 8.9.

The beam efficiencies constructed from these raster maps (see Sec. 8.3.2) were fitted with a 2D Gaussian. The peak positions of the fitted Gaussians were in turn fitted with the polynomial function for each pair of chopping angles ($\pm$), and the centred chopper position. For the centred and small chopping angle throw, the fitted polynomials are of order 2, while for medium and large chopper angles

Table 8.9: Neptune raster observations used to derive the spectrometer's spatial calibration

OBSID	OD Number	Raster positions	Chopper position
1342186678	174	40x40	0
1342186686	175	25x25	+large
1342186687	175	25x25	+medium
1342186688	175	25x25	+small
1342186689	175	25x25	-small
1342186690	175	25x25	-medium
1342186691	175	25x25	-large

the order is 3. The calibration file `ArrayInstrument` contains the polynomial orders N,M,O and the coefficients a_{ijk}, b_{ijk}, for the different standard chopping angles and per band. The positions of the spaxels are shown in Fig. 8.13.

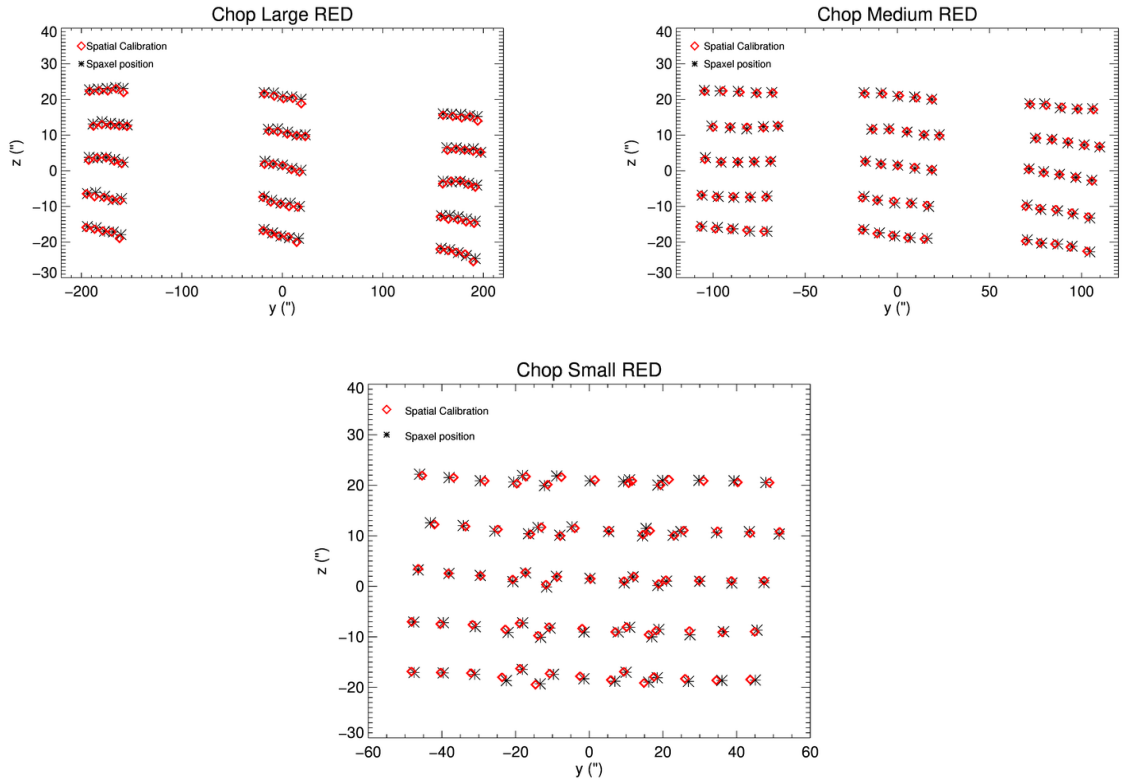

Figure 8.13: Positions in spacecraft coordinates for each spaxel beam centre and polynomial fit results at the three chopper angle positions for the three standard chopping throws (large: 6′, medium: 3′and small: 1′). (The 5×5 of the IFU is in each of the three "columns" on the plots.)

8.3.2 Beam profiles

The PACS spectrometer beam efficiencies are maps of the response of each detector on the sky. They describe the (relative) coupling of a point source to each spaxel as a function of its (the source) position

in the field-of-view.

To characterise the PACS spectrometer beams, Neptune raster maps at a set of wavelengths (55, 62, 68, 73, 75, 84, 94, 110, 125, 136, 145, 150, 168, and 187 μm) were observed during the *Herschel* mission. These Neptune raster maps were obtained in two configurations:

- Coarse 25×25 (40×40 at 62 μm) raster maps with step size 2.5$''$ covering the FOV of all 25 spaxels
- Fine 5×5 raster maps with raster step size 2$''$ covering the central spaxel.

The combination of four such fine rasters at a given wavelength, offset from each other by 1$''$, provided a very high sampling for computing the central spaxel beam efficiency only.

A summary of these observations is provided in Table 8.10

All raster maps were observed with only one chop-off position (i.e. these were asymmetric chopNod observations, which is further described in Sec. 8.3.2.1). The data were processed using the telescope background normalisation scheme to obtain the telescope-normalised signal per spaxel.

The different spatially-sampled measurements were aligned in shape using least-squares minimisation in coordinates and gain. A synthetic beam was constructed with the coarse raster outside the area covered by fine raster, and from the Gaussian fit to the matched-fine raster inside that area. An example is shown in Fig. 8.14. Finally, these synthetic beams were interpolated into a regular 0.5$''$grid.

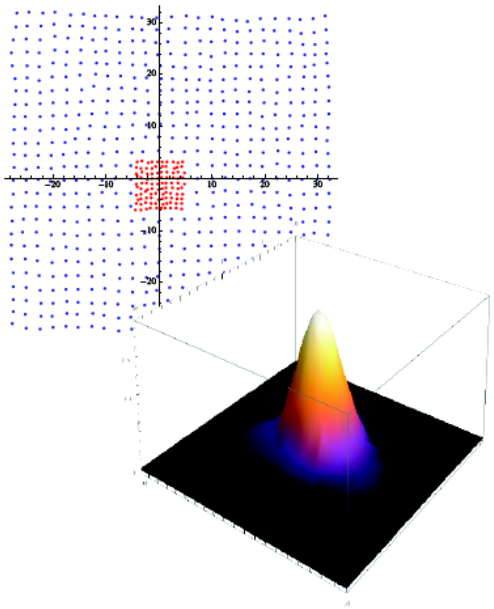

Figure 8.14: **Top**: coarse and fine raster positions over a 60$''$ FOV. **Bottom**: Gaussian fit to the fine raster datapoints.

Table 8.10: Neptune raster observations used to derive the PACS Spectrometer beam efficiencies

OBSID	OD Number	Raster positions	$\lambda_{\rm blue}$/band (μm)	$\lambda_{\rm red}$ (μm)	Grid	XYOffset ($''$)
1342222162	751	25x25	55/B2A	110	Coarse	
1342257225	1311	5x5	55/B2A	110	Fine	(0,0)
1342257226	1311	5x5	55/B2A	110	Fine	(0,1)
1342257227	1311	5x5	55/B2A	110	Fine	(1,0)
1342257228	1311	5x5	55/B2A	110	Fine	(1,1)
1342186678	174	40x40	62/B2A	125	Coarse	
1342257229	1311	5x5	62/B2A	125	Fine	(0,0)
1342257230	1311	5x5	62/B2A	125	Fine	(0,1)
1342257231	1311	5x5	62/B2A	125	Fine	(1,0)
1342257232	1311	5x5	62/B2A	125	Fine	(1,1)
1342219846	717	25x25	68/B2A	136	Coarse	
1342257233	1311	5x5	68/B2A	136	Fine	(0,0)
1342257234	1311	5x5	68/B2A	136	Fine	(0,1)
1342257235	1311	5x5	68/B2A	136	Fine	(1,0)
1342257236	1311	5x5	68/B2A	136	Fine	(1,1)
1342219847	717	25x25	68/B3A	204*	Coarse	
1342257237	1311	5x5	68/B3A	204*	Fine	(0,0)
1342257238	1311	5x5	68/B3A	204*	Fine	(0,1)
1342257239	1311	5x5	68/B3A	204*	Fine	(1,0)
1342257240	1311	5x5	68/B3A	204*	Fine	(1,1)
1342219848	717	25x25	73/B2B	145	Coarse	
1342257257	1312	5x5	73/B2B	145	Fine	(0,0)
1342257258	1312	5x5	73/B2B	145	Fine	(0,1)
1342257259	1312	5x5	73/B2B	145	Fine	(1,0)
1342257260	1312	5x5	73/B2B	145	Fine	(1,1)
1342208866	574	25x25	75/B2B	150	Coarse	
1342257261	1312	5x5	75/B2B	150	Fine	(0,0)
1342257262	1312	5x5	75/B2B	150	Fine	(0,1)
1342257263	1312	5x5	75/B2B	150	Fine	(1,0)
1342257264	1312	5x5	75/B2B	150	Fine	(1,1)
1342219849	717	25x25	84/B2B	168	Coarse	
1342257265	1312	5x5	84/B2B	168	Fine	(0,0)
1342257266	1312	5x5	84/B2B	168	Fine	(0,1)
1342257267	1312	5x5	84/B2B	168	Fine	(1,0)
1342257268	1312	5x5	84/B2B	168	Fine	(1,1)
1342219850	717	25x25	94/B2B	187	Coarse	
1342257269	1312	5x5	94/B2B	187	Fine	(0,0)
1342257270	1312	5x5	94/B2B	187	Fine	(0,1)
1342257271	1312	5x5	94/B2B	187	Fine	(1,0)
1342257272	1312	5x5	94/B2B	187	Fine	(1,1)

* Beams not provided, as the wavelength falls in the R1 order-leak spectral region.

The beam efficiencies were normalised so that a point source of flux 1 at the centre of spaxel 12 has an integral of the (idealised) instrument response equal to 1 (see eqn 8.69 in Sec. 8.3.4). In other words, the beam profile was normalised to the total flux of the source.

The beams coordinate reference system *y,z* is defined with respect to the centre of the beam in the central spaxel (Fig. 8.12). The WCS associated with the beams is in sky coordinates for position angle 0 and the pixel angular size is 0.5″.

The final maps are a reconstruction of what each spaxel "sees" as the planet was rastered across its aperture on the sky (specifically across that of the spectral pixels of the module). Since *y,z* describe a position of a source in our focal plane, fixing y and z and looking at the beams of all spaxels at that position, is the equivalent of a discrete measurement of a point source as seen by the full array, i.e. the instrument response.

The PACS spectrometer beams are provided in the calibration files `BeamsPerSpaxelXXX`. There is one such calibration file for each `XXX` band, i.e. four in total (B3A, B2A, B2B and R1).

8.3.2.1 Telescope background normalisation for asymmetric chopNod

A particular flavour of the telescope background normalisation method was created to calibrate the Neptune raster maps, which were observed in the asymmetric chopping mode. In this non-standard observing mode, the source was placed at the chopper central position, while the reference position was visited by commanding the chopper off to only one side. This is different from the normal chopNod procedure where we have a symmetric chopping pattern to sample the different regions of the mirror used. As a consequence, the telescope offset (between T_A and T_B) is not removed. However, since while the raster is taken the source illuminates each detector for only a small fraction of the time, one can estimate the pure telescope emission in both chopper positions, on each detector.

The assumption of this method is that the telescope flux does not vary with time over the duration of the observation (which is a fair assumption given the very slow evolution of the telescope temperature), so that any observed variations can be attributed to drifts in the detector's response. The latter can then be cancelled by the principle of the method.

The normalised signal is defined as follows,

$$norm = \frac{A - B}{A + B} \tag{8.56}$$

where A and B are the signals detected in the two chopper positions at any give time. We assume that the source, when detected, is detected in the A position. Taking T_A and T_B as the telescope fluxes at positions A and B, and s the source's signal, we can rewrite $norm$ as:

$$norm = \frac{(T_A + s) \times g - T_B \times g}{(T_A + s + T_B) \times g} \tag{8.57}$$

$$= \frac{(T_A + s)/T_B - 1}{(T_A + s)/T_B + 1} \tag{8.58}$$

$$= \frac{f + f \times s/T_A - 1}{f + f \times s/T_A + 1} \tag{8.59}$$

where f is the ratio of the two pure telescope fluxes in positions A and B:

$$f = \frac{T_A}{T_B} = \frac{A}{B} \tag{8.60}$$

In this expression A and B are the signals when no source is detected. This ratio is stable over time for all modules (spaxels) and all their spectral pixels (provided the source is not visible). Analogously to the standard telescope background normalisation method, the aim is to express the source signal s as a function of telescope background (T_A, according to the assumption that the source always falls in position A):

$$x = \frac{s}{T_A} \tag{8.61}$$

With this definition we can rewrite the normalised signal as:

$$norm = \frac{f + f \times x - 1}{f + f \times x + 1} \tag{8.62}$$

and solve for x

$$x = \frac{f - 1 - norm \times (f + 1)}{f \times (norm - 1)} \tag{8.63}$$

This spectro-photometric calibration scheme is also used in the Pointing Offset Correction pipeline (see Sec. 9.2.2.3) and in all pipelines when using the drizzle projection algorithm to produce spectral cubes.

Documentation concerning the derivation of the PACS spectrometer beams can be found on HELL L3, and the results of these investigations (i.e. the beam maps) can be found on HELL L2.

8.3.3 Point source corrections

As outlined in Sec. 8.2.2.1, the basic principle of the flux calibration is to link observations of science targets to observations of point sources with known flux density [Jy] via a standard candle, this being either the "telescope" or the internal calibration sources.

Therefore, the link between the detector signal created by the flux density of a point source [Jy] or by the surface brightness [Jy/spaxel, MJy/sr, ...] of an extended source, and the signal created by the telescope background, needs to be established for each spaxel.

We express our measurements in units of [telescope], i.e. in terms of detector signal ratios:

$$x_{\text{source}} = signal(\text{source})/signal(\text{telescope}) \tag{8.64}$$

The PACS telescope calibration is based on a set of point sources measurements (see Sec. 8.2.4). For the sake of simplicity, here we consider the use of a single celestial standard, e.g. Ceres.

In the calibration process, we attribute a flux density [Jy] to the telescope signal. Since most of the flux of a point source falls onto one single spaxel (normally, the central one[6]), we also make an assumption about what fraction of the total flux is detected by the central spaxel, for a point source centred on it. We call this fraction the Point Source Correction Factor (*PSCF*).

$$x_{\text{Ceres}} = PSCF \times F_{\text{Ceres}}/F_{\text{telescope}} \tag{8.65}$$

$$F_{\text{telescope}} = PSCF \times F_{\text{Ceres}}/x_{\text{Ceres}} \tag{8.66}$$

[6]Calibration observations placed the point source in the centre of the central spaxel, and all astronomical observations aimed to do this as well.

where F_{Ceres} denotes Ceres' model, i.e. a known quantity, expressed in [Jy], and $F_{\mathrm{telescope}}$ is our telescope spectrum, also in [Jy], from now on obtained from this equation (8.66).

When measuring point sources with the central spaxel, we then get

$$F_{\mathrm{Source}} = x_{\mathrm{Source}}/PSCF \times F_{\mathrm{telescope}} \tag{8.67}$$

$$= x_{\mathrm{Source}}/x_{\mathrm{Ceres}} \times PSCF/PSCF \times F_{\mathrm{Ceres}} \tag{8.68}$$

and we see that, as long as we make sure to use the same *PSCF* when we establish our calibration as later on when using it on all sources, it cancels out. This is equivalent to choosing an integration radius to perform aperture photometry: as long as one uses the same for the photometric calibrators as for the other targets, the exact radius does not impact the photometry.

Before addressing the derivation of the PSCF, we return briefly to the notion of beams. The beams describe the relative coupling of a point source to each spaxel as a function of its (the source's) position in the FOV. Since they are also originally expressed as ratios x relative to the telescope, as seen by each spaxel, they reflect any variation in the active spaxel aperture area, as this changes the coupling ratio between a flat, extended source (such as the telescope) and a point source optimally falling into the active "window" of the spaxel.

The beams of the 25 spaxels are unitless, and we represent them on a common *y,z* reference frame, centred on the central spaxel, i.e. (0,0) is the centre of spaxel 12. They are also normalised, to ensure that the integral of the instrument response to a point source of flux 1 at the centre of spaxel 12 is 1, at all wavelengths:

$$nbeam_s(y,z) = \frac{beam_s(y,z)}{\sum_{s=0}^{\infty} beam_s(0,0)} \tag{8.69}$$

Consequently, $nbeam_s(0,0)$ represents the fraction of flux seen in spaxel s when a point source is centred on the central spaxel. The Point Source Correction Factor is then just a special case of the normalised beams:

$$PSCF = nbeam_{12}(0,0) \tag{8.70}$$

In reality we do not have an infinite FoV with an infinite number of spaxels but are limited to the existing 25 spaxels. The original derivation of the *PSCF* dealt with this issue by estimating the amount of power falling outside of our FOV from a detailed diffraction calculation of the telescope optical system, hence producing a correction c we have to apply to extrapolate from the power collected in the 5×5 spaxels to the total power:

$$nbeam_s(y,z) = \frac{beam_s(y,z)}{c \sum_{s=0}^{24} beam_s(0,0)} \tag{8.71}$$

The correction factor, referred to as the "5x5-to-total $PSCF_{5x5/tot}$" is a weak function of wavelength: typically $1/c \sim 0.95$.

When we first derived the *PSCF*, we assumed that the spaxels had a flat response over their full entrance aperture of nominally $9.4'' \times 9.4''$, and no gaps between them. However, the beam measurements later performed on Neptune showed that this is not quite correct. For instance, the sum of the source's signals x in all 25 spaxels (equivalent to the sum of the 25 beams) shows variations as a function of the source position within the spectrometer FoV. This, as well as the observed beam shape compared to the PACS photometer PSF, led to the conclusion that the actual beams are better represented by an active spaxel area of about $8'' \times 8''$, rather than the nominal $9.4'' \times 9.4''$, leaving some 'dead' space between spaxels – the spaxels are not contiguous.

Figure 8.15 displays field-of-view maps, built from actual beams, compared with those modeled for spaxels with a perfectly flat response over $8'' \times 8''$ and $9.4'' \times 9.4''$, where the FoV map $fov(y, z)$ can be expressed as:

$$fov(y, z) = \sum_{s=0}^{24} beam_s(y, z) \tag{8.72}$$

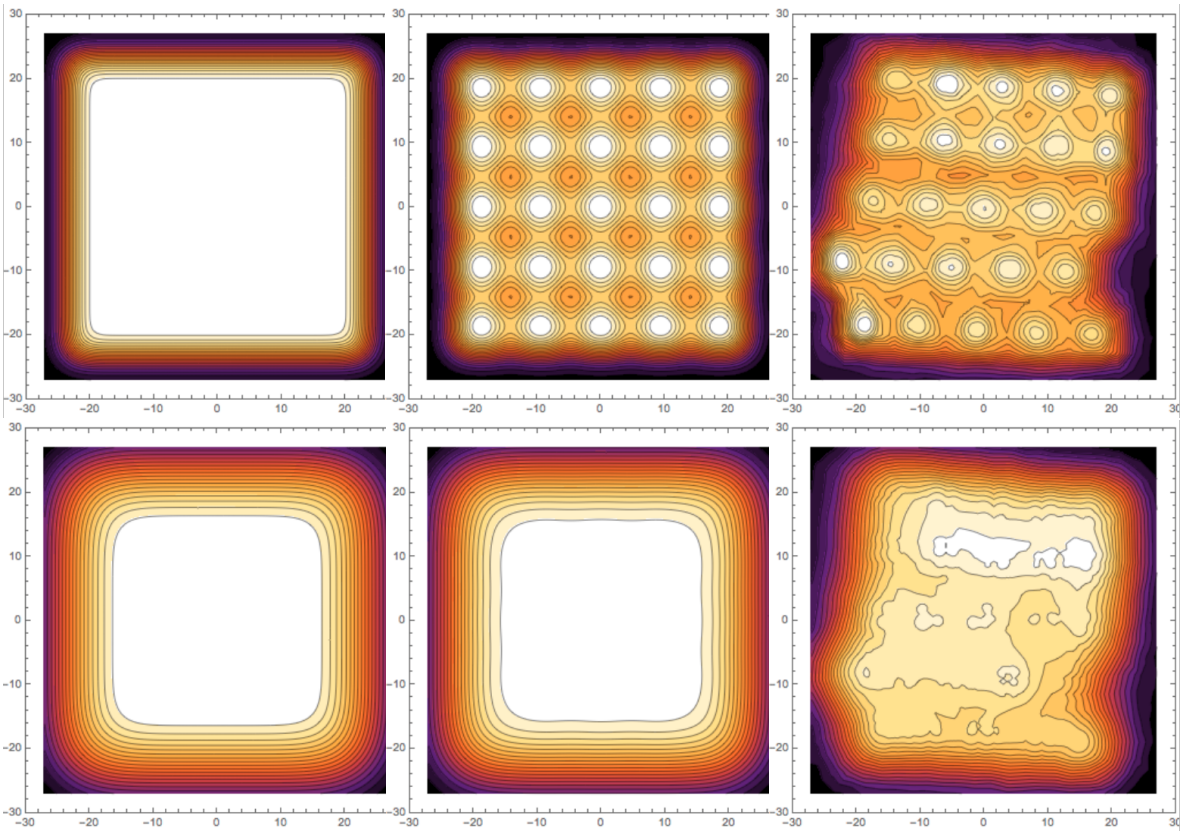

Figure 8.15: Maps of PACS spectrometer FoV at 62 μm (*top*) and 145 μm (*bottom*). **Left**: modelled with "perfect" beams, i.e. contiguous spaxels of $9.4'' \times 9.4''$ with flat response. **Centre**: ibid., this time with active surfaces of $8'' \times 8''$. **Right**: measured beams.

For a consistent normalisation of the individual beams and, implicitly, a re-derivation of the *PSCF*, we calculated the theoretical power in the 5×5 spaxels FoV and that in an infinite FoV by convolving

the telescope PSF from the diffraction model with an $8'' \times 8''$ aperture (with a $9.4''$ spacing) for the two FoVs, and compared them to each other. In this process, the diffraction model was only used to estimate the power on scales (much) larger than the beam radius. Smaller spatial characteristics came from the measured beams.

From this, we re-checked the central spaxel beam peak values against the original *PSCF* and did not find any significant deviation, within the scatter between the individual raster observations. Fig. 8.16 displays this comparison between the measured values and the calibration file.

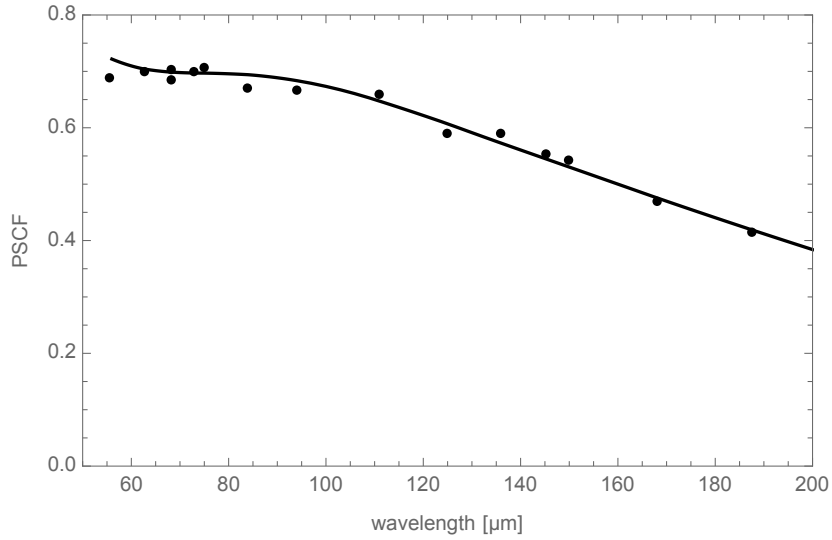

Figure 8.16: Comparison of the *PSCF* (central-to-total), as derived from the measured beams (dots) and as in the calibration file, originally derived from a diffraction model of the instrument assuming idealised detector beams.

The new normalised beams give the coupling of a point source (or δ-function in surface brightness) to each of the 25 spaxels as a function of the source position in the FoV[7]. More information can be found in HELL L2 ("Spectrometer Calibration→Beams" and also in this version control document). They thus serve as the *PSCF* for each spaxel. So, if a point source falls mostly on spaxel s, and assuming y and z are known, one could retrieve its flux density as:

$$F_{\rm source} = x_s / nbeam_s(y,z) \times F_{\rm telescope} \tag{8.73}$$

Under the same assumptions, if the source fell right between two (or four) spaxels, one could use

$$F_{\rm source} = \overline{x_s / nbeam_s(y,z)} \times F_{\rm telescope} \tag{8.74}$$

Hence, in principle it is possible to produce a point-source correction for a point source located anywhere in the FoV. In practice, however, the following points also need to be considered.

- A sufficiently accurate determination of the position of the source *y,z* requires a very specific analysis and is not always possible: the spatial resolution of PACS is sufficiently low that even

[7]The beams computed previously were normalised to a peak of 1. The final beams, computed here, are normalised to an integrated flux of 1

with a mapping observation, it is not possible to measure the location to better than a few arcsec. Hence we do not offer a generic PSCF(y,z) correction ($= nbeams_s(y,z)$) but only that assuming a well-pointed point source, i.e. PSCF(0,0) as described by eqn 8.70.

- To be robust against (slight) pointing errors, throughout the flux calibration we have used the central 9 spaxels instead of the central one only, i.e. we use the equivalent of a "meta-spaxel", the central 3×3 spaxels. Provided we replace the central spaxel by that meta-spaxel, all relations above still hold, except that we need a "3×3-to-total *PSCF*" ($PSCF_{3\times3/tot}$) instead of the just derived "central-to-total *PSCF*— ($PSCF_{1\times1/tot}$).

This $PSCF_{3x3/tot}$ corresponds to:

$$PSCF_{3\times3/\mathrm{tot}} = \sum_{s\in3\times3} nbeam_s(0,0) \tag{8.75}$$

Or, defining $PSCF_{1\times1/3\times3}$ as the ratio of the fractions of the global instrument response to a well-pointed point source seen by the central spaxel and by the central 3x3 meta-spaxel respectively:

$$PSCF_{1\times1/3\times3} = \frac{nbeam_{12}(0,0)}{\sum_{s\in3\times3} nbeam_s(0,0)} \tag{8.76}$$

$$\tag{8.77}$$

and using equation 8.70, we can also write:

$$PSCF_{3\times3/\mathrm{tot}} = \frac{PSCF_{1\mathrm{x}1/\mathrm{tot}}}{PSCF_{1\times1/3\times3}} \tag{8.78}$$

Application of the point source correction is provided via a task that is explained in Sec. 11.2.1.

8.3.4 Extended source corrections

Given the normalised beams introduced in the previous section, an arbitrary spatial distribution of surface brightness $f_{\mathrm{source}}(y,z)$ is coupled to the spaxels via

$$F_s = \int\int_{(beam)} f_{\mathrm{source}}(y,z)\, nbeam_s(y,z)\, dy\, dz \tag{8.79}$$

Unfortunately, the inversion of this problem is generally not possible. Hence, we have either model or assume a flux distribution of the source to be able to provide a solution for the flux calibration of that source (i.e. to correct for the irregularly-sampled footprint of PACS). However, a generic calibration with the assumption of an infinitely extended source with a constant surface brightness has been made. The corrections necessary for slightly-extended sources with arbitrary surface brightness are addressed in Sec. 8.3.5.2, and corrections for any other type of source (i.e. not a point, not slightly-extended, and not infinitely extended) are addressed in Sec. 8.3.5.2.

Assuming a surface brightness $f_{\rm source}$ for our extended source, and considering spaxel s, we measure the signal x_s, in [telescopes]:

$$x_s = \frac{signal_{\rm source}}{signal_{\rm telescope}} \tag{8.80}$$

$$= \frac{f_{\rm source}\,\Omega_s}{f_{\rm telescope}\,\Omega_s} \tag{8.81}$$

where Ω_s is the solid angle of the beam of spaxel s.

The telescope emission is sufficiently homogeneous and isotropic, such that $f_{\rm telescope}$ can be assumed to be the same for all spaxels, and the effective beam solid angle, which may vary from spaxel to spaxel, cancels (as do the telescope area and the system throughput, which have not been included for the sake of clarity). To solve for $f_{\rm source}$, the only remaining unknown is the telescope surface brightness $f_{\rm telescope}$, which is defined through:

$$F_{\rm telescope} = \iint_{(beam)} f_{\rm telescope}\, nbeam_{12}(y,z)\, dy\, dz \tag{8.82}$$

$$f_{\rm telescope} = \frac{F_{\rm telescope}}{\iint_{(beam)} nbeam_{12}(y,z)\, dy\, dz} \tag{8.83}$$

In this form, $f_{\rm telescope}$ is expressed in [Jy/beam]. We want to express it in [Jy/spaxel] instead, where "spaxel" now stands for *idealised detector with a nominal size of 9.4″ and a uniform response*. In other words, we want to define the telescope surface brightness as the telescope flux density divided by the nominal spaxel solid angle:

$$\hat{f}_{\rm telecope} = F_{\rm telescope}/(9.4{\rm arcsec})^2 \tag{8.84}$$

This being done, we can provide an Extended Source Correction Factor, *ESCF*, to account for the change of units, from [Jy/beam] to [Jy/spaxel], or in other words, to account for losses "between the beams", such as was done previously for point sources.

To calculate the *ESCF*, we used the re-normalised beams and compared the measured beam solid angle with the ideal one. The Extended Source Correction Factor is the same for all spaxels, as Ω_s cancels out in eqn 8.81. Therefore, we only need to calculate it for the central spaxel, as this is the one to which the telescope is linked in our calibration scheme:

$$ESCF = \Omega_{12}/(9.4{\rm arcsec})^2 \tag{8.85}$$

with

$$\Omega_{12} = \iint_{(beam)} nbeam_{12}(y,z)\, dy\, dz \tag{8.86}$$

With this at hand, we finally obtain the surface brightness of the source in [Jy/spaxel] from eqn 8.81:

$$\hat{f}_{\rm source}[Jy/spaxel] = x_s \times \hat{f}_{\rm telescope}[Jy/spaxel] \tag{8.87}$$

$$= x_s \times f_{\rm telescope}[Jy/beam] \times \frac{beam}{\Omega_{12}} \times \frac{(9.4)^2}{spaxel} \tag{8.88}$$

$$= x_s \times \frac{f_{\rm telescope}[Jy/beam]}{ESCF[spaxel/beam]} \tag{8.89}$$

A set of slides describing the uneven illumination of the spectrometer FoV can be found on HELL L2.

The extended source correction is part of the standard calibration provided in all spectrometer pipelines.

8.3.5 Semi-extended source corrections

In the previous sections we addressed the necessary corrections to the flux density and surface brightness for point sources and fully extended sources. However, science targets do not necessarily fall in either category. A generalisation of the source–spaxel coupling and the correspondent corrections are explained in the following sections. For such purpose, a detailed characterisation of the detector beam efficiencies and an a-priori knowledge of the source's surface brightness distribution in the IR are mandatory (in other words, the user needs to have a model of the morphology of the source).

8.3.5.1 Extended-to-point source flux density correction for small sources

The PACS spectrometer flux density calibration is tied to the known flux density of a point source calibrator via the telescope spectrum calibration, as explained in Sec. 8.3.4. For a point source science target centred in the central spaxel, this is reflected in Eqn 8.68. In the case of a source whose spatial extent is slightly larger than the beam efficiency size, the *PSCF* does not reflect the fraction of the flux detected by the central spaxel to the total flux, and we need to specifically calculate the aperture correction for the signal detected in the central spaxel η, relative to the $PSCF$. The expression of the flux density calibration is:

$$F_{\rm source} = x_{\rm source}/x_{\rm Ceres} \times PSCF/\eta_s \times F_{\rm Ceres} \tag{8.90}$$

with

$$\eta_s = \frac{F_{\rm s}}{F_{\rm point}} = \frac{\iint_{(beam)} f_{\rm source}(y,z)\, nbeam_s(y,z)\, dy\, dz}{\iint_{(beam)} \delta(0,0)\, nbeam_s(y,z)\, dy\, dz} \tag{8.91}$$

representing the coupling ratio between any given source of surface brightness spatial distribution $f_{\rm source}(y,z)$ and a point source, represented by a centred δ-function in surface brightness. η_s is also referred to as extended-to-point correction (E2PCF), and it must be consistent with the detector area considered for the telescope background calibration (i.e. the source must be located within the central spaxel and certainly must be fully contained in the central 9 spaxels). For a comparison of the functions for a Gaussian source of various sizes, see Fig. 8.17.

$$\eta_{1\times1} = \frac{\iint_{(beam)} f_{\rm source}(y,z)\, nbeam_{12}(y,z)\, dy\, dz}{nbeam_{12}(0,0)} \tag{8.92}$$

$$= \frac{\iint_{(beam)} f_{\rm source}(y,z)\, nbeam_{12}(y,z)\, dy\, dz}{PSCF_{1\times1/\rm tot}} \tag{8.93}$$

$$\eta_{3\times3} = \frac{\sum_{s\in3\times3} \iint_{(beam)} f_{\rm source}(y,z)\, nbeam_s(y,z)\, dy\, dz}{\sum_{s\in3\times3} nbeam_s(0,0)} \tag{8.94}$$

$$= \frac{\sum_{s\in3\times3} \iint_{(beam)} f_{\rm source}(y,z)\, nbeam_s(y,z)\, dy\, dz}{PSCF_{3\times3/\rm tot}} \tag{8.95}$$

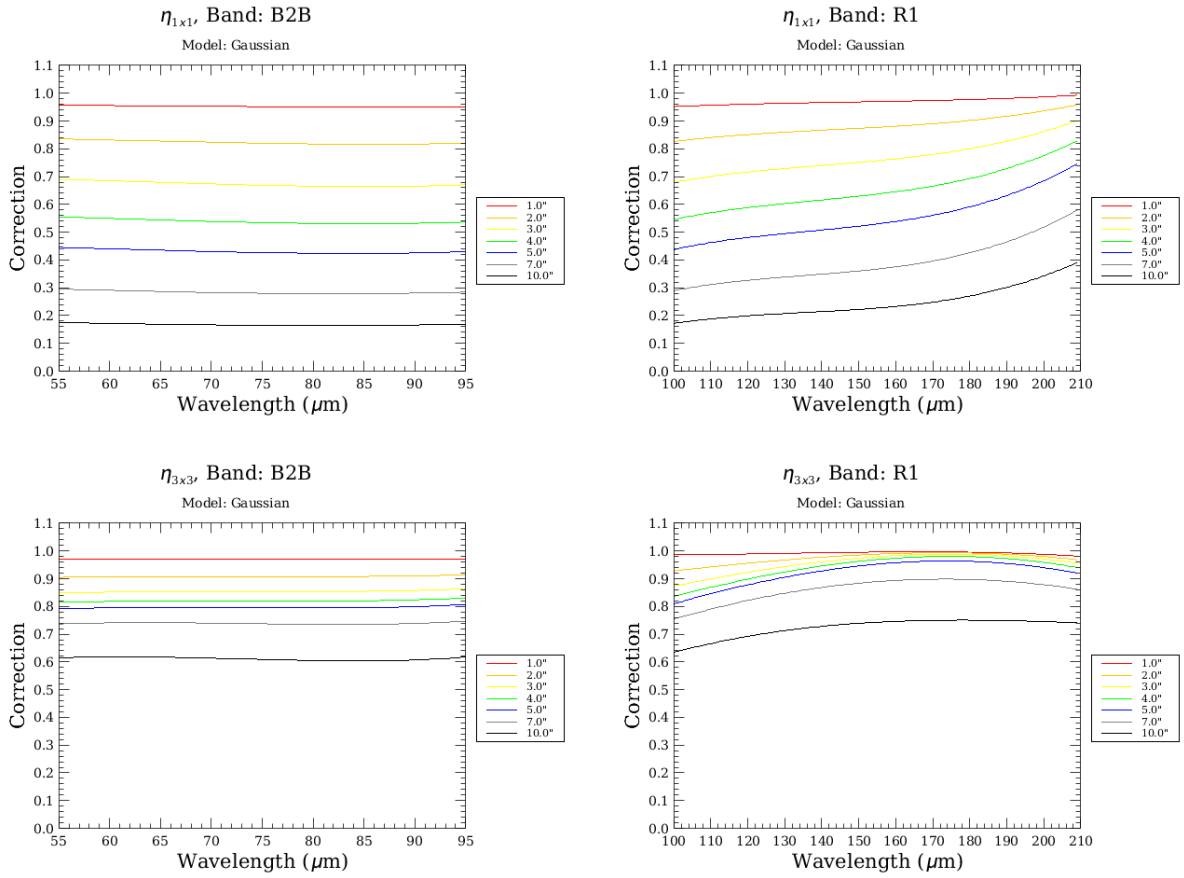

Figure 8.17: E2P corrections with symmetric Gaussian model of FWHM between 0.1″ and 10″ for central and central 9 spaxels in the B2B and R1 bands.

This correction assumes that most of the total flux from the semi-extended source is located within the PACS spectrometer FoV. Hence, the correction is meaningful for sources for which 90% of the flux falls in the central 9 spaxels (i.e. FWHM$<$ 15″).

Application of this correction is provided via a task that is explained in Sec. 11.2.2.

8.3.5.2 Forward model for irregular extended sources

The non-uniform illumination of the PACS spectrometer FoV is the culprit of flux losses "between the beams", as explained in Sec. 8.3.4. By assuming a reduced spaxel active area ($\sim 8'' \times 8''$, instead of the idealised detector with a nominal size $9.4'' \times 9.4''$ and a uniform response) we can achieve a flux loss comparable to that which is observed. This flux loss is accounted for in the calibration scheme for fully-extended sources, via the standard flux calibration of all PACS pipelines. However, these corrections are actually science-case dependent, as they depend on the surface brightness distribution of the source over the observed field. As a consequence, for the following particular cases:

- off-centred point sources
- crowded fields (i.e. with much variation in the flux distribution over the observed field)
- semi-extended structures (including the small sources discussed in Sec. 8.3.5.1 and larger sources which are not "infinitely" flat)

aperture extraction for on the cubes will not produce the correct fluxes, as the flux calibration has not accounted for the flux losses. However, if an analytical model of the source's flux distribution is provided, the source–instrument coupling per detector can be estimated by simulating a PACS observation using a task in HIPE, and the proper calibration correction for the source can be computed. Applying this "forward modelling" is explained in Sec. 11.2.3.

The surface brightness calibration performed by the Standard Generation Processing (SPG) pipeline is

$$f_{\rm source}[Jy/beam] = x_s \times f_{\rm telescope}[Jy/beam] \tag{8.96}$$

The pipeline includes an additional extended-source correction (ESCF) to account for losses between the beams in the case of a fully extended source, which corresponds to the solid angle ratio between the beam efficiency of the central spaxel and the nominal size of $9.4'' \times 9.4''$. This effectively changes the units of surface brightness from [Jy/beam] to [Jy/spaxel] in the following way

$$\hat{f}_{\rm source}[Jy/spaxel] = x_s \times \frac{f_{\rm telescope}[Jy/beam]}{ESCF[spaxel/beam]} \tag{8.97}$$

The Forward Model Tool (FMT) generalises the calculation of the coupling factor for each detector s to create a PACS forward model in units of [Jy/beam].

$$f_{\rm sim}[Jy/beam] = \xi_s[Jy/beam] = \iint_{(beam)} f_{\rm source}(y,z)\, nbeam_s(y,z)\, dy\, dz \tag{8.98}$$

The source model $f_{\rm source}(y,z)$ is defined in units of [Jy/pixel] and coordinates of the beam efficiency maps, with centre (0,0) on the central spaxel centre, and a grid scale $d_{\rm pix}$ =0.5″.

The point- and extended-source corrections are recovered when considering a very small spatially extended source (delta function), as $\xi_{12} = PSCF$, and a fully extended source of $f_{\rm source}(y,z)$ Jy/pixel, for which

$$\xi_{12} = ESCF \times (9.4)^2 \tag{8.99}$$

The ratio between the simulated and the observed surface brightness (once the ESCF has been removed) yields a pixel-to-pixel correction over the field sampled by the raster observations.

The FMT will compute the correction to the *fluxes* of the source, but it does not correct for the distortions to the line profiles that are caused by point-like features moving out of/in to the PACS detector slit (Sec. 8.4.2.2). These distortions take the form of a skew to the line profile, which causes the line centre to shift and line profile to change. Therefore, the ratio values produced by the FMT in the wings of spectral lines should not be over-interpreted. This effect is averaged out when considering spatially symmetric apertures for spectra extraction over the spectral mosaic cube.

8.4 Spectral calibration

8.4.1 The line profile

The instrumental line profile was measured during FMILT from monochromatic laser lines, and was fit with a Voigt. For most unresolved lines observed from in-flight data, a single Gaussian will fit the profiles well, but for sufficiently bright lines a single Gaussian will leave behind a small percentage of the flux in low-level wings. Inspection of the residuals of the fits to these brighter lines will clearly show these wings, allowing them to be dealt with easily by the astronomer.

8.4.2 Wavelength calibration

The PACS wavelength calibration relates the diffraction grating position to the wavelength seen in every detector pixel. This calibration was derived from laboratory measurements of a water vapour absorption cell, and further refined inflight based on fine structure lines in planetary nebulae.

8.4.2.1 Wavelength calibration accuracy

For ideal extended sources the required accuracy of better than 20% of a spectral resolution element is met throughout all bands. Values even better than 10% are obtained in band centres, while at the band borders, due to leakage effects and lower SNR, the RMS calibration accuracy is closer to 20%. However, for point sources the wavelength calibration may be dominated by pointing accuracy.

8.4.2.2 Wavelength shifts with point source position and source spatial extent

The 5×5 spaxels of the IFU are imaged by the slicer onto a 1D-slit (Fig. 2.18. The 1D-slit image is then dispersed by the diffraction grating. As with any diffraction grating spectrometer, moving the point source centre with respect to the slit centre in the dispersion direction will result in a slight shift of the wavelength seen in a detector pixel. Therefore, spectral lines observed from a point source with PACS will appear slightly shifted in wavelengths if the source is not perfectly centred on the spaxel. A discussion of these shifts can be found in Sec. 5.8.3.

Chapter 9

The PACS Pipelines

All *Herschel* observations were processed automatically by SPG (systematic/standard product generator) pipelines at the HSC, and placed in the HSA for users to download. In Chp. 10 the products found in these so-called *ObservationContexts* are described, and in this chapter the pipelines that were run to create those products are explained.

The SPG pipeline scripts, together with a selection of interactive pipeline scripts, can be found in HIPE. There are scripts provided for the various AOTs (observing modes) or for various science cases. All script variations are based on the SPG pipelines, and usually vary only in the parameters used for some of the tasks, or by having extra tasks added with which the user can try to improve on the standard reduction (but for which the results are not guaranteed to be better than the SPG). The interactive pipeline scripts are explained in full detail in the PACS Data Reduction Guide (PDRG) for spectroscopy and photometry. All pipeline scripts are run separately for the red and blue camera data, and in turn the ObservationContexts produced by the SPG contain data products of a red and blue variety – these are identified by an R or a B at the end of the product name, for a subset of products a G(reen) at the end of the name (this being a blue filter), and for a subset of others no colour is indicated because all are included. All product names start with HPS (Herschel PACS Spectroscopy), or HPP (Herschel PACS Photometry).

In HIPE, there are four submenus in the Spectroscopy Pipeline menu do deal with: chop-nod range spectroscopy, chop-nod line spectroscopy, unchopped range spectroscopy, and unchopped line spectroscopy (which also deals with the few wavelength switching observations in the archive). In each submenu is the SPG script (separated on Level) and one to a few interactive pipelines. Every pipeline script can deal with observations that include multiple wavelength ranges and with both pointed and mapping AORs. In the HIPE Scripts menu you can find various useful scripts that mostly work on fully-processed data (i.e. Level 2 or 2.5). These scripts cover the following topics: how to fit spectra, combine observations, produce the so-called standalone browse products, create mosaic cubes of different spaxel sizes, or combine observations on the same field but of different programmes.

For photometry there are two submenus in the Photometry Pipeline menu to deal with scan-mapping and chop-nod observations, and both contain the SPG scripts for that AOT. For the scan-mapping menu there are additional submenus that differ on the mapper used (generally being suitable for different types of source). Science-ready maps are produced by the SPG pipeline with the high-pass filter method (up to Level 2.5 products), JScanam and Unimap (up to Level 3 products); MADMap maps, which were created by the SPG only early in the mission, can be generated by means of an interactive

script. Scripts to do photometry or convolution on the fully-reduced maps are offered in the *Scripts* menu.

On HELL L1 you can find the launch pages for the photometer and spectrometer. These are mostly focussed on data reduction and analysis in HIPE. The full data-reduction guides for each instrument can also be found on HELL L1. On the whole it is not necessary to re-reduce PACS data, and so most of you will not read these data reduction guides. Nonetheless, it is worth looking at them to understand some of the details of how the various products are made. While much this information is given in this chapter, there are some details that are only in the data reduction guides.

9.1 Photometer pipelines

In this section we describe how to reduce photometer data using the interactive pipeline scripts in HIPE, summarising the advice given about the best way to use the pipelines for different types of sources. A more detailed step-by-step walkthrough of the processing can be found in the PDRG (phot).

A summary of the product levels and the pipeline processing for a standard photometry observation is given in Table 9.1.

Table 9.1: Summary of the levels in a photometry observation and the main pipeline-processing steps

Level 0	Raw data, formatted from the raw telemetry by an external pre-processing stage. The scientific data are in products called *Frames*, the data therein being the averaged signal of the detector pixels, for the red and blue detector arrays. Other products used by the pipeline are: instrument status table, spacecraft pointing, time correlation, spacecraft housekeeping information, raw data for some pixels.
Level 0.5	Engineering conversions, pointing information computed, data organised in blocks and internal calibration block removed. Level 0.5 data are the uncalibrated, uncorrected timelines.
Level 1	Data taken during telescope slews and from bad detector pixels are masked out, as are cross-talk and saturation. Flatfielding and non-linearity corrections applied. For SSOs the coordinate system is set so the object is in a fixed position on the sky at all times. Level 1 data are still timelines but are flux calibrated (units of Jy per detector pixel).
Level 2	The timeline detector data from Level 1 are projected on to a sky grid (via the *highPass* filtering + *photProject* tasks): one red and one blue map for each observation. Data glitches are masked out, the source masked, timelines cleaned with the *highpassFilter* task and the data projected using the *photProject* task. Level 2 data are maps in units of Jy/(map pixel).
Level 2.5	For observations with a scan and cross-scan AOT, the Level 2 data are combined into a single (red and blue) map using *photProject*, *Jscanam*, *Unimap*. The *Jscanam* and *Unimap* tasks are run on the scan and cross-scan Level 1 data to produce directly Level 2.5 maps. Pixel sizes for all maps are $3.2''$ for blue/green parallel mode AOTs and $1.6''$ for the blue/green prime mode, and $3.2''$ for all red band data. Level 2.5 data are maps in units of Jy/(map pixel).
Level 3	For observations that are otherwise unrelated (e.g. were not part of the same programme) but overlap on the sky and have the same AOT, a mosaic is created from all the available observations.

The photometry pipeline scripts are the same for all observations up to Level 1, and after that they separate on mapper. In general, the SPG scripts are the same as the interactive pipeline scripts described here when run with the default parameters.

9.1.1 Scan map

9.1.1.1 Level 0 to 1

The first steps of the pipeline are the same for all observations. Two scripts take the raw data to a fully-calibrated Level 1 *Frames*, which are data-cubes calibrated in units of Jy/detector pixel. The first script starts from Level 0 and makes sure that all the necessary meta data entries are present, detects and removes the calibration blocks from the beginning of the observation, and adds basic astrometric information. The second script starts from the Level 0.5 product, and performs some basic calibration steps:

- flags bad and saturated pixels
- masks the columns affected by cross-talk
- converts the digital units to volts (necessary for the responsivity calibration)
- applies the flat field and responsivity correction
- applies the non-linearity correction (where necessary)
- applies the correction needed to alleviate the response changes of the bolometers due to the changes in the evaporator temperature (Moór et al., 2014)
- if the the target is an SSO, it converts the spatial frame to the reference frame of the moving object

9.1.1.2 Level 1 to the end: introduction

The handling of scan-map observations depends strongly on the scientific goal:

- High pass filtering and photProject: suitable for point and slightly extended sources.
- Generalised Least Square (GLS) mapmakers: two mapmakers are provided – Unimap and MADMap – that exploit the GLS method. Before SPG 13.0 the MADMap maps were provided in the HSA, but thereafter Unimap was used and these are the maps provided in the HSA download.
- Destriper mapmaker: JScanam is the HIPE implementation of the IDL mapmaker called Scanamorphos.

Unimap (MADMap) and JScanam are suitable for point sources and extended sources: they give similar results and it is up to the user to decide which to use. They both exploit the spatial redundancy provided by the observations and they only generate Level 2.5 products; they also only work if a scan and cross-scan observation was performed. The high-pass filter method is different: it is applied to a single observation to create a Level 2 product, and then used to create a Level 2.5 produce if both a scan and cross-scan observation was performed.

9.1.1.3 Level 1 to the Level 2: HighPass filter and photProject

The HPF+photProject script processes scan-map and mini-scan map observations, starting from Level 1, producing Level 2 maps with units of Jy/map pixel. The individual maps created from the scan and cross-scan observations are combined with the *mosaic* task, to create Level 2.5 maps. This script uses the high-pass filter (HPF) method (task *highpassFilter*) to remove the 1/f noise, and the task *photProject* to project the timeline data onto a map. This HPF does not work well for observations with extended emission present – it removes large-scale structures as they cannot be properly protected (masked) from the filtering – and therefore this script is intended for observations of point-like or relatively small extended sources.

The interactive pipeline script is described here. The SPG script is the "default" version of this script, with some simplifications because it needs to deal with many different types of observed fields.

The interactive script can combine several observations (obsids), but it is also useful for processing a single obsid. A first pass of HPF+photProject is done employing a S/N filtering of the timeline, and sources are detected and masked out with a circular patch, and then a second pass is done. The placement of the circular patch is very important for ensuring correct masking. Three options are offered:

- Source fitting: if the source is the brightest object in the FoV, source fitting will find the source and set the centre of the patch to its fitted coordinates.
- Target coordinate list: the script reads the coordinates given in a text file and sets the coordinates to the centre of the patch.
- Target source list and source fitting: if the coordinates are only approximate, a source fitting is done on a sub-image centred on the given coordinates. The small size of the sub-image ensures that the fitting does not diverge while seeking the brightest object in the image.

Beside the appropriate placement of the mask, correct filtering of the data also relies on a good choice for the value of the high-pass filter width. An optimum value is given as default but it can be modified as desired and/or necessary for specific science cases. If the HPF width is too tight, some extended features of the compact sources will be filtered out, while a too-large width will increase the residual 1/f noise.

An important parameter for the combination HPF and photProject is the size of the output pixel that the data are re-grided onto and the active pixel fraction, both of which strongly influence the noise in the resulting map. A smaller drop size or output pixel size will allow for a better PSF sampling.

The processing itself consists of four main steps:

1. A map for each individual obsid is created with highpass filtering, and from this map source(s) are detected using a S/N threshold, to create circular source mask(s). Similar to the procedure in the SPG script.
2. Next, all obsids are reduced and a combined map created, incorporating the previously-created mask. This map has a superior SNR than any single map, and from it a S/N-thresholding is again used to identify source(s) and to create circular mask(s).

3. Another round of creating a combined map (again using the HPF method on the *Frames* and photProject), incorporating this second mask, is done. From this the final circular source mask(s) are created.

4. This final mask is then applied to the original *Frames*, running the HPF and photProject but this time also deglitching the data, resulting again in a combined (mosaic) map. From this map, additional sources (e.g. fainter ones) can be identified, creating a multiple-source mask. If a file with the coordinates of the expected source(s) on the maps is provided, this can be used to create a mask or masks with 20″ radii. To ensure that the coordinates are accurate, a Gaussian can be fit to each source to refine the coordinates. If the sources are too faint, the supplied coordinates are used without refinement. If there is no target list given the script will use the source coordinates given in HSPOT as a centre for the circular patch.

In the SPG pipeline, these four steps are done differently because it has to accommodate many different kinds of observation. Here, the first pass is done with a very crude high-pass filtering (HPF width = 100) and a sources are detected on intermediate maps using a S/N threshold. Then a second pass of high-pass filtering is done using the mask and a smaller filter width (15 and 25 in blue and red respectively).

After having created the mask(s), the next step is the actual map-making.

- The *Frames* are highpass filtered and deglitched using the final combined mask.
- The spacecraft turnovers are removed from the datastream.
- The data are projected onto the final individual maps, with the requested pixfrac and map pixel size. An extra map with a pixfrac = 1 is created for comparison (this is not done in the SPG pipeline where the pixfrac is always 0.1 and the pixel size is half of the native pixel size).
- The final mosaics are then created from the scan and cross-scan maps.

In the interactive pipeline script, the user can then chose to perform aperture photometry on the final maps, using several apertures and including measurements of the sky level and sky noise from the sky apertures. The resulting photometry for the source (with and without background subtraction) and sky apertures is given. The apertures on sky are chosen such that they overlap as little as possible with the source.

By definition, the HPF method removes the sky contribution from the maps, i.e. the sky background values of the mosaics should be distributed around zero. In the real world this is not always the case, and an offset (positive or negative) may be present. The aperture photometry task takes this into account.

9.1.1.4 Level 1 to the Level3: JScanam

JScanam is the HIPE implementation of the IDL map-maker Scanmorphos (Roussel, 2013), with a pre-processing fine tuned for PACS data. The interactive pipe script starts from Level 1 *Frames* and creates a Level 2.5 map from the input obsids. The standard processing always combines two obsids (scan and cross-scan) and multiple pairs are dealt with by another script. Level 2.5 maps belonging to the same sky region, and acquired with the same observational setting, are combined with the *mosaic* task to create deeper, Level 3 products.

JScanam does not rely on a noise model nor filtering, rather it exploits the spatial redundancy to derive the detector drifts from the data. Short and long timescale drifts are removed by comparing, at each map point, the time-line signal in a detector pixel from the scan observation with the same values from the cross-scan observation or with the values from another scan leg.

The first steps are to remove the unnecessary frames that were taken during the turnaround of the spacecraft, and to mask long-term glitches (creating the mask `Scanam_LongTermGlitchMask`). The origin of the long-term glitches are cosmic ray hits on the instrument electronics. The user can, at any step in the interactive pipeline, project the scan or/and the cross-scan *Frames* using the *photProject* task to inspect the results of intermediate steps of the reduction chain.

The next step is to create a source mask (`Scanam_LongTermSourceMask`), used to evaluate the offset and drift corrections using only background pixels. The data of the *Frames* are treated by scan leg – one scan leg contains all the timeline data taken during one continuous straight scan on the sky. The first step is to fit a linear baseline to the signal of each scan leg in every detector pixel, and to subtract that baseline. The objective is to remove signal drifts with timescales larger than a scan-leg, while preserving real sources as much as possible, and with the intention of creating a first-order map that can be used to create a source mask.

These are the main algorithm steps for the baseline subtraction:

- Select the unmasked timeline data for each instrument pixel and every scan leg. If a source mask is provided, the datapoints in this mask will not be used.
- If there are enough points, fit with a linear baseline. If this is not the case, calculate the median value.
- The linear baseline fit is performed in a iterative way. The unmasked data are fitted first. Fit positive outliers are then removed, and the fit is performed again. The same steps are repeated until the iteration converges: either no new outliers are found, the number of iterations is larger than 50, or there are too few datapoints to continue with the fitting process. In this last case, the median of the unmasked data is calculated instead.
- Subtract the fit (or the median) from the whole scan-leg signal, including from the masked values.

Scan and cross-scan are combined to improve the SNR and from that to create the source mask to attach to the scan and cross-scan *Frames*. The processing begins on the original *Frames* by removing the general signal offset: the median signal value in every detector pixel and each scan-leg is computed and subtracted. Only the data not included in the mask is considered here.

Next the signal drifts produced by the calibration block are identified and masked. Each observation starts with a staring at the (bright) internal calibration sources, and this can cause response drifts in the subsequent signals (i.e. those from the sky). The typical time-length of this drift is 1000 time indices. The mask is activated after the execution of the task.

The baseline subtraction is run again and signal drifts with timescales longer and shorter than a scan-leg are then removed by means of two subsequent tasks: *scanamorphosDestriping* and *scanamorphosIndividualDrifts*. The first (the so-called de-striper), assumes that the scan and the cross-scan observations have perpendicular scan directions (which was the recommendation of the AOR): as a result the projected maps will have different drift gradients. The long scale drift removal technique is based on the following:

- The drift power increases with the length of the considered timescale (1/f noise). For this reason, the task starts by removing the strongest drift component with a timescale equal to the length of the entire set of scan legs, decreasing this scale in the next step to four scan-legs, and finally to one scan-leg. In each step the remaining drifts become weaker.
- Back-projecting a map obtained from a given scan direction to the perpendicular direction; this will transform the generally increasing or decreasing signal drifts into oscillatory drifts, which cancel out on large timescales.

These are the main algorithm steps:

- Construct a map index with a large pixel size in order to have a significant number of crossings per pixel. The map index pixel size is calculated iteratively using the median scan velocity, the scan direction and the readout frequency. The convergence condition is that it should be big enough to guarantee that more than 70% of the crossings have a size equal or larger than the minimum accepted crossing size (default is 6). The value of the minimum crossing size can be changed with the task optional parameter "minimumCrossingSize".
- Collect all the bolometer crossings for every pixel in the map with a size larger than the minimum crossing size.
- Discard crossings with a flux standard deviation much larger than the bolometer threshold noise (i.e. they are affected by strong real sources).
- Subtract the source emission to the crossings signal using the back-projected signal of a high resolution map of the frames. This step assumes that the global effect of the drifts on the high resolution map is much smaller than the individual drifts signal, because they cancel each other.
- Calculate the average flux of all crossings of a given map pixel and subtract it to the crossings in that pixel.
- Calculate the average flux and the average time of each bolometer crossing, and add it to the bolometer drift timeline. The drift timeline time resolution is increased in each iteration, from 1/6 the size of the scanleg to the shortest time resolution (one time index).
- Interpolate the missing values in the drift timeline.
- Subtract the calculated drift timelines from the bolometer timelines.
- Create a new high resolution map to subtract the drifts. The drifts in this map should be weaker than in the previous map.
- Repeat all steps again starting from step 2, using each time a shorter timescale for the drift timelines calculation.
- The final convergence is reached when the bolometer drifts standard deviation is smaller than the bolometer high-frequency noise, for all bolometers. The maximum number of iterations is also controlled by the task optional parameter "maxIterations" (default is 6).

The final map is created using photProject with the desired pixel size and pixfrac.

Two flavours of interactive scripts for the JScanam pipeline are available: one designed to run on a pair of scan and cross-scan observations – the SPG script is this script with all its default parameters – and the other usable on an arbitrary list of observations.

9.1.1.5 Level 1 to Level 3: Unimap

Unimap is a Generalised Least Squares (GLS) mapmaker developed in MATLAB and released by the DIET department of the University of Rome "La Sapienza" (Piazzo et al., 2015): the documentation can be found here, otherwise see the PDRG (phot). The Unimap interactive script reads Level 1 *Frames* and generates a map from the input obsids. The interactive script can be used for combining any number of obsids; the standard processing up to Level 2.5 concerns the combination of only two obsids (scan and cross-scan); if there are a sufficient number of obsids that cross the same sky area then Unimap is used on all of these to create Level 3 products.

Unimap performs a pre-processing to clean the data of systematic effects (offsets, drifts, glitches), and it uses the GLS algorithm to remove the correlated 1/f noise while preserving the sky signal over large spatial scales.

The GLS estimator provided by Unimap can introduce distortions at the positions of bright sky emission, especially if the source is point-like. The distortions, which generally appear as cross-like artifacts, are due to the approximations of the signal model and to an imperfect compensation of disturbances at the pre-processing stage.

In the first Unimap releases (up to Unimap v. 6.3, or SPG of and before v. 14.0.1) the distortions were estimated and removed by means of a post-processing. In this post-processing, a high-pass filtering approach was implemented within Unimap to remove these distortions within a specified spatial scale and on limited regions of the map identified by means of a masking procedure (PGLS and WGLS maps). The distortions that the post-processing removed by means of an empirical approach were mainly due to the pixel noise, that is the noise that is introduced by digitally sampling (with pixels) a continuum signal (sky emission). The pixel noise represents the random displacement of the sampling point with respect to the centre of the sky pixel.

Starting from Unimap v. 6.3 (and SPG 14.2, i.e. for the observations served via the HSA) a new method which takes the pixel noise into account was developed. Compensating for the pixel noise within the GLS algorithm is the most convincing way of preventing distortions, rather than removing them by means of the post-processing. However, accounting for the pixel noise makes the GLS heavier from a computational point of view, increasing the processing time up to a factor 40. For this reason, for large datasets it may be necessary to run the GLS without the pixel noise compensation and apply the post-processing to remove the distortions instead. In the SPG the decision about which approach to take is made based mainly on the dimensions of the maps.

The values of parameters that contribute to the generation of the GLS, PGLS and WGLS maps depend on the characteristics of the sky emission and on the level of accuracy to be achieved by the different estimators. The best choice for the parameter values is automatically set by Unimap by performing a statistical analysis of the sky emission, and this is also what is done in the SPG script. These parameters can always be fine-tuned by the users according their purposes. Unimap v. 6.3 and later can combine the pixel noise and the electronic noise to produce an estimate of the noise affecting the final map and to generate an error map associated directly with the final map.

Unimap makes use of a large number of parameters that are defined and managed in a "unimap_par.txt" file. In the interactive script, a limited number of parameters (9) are included and propagated. More advanced use-case parameters are also included in this file (the use of these is explained in the PDRG (phot)).

The parameters that the user can edit within the interactive script are:

- numProc: how many logical processors do you want to use? If a negative number is given, Unimap detects the number of available processors.
- sync: the component of the Relative Pointing Error due to the time shift along the scan leg can be compensated. If sync=2, the synchronisation is applied, while it is skipped if sync=0. If a negative number is given, Unimap evaluates whether the image is signal-rich enough to apply a reliable sync compensation. This is what is done in the SPG script.
- pixelNoise: the gain to apply to the estimated pixel noise in the GLS pixel noise compensation. 0 means no pixel noise compensation, 0.5 means half of the estimated pixel noise is compensated, 1 all of it, and so on. If a negative number is given (which is the value in the SPG script), Unimap decides if the field is suitable for pixel-noise compensation, according the dimension of the dataset and the amount of signal.
- minimumChange: expressed in dB, it is the minimum change in the GLS map to keep iterating. If it is set to a positive number, the stop level is selected automatically by taking into account the morphology of the map. This is what is done in the SPG script.
- startImage: is the initial guess adopted by the GLS for starting the iterations. It can be: 0 for a zero (flat) image, 1 for a naïve map, 2 for a mixture map and 4 for a Alternating Least Squares (ALS) map (for Unimap v. 6.4.2 or later, this being also SPG 14.2 and later). If 3 (the value in the SPG script), the optimal starting image is set by performing a statistical analysis on the naïve map. The mixture map is composed of portions of a flat map at the positions recognised as background regions, and portions of the naïve map where signal regions are detected. The number of iterations required by the GLS to converge depends strongly on the adopted starting image, thus the selection of proper initial guess can affect the quality of the final maps and it can significantly reduce the process running time.
- filterSizeInArcsec: sets the dimension (in arcseconds) of the high-pass filter adopted by the PGLS method for removing possible distortions introduced by the GLS. If it is 0, Unimap calculates the best dimension of the PGLS filter using an iterative approach, where the convergence is controlled in the similar way as it is for the GLS algorithm.
- wglsDThreshold: the threshold for the detection of distortions introduced by the GLS algorithm, for building the WGLS mask. The greater the value, the smaller the number of detected artefacts. The optimal value is computed by setting this parameter to 0.
- wglsGThreshold: the threshold for building the WGLS mask, starting from the anchor points provided by the "wglsDThreshold" parameter. The greater the value, smaller the extent of the masked artefacts. The optimal value is computed by setting this parameter to 0.
- maskToUse: the masks that should be considered by Unimap. A JScanam module is used within the Unimap pre-processing to remove the detector drift due to the calibration blocks, adding a calibration block mask at the same time.
- FramesFitsFiles: set to True if you want to generate the FITS files used by Unimap as the input dataset and to save them in the data directory
- ParametersFile: set to True if you want to rewrite the parameter file in the data directory
- cleanDataDir: set to True if you want to remove input and output files from the data directory

The pixel size for the final map in chosen in arcsec. The values used for the SPG are $1.6''$ non-parallel blue observations and for $3.2''$ otherwise.

After setting the initial parameters, the first part of the script creates a list with the Level 1 *Frames* of the observations that you want to reduce and passes that to the *runUnimap* task, together with various parameter values. *RunUnimap* works in two steps: the first converts the Level 1 *Frames* into FITS files suitable for Unimap and writes the Unimap parameter file, the second spawns Unimap from HIPE and creates the final maps, together with intermediate evaluation products.

The main steps of the pipeline are:

1. TOP: Time Ordered Pixels. In the first step a sky grid is built and every readout is assigned to a sky pixel according the specified coordinate system. In addition, offsets are removed by subtracting the median value from each timeline, and the coverage map is generated.

2. Pre: this module works on the detector timelines. Signal jumps are identified and flagged, and onsets are corrected by subtracting an exponential fit.

3. Glitch: this module detects and flags glitches via a sigma-clipping approach that exploits the spatial redundancy. To simplify the glitch detection, a high-pass filter is first applied over the timelines, to remove long-scale drift and 1/f noise. A glitch mask is created by this module.

4. Sync: this module corrects the shift along the timelines that may be due to errors in the timing system or to delay in the processing chain.

5. Drift: this module removes the drift affecting the timelines by performing a polynomial fitting. The fit procedure is based on an iterative approach that uses the Subspace Least Square drift estimation.

6. Noise: this module performs four important steps in the reduction chain. 1) It estimates the noise spectrum and constructs the noise filters to be used by the GLS algorithm. 2) It uses the flag-removed TOP to make a simple projection and generate a naïve map. 3) It estimates the pixel noise by adopting a destriper map, obtained by fitting the timelines with a piecewise function within an ALS approach. 4) It generates an error maps by combining the contributions of the pixel noise and the electronic noise.

7. GLS: this module (the most time-consuming) computes the GLS estimator via an iterative approach. GLS is used for removing 1/f noise; for an accurate result, all other sources of noise (glitch, drift, offset) must be removed by the previous tasks. An additional iterative algorithm can be nested inside the GLS method to control the pixel noise removal. This compensation avoids the introduction of distortions in the GLS map at the positions of bright sky emission and strong signal gradients, with the drawback of increasing the computational time. If the increase of running time is not acceptable, the pixel noise compensation can be disabled and the distortions introduced by the GLS algorithm can be estimated and removed by means of the post-processing modules.

8. PGLS: this module estimates the GLS distortions via a non-linear, median high-pass filtering and subtracts them from the GLS image, to produce a Post-GLS map. The critical parameter is the dimension of the high-pass filter, which should be large enough to include the distortions but not so large as to amplify the background noise of the image. Generally, the increase of the noise level introduced by the PGLS is negligible for images with a high SNR, which are also

the images for which these distortions are generally present. The PGLS module also saves the GLS to PGLS difference map, from which the distortions can be checked.

9. WGLS: this module applies the PGLS method only in the map sky regions where the distortions are relevant (Weighted-GLS), by minimising the injection of background noise generated by the PGLS. Distortions are detected and masked.

The output of *runUnimap* is a single SimpleImage, called unimapMap, with several 2D datasets:

- "image" is the WGLS map or the GLS map (if the pixel noise compensation is applied),
- "pgls"/"als" is the Post-GLS map or the ALS map (the second if the pixel noise compensation was applied, the first if pre-processing was done instead).
- "gls" is the GLS map
- "naïve" is the naïve map
- "error" is the error map,
- "coverage" is the coverage map obtained with no flagged data
- "unimapLog" is the unimap log file

The SPG script for the generation of standard products uses the default parameter values adopted in the interactive script. A further Unimap interactive script is provided (memory-optimised) that does not exploit *runUnimap* but, by subdividing the processing chain in two subsequent steps, it can save on RAM.

9.1.1.6 MADmap interactive script

The Microwave Anisotropy Dataset Mapper (MADmap), loosely based on the CMB code bearing the same name (see here), is – like Unimap – a Generalised Least Square (GLS) map-making technique that allows a user to generate maximum likelihood sky maps from the ToDs (Time-ordered-Data). The point of using MADmap is to correct for signal drifts due to 1/f noise while preserving emission at all spatial scales. One of the main differences between MADmap and Unimap is that in MADmap the (uncorrelated) noise properties of the detectors are not estimated directly from the data, but rather taken from a fixed model passed to MADmap by means of specific calibration files, typically referred to as InvNtt (Inverse Time-Time Inverse Noise) files. The MADmap algorithm implemented in HIPE assumes that the noise in the time streams is purely uncorrelated. In reality the PACS bolometers are also affected by correlated noise, as well as by pixel-to-pixel electronic offsets. Both the effect of uncorrelated noise and the pixel-to-pixel offsets have to be corrected for before applying the *MADmap* task. The combined removal of correlated noise and pixel-to-pixel offsets from the timelines is the MADmap pre-processing.

The MADmap interactive pipeline script starts from Level 1 *Frames* and ends with the creation of an artifact-free map. The interactive pipeline script is organised into four parts: 1) variables setting; 2) MADmap pre-processing; 3) MADmap run; 4) MADmap post-processing. Note that the script only works for one or more pairs of obsids (scan and cross-scan) – it is not designed to generate Level 2 products from a single obsid.

Part 1. The user sets the values of: obsids; camera (red or blue); and whether the observations are of SSOs. The user can tweak the values of the pre-processing parameters and those entering the call to the task.

Part 2. The MADmap pre-processing initially consists of:

- Level 1 *Frames* refinement: build the pointing cube, remove glitches, apply optical distortion correction
- Removal of the pixel-to-pixel offsets
- Correction of the exponential drift

The exponential drift correction starts with an initial guess of the average drift, which is removed from the time streams; then an approximate map is generated, back-projected and subtracted from the time lines; finally an exponential model is fit to each pixel timeline. The user can decide whether to perform the initial guess or ignore it. If choosing to perform – this being suited to bright sources – the median array, which is created by taking the median of all detector readouts at each given time, is divided into N bins (N is typically 1000 readouts); then the minimum in each bin is computed and a polynomial is fit to the resulting distribution of minimum points. If the timelines contain only weak sources, it is best to fit the median values of the N readout bins with a polynomial, and then repeat the steps described above, that is: the fit is removed from the time streams; an approximate map is generated; this is back-projected and subtracted from the time lines; an exponential model is fit to each pixel time line. These processing steps are applied to each input obsid. Before moving further, all the scans and cross-scans are merged into a single structure. At this point, the time streams are still affected by some residual drift. To fully remove this remaining correlated noise, the following iterative loop is executed: at the start of the iterations, the current best-estimated map is generated, back-projected and subtracted from the timelines; then the residual drift is fit with a baseline (i.e. a first order polynomial) and subtracted from the timelines; a new map is created. The procedure is repeated for a user-selected number of iterations (by default set to 5). With the removal of the global drift (i.e., the correlated noise), the MADmap pre-processing is complete. Next, a deglitching is performed. The reason why glitches are removed only at this stage is that it is much easier to perform this operation once the global correlated drift has been corrected for.

Part 3. The actual MADmap processing. The call to the MADmap routine requires that the PACS timelines are re-arranged in a specific format, creating ToDs on disk. The script contains a choice of two calls: one will generates a naïve map, which is a straightforward combination of scans and cross-scans and which is not corrected for uncorrelated 1/f noise. This map allows the user to see any residual correlated drift, and hence to track down potential problems with the pre-processing phase; the second will generate a GLS map corrected for 1/f noise, as well as a corresponding coverage map, and an indicative error map which is based on the coverage map, by using the same algorithm that generates the sensitivity estimates in HSPOT.

Part 4. The *MADmap* post-processing. This part takes care of correcting for artefacts – in the form of *crosses* at the location of bright sources – that are typically introduced by GLS mappers such as MADmap and Unimap. Indeed, the algorithm used in the task to estimate and subtract the artifacts was designed within the Unimap framework and later adopted by *MADmap*.

9.1.1.7 Comparison of map-makers

Two map-making challenges were organised during the PACS Post Operation Phase, with the ultimate goal of selecting a map-making code for the generation of the PACS photometer legacy archive data. For the implementation in the SPG pipeline, the selected map-making code – which would be added to the High-Pass Filter code because of its limitations for sources with extended emission – had to satisfy two main requirements: 1) preservation of the emission on all angular scales; 2) high photometric accuracy.

The first challenge was held at ESAC in 2013, and the report summarising the outcome of the challenge was released to the astronomical community. The report contained a preliminary assessment of the performance of six map-making codes: Jscanam, MADmap, SANEPIC, IDL Scanamorphos, Unimap, Tamasis. Following the document release, the PACS ICC, with the endorsement of the Herschel Science Team and Herschel User Group, decided to implement Unimap in the SPG pipeline for a target SPG 13. Given that the Unimap implementation in SPG encountered some delay, and that other codes (e.g. MADmap, JScanam) were greatly improved in the meanwhile, the ICC requested a re-assessment of the status of the various software, this time limiting the challenge to the codes either already present in the pipeline (MADmap, JScanam), or under consideration for implementation, i.e. Unimap. A second report was produced in 2014.

The two challenges were carried out following a common philosophy, namely: first a selection of representative datasets was done, assuring that the chosen fields contained both faint and bright sources, and/or flat/highly structured background; then the selected data sets were processed with the map-making codes participating in the challenge; finally several metrics were used to evaluate the performance of the codes. The main metrics were: 1) power spectrum analysis; 2) difference matrix analysis; 3) point-source photometry analysis. Metric 1) consisted of computing a 2-d power spectrum from the final maps, and allowed the estimation of the amount of flux-loss on different angular scales. Metric 2) was applied by taking the difference between the maps generated by the different codes and a reference map assumed to be artefact free. This metric was a powerful tool for revealing potential residual artefacts in the maps. Metric 3) consisting of performing photometric measurements of faint and bright sources in the maps generated by the various mappers, while comparing the measured fluxes to reference values. This metric made it possible to test the photometric accuracy of each method.

As a result of the first challenge, JScanam, Unimap and MADmap turned out to have the best performance among the participating map-making codes, while the second challenge highlighted the slight superiority of JScanam and Unimap compared to MADmap. As a consequence, both methods (JScanam and Unimap) were implemented in the SPG environment and used for the generation of the legacy archival products, while MADmap was provided to users, in the form of a HIPE interactive pipeline script, as an alternative mapping method.

9.1.2 Chop-Nod

There are a number of differences in the data structures of chop-nod and scan-map observations that are reflected in the processing steps and the tasks that are applied. In short, chopped data do not need high-pass filtering nor deglitching. The latter is done automatically when co-adding the individual frames of a chopper position via a sigma-clipping algorithm. In addition, the final map is created with a shift-and-add procedure that combines the four images of two chopper and the two nod positions into a single combined signal.

The chop-nod processing pipeline works on sliced data (*Frames* products) and starts the processing from Level 0. The default slicing rule structures the data according to the nod cycles. The tasks internally loop over the slices when performing the processing steps.

The basic calibration steps are done first: saturation and bad-pixel flagging, adding basic pointing information, applying flat-field and responsivity correction. Then the specific chop-nod-specific calibrations are applied, starting with the calibration of the chopping mirror. Here, the digital position sensor readout is converted into chopping angles, so that data that were taken during the transition between two chopper plateaux is masked, i.e. the chopper was neither at the off nor the on position. Then the particular chop/nod pattern for the observation is recognised. During the planning of the observation the observer could specify whether the chopper should perform a dithering pattern. This displaces the on and off positions by a few fractions of a pixel for each chopping cycle.

There are four readouts per chopper on- and off-position. The corresponding flux values are averaged. The first of each of the four readouts are discarded as it is still affected by the chopper movement. The pointing information is then added to each detector pixel.

Next is to produce the differential signal of the chopping cycles per dither position and subtract a constant signal component that is dominated by the telescope mirror emission. At this stage, a few flux corrections that are based on a thorough investigation of detector response effects are applied. Note that the order of applying these corrections matters. The individual corrections are:

- Detector non-linearity: For very high source fluxes, the bolometers exhibit a non-linear relationship between the incident signal and the detector response.
- Evaporator temperature: The temperature of the evaporator of the 3He cooler has a small but measurable effect on the detector response (Balog et al., 2014).
- Scan-map based flux calibration scheme: The flux calibration of the PACS photometer is based on scan-map measurements, which introduces a time-dependent flux scaling difference for chopped observations (Nielbock and Klaas, 2013).

Then the three dithering positions are averaged. At the same time, a sigma-clipping algorithm is applied to account for and mask out glitches.

With a full set of differential signals of the chopper cycles having been created, the nod positions are next subtracted from each other. In this way, small-scale differences in the telescope background due to the varying line-of-sight caused by the chopper positions cancel out. Finally, all the data are combined into a single coherent signal timeline. If the object is bright enough, one should be able to see the characteristic 2x2 chop/nod pattern on each of the individual frames.

To improve the SNR, the flux of the four object images are combined with a shift-and-add algorithm. This is done per slice, and produces one map each. In this way, only the centre of the map contains the valid co-added image of the source. The eight images around the central one are to be disgarded. In particular, they should not be used to try to improve the SNR of the target. The central image is already the final result. This image cube is finally merged to a single map product by applying the *mosaic* task.

The result is a single Level 2 map that contains the final image and a coverage map. Finally, a noise map is produced from the coverage map and added to the Level 2 product.

9.1.3 PACS–SPIRE parallel mode

The processing of the PACS part of the PACS–SPIRE parallel mode observations is identical to that of the standalone PACS observations. The PACS part of the data can be downloaded and processed independently from the SPIRE part.

9.2 Spectroscopy pipelines

There are a number of spectroscopy pipeline scripts offered in HIPE. Each of the four main AOT divisions – chop-nod line, chop-nod range, unchopped line, unchopped range – has one main pipeline, which is that used also by the SPG processing. Additional pipeline scripts are offered for all four AOT variations: one for both of the unchopped modes, to apply specific transient-correction tasks; and a few extra for the chop-nod modes, being a point-source pointing-offset correction script, a script to create separate on-source and off-source cubes, and a script that applies the calibration-block flux-calibration method). Here we explain the SPG scripts, as the observations a user gets from the HSA were processed through these. The additional pipelines are summarised in Sec. 9.2.2, and explained detail in the PDRG (spec).

A summary of the product levels and the pipeline processing for a standard spectroscopy observation is given in Table 9.2.

Table 9.2: Summary of the levels in a spectroscopy observation and the main pipeline-processing steps

Level 0	Raw data, formatted from the raw telemetry by an external pre-processing stage. The scientific data are in products called *Frames*, the data therein being the measured ramps, i.e. the fitted slopes of the signal (Sec. 2.5.5) from the 16×25 detector arrays. Other products used by the pipeline are: instrument status table, the spacecraft pointing, time correlation, spacecraft housekeeping information, raw data for some pixels.
Level 0.5	Engineering conversions, timing and pointing information computed, bad-data masking, data organised in blocks. For SSOs the coordinate system is set so the object is in a fixed position on the sky at all times. Level 0.5 data are signal timelines, uncalibrated but with the first spectral and spatial conversions done.
Level 1	Glitch masking performed, and the data are organised into the first cube of the pipeline, with dimensions $5 \times 5 \times$[nr. readouts]. The signal of chop-nod AOTs are dark- and background-subtracted and for unchopped AOTs are dark-subtracted. Level 1 data are organised as timelines and are calibrated: Jy for unchopped AOTs and "telescopes" for chop-nod AOTs.
Level 2	Data are spectrally flatfielded and a second de-glitching performed. A common wavelength grid is created for each spaxel of the cube and the signal spectrally resampled along this grid, to create "native" (aka "rebbined") cubes. For unchopped line scans the background is subtracted. For pointed and tiling observations, interpolated cubes are created. For mapping observations the cubes created depend on the AOT: the choices are drizzled, projected, and interpolated. The stddev/error array is computed. Rebinned cube tables are created from the rebinned cubes and point-source tables created for all pointed AOTs. Level 2 data have units of Jy/pixel, where the "pixel" refers to the spaxel in the cube, which is a $9.4''$ spaxel for rebinned cubes, and a smaller (1.5–$3''$) for all other cubes.
Level 2.5	For unchopped range-scan observations with an associated off-source observation, the two observations are reduced to Level 2. Extended processing then subtracts the off-source data from the on-source data to produce the same set of, background-subtracted, products in Level 2.5
Level 3	This level is provided for pointed chop-nod observations of SED mode for which sufficient observations were performed to cover the full PACS range of the same source. The red and blue point source tables for all observations are concatenated into a single table.

9.2.1 The SPG pipelines

The first levels of the SPG pipeline, and what steps take place to produce each level, are outlined in Fig. 9.1 (Level 0 to 1), Fig. 9.2 (Level 1 to 2 for chop-nod AOTs), and Fig. 9.2 (Level 1 to 2.5 for unchopped AOTs). The very final cubes and tables produced by the pipeline (for all AOTs) are shown in Fig. 9.4. The information in these figures is discussed in the following sections.

9.2.1.1 Level 0 to 0.5: AOT independent

The steps in this part of the pipeline do basic corrections and conversions. The end result is a *Frames* product (HPS3DFIT[R|B] in an ObservationContext). The steps are:

- Extract the pointing product and the orbit ephemeris (to later add pointing information), the

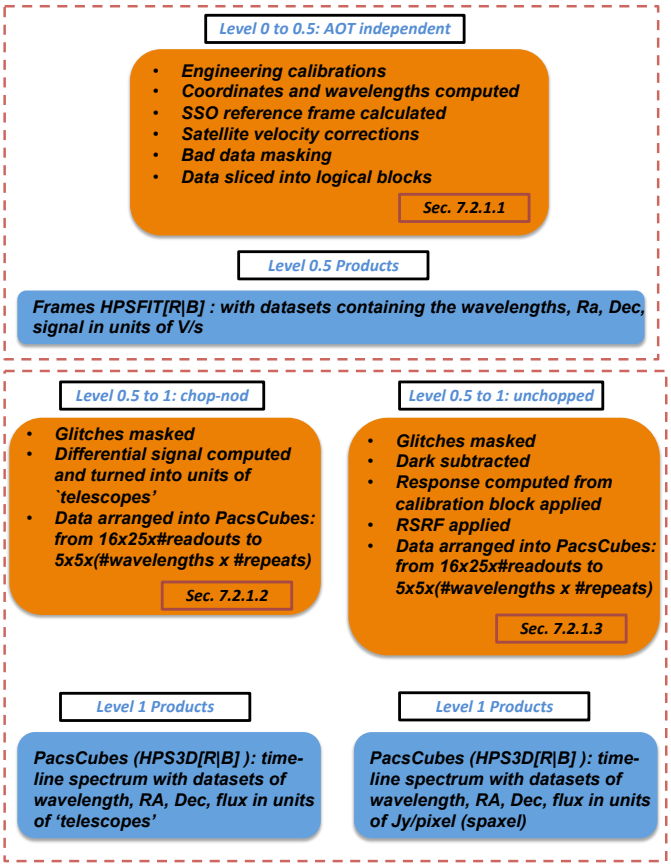

Figure 9.1: The SPG pipeline Levels 0 to 1 (addendum: section references should being with 9, not 7)

horizons product (used for SSO coordinate setting), and time correlation (used to set the UTC in the data).

- Extract two science data products – the *Frames* containing all the science data and the *RawRamps* which contain slopes for a single pixel and will be used to detect saturation – and the DecMec data product, which contains the detector and mechanism information, and will be used to organise the data into logical blocks.

- Mask out saturated data in the *Frames*, adding the masks SATURATION and RAWSATURATION.

- Convert the units from ADU to V/s (calibration file `Readouts2Volts`), detect where the calibration block data lie, add the UTC to each readout.

- Add the pointing information of the central spaxel (uses the `Siam` calibration file), and for SSOs, move the target to a fixed position on the sky.

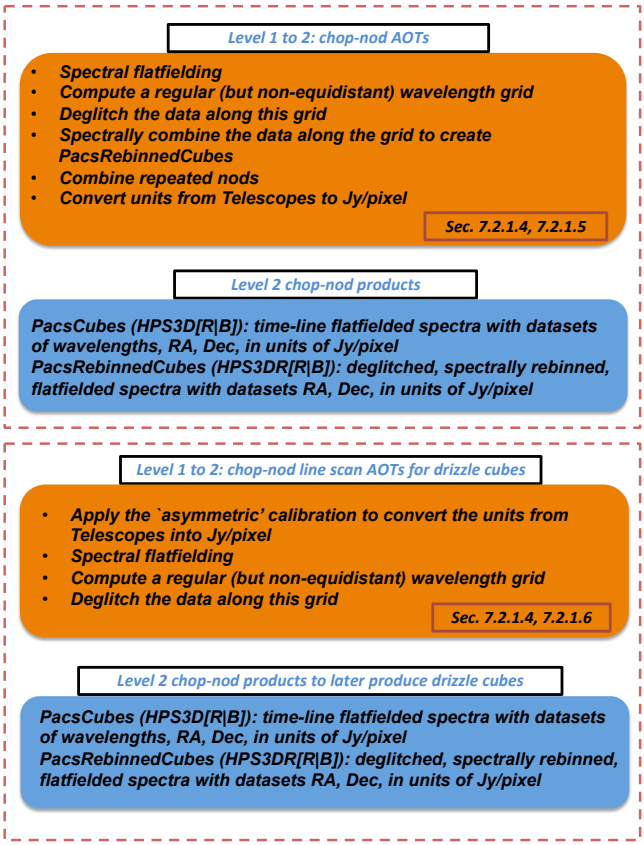

Figure 9.2: The SPG pipeline Levels 1 to 2 for chop-nod AOTs (addendum: section references should being with 9, not 7)

- Add grating and chopper information (using calibration file `ChopperThrowDescription`) and convert the chopper readouts to an angle with respect to the focal plane unit and the sky (calibration files `ChopperAngle` and `ChopperSkyAngle`).
- Add the sky positions (the RA, Dec datasets) to each pixel (calibration files `ArrayInstrument` and `ModuleArray`).
- Add wavelengths to each pixel (calibration file `WavePolynomes`). Correct the wavelengths for the spacecraft velocity, using the pointing, orbitEphemeris and TimeCorrelation product. This task also sets a mask, OUTOFBAND, to flag data-points in spectral regions that lie outside of the wavelength range of the band.
- Find the logical blocks of this observation (calibration file `ObcpDescription`).
- Mask out bad and noisy pixels in the masks BADPIXELS and NOISYPIXELS (using the calibration files `BadPixelMask` and `NoisyPixelMask`). Mask the data taken while the chopper

and gratings were moving, placing them in the masks UNCLEANCHOP and GRATMOVE. None of masked data will be used furthermore.

- Finally, "slice" the data into logical blocks defined by spectral range, raster position, nod position and cycle, on or off position, and per band. In this way, the data can be reduced with the pipeline while still honouring differences in pointing on sky (for mapping observations), wavelength range (as requested by the observer), nod position (chop-nod AOTs) and on or off pointing (unchopped AOTs).

The task that masks for saturation requires a little more explanation (see also Sec. 8.2.6). In the main mask, SATURATION, a flag is set for all datapoints above the limit found in the calibration file `SignalSatLimits`. A warning mask, RAWSATURATION, is also added, to indicate *potential* saturation. This warning is based on an inspection of the raw slopes that are found in *RawRamps*. These raw slopes are a more secure way to detect saturation, however it was not possible to downlink from *Herschel* the raw slopes for all 16×25 pixels for both detectors: the slopes from only one spectral pixel of the red and the blue detector each were downlinked. Therefore, the slopes from these two pixels are compared to the raw saturation limits in the calibration file `RampSatLimits`, and if saturation is detected there, then all the readouts taken *at that same time* for *all* the pixels of *all* the modules are *also* flagged. This mask was intended only a warning: this single pixel is not only the most responsive (and hence will saturate earlier), but being in the centre of the FoV is more likely to have the brightest part of the source in it (and hence more likely to have high fluxes). *Therefore, saturation in this pixel did not necessarily mean saturation in all pixels of all modules.* It was intended that the users inspect their data to decide whether to use this warning mask, or not. However, while this mask is not explicitly activated in the pipeline when the final products are created, it *is* activated for the spectral flatfielding task, and this effectively means it is activated also the final product creation. *Hence, for the few PACS observations of extremely bright sources where the centre of the FoV is saturated, it is possibly that the outer parts of the FoV are incorrectly masked out as saturated.* Data masked as saturated – as with all activated masks – do not find their way into the final products, and these datapoints will be NaNs instead. Saturated data are usually easy to spot: bright spectral lines with missing centres or very high-flux continuua with missing stretches.

9.2.1.2 Level 0.5–1: chop-nod AOTs

The steps in this part of the pipeline are:

- Mask out glitches (adding the mask GLITCH), going over the timeline spectrum of each of the 16 pixels of each of the 25 modules.
- Convert the signals to the value appropriate for a standard capacitance setting (if that was not used: uses the `capacitanceRatios` calibration file).
- Calculate the differential–ratio signal by subtracting the off-source readouts from the on-source readouts and dividing by the sum (see below). At the same time, the data are dark and background subtracted and converted to units of "telescopes".
- Convert the format of the data from *Frames* (with dimensions $16 \times 25 \times$no. of readouts) to the first cube of the pipeline, *PacsCubes*, with dimensions $5 \times 5 \times$[$16 \times$no. spectral repeats$\times$no. wavelength points]. In each of the 25 spaxels of this cube are the spectra in each from the

16 pixels, these spectra themselves being repeated if multiplied scans on the wavelength range were requested.

The differential–ratio signal. The standard observing pattern for chop-nod observations had two consecutive on-on-off-off-off-off-on-on chopping patterns per grating plateau[1] (see Sec. 3.3.1.1). The task breaks this pattern into four blocks (two each of on-on-off-off and off-off-on-on), and computes the pairwise difference–ratios for each: (on(a)-off(b))/(on(a)+off(b)), where a and b are $1^{\rm st}$ and $2^{\rm nd}$ chopping block. All four possible combinations of the ons and offs in the blocks are computed. This subtracts the telescope background signal (the off-source signals) *and* converts the signals into units of "telescopes" (this calibration is explained in Sec. 8.2.2.1). Conversion from telescopes to Jy requires multiplying by a smoothed telescope background spectrum, and this is done near the end of the pipeline.

The science data at the end of this part of the pipeline are *Frames* and *PacsCubes* (HPSFIT[R|B] and HPS3D[R|B] in an ObservationContext). These products contain exactly the same data, but organised differently. Both have datasets of wavelength, RA, Dec, are stored in timeline order, and are calibrated in units of "telescopes".

For the range scan AOTs, the next part of the pipeline actually starts on the *Frames* and for line scan AOTs, on the *PacsCubes*. This is because of formalities with the way the first task of Level 2 accesses these products.

9.2.1.3 Level 0.5–1 for unchopped AOTs

The steps in this part of the pipeline are:

- Mask out glitches (adding the mask GLITCH), going over the timeline spectrum of each of the 16 pixels of each of the 25 modules.
- Convert the signals to the value appropriate for a standard capacitance setting (if that was not used: uses the `capacitanceRatios` calibration file).
- Compute the response for that observation, comparing the signals of the calibration block data taken at the beginning of the observation to the values in the calibration files `observedResponse` and `calSourceFlux`.
- Subtract the dark current (`darkCurrent` calibration file).
- Divide by the relative spectral response function, taken from the calibration files: `rsrfR1`, `rsrfB2A`, `rsrfB2B` or `rsrfB3A` (depending on the band of the data).
- Divide by the response computed previously.
- Convert the format of the data from *Frames* (with dimensions $16 \times 25 \times$no. of readouts) to the first cube of the pipeline, *PacsCubes*, with dimensions $5 \times 5 \times$[$16 \times$no. spectral repeats$\times$no. wavelength points]. In each of the 25 spaxels of this cube are the spectra from each of the 16 pixels, these spectra themselves being repeated if multiplied scans on the wavelength range were requested.

[1] plateau refers to a single chopper, nod, or grating position where a continuous sequence of data-points were collected

The science data at the end of this part of the pipeline are also *Frames* and *PacsCubes* (HPSFIT[R|B] and HPS3D[R|B] in an ObservationContext). These products contain exactly the same data, but organised differently. Both have datasets of wavelength, RA, Dec, and which are stored in timeline order. These data are calibrated in units of Jy/pixel.

For the range scan AOTs, the next part of the pipeline actually starts on the *Frames* and for line scan AOTs, on the *PacsCubes*. This is because of formalities with the way the first task of Level 2 accesses these products.

9.2.1.4 Level 1–2: common to chop-nod and unchopped AOTs

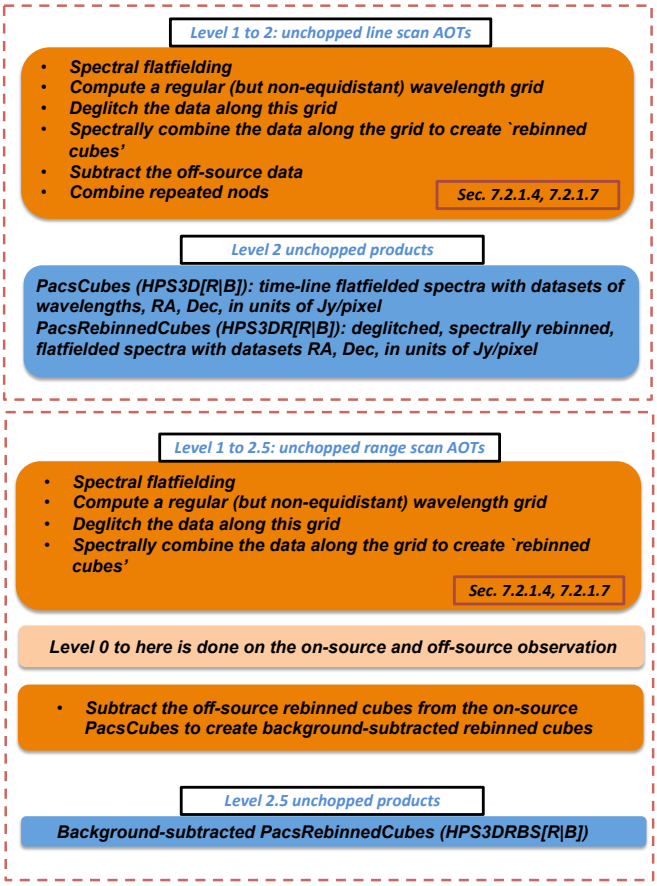

Figure 9.3: The SPG pipeline stages 1 to 2.5 for unchopped AOTs (addendum: section references should being with 9, not 7)

Many of the steps in this penultimate part of the pipeline are the same for the chop-nod and unchopped AOTS.

1. The spectral flatfielding. For range scans this is done on the *Frames* of Level 1 which are subsequently turned into *PacsCubes*, and for line scans it is done on the *PacsCubes*. Various

flatfielding-related masks are created, the most interesting of which is: NOTFFED (for data that fall into the order leak regions (Sec 5.4).

2. Build a single wavelength grid from the wavelengths present in the *PacsCubes*.

3. Detect and mask outliers along this regular wavelength grid (create mask OUTLIERS).

4. Then spatially rebin the data of the *PacsCubes* in each spaxel: averaging the datapoints that fall into each bin of the wavelength grid (in this way improving the SNR). The output cubes are called *PacsRebinnedCubes* (HPS3DR[R|B] in an ObservationContext). When these *PacsRebinnedCubes* are created, most of the previously-masked data are excluded: those for all instrument movements (Level 0–0.5 pipeline), the glitches and outliers, saturated data (as explained in Sec. 9.2.1.1).

9.2.1.4.1 The spectral flatfielding

The flatfielding task is explained in detail in the PDRG (spec). The flatfielding is done on *Frames* for range scan AOTs and *PacsCubes* for line scan AOTs, but this is a formality of the way the tasks work, these two products contain exactly the same data as each other by the time the flatfielding is done.
The essence of the task is this:
In each spaxel of the IFU of PACS, there are 16×no. repeats spectra, from the 16 separate detectors that gather the spectrum for each spaxel. These spectra are usually slightly offset wrt. each other, because of independent response drifts during the observing and because of the slight response differences of the 16 detector pixels. If you were to average the 16 sets of spectra together, the scatter in the resulting spectrum would not just reflect the noise in the individual spectra, but also the offset of each spectrum wrt. the rest. In other words, the instrumental signature will not have been completely removed. To overcome this, each of the 16 spectra of each spaxel are normalised to the flux level of the *mean* spectrum of the entire spaxel: this brings those spectra with fluxes too high, down, and those spectra with fluxes too low, up. The mean spectrum of the spaxel is again created, now without the detector offsets.
For line spectroscopy, a few steps are performed before the actual flatfielding task, to identify and then mask out spectral lines in each spectrum of each spaxel of the cube so that the normalisation is done on continuum signals only. Note that the masking of lines does not work well for line-forests or for absorption lines, and the flatfielding may be less reliable for these cases. For range spectroscopy ($> 5\,\mu$m), rather than identifying the lines to mask them out, the spectra are heavily smoothed and then fitted with a spline, and these fits are used to compute the normalisation factors.
In the interactive pipeline scripts, the flatfielding tasks allow users to limit the flatfielding to certain wavelength regions, e.g. to concentrate on a certain part of the spectrum, but of course this is not done in the SPG pipeline. However, what *is* done in the SPG pipeline is to *not* flatfield the regions that lie in the "red leak" region above 190 μm, as this region is anyway affected by a leak (Sec. 5.2.3), and the blue end below 55 μm is also cut out. These data are flagged in the mask NOTFFED.

9.2.1.4.2 The wavelength grid

The wavelength grid created in step 2 is used for the spectral rebinning of a *PacsCube* into a *PacsRebinnedCube*. When doing this, the average of the unmasked *PacsCube* fluxes in each bin of the

wavelength grid become the fluxes in each spectrum of the *PacsRebinnedCube* (for each spaxel independently), and the scatter in those datapoints is added to the "stddev" dataset of the rebinned cube. The wavelength grid chosen will obviously dictate the spectral sampling achieved in the spectra of the rebinned cubes (not the resolution, only the sampling). The bins size in the wavelength grid scales with the spectral resolution, which scales with wavelength, such that bins are generally smaller at shorter wavelengths and larger at longer wavelengths. This is done so that the spectral sampling can be at least Nyquist at all wavelengths (plots of the resolution vs. wavelength for each band can be found in the PDRG (spec), where plots of spectral lines for different choices of grid can also be found). The grid parameters used by the pipeline task to create the SPG products can be found in the "upsample" and "oversample" meta data (see meta data tables in the PACS Products Explained).

9.2.1.5 Level 2: chop-nod AOT steps

The steps unique to the chop-nod AOT are:

- Combine repeat nods, and then add nod A and nod B.
- Compute the telescope background spectrum for each observation (includes the effect of telescope aging), to turn the fluxes from "telescopes" to Jy/pixel (actually Jy/spaxel, but that unit was not allowed in HIPE).

In Sec. 8.2.2.1 to learn more about the flux calibration concept, including the importance of combining nod A and Bs to have properly-calibrated final cubes.

A note about the *PacsCubes* (HPS3D[R|B]) that are put into the Level 2 of an observation context for all chop-nod AOTs. It was a requirement of the HSC that all products in Level 2 be fully calibrated, however for the chop-nod AOTs the calibration to Jy/pixel only occurs near the end of the level, for the rebinned cubes. In order to have Level 2 *PacsCubes* also be calibrated, these cubes were converted from "telescopes" to Jy/pixel using the so-called "asymmetric calibration" (Sec. 8.3.2.1). These *PacsCubes* are not the ones used in the Level 2 part of the pipeline except for the creation of drizzled cubes, which is explained next.

9.2.1.6 Level 2: chop-nod AOT steps for creating drizzled cubes

For Nyquist and oversampled line-scan chop-nod AOTs, for which drizzled cubes are one of the final pipeline products, it was necessary to apply the flux calibration (from "telescopes" to Jy/pixel) to the *PacsCubes*, i.e. at the beginning of the Level 2 pipeline rather than at the end, since *drizzle* works only on *PacsCubes*. However, the calibration task used in the pipeline does not work on *PacsCubes*-formatted data. Therefore a so-called "asymmetric" calibration was adopted, which had been created for a different pipeline script and which does work on *PacsCubes*. The calibration data in these two calibration files (asymmetric and standard) are only very slightly different to each other: the calibration are explained in Secs 8.3.2.1 and 8.2.2.1. Note that all other cubes and spectrum tables in these observations are created with the standard calibration.

9.2.1.7 Level 2/2.5: unchopped AOT steps

The steps taken for unchopped range- and line-scan AOTs differ slightly because of the way the off-source (the "telescope background") data were observed. For line scans, the off-source pointings

were taken during the observation of the source itself, but for range scans it was necessary to request a second, off-source, observation. Hence each observation needed to be reduced before being combined.

After the common pipeline steps explained in Sec. 9.2.1.4, those unique to the unchopped AOTs are related to the background subtraction:

- *For unchopped line scans* the background subtraction is done using the separate on-source and off-source blocks in the observation. The cubes from repeated nods are then combined. The science data that are added to the ObservationContext are the *PacsCubes* and *PacsRebinnedCubes* (HPS3D[R|B] and HPS3DR[R|B]) which are both flatfielded, background subtracted, and have units of Jy/pixel.
- *For unchopped range scans*, the Level 2 data at this point are either of the source (the on-source observation) or of the telescope background (the off-source observation). The next stage is for the off-source cubes to be subtracted from the on-source cubes. For this, the *PacsRebinnedCubes* from the off-source observation were used, but the *PacsCubes* from the on-source observation: the reason being that *PacsRebinnedCubes* are created from *PacsCubes* and are effectively a smoothed version of them, hence the subtraction introduces less noise than otherwise.

9.2.1.8 Final products (all AOTs): Levels 2, 2.5 and 3

The final pipeline steps, run on all AOTs, start with the *PacsRebinnedCubes* or *PacsCubes*, and create mosaic cubes and spectral tables therefrom. The type of cubes and tables create depend on the observing mode – for more information, see the explanation and tables in Chap. 10.4. Here we summarise this information.

9.2.1.8.1 Mapping observations

For mapping observations two or three types of mosaic cubes could be created (Sec. 10.4.2.2), and one spectral table (Sec. 10.4.2.3). All mosaic tasks start by creating a spatial grid encompassing the entire sky field of the mapping sequence, and they map the fluxes of the input cubes (one per raster position) onto this grid. The difference between the tasks is the way this mapping is done. The simplest task is *specInterpolate* and it creates interpolated cubes: it uses Delaunay triangulation to create the output grid from the input grid points, and does a simple interpolation of the input fluxes onto this grid. As it uses a basic interpolation, the result is effectively an undersampled version of the observed field: this is why these cubes are recommended only for undersampled observations, where a better spatial sampling is anyway not available. A more complex task is *specProject*, which creates projected cubes: the sky grid is created by overlaying the input grids and projecting the fluxes of the input cubes onto this grid, weighting by the overlapping spaxel areas. These cubes can be used for any type of observation, but with some disadvantages for undersampled observations (the spaxel-shapes and spaxel-grid pattern of the original footprints can clearly be seen). The most complex task is *drizzle*, which creates drizzled cubes: its output grid has spaxel sizes that are optimised to Nyquist-sample the beam at the wavelength of the observation, and the fluxes on this grid are created by the drizzle algorithm (Fruchter and Hook 2002; Regibo 2012). These cubes are created only for Nyquist and oversampled line scans – as the spaxel size is optimised to the wavelength of the observation, the wavelength range of the observation must be very short. All of these tasks are explained in more detail

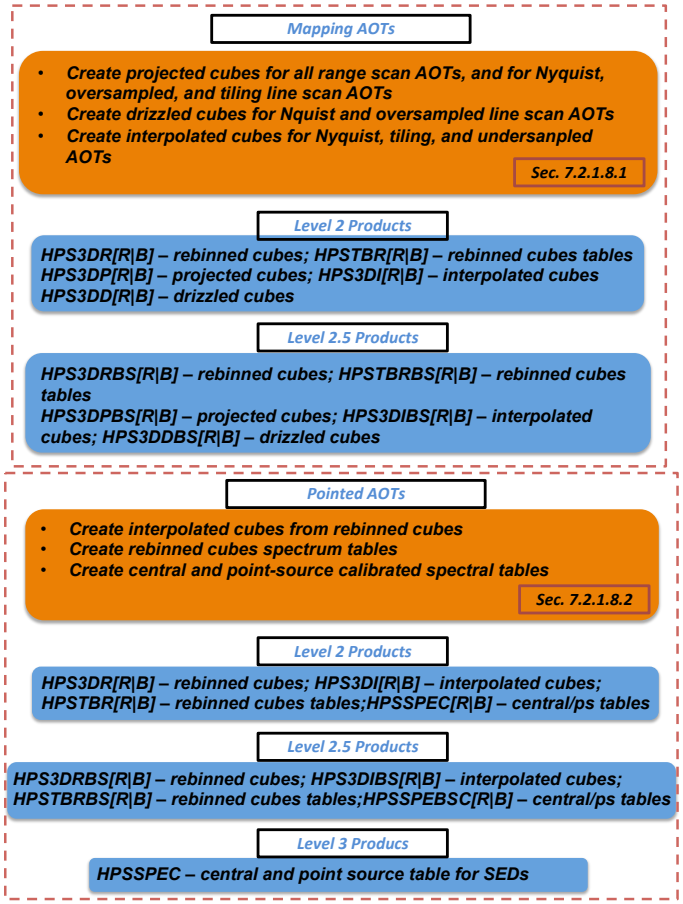

Figure 9.4: The final science-grade products created at the end of the SPG pipeline (addendum: section references should being with 9, not 7)

in the PDRG (spec).
Which of the mosaic cubes are produced depends on the type of mapping AOT used to create the observation. The decision is made for each camera separately, hence a different type of cube may be provided in the red and blue camera for an observation. See Sec. 10.4.2.1 for information about the definitions of the different mapping modes.

- For *Tiling* observations, i.e. with a large offset and taken with the purpose of mapping a large sky field: interpolated cubes (spaxel size $3''$) and projected cubes (spaxel size $1.5''$) are produced.
- For *Nyquist-sampled range spectroscopy*, with offsets of about $\frac{1}{3}$ to $\frac{1}{2}$ a cube: interpolated and projected cubes are produced, both with spaxel sizes of $3''$.
- For *oversampled range spectroscopy*, offsets much less than a spaxel: only the projected cubes (spaxel size $3''$) are produced.
- For *Nyquist and oversampled line spectroscopy*: drizzled and projected cubes are created. The

spaxel size is optimised to the central wavelength and is generally $< 3''$. The drizzle cubes are created from the *PacsCubes*, whereas all other mosaic cubes are created from the *PacsRebinnedCubes*.

Tables 10.7 and 10.6 can be used to work out what mapping mode any particular observation had.

9.2.1.8.2 Pointed observations

For pointed observations, the SPG creates two mosaic cubes (Sec. 10.4.2.2), and two or three spectral tables (see Sec. 10.4.2.3).

- The *cubes* created are: interpolated cubes (spaxel size $3''$) and projected cubes (spaxel size $1.5''$).
- The *spectral tables* created are: the data of the rebinned cubes, but organised as a table instead of as a cube; a table with the central-spaxel spectrum and two or three point-source corrected spectra, both taken from the *PacsRebinnedCubes*.
- One spectrum table is also provided at Level 3 for the chop-nod pointed observations taken in SED range spectroscopy mode: the table of point-source corrected spectra, with the red and blue camera results combined into a single table (for all other products, the red and blue products are separate), and with the data from all observations that were taken of that source in SED mode, combined.

For pointed observations of extended sources, science can be done with both the rebinned and the interpolated cubes. For pointed observations of point source which are located in the central spaxel and have no contaminating emission, the point-source spectrum tables contain the necessary science product. For slightly-extended sources (that still fit fully in the central 3x3 spaxels) the *PacsRebinnedCubes* together with the appropriate tasks should be used to extract a fully calibrated spectrum (for which, however, the shape of the source is an input).

9.2.2 The interactive pipelines

The range and use of the interactive pipelines provided in HIPE to reduce PACS spectroscopy observations is explained in the PDRG (spec). Here the purpose of the most interesting of these interactive scripts is explained.

9.2.2.1 Chop-nod: two flux calibration schemes (and checking for off-source contamination)

For the chop-nod modes (line and range scan), two pipeline scripts that differ on the flux calibration scheme are offered: "Telescope normalisation" (TN) and "Calibration source and RSRF" (CS). These two calibration schemes are explained in Sec. 8.2. The first script applies the same calibration as used in the SPG pipeline for chop-nod observations: that based on the spectrum of the telescope itself. The second script was the pipeline created for PACS spectroscopy observations in the first few years of

the mission, and the calibration scheme is the same as used for unchopped observations: using the data from the internal calibration sources and the RSRF. In fact, with minor changes, this pipeline is the same as that used to produce the 'red leak' HPDPs (Sec. 10.4.4.2). The 'Telescope normalisation' pipeline is used for the SPG reductions because it gives usefully better results for the bulk of PACS observations.

The TN pipeline script is essentially the SPG script, and the final products produced by running this script in HIPE would therefore be the same as those in an HSA-obtained observation.

When would it be appropriate to re-pipeline an observation using CS script? The two calibration schemes produce results consistent with each other, it is therefore not particularly useful to run the script to check on that. One – perhaps unexpected – use of this pipeline script for archive users is to look for *spectral contamination in the off-source pointings*. In the TN script, the off-source chopper data are subtracted from the on-source chopper data as a ratio (an $(A-B)/(A+B)$), but in the CS script it is a simple subtraction (an $A-B$). Hence, if there is contamination in the off-source chopper data (e.g. line emission from sources that are in the off-source pointings only), the spectra in the cubes resulting from the two schemes will differ. For the case of line contamination, there should be a sharp difference at the position of the contaminating line in the Level 2 cubes. For the case of continuum contamination the difference will be in the continuum level, and perhaps more difficult to establish as it will depend on the relative level of contamination.

If running the CS script in HIPE to check for contamination, we recommend running the TN one as well, to be sure that exactly the same parameters are used so that the only difference is the calibration scheme. We also point out that the degree of difference between the two, in the presence of contamination, depends on the level of the contamination compared to the "wanted" data, and *while a difference does point to contamination, a lack of difference does not definitively point to no contamination.*

9.2.2.2 Chop-nod: split on- and off-source (and dealing with contamination)

If it is established that there is unwanted emission in the off-source positions – either because the CS script produces very different results from the TN script or because unexpected absorption features can be found in the Level 2 cubes – dealing with that contamination is not so simple, as the off-source data are subtracted from the on-source data at Level 0.5 for chop-nod AOTs. However, the "Split on off" interactive pipeline script that is offered in HIPE can be used to create separate on-source and off-source cubes. The SNR of these cubes will be (slightly) lower than that of the SPG cubes (because not doing the normal off-source subtraction produces an inferior result), however this does provide an easy way to produce a contamination-free result. If working with such cubes, please remember that the on-source cubes will *not* have been corrected for the off-source spectrum: since this spectrum is primarily that of the telescope, the on-source cubes will have a *very* different continuum level than the SPG cubes.

The calibration scheme used in this pipeline is that of the CS pipeline script (see above), i.e. it uses the internal calibration block rather than the telescope spectrum.

"On-source Off-source" HPDPs have been produced for all chop-nod observations, where the on-source and off-source cubes are provided separately to each other (Sec. 10.4.4.2).

9.2.2.3 Chop-nod: pointing-offset point-source pipeline

For chop-nod pointed observations of point sources, an interactive pipeline script is offered in HIPE to fully reduce the data (starting from Level 0.5 is sufficient) and to produce, as the final science product, a point-source calibrated spectrum. The calibration scheme used in the pipeline is that of the telescope normalisation pipeline (i.e. that of the SPG products), and the science-use end result of this pipeline is a point-source calibrated spectrum. This difference in this script compared to the SPG scripts is that the POC script includes tasks that can compute and correct the flux levels for pointing offsets and pointing jitter. If the pointing jitter was bad during an observation, or if the point source is offset from centre of the FoV by up to $\sim 10''$ (one spaxel), the point-source spectrum resulting from this script can have a cleaner shape and a slightly higher continuum level than the point-source spectrum provided in the observations gotten from the HSA. This script is particularly useful for sources with broad-band features or for which the continuum shape is very important – for sources where emission lines are the only interest, differences are expected to be less significant. The correction works best for brighter sources (> 10 Jy continuum level) and those taken in the range scan mode – for faint sources and line scans it is strongly recommended to compare the results to the equivalent point-source spectra obtained from the SPG product before deciding which result to adopt. The pointing offset correction technical note can be found on HELL (here).

9.2.2.4 Chop-nod: drizzled cubes

For chop-nod line scan mapping observations for which drizzled cubes are to be created, the interactive pipeline script for '..drizzled cubes' is offered. The flux calibration scheme used to create chop-nod drizzled cubes is the TN scheme, i.e. the same as used for all other cubes, however the implementation differs for formal reasons (the product the calibration is applied to when creating drizzled cubes has a different organisation that the product the calibration is applied to when creating the other cubes). For those wishing to know more, the PDRG (spec) can be consulted. However, this pipeline script does the same as the SPG pipeline for the drizzled cubes, and hence will product the same results as obtained from the HSA.

9.2.2.5 Unchopped: transient corrections

For the unchopped modes (line and range-scan), there are two pipeline scripts offered in HIPE, which differ only in the specific tasks they use to correct for transients. No such correction is carried out by the SPG pipelines, however the SPG script is otherwise exactly the same as the two interactive scripts.

The most recent scripts (called "...with transient correction" in the pipeline menu) should be preferred over the original (called "Calibration source and RSRF") if re-reducing data in HIPE, as its transient correction tasks are more effective: see Fadda et al. (2016) for more information on these tasks. *However*, it should be noted that while these tasks have been used to produce good results for some targets (e.g. Fadda et al. 2016) they have not been tested on a wide range of observations. The user should check all intermediate results while running the scripts, and should compare the final rebinned cubes to the SPG rebinned cubes – the transients correction tasks should result in smoother and less noisy continuum spectra, but they *should not* substantially change the fluxes in the emission lines. Note that the continuum uncertainty in the unchopped mode is high (Sec 5.2.6) and using the transients correction tasks does not necessarily reduce this particular uncertainty.

Note added late in the post-operation phase: after testing out the "....with transient correction" pipeline scripts, it turns out that their transients correction tasks do a similar job improving the data as does the spectral flatfielding task, which is part of all pipeline and SPG scripts. Hence, most observations will probably not be dramatically improved after being processed by the interactive transients-correction pipeline scripts.

Contamination. However, there is one case where running the unchopped line-scan pipeline script in HIPE would be useful, and that is to check for contamination in the off-source pointings. Comparing the off-source and the on-source cubes for unchopped range-scan observations is easy, since the two can be found in the Level 2 of the separate observations. For unchopped line-scans, all pipeline scripts produce on-source and off-source cubes at Level 2, *however* these are not saved in the SPG product that is stored in the HSA. To check for contamination it will be necessary to run the unchopped line-scan pipeline script in HIPE. The "On-source Off-source" HPDP can also be inspected to check for contamination (Sec. 10.4.4.2).

f

Chapter 10

PACS data products

10.1 Introduction

In this chapter we explain the products created by the PACS SPG (systematic/standard product generator) pipeline run at the HSC and the Standalone Browse products (SBPs), which are specific SPG products provided with a first look purpose in mind. Highly-Processed Data Products, which are what the name implies, are also explained here. For some observations, interactively-reduced User Provided Data Products (UPDPs) are available in the HSA. These originate in the community, originally for the key programmes but also on a voluntary basis for other observations. Their content and format is not described here.

PACS products are provided via the HSA as: an *ObservationContext*, which is a wrapper (context) containing the raw data and the processed data products created by the pipeline for each observation; or as standalone FITS files wrapped up in a tarball.

- An **ObservationContext** includes raw science data, instrument and satellite housekeeping data, pointing data, and the SPG-reduced data from the various pipeline levels. The HSA offers the choice of downloading an entire ObservationContext, or only the contents of a specific Level (0–3). For photometry and spectroscopy both, the science-quality results are found in Levels 2 to 3, depending on the observing mode and science use of the data. To re-reduce the data in HIPE it is necessary to download an entire ObservationContext.
- The **SBPs** are a selection of Level 2, 2.5, and 3 products provided as individual FITS files in a tarball. They are intended to be easy to read into any software (although this is otherwise difficult only for the spectral cubes), and they represent the most useful products for a first look at the data; they are generally also suitable for science work if the user makes themselves aware of their limitations.
- **HPDPs** are products that have been manually processed at the HSC, and are intended to supplement or replace the equivalent product in the SPG ObservationContext. They are also provided as standalone FITS files wrapped up in a tarball, with a flat directory structure. A release note for the HPDP is provided in each download.

PACS ObservationContexts are discussed in detail in the PACS Products Explained (PPE), including how to navigate through the wealth of FITS files that make up an ObservationContext on disk. The

pipeline tasks that create all the products are explained in the PACS Data Reduction Guide (PDRG) for spectroscopy and photometry. A brief summary can also be found in the pipeline chapter (Chp. 9).

10.2 A PACS ObservationContext

For every new user release of HIPE, the entire Herschel archive was re-reduced automatically with a chosen set of pipelines (per instrument and per observing mode). The resulting SPG products were then made available through the HSA. The SPG processing for PACS ended with HIPE v 14.2.

All PACS data products are grouped into *contexts*. A context is a HIPE product that links other products together in a coherent structure, and can be thought of as an inventory or catalogue. The PACS processed observations consist of many contexts – one for each pipeline level – enclosed within one grand *ObservationContext*. There are up to six processing levels for any PACS observation: 0 (raw data), 0.5 (partially reduced), 1 (instrumental signature removed and astronomical units added), 2 (fully-calibrated cubes, images, or tables), 2.5 (combined Level 2 data from two related observations), and 3 (a combination of observations of the same field of view [phot] or of that source [spec]). In addition to the contexts containing these levels, an ObservationContext contains contexts for calibration products, for auxiliary products (e.g. telescope pointing, mirror temperatures etc.), and a quality control. The contexts found in an PACS ObservationContext are introduced in Fig. 10.1 and outlined in Tables 9.1 and 9.2. Entries that are common to both are listed in Table 10.1 – these products are used by the pipeline, but are not discussed any further in this chapter. It is the science-data contexts created by the pipeline processing are discussed here.

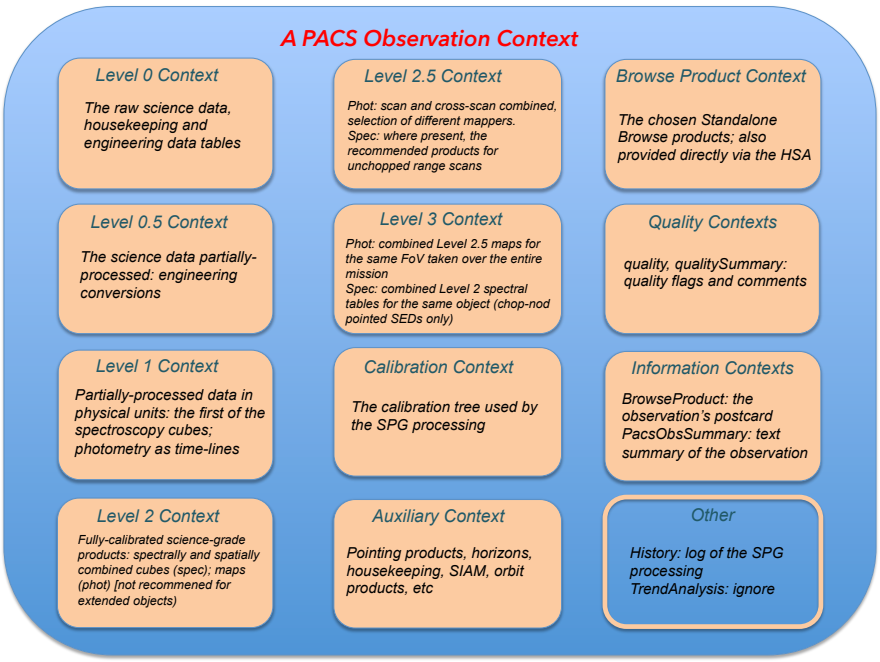

Figure 10.1: The general contents of a PACS ObservationContext

Table 10.1: The contents of an ObservationContext common to photometry and spectroscopy

Context	Description
PacsObsSummary	An observation summary (observer, date, observing mode, wavelength ranges, and comments)
History	A history of the SPG processing done to the observation, however this was added to continuously and can be difficult to interrogate usefully
Auxiliary	Satellite and instrument housekeeping, timing, pointing information, etc, required to run the pipeline
BrowseImageProduct	The "postcard" for the observation
BrowseProduct	The SBPs, which are also located in Level 2, 2.5, or 3
Calibration	The calibration tree that the SPG pipeline used to reduce the data
Quality	Contains a full history of the quality reports (flags added during the observing or processing) created during each SPG processing
QualitySummary	Contains the latest flags and any information added manually by the HSC that is relevant to the quality of the data or to the science possible with the observation. The qualitySummary is of more interest to archive users of PACS data than the quality entry
TrendAnalysis	To be ignored

10.2.1 Viewing an observation in HIPE

After downloading an observation into HIPE, the contents can be inspected using the ObservationViewer in HIPE. Fig. 10.4 is a screenshot of a spectroscopy observation viewed in HIPE; the outline of a photometry observation is very similar to what is shown there. The ObservationViewer allows one to inspect the contents of an observation, the datasets therein, their Meta data, and to open the appropriate data viewers on the products. It is also possible to send single products (maps, cubes, tables) to FITS files on disk from the viewer.

10.3 Photometry observations: pipeline products

The most important PACS photometry pipeline products are *Frames* and *SimpleImages* (although it is only the images that archive users will interact with). These each contain multiple datasets that are produced by the pipeline, such as fluxes, WCS, errors.

Fig. 10.2 is an overview of the photometry processing levels in an ObservationContext and their relationship to the SPG pipeline. Of most interest are Level 2.5 and 3 (and in a few cases, Level 2) and these levels are explained in this handbook. For those wishing to re-run the pipeline or wishing to use lower-level products, the PDRG (phot) and the PPE should be consulted.

10.3.1 Viewing a photometry observation on disk

Observations can be downloaded from the HSA as a tarball. When unpacked it produces a directory tree which has a similar layout to that of the ObservationContext in HIPE. Here the products most astronomers will be interested in are located in the Level 2, 2.5 and 3 directories. The maps in Level 2 have file names built as "hpacs" + the obsid + the level + product name + slice

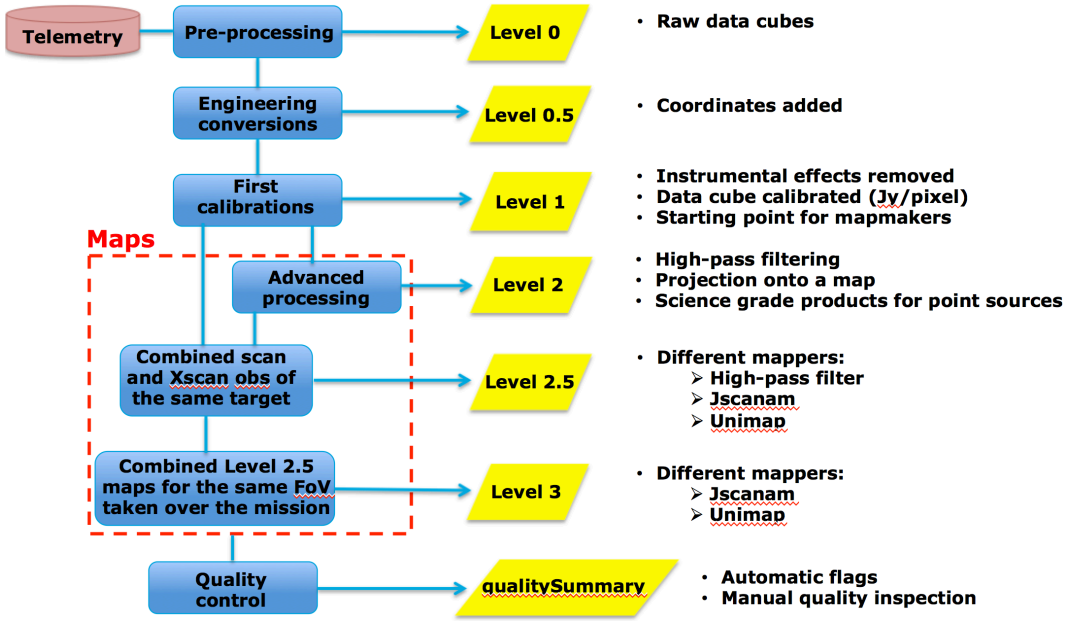

Figure 10.2: The Levels in a PACS photometry ObservationContext and their link to the SPG pipeline, with key pipeline steps mentioned

number (which is always 00 because all photometer observations contain only one slice), e.g. hpacs1342223608_20hpppmapb_00.fits" for obsid 1342223608 from level "20" (=2.0) with product name "hppmapb" (which in HIPE you see listed in an ObservationContext as HPPMAPB). The maps in Level 2.5 and 3 have file names built as "hpacs" + the level ("30" or "25") + product name in capitals (e.g. "HPJSMAPB" or "HPUNIMAPB") + ra+dec (e.g. "1318_m1819") +"00" + version number (e.g. "v1.0").

Table 10.2 outlines the folder structure and all possible FITS files that can be found in the unpacked tarball of a full photomery observation, below the directory with the obsid (1342...) as the name (excluding the engineering, housekeeping, and auxiliary directories and products).

10.3.2 The high-level pipeline products

The photometry pipeline products from Level 2 are science quality maps. These maps contain the image in Jy/pixel, the coverage, some measure of error plus several mapmaker-related auxiliary images. It is always recommended to use the Level 2.5 or Level 3 if you can, as these maps have a better SNR, being a combination of several observations. If these Levels are not available, Level 2 maps are the only standard science products that can be used, however neither the Level 2 nor the Level 2.5 high-pass filter maps should be used for extended source science. For such cases, it is possible that an HPDP has been generated.

10.3.2.1 Science-ready pipeline products

In a PACS photometer ObservationContext there are products produced by the three mappers of the pipeline. The JScanam and Unimap Level 2.5 and Level 3 are science-ready maps for any kind of

source emission (point and extended) while Level 2.5 high-pass filter maps can be used only for point or very slightly extended sources. These mappers are explained in detail in the PDRG (phot), and interested readers should consult that document to understand how they work. These mappers are also discussed in Chp. 9. We summarise these three map types here.

10.3.2.1.1 HighPass filtering + photProject

In Level 2 and 2.5 one can find maps processed using the highPass filtering method. We emphasise that these products are suitable for science only in the case of point sources and if there is no extended emission present in the maps.
These maps (called HPPMAP[B|R] in Level 2 and HPPHPFMAP[B|R] in Level 2.5) contain several datasets. The "image" dataset is calibrated in Jy/pixel. The "coverage" dataset is a measure of the number of readouts that were used to assign flux to a spatial map pixel, and in mappers using *photProject*, the general level of the coverage values strongly depends on the parameter pixfrac used in the task. The "error" dataset is described in the PDRG (phot) is estimated via the coverage using an empirical calibration established on cosmological fields (see Popesso et al. 2012). The "stDev" is the standard deviation of the fluxes from the detector pixels that fed into the projected pixels of the map, and finally the "HPFMask" is the mask used for high-pass filtering.

Table 10.2: FITS files from an unpacked photometry observation

Folder	**Sub-folder**	**Filename pattern**	**Description**
browseImageProduct		hpacsbrowseimage_<NNN>	The postcard
browseProduct	blue_Jscanam_map	hpacs_25HPPJSMAPB_blue_<RA>_<DEC>_00_v1.0_<NNN>	Level 2.5 SBP
	blue_Jscanam_map	hpacs_25HPPJSMAPB_green_<RA>_<DEC>_00_v1.0_<NNN>	
	red_Jscanam_map	hpacs_25HPPJSMAPR_<RA>_[p|m]<DEC>_00_v1.0_<NNN>	
	blue_projected_map	hpacs<OBSID>_20hppmapb_00_<NNN>	Level 2 SBP
	red_projected_map	hpacs<OBSID>_20hppmapr_00_<NNN>	
Level 0	HPPAVG<B|R> /herschel.pacs.signal.Frames	hpacs<OBSID>_00hppavb<b|r>s_00_<NNN>	timeline data
Level 0_5	HPPAVG<B|R> /herschel.pacs.signal.Frames	hpacs<OBSID>_05hppavb<b|r>s_00_<NNN>	timeline data
Level 1	HPPAVG<B|R> /herschel.pacs.signal.Frames	hpacs<OBSID>_10hppavb<b|r>s_00_<NNN>	timeline data
Level 2	HPPMAP<B|R>	hpacs<OBSID>_20hpppmap<b|r>_00_<NNN>	projected maps
Level 2_5	HPPHPFMAPB	hpacs_25HPPHPFMAPB_blue_<RA>_<DEC>_00_v1.0_<NNN>	projected maps
	HPPHPFMAPB	hpacs_25HPPHPFMAPB_green_<RA>_<DEC>_00_v1.0_<NNN>	(scan+cross-scan)
	HPPHPFMAPR	hpacs_25HPPHPFMAPR_<RA>_<DEC>_00_v1.0_<NNN>	
	HPPJSMAPB	hpacs_25HPPJSMAPB_blue_<RA>_<DEC>_00_v1.0_<NNN>	Jscanam maps
	HPPJSMAPB	hpacs_25HPPJSMAPB_green_<RA>_<DEC>_00_v1.0_<NNN>	(scan+cross-scan)
	HPPJSMAPR	hpacs_25HPPJSMAPR_<RA>_<DEC>_00_v1.0_<NNN>	
	HPPUNIMAPB	hpacs_25HPPUNIMAPB_blue_<RA>_<DEC>_00_v1.0_<NNN>	Unimap maps
	HPPUNIMAPB	hpacs_25HPPUNIMAPB_green_<RA>_<DEC>_00_v1.0_<NNN>	(scan+cross-scan)
	HPPUNIMAPR	hpacs_25HPPUNIMAPR_<RA>_<DEC>_00_v1.0_<NNN>	
Level 3	HPPJSMAP<B|R> and HPPUNIMAP<B|R>	same as Level 2.5 but “30” in place of “25”	multiple obsids combined

<RA> is the hour+minute, <DEC> is the <p|m>degree+arcminute. <NNN> is a timestamp. The SBPs provided are Level 2.5 maps unless only Level 2 is present. All observations have a red, and either a blue or green map, however only Level 2.5 includes the words “green|blue” in the name. The bands present at Level 3 depends on the common bands in the combined observations.

10.3.2.1.2 JScanam

The maps created with the *JScanam* task are present at Level 2.5 and 3. At Level 2.5 they are called HPPJSMAP[B|R] for the [Blue|Red] camera respectively (irrespective of the blue filter used), while at Level 3, for the blue camera, the distinction between 70 μm (blue) and 100 μm (green) filter is carried into the name (HPPJSMAPB or HPPJSMAPG).

The datasets contained in these maps are the same as those in highPass filtered products, however the "error" and "HPFMask" datasets are not provided. Jscanam does provide an "stDev" extension, which can be considered a good representation of the map noise since Jscanam maps are created as projected timelines.

10.3.2.1.3 Unimap

At Level 2.5 they are called HPPUNIMAP[B|R] for the [Blue|Red] camera respectively (irrespective of the blue filter used), while at Level 3, for the blue camera the distinction between 70 μm (blue) and 100 μm (green) filter is carried into the name (HPPUNIMAPB or HPPUNIMAPG).

The datasets contained in these maps are the "image" and the "coverage" (the same as the other two map-makers), the error map ("error"), and all the other maps generated by the Unimap pipeline (GSL, PGLS, Naive) according to scheme reported at the end of the section 9.1.1.5. The "error" map is computed within the framework of the mapper. Finally, the Unimap log is saved in a further dataset ("unimapLog").

10.3.3 Photometry Standalone Browse products

PACS photometry SBPs are JScanam Level 2.5 maps. These maps are explained in Sec. 10.3.2. The SBPs can be found in the browseProduct entry of an ObservationContext viewed in HIPE, and in the browseProduct directory in an unpacked tarball gotten from the HSA.

10.4 Spectroscopy observations: pipeline products

The SPG pipeline products that are of interest to the archive user are explained here. A large range of products were created by the SPG pipelines, as which are useful depend on the observing mode and the target type. For advice on using these products for your own observation, see Chp. 11.

A unique pipeline script was run for the following spectroscopy observing modes: chop-nod line scan, chop-nod range scan, unchopped line-scan and wavelength switching, and unchopped range-scan (see Sec. 10.4.2.1 for a definition of these modes). The range of products created by these four pipelines are exactly the same up to Level 2, and from Level 2 upwards the differences depend on the AOT.

Fig. 10.3 is an an overview of the processing levels in an ObservationContext and their relationship to the SPG pipeline. Of most interest are Level 2, 2.5, and 3 and these levels are explained in this handbook. For those wishing to re-run the pipeline or wishing to use lower-level products, the PPE and PDRG (spec) can be consulted.

Fig. 10.4 shows a spectroscopy observation viewed in HIPE with the ObservationViewer. At the top part of this viewer is a Summary of the observation and a click-onable 'postcard" (which is also

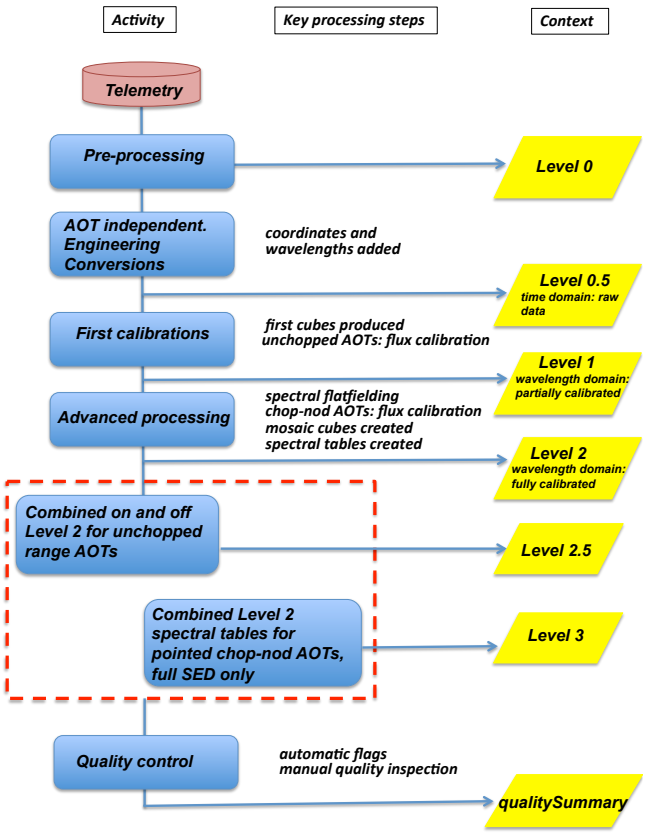

Figure 10.3: The Levels in a PACS spectrometer ObservationContext and their link to the SPG pipeline, with key pipeline steps mentioned

provided with the HSA search results). Below the summary panel is the Meta data panel, these meta data belonging to the context/product that is currently highlighted in the Data panel. The Data panel lists all the data provided in the ObservationContext. Hovering the mouse over the entries in this directory will bring up a tooltip with information about the contents. The contents of Level 2, 2.5, and 3 are explained in Sec. 10.4.2, and the SBPs, which are taken from these levels and are also provided in the browseProduct context, are explained in in Sec. 10.4.3.

10.4.1 Viewing an observation on disk

An observation from the HSA is provided as a tarball, which when unpacked has a layout similar to that of the ObservationContext in HIPE: see Table 10.3 (Level 0–1), Table 10.4 (Level 1–3), and Table 10.5 (SBPs) for a listing of the FITS files from an unpacked HSA tarball. All the products are held as FITS files organised in directories with the names of the contexts they belong to. The only product missing in the unpacked tarball is the PacsObsSummary, however this can be viewed in

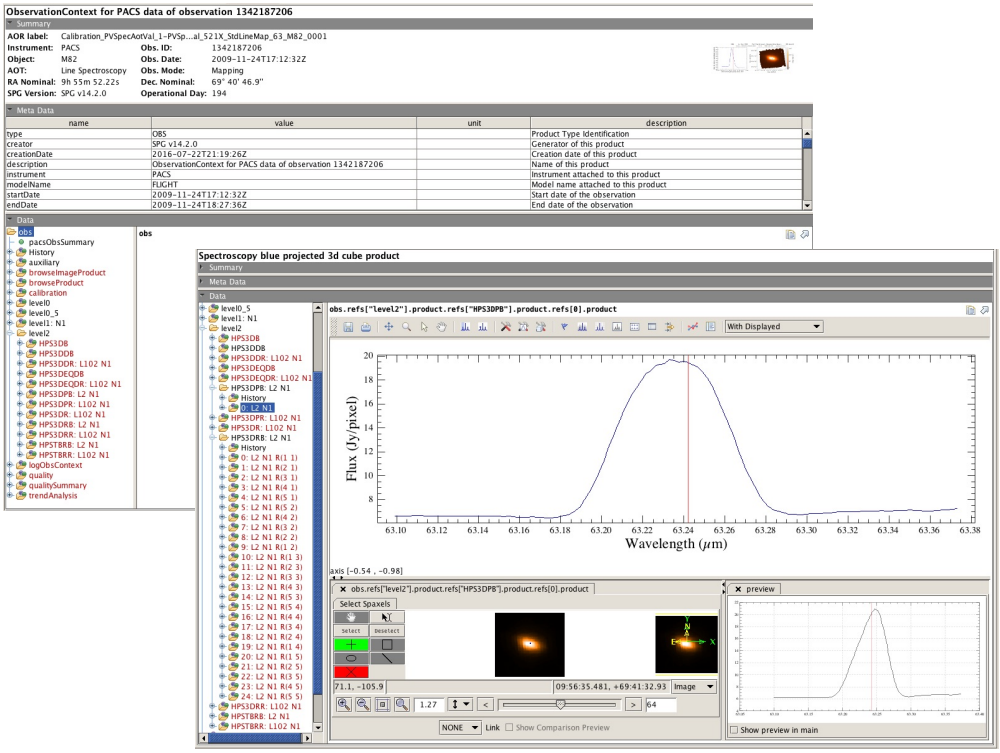

Figure 10.4: A PACS spectroscopy observation (chop-nod mapping observation) viewed in HIPE. The upper image shows the full contents of an ObservationContext. The lower image shows the contents of Level 2: in the long list of 'rebinned" cubes (HPS3DRB: starting with '0: L1 N1 (R1 1)") each cube is for a single pointing in this mapping observation. These are combined into various types of 'mosaic" cubes by the pipeline, and one of these (the blue-highlighted 'drizzled" cube) has been selected and is also displayed.

the HSA search results. A few of the products – the History, the quality and qualitySummary – are awkward to read without the HIPE viewers; the qualitySummary is best read from the search results page of the HSA.

The cubes and spectral tables that most astronomers will be interested in are found in Levels 2 and higher. The names of the FITS files are built from: "hpacs" + observation id + level [e.g. 20 = 2.0] + the name of the context it comes from + "s"+slice number + a time stamp: e.g. hpacs1342197886_10hpsfitbs_01_149611734008.fits for the second (**s_01** as the counting starts at 00) level 1 (**10**) blue frames (**hpsfitb**), and this file will be found in the directory 1342197886/level1/HPSFITB/herschel.pacs.signal.frames/. The naming convention for the FITS files at Level 2.5 and 3 is slightly different than that to the other levels – e.g. hpacs1342197886_25HPS3DRBBS_<RA>_<DEC>_<##>_v1.0_159622734338.fits – for purely formal reasons, to conform with the general *Herschel* standard. The slice number (e.g. s_01) refers to the index of the cube in the set of cubes that are present. These "slices" are distinct on wavelength range and/or pointing on the sky (position in the raster); the level 0.5 data are sliced into these units by the pipeline, and they remain sliced until the end. If more than one wavelength range was requested

by the observer, then multiple slices for each product will be present. For mapping observations, there will additionally be one slice per position in the raster for the rebinned cubes only, since for the mosaic cubes these raster positions will have been combined into a single cube/slice. <NNN> in the filenames is a timestamp. All products have a red and blue camera version, indicated by "[b|r]" in the filename and "[B|R]" in the directory name.

The AOT for which the product is provided is indicated in the Description column of the tables. For the table of SBPs (Table 10.5), in the final column an *AOT* of e.g. *[Nyquist, oversampled] + range-scan* means >for all Nyquist or oversampled mapping AOTs *that are also* range-scans<. For the Level 2–3 table (Table 10.4), in the final column an *AOT* of e.g. *(Nyquist+range-scan, all pointed and tiling)* means all observations that are >Nyquist-mapping *and* range-scan, or all pointed and tiling observations<. If no AOT details are given, the product is provided for all AOTs.

Table 10.3: FITS files in an unpacked spectroscopy observation: Level 0–1

Folder	Sub-folder	Filename pattern	Description
Level 0	HPSFIT[B|R]/ herschel.pacs.signal.Frames	hpacs<OBSID>_00hpsfit[b|r]s_00_<NNN>	Fitted time-line data
	HPSRAW[B|R]/ herschel.pacs.signal.Tramps	hpacs<OBSID>_00hpsraw[b|r]s_00_<NNN>	Raw time-line data
Level 0.5	HPSFIT[B|R]/ herschel.pacs.signal.Frames	hpacs<OBSID>_05hpsfit[b|r]s_<##>_<NNN>	Fitted time-line data
Level 1	HPSFIT[B|R]/ herschel.pacs.signal.Frames	hpacs<OBSID>_10hpsfit[b|r]s_<##>_<NNN>	Fitted time-line data
	HPS3D[B|R]/ herschel.pacs.signal.PacsCube	hpacs<OBSID>_10hps3d[b|r]s_<##>_<NNN>	First cube of the pipeline

Table 10.4: FITS files in an unpacked spectroscopy observation: Level 2–3

Folder	**Sub-folder**	**Filename pattern**	**Description**
Level 2	HPS3D[B|R]/ herschel.pacs.signal.PacsCube	hpacs<OBSID>_20hps3d[b|r]s_<##>_<NNN>	earliest cube *not for science*
	HPS3DR[B|R]/ herschel.pacs.signal.PacsRebinnedCube	hpacs<OBSID>_20hps3dr[b|r]s_<##>_<NNN>	native/rebinned cube
	HPSTBR[B|R]/ herschel.pacs.signal.PacsSpecTable	hpacs<OBSID>_20hpstbr[b|r]s_<##>_<NNN>	rebinned cube table
	HPS3DP[B|R]/ herschel.ia.dataset.spectrum.SpectralSimpleCube	hpacs<OBSID>_20hps3dp[b|r]s_<##>_<NNN>	projected cube
	HPS3DI[B|R]/ herschel.ia.dataset.spectrum.SpectralSimpleCube	hpacs<OBSID>_20hps3di[b|r]s_<##>_<NNN>	interpolated cube *(Nyquist+range-scan]* *all pointed and tiling)*
	HPS3DD[B|R]/ herschel.ia.dataset.spectrum.SpectralSimpleCube	hpacs<OBSID>_20hps3dd[b|r]s_<##>_<NNN>	drizzled cube *(line-scan+* *Nyquist and oversampled)*
	HPSSPEC[B|R]/ herschel.pacs.signal.PacsCentralSpectrum	hpacs<OBSID>_20hpsspec[b|r]s_<##>_<NNN>	point-source table *(pointed)*

Table 10.4: ...continued

Folder	Sub-folder	Filename pattern	Description
Level 2.5	HPS3DRBS[B|R]/ herschel.pacs.signal.PacsRebinnedCube	hpacs_25HPS3DRBS[B|R]S _<RA>_<DEC>_<##>_v1.0_<NNN>	native/rebinned cube
	HPSTBRBS[B|R]/ herschel.pacs.signal.PacsSpecTable	hpacs_25HPSTBRBS[B|R]S _<RA>_<DEC>_<##>_v1.0_<NNN>	rebinned cube table
	HPS3DPBS[B|R]/ herschel.ia.dataset.spectrum.SpectralSimpleCube	hpacs_25HPS3DPBS[B|R]S _<RA>_<DEC>_<##>_v1.0_<NNN>	projected cube
	HPS3DIBS[B|R]/ herschel.ia.dataset.spectrum.SpectralSimpleCube	hpacs_25HPS3DIBS[B|R]S _<RA>_<DEC>_<##>_v1.0_<NNN>	interpolated cube *(Nyquist+range-scan, all pointed and tiling)*
	HPS3DDBS[B|R]/ herschel.ia.dataset.spectrum.SpectralSimpleCube	hpacs_25HPS3DDBS[B|R]S _<RA>_<DEC>_<##>_v1.0_<NNN>	drizzled cube *(line-scan+ Nyquist and oversampled)*
	HPSSPECBS[B|R]/ herschel.pacs.signal.PacsCentralSpectrum	hpacs_25HPSSPECBS[B|R]S _<RA>_<DEC>_<##>_v1.0_<NNN>	point-source table *(pointed)*
Level 3	HPSSPEC	hpacs_30HPSSPEC_<RA>_<DEC>_v1.0_<NNN>	point-source table (pointed+chop-nod+SED)

Table 10.5: FITS files in an unpacked spectroscopy observation: standalone browse products

Folder	**Sub-folder**	**Filename pattern**	**Description** *AOT*
browseProduct	HPSTBR[B|R]/ herschel.pacs.signal.PacsSpecTable	hpacs<OBSID>_20hpstbr[b|r]s_ <##>_<NNN>	rebinned cube table (L2)
	HPSTBRBS[B|R]/ herschel.pacs.signal.PacsSpecTable	hpacs_25HPSTBRBS[B|R]S_ <RA>_<DEC>_<##>_v1.0_<NNN>	rebinned cube table (L2.5)
	HPSSPEC[B|R]/ herschel.pacs.signal.PacsCentralSpectrum	hpacs<OBSID>_20hpsspec[b|r]s_ <##>_<NNN>	point-source table (L2) *(pointed)*
	HPSSPECBS[B|R]/ herschel.pacs.signal.PacsCentralSpectrum	hpacs_25HPSSPECBS[B|R]S_ <RA>_<DEC>_<##>_v1.0_<NNN>	point-source table (L2.5) *(pointed)*
	HPSSPEC	hpacs_30HPSSPEC_<RA>_<DEC>_ v1.0_<NNN>	point-source table (L3) *(pointed+chop-nod+SED)*
	HPS3DP[B|R]/ herschel.ia.dataset.spectrum.SpectralSimpleCube	pacs<OBSID>_20hps3dp[b|r]s_ <##>_<NNN>	projected cube (L2) *[Nyquist, oversampled]* *+ range-scan*
	HPS3DPBS[B|R]/ herschel.ia.dataset.spectrum.SpectralSimpleCube	hpacs_25HPS3DPBS[B|R]S_ <RA>_<DEC>_<##>_v1.0_<NNN>	projected cube (L2.5) *[Nyquist, oversampled]* *+ range-scan*
	HPS3DD[B|R]/ herschel.ia.dataset.spectrum.SpectralSimpleCube	hpacs<OBSID>_20hps3dd[b|r]s_ <##>_<NNN>	drizzled cube (L2) *[Nyquist, oversampled]* *+ line-scan*
	HPS3DDBS[B|R]/ herschel.ia.dataset.spectrum.SpectralSimpleCube	hpacs_25HPS3DDBS[B|R]S_ <RA>_<DEC>_<##>_v1.0_<NNN>	drizzled cube (L2.5) *[Nyquist, oversampled]* *+ line-scan*
	HPS3DI[B|R]/ herschel.ia.dataset.spectrum.SpectralSimpleCube	hpacs<OBSID>_20hps3di[b|r]s_ <##>_<NNN>	interpolated cube (L2) *[tiling, pointed, all other]*
	HPS3DIBS[B|R]/ herschel.ia.dataset.spectrum.SpectralSimpleCube	hpacs_25HPS3DIBS[B|R]S_ <RA>_<DEC>_<##>_v1.0_<NNN>	interpolated cube (L2.5) *tiling, pointed, all other*

10.4.2 The high-level spectroscopy pipeline products

In this section we explain the cubes and spectrum tables that are the high-level pipeline products on which science can be carried out. The range of products provided for an observation depends on the AOT of that observation. To know the AOT for any observationit is necessary to inspect the FITS keywords of any Level 2 and higher product (as details are not completely provided by the HSA's search results). To help the archive user in this rather tedious search, a spreadsheet of the important keywords for all standard PACS spectroscopy products in the HSA can be found here. Alternatively, it is possible to obtain a summary of the observation for each returned search result in the HSA – the PACS Observation Summary. The AOT details are also given there.

Here we will explain how to determine the AOT of an observation, and following that we introduce the cubes and tables created at Level 2, 2.5, and 3 for the different AOTs.

10.4.2.1 Establish the observing mode

The observing modes that were offered for PACS spectroscopy are explained in detail in Chp. 3. In summary they were:

- *Chop-nod or unchopped*: refers to the two ways of gathering data from the sky background (aka telescope background) during an observation.
  Chop-nod was the most common mode: while the spectra were being gathered, a mirror *chopped* extremely rapidly between the on-source and an off-source position on the sky. After a full spectral range had been completely gathered, the telescope *nodded* to near-by location and the spectra (with the same chopping pattern) were taken again. The data from the two nod positions are combined into the final, background-subtracted cubes by the pipeline.
  The unchopped mode was used for crowded fields where no emission-free location could be reached by the maximum range of the chopper: the complete spectral range of the on-source position was taken without any rapid chopping, the telescope then nodded to an off-source location to obtain the complete spectral range on the background. The data from the off-source nod position are subtracted from the on-source nod position data by the pipeline to create the final cubes.
  Wavelength switching was an early AOT that was superseded by the unchopped line-scan mode.
  Part of the name of the products and the directories they can be found it depends on whether the observation was chop-nod or unchopped.

- *Pointed or mapping*: observations were either taken as a single pointing or as a raster used to create a mapping observation. Mapping observations came in three flavours, varying on the raster step sizes and number of steps: tiling, Nyquist-sampled, or oversampled.
  The cubes that should be used for science depend on the pointing/mapping mode.

- *Range scan or line scan*: refers to the wavelength coverage. A range scan could cover any requested range up to the entire range of the filter used (aka SED mode), and a line scan would cover one unresolved line and the necessary continuum to study that line. More than one range or line could be requested in any observation, except for SED mode where at least two observations had to be taken to cover the full spectral range of PACS.
  Some of the mapping cubes that can/cannot be used for science depend on the wavelength mode.

To determine which of these three classes of AOT any particular observation had (and this will include a choice from each class), use the entries of Table 10.6, were we list the Meta data and FITS header keywords (found in the first extension of the FITS file of any cube) that identify these particular AOT details.

Table 10.6: The Meta data and FITS keywords indicating the AOTs for a PACS spectroscopy observation, found in any Level 2/2.5 product

Observing mode	Meta datum	FITS keyword	Value
chop-nod	ChopNod	CHOPNOD	True
unchopped, wavelength switching	ChopNod	CHOPNOD	False
line scan	instMode	INSTMODE	PacsLineSpec
range scan	instMode	INSTMODE	PacsRangeSpec
pointed	obsMode	OBS_MODE	Pointed
mapping	obsMode	OBS_MODE	Mapping
Also useful:			
wavelength	min|maxWavelength	MIN|MAXWAVE	
slice number	sliceNumber	SLICENUM	

For the mapping modes, it is necessary to also distinguish between the spatial sampling factors, since different mosaic tasks (and hence different types of cubes) were applied to different types of mapping observations by the SPG pipeline. Three mapping modes were offered, each of which had a recommended number and size of steps between the pointings of the raster sequence (and most observers did follow the recommendations). The step sizes and number of steps that were recommended for the three mapping modes are listed in Table 10.7, along with the Meta data and FITS keywords where the settings used for the observation can be found.

- *Nyquist*-sampled mapping observations were taken to allow for the eventual mosaic cubes (the combination of all the cubes of the raster) to have a spatial sampling that Nyquist-sampled the beam. Step sizes were super-spaxel.

- *Oversampled* observations had sub-spaxel step sizes. They had the aim of allowing for a better image reconstruction with the mosaic tasks of the pipeline than can be achieved for Nyquist mapping observations, and where the advantage of the larger field that one can get with the Nyquist mapping was not necessary.

- *Undersampled and tiling* observations. Tiling observations were taken to cover a large field-of-view and were essentially a set of pointed observations with a very small overlap (usually one spaxel or less). Tiling – as well as pointed – observations spatially undersample the beam. In addition, any other mapping observation for which the observer requested *either* too few steps compared to the recommendation *or* steps larger than the Nyquist recommendation, was considered to be undersampled. Noting that the recommended number of mapping steps in the blue (3×3) is more than that in the red (2×2), this means that an observation taken to be Nyquist sampled in the red is, as a consequence, undersampled in the blue. In this case, the blue cubes provided will be those appropriate for Nyquist observations but the red cubes will be those appropriate for undersampled observations.

Table 10.7: The raster pattern data that were recommended for oversampled, Nyquist-sampled, and tiling mapping observations. For the Nyquist and oversampled cases, all four conditions (i.e. the value limits for the four meta data) must be met for the observation to be considered to fall within that mode. *Any choices outside of these – either too few steps or steps too large on the sky – are considered to be undersampled.* The blue and red camera data are considered separately when this determination is made. Tiling (and pointed) observations are undersampled.

Spatial sampling	Meta datum	FITS keyword	Value
Oversampled (red camera)	numRasterCol	RASSTEPC	≥ 2
	numRasterLine	RASSTEPL	≥ 2
	pointStep	NRASTCOL	$\leq 4.5''$
	lineStep	NRASTLIN	$\leq 4.5''$
Oversampled (blue camera)	numRasterCol	RASSTEPC	≥ 3
	numRasterLine	RASSTEPL	≥ 3
	pointStep	NRASTCOL	$\leq 3''$
	lineStep	NRASTLIN	$\leq 3''$
Nyquist (red camera)	numRasterCol	RASSTEPC	≥ 2
	numRasterLine	RASSTEPL	≥ 2
	pointStep	NRASTCOL	$\leq 24''$
	lineStep	NRASTLIN	$\leq 22''$
Nyquist (blue camera)	numRasterCol	RASSTEPC	≥ 3
	numRasterLine	RASSTEPL	≥ 3
	pointStep	NRASTCOL	$\leq 16''$
	lineStep	NRASTLIN	$\leq 14.5''$
Tiling (red camera)	numRasterCol	RASSTEPC	any
	numRasterLine	RASSTEPL	any
	pointStep	NRASTCOL	$38''$–$47''$
	lineStep	NRASTLIN	$38''$–$47''$
Tiling (blue camera)	numRasterCol	RASSTEPC	any
	numRasterLine	RASSTEPL	any
	pointStep	NRASTCOL	$38''$–$47''$
	lineStep	NRASTLIN	$38''$–$47''$

10.4.2.2 The types of cubes produced

The range of cubes and tables created by the SPG pipeline at the final levels depends on the observing mode. The products of interest to the astronomer are found in Level 2, Level 2.5, Level 3, and in the browseProduct contexts. A decision tree to guide the user through the products to use, depending on the nature of the target (point source, small source, extended sources) and the type of observation (mapping, pointed, unchopped, chop-nod), can be found in the HELL.

10.4.2.2.1 Rebinned cubes: for all observations

Rebinned cubes are particularly recommended as the science product to use for observations of point or slightly extended sources. Rebinned cubes have the footprint of the PACS IFU – a 5×5 irregular spatial grid (see Fig. 5.9) with spaxels of $9.4''$on a side – and a regular, but non-equidistant spectral grid (see Sec. 10.4.3). As neither spectral nor spatial grid are regular, these information are not contained in the WCS of the cube, but instead the wavelength grid, spatial coordinates (RA, Dec), fluxes, and errors are all contained in datasets within the cube, and extensions within the FITS file: see Table 10.9.

These cubes are the recommended product to use for point and small sources because the necessary flux correction tasks that are provided in HIPE (i.e. the point-source/small-source corrections) work on the rebinned cubes only. The calibration behind these corrections are explained in Secs 8.3.3 and 8.3.5. For these corrections to work, it is always necessary that the source is centred within the FoV (i.e. in or close to the central spaxel), and that all the emission detected is from the source alone.

For all pointed observations, point-source calibrated spectra are provided as one of the spectrum tables of Level 2/2.5 and 3 (see Sec. 10.4.2.3). Hence, if the source is known to be a point source, it is centred in the FoV and is not contaminated by other emission sources, this table is the science-grade product to use for that observation. More information about point and slightly-extended sources and how to deal with them as an archive user can be found in Chp. 11.

10.4.2.2.2 Projected cubes: mosaic cubes for all observations

Projected cubes are provided for every type of observation. They are created with the pipeline task *specProject*, which was developed for Nyquist and oversampled mapping observations. The task works by projecting, at each wavelength, the fluxes of the rebinned cubes taken in the raster onto a spatial grid that covers the entire field of the map. Where spaxels cross each other (i.e. those from different pointings) the fluxes are averaged with weighting by area overlap. In this way, a single mosaic cube, with a regular spatial grid, is created for each spectral line/range in the observation. The spaxel sizes are $3''$ for range-scan mapping observations, and for line-scan mapping observations the spaxel size is set by that of the accompanying drizzled cubes of the same observation (see later).
It is possible (and easy) to use the task in HIPE to create projected cubes with any other spaxel size. The spectral grid of the projected cubes is the same as that of the rebinned cubes, i.e. regular but non-equidistant.
Projected cubes are also provided for tiling observations, although the interpolated cubes are generally the recommended product for this mode. The spaxel sizes of projected cubes of tiling observations are $1.5''$.
Projected cubes are also provided for pointed observations. For observations of extended sources, these projected cubes (and the interpolated cubes: see below) are possibly more useful that the rebinned cubes, because (i) the rebinned cubes are not easy to read in cube-viewing software outside of HIPE due to their irregular spatial and spectral grid, and (ii) "visualising" an extended source from a rebinned cube can be difficult (compare a rebinned cube to an interpolated cube for an extended source, and you will rapidly see why). Therefore, projected and interpolated cubes were also created for this observing mode. The spaxel sizes for the projected cubes of pointed observations are $0.5''$, and this small size ensures that the native 5×5 IFU footprint can still be seen (what this means will be obvious when you look at the cube). A downside of the small size of the spaxels is, however, the consequently large number of spaxels, and this makes the cubes cumbersome to use: the interpolated cubes do not have this issue.

10.4.2.2.3 Drizzled cubes: mosaic cubes for Nyquist or oversampled mapping observations

Drizzled cubes are created by the pipeline task *drizzle*: this task uses the method developed by Fruchter and Hook (2002) for *HST WFC* images, to "drizzle" the fluxes of the input rebinned cubes of the raster onto a regular sky grid to create a single drizzled cube. This task optimises the chosen spaxel size for the drizzled cube to allow for a Nyquist sampling of the beam *at the wavelength of the observation*: because this optimisation is suitable for a short wavelength range only, drizzled cubes

are only provided for line-scan mapping observations, not also for the range-scan.
Since the spaxel sizes are determined by the central wavelength of the cube, different cubes of the same observation will have different spaxel sizes. It is possible to use drizzle in HIPE to create cubes with any other spaxel size.
The spatial grid is also regular and is defined in the WCS, in units of degrees, but the spectral grid is as with the other cubes: regular but non-equidistant.
Whether to use the projected or drizzled cubes where both are provided in an observation is a decision the user has to make. See the PDRG (spec) to learn more about these tasks, and compare the cubes yourself.

10.4.2.2.4 Interpolated cubes: for all undersampled observations.

Interpolated cubes are provided for all tiling and pointed observations, and those that are otherwise classified as undersampled. They are created with the task *specInterpolate*, which creates a sky grid via Delaunay interpolation over the input grids of the cubes in the raster, or from the single input grid from the single pointed cube, and then interpolates the fluxes of the input cubes(s) on this grid. The spaxels sizes are $3''$, and as with the other mosaic cubes the sky grid is regular and defined in the WCS. The spectral grid is also the same as for the other mosaic cubes: regular but non-equidistant.
It is possible to use specInterpolate in HIPE to create the cubes with any other spaxel size. These cubes are created for undersampled mapping observations to create a mosaic cube, and also for the pointed observation to create cubes with a regular spatial grid, which software outside of HIPE finds easier to handle.

10.4.2.2.5 Equidistant cubes: cubes with a regular spectral and spatial grid

As mentioned in these explanations, the cubes created by the pipeline have a spectral grid that scales with the spectral resolution, i.e. the grid is non-equidistant (Sec. 9.2.1.4) because the size of the wavelength bins changes with wavelength. Such cubes can be difficult to read in software outside of HIPE, and therefore one of the mosaic cubes from each of Level 2 and 2.5 are copied to a version with an equidistant spectral grid, and these cubes therefore have both spatial *and* spectral grids defined by the WCS. The bin sizes of this grid are very small, which was necessary so that the output spectra look the same as the input spectra. These cubes are provided as SBPs and are explained in more detail in Sec. 10.4.3.

10.4.2.2.6 Background subtracted cubes: for the unchopped range scan observations

For the unchopped range observing mode, the Level 2 contains the standard products created by the pipeline. The Level 2 of the off-source observation is then subtracted from the Level 2 of the on-source observation to create the same set of products (but now with a “B(ackground)S(ubtracted)” in the product names) at Level 2.5.

10.4.2.3 The types of spectrum tables produced

There are three types of spectral tables provided by the pipeline.

10.4.2.3.1 Rebinned cube spectral tables for all observations.

The rebinned cube spectrum tables contain the data of the rebinned cubes organised in a tabular format. As the rebinned cubes have neither an equidistant spectral *nor* spatial grid, i.e. none of the WCS axes can be properly filled, the tabular format is an alternative for reading the data into software other than HIPE. The rows of each table contains the wavelength, flux, error, spaxel number and coordinate, spaxel RA and Dec, spectral band, and raster coordinate. The spectra iterate over spaxel number (the entire spectrum of spaxel 0 is given first, then spaxel 1, etc) and then raster position. One table is provided for each wavelength range the observer requested (red and blue camera both).

10.4.2.3.2 Central and point-source spectrum tables for all pointed observations.

The central-spaxel spectrum and up to three variations of the point-source corrected spectrum are contained in a table provided at Level 2. There is one spectrum table for each wavelength range requested by the observer (red and blue camera each). Columns of wavelength, flux, error are provided for each spectrum. The three point-source corrected spectra are the three outputs of the pipeline task *extractCentralSpectrum*. The calibration used in this task is explained in Sec. 8.3.3. For more detail on the task itself – on how it works and on the quality assessments it produces when used in HIPE – see the PDRG (spec) (sec. 8.5). The columns "pointSourceScaledFlux|Error" are the "c129" output from this task and these are the recommended data for all except the very faintest sources. However, this spectrum is invalid for unchopped observations and is not provided, instead the columns "pointSourceCen3x3Flux|Error" ("c9" from the task) are the recommended data, again except for the faintest sources. For very faint sources, where hardly any flux is outside of the central spaxel, the columns "pointSourceFlux|Error" ("c1" from the task) are usually the best data to use, as the other two will be noisier and may even contain less flux overall. Note that the calibration applied by extractCentralSpectrum requires that the point source is located within the central region of the cube (ideally with an offset of no more than a few arcsec) and that all the flux in the spectrum arises from the point source itself.
Note that the point-source corrected spectrum tables are provided for all pointed observations regardless of the type of source: it has *not* been first determined that the target actually is a point source. That evaluation needs to be made by the user of the data. More recommendations about dealing with point sources can be found in Chp. 11.

10.4.2.3.3 SED spectrum table: for chop-nod pointed observations with full SED coverage.

This Level 3 product was created to allow the user to have the full SED (55–190 μm) of point sources for which the full SED was actually observed (in two or more observations), in a single product. This single table is a combination of all the Level 2 point-source spectrum tables from the red and blue camera for each observation of that source that was taken to produce the full spectral coverage.

10.4.2.4 Summary

Table 10.8 lists the cubes and tables that can be found at Levels 2, 2.5, and 3. The context name (HPSXXX) is the same as the directory name that these products are located in within the HSA download (Sec. 10.4.1). All cubes have units of Jy/pixel (where "pixel" refers to the spatial pixel/spaxel) and μm. An "SBP" in the Level column indicates that this product is also provided as a standalone SBP.

In Table 10.9 the datasets (and hence the extensions in the FITS files) that can be found in the cubes and spectral tables from Levels 2, 2.5, and 3 are listed. No single product will have all of these extensions, this serves rather as a look-up table.

Table 10.8: The Level 2, 2.5, and 3 products provided for PACS spectroscopy observations of different observing modes. In the column "spectral grid", *non-equi.* refers to the standard spectral grid, with bin sizes that scale with the wavelength, and *equi.* refers to the equidistant grid. An "optimised" spaxel has a size optimised to the wavelength of the cube, as created by drizzle, and "=drizzled" means this cube has the same spaxel size as the drizzle cube also created. A native spaxel is the 9.4″ spaxel size of the PACS IFU. The key for the AOT names is as follows: point(pt), tile(tl), nyquist(nq), oversampled(ov); chop-nod(cn), unchop(un); line-scan(ls), range-scan(rs).

Level	Context HPS...	Common name	Spectral grid	Spaxel	AOTs
2	3D[R|B]	pacs cube[a]	irreg.	native	all
2,	3DR[R|B]	rebinned cube	non-equi.	native	all
2, SBP	3DP[R|B]	projected cube	non-equi.	0.5″	pt; cn,un; ls, rs
				1″.5	tl; cn,un; ls, rs
				3″	nq, ov; cn, un; rs
				=drizzled	nq, ov; cn, un; ls
2	3DD[R|B]	drizzled cube	non-equi.	optimised	nq, ov; cn, un; ls
2	3DI[R|B]	interpolated cube	non-equi.	3″	pt, tl; cn, un; ls, rs
2, SBP	3DEQP[R|B]	projected cube	equi.	3″	nq, ov; cn, un; rs
2, SBP	3DEQD[R|B]	drizzled cube	equi.	optimised	nq, ov; cn, un; ls
2, SBP	3DEQI[R|B]	interpolated cube	equi.	3″	pt, tl; cn, un; ls, rs
2, SBP	TBR[R|B]	rebinned cube table	non-equi.	n/a	all
2, SBP	SPEC[R|B]	spectrum table	non-equi.	n/a	pt; cn, un; ls, rs
2.5	3DRBS[R|B]	rebinned cube	non-equi.	native	all
2.5, SBP	3DPBS[R|B]	projected cube	non-equi.	0.5″	pt; un; ls, rs
				1″.5	tl; cn, un; ls, rs
				3″	nq, ov; un; rs
				=drizzled	nq, ov; un; ls
2.5	3DDBS[R|B]	drizzled cube	non-equi.	optimised	nq, ov; un; ls
2.5	3DIBS[R|B]	interpolated cube	non-equi.	3″	pt, tl, nq; un; ls, rs
2.5, SBP	3DEQPBS[R|B]	projected cube	equi.	3″	nq, ov; un; rs
2.5, SBP	3DEQDBS[R|B]	drizzled cube	equi.	optimised	nq, ov; un; ls
2.5, SBP	3DEQIBS[R|B]	interpolated cube	equi.	3″	pt, tl; un; ls, rs
2.5, SBP	TBRBS[R|B]	rebinned cube table	non-equi.	n/a	all; un; all
2.5, SBP	SPECBS[R|B]	spectrum table	non-equi.	n/a	pt; un; ls, rs
3, SBP	SPEC	spectrum table	non-equi.	n/a	pt; cn; sed

a: not to be used for science

10.4.3 Spectroscopy Standalone Browse Products (SBPs)

PACS spectroscopy SBPs are cubes and spectral tables taken from Levels 2, 2.5, or 3. These cubes and tables are explained in Sec. 10.4.2, including which products are provided for which observing modes (Table 10.8), and how to determine the observing mode for an observation (Tables 10.6 and 10.7). Exactly which of the cubes and tables produced by the SPG pipeline are then provided as SBPs also depends on the observing mode. The SBPs can be found in the browseProduct entry of

Table 10.9: The datasets in PACS cubes (which are the extensions in the FITS files)

Name	Description
image, flux	The fluxes (Jy/pixel[aka spaxel or spatial pixel]) as a 3D array ("flux" in a pacs cube, "image" in all other cubes)
coverage, exposure	A measure of the amount of data from the preceding cube that became data in this cube during pipeline processing
error, stddev	The error (Jy/pixel) as a 3D array ("error" in mosaic cubes, "stddev" in rebinned cubes)
wcs-tab	The wavelengths, for cubes with a non-equidistant spectral grid, WCS-complient
ImageIndex, waveGrid	The wavelengths, for cubes with a non-equidistant spectral grid
ra, dec	The ra and dec as a 3D array (per spaxel and per wavelength)
qualityControl	Ignore
flag	The 3D array indicating data-points masked during the pipeline (see named masks in entry below); these are difficult to read outside of HIPE, but a guide is provided in the PPE
Mask	The context holding the masks (see entry below), found only in the pacs cubes (which are not science-grade products)
BLINDPIXELS, [RAW]SATURATION, OUTOFBAND, ...	3D datasets of values indicating data masked for the named flag; these are very difficult to read outside of HIPE and but a guide is provided in the PPE
spectra	In the spectrum and rebinned cube tables, and contains the tabulated spectral data
Status	The Status table contains engineering information, not of interest to the vast majority of PACS users
BlockTable	The table of the data-block organisation, not of interest to the vast majority of PACS users
History, HistoryScript, HistoryTasks, HistoryParameters	The history of the processing (is added to continuously so can be difficult to interrogate)

an ObservationContext viewed in HIPE, and in the browseProduct directory in an unpacked tarball gotten from the HSA.

The cubes provided as SBPs are:

- For Nyquist and oversampled mapping line scan observations: *equidistant drizzled cubes.*

  In HIPE these cubes are contained in a context called HPS3DEQDR (Herschel PACS Spectroscopy 3d [cube] equidistant drizzled red) and HPS3DEQDB (...blue).

- For Nyquist and oversampled mapping range scan observations: *equidistant projected cubes.*

  In HIPE these cubes are contained in a context called HPS3DEQPR (... projected red) and HPS3DEQPB (...blue). On disk the FITS files are in the Level2 directory with the same name.

- For all other observations: *equidistant interpolated cubes.*

  In HIPE these cubes are contained in a context called HPS3DEQIR (... interpolated red) and HPS3DEQIB (...blue).

- For all of these cubes: on disk the FITS files are in the Level2 directory with the context name. For unchopped range scans the cubes for each particular observation (i.e. the on-source and off-source) are provided *and* the background subtracted cubes are provided – these are located in the Level2.5 directory and have a "BS" appended to the names.

For each wavelength range that was requested by the PI of an observation, there will be one red and one blue cube. The names of these FITS files are built from: the "hpacs" + observation id + level (e.g. 20 = 2.0) + the name of the context it comes from + a unique identifier.

These "equidistant" cubes are copies of the Level 2 or 2.5 cubes, but with one difference: they have an equidistant spectral grid. The default wavelength grid for all PACS spectral products is not equidistant – the bin size scales with the spectral resolution (see the PDRG (spec) for more information) – because PACS spectra can cover a large wavelength range and the spectral sampling was chosen to reflect the spectral resolution at each wavelength. However, non-equidistant spectral products can be difficult to read into software other than HIPE, since the spectral part of the WCS is not defined. Therefore, the SBP cube for each observation is created by a task that spectrally resamples the chosen cubes on to an equidistant spectral grid. This grid chosen is finer than the original grid, so that the spectra are practically identical in appearance to the original spectra. The only two things the user must be aware of when using these cubes are (i) the finer spectral sampling results in spectra with very many more datapoints and so they are larger on disk, and (ii) the spectral sampling is no longer a reflection of the spectral resolution, being much finer.

Three types of spectrum tables are also provided as SBPs. These are the same tables that are described in Sec. 10.4.2.3. The "rebinned cube tables" provided as SBPs are taken from Level 2, and also from 2.5 for unchopped range observations, as are the "central and point-source spectrum" tables for all pointed observations. The "SED point-source spectrum tables" are taken from Level 3 for all pointed chop-nod full SED spectral coverage observations.

10.4.4 Highly-Processed Data Products

Highly Processed Data Products (HPDPs) are sets of products generated by expert scientists, generally from the Herschel Science Centre (HSC), the NASA Herschel Science Center (NHSC), and the Instrument Control Centres (ICC). The HPDPs improve upon the standard pipeline-generated products, provide alternative products that are better for a particular science analysis, or are complementary products which can be used to check on or inspect a certain aspect of the data.

The HPDPs are available at the HSC legacy repository[1], and they will also be served from the HSA. All available Highly Processed Data Products are listed in a specially dedicated page[2] available at the Herschel Science Centre portal.

Here we list and briefly describe the PACS HPDPs. Each sub-folder in the HPDP/PACS folder contains the products and a release note with details on the methods used to generate the products. The HPDP products are explained in their respective Release notes. If not available directly via the HSA (as part of the search results or via a direct download from the HSA), the HPDPs can be obtained from the above-given link.

[1] URL: http://archives.esac.esa.int/hsa/legacy/HPDP/PACS
[2] URL: https://www.cosmos.esa.int/web/herschel/highly-processed-data-products

10.4.4.1 Photometer

Several of the photometry HPDPs are combinations of observations to produce superior maps. The PACS Point Source Catalogue is also provided as an HPDP.

- JScanam large field maps. The main purpose of these HPDPs is the provision of higher-quality JScanam maps of very extended regions. These regions could not be covered by a single PACS observation and required several pointings. Combining these separate pointings into a single map covering the entire region could not be done by the SPG, nor could the extra work required to match the background fluxes in the overlap regions, and to account for the higher noise at the map edges when mosaicking the fields together. Examples of these kind of maps are those of the Milky Way, the Orion star forming region and the Large and Small Magellanic Clouds. The MCs are a special case because they were not observed with the standard scan+cross-scan mode, and hence JScanam maps were not even produced by the SPG pipeline.

- Unimap extra maps. This HPDP has a similar goal as the JScanam large fields, but here Unimap maps will be produced. The fields include the North and South Galactic Poles, Bootes-Spitzer field, the MCs and the Bridge Region, L 1521, Draco cloud, Video-XMM fields, and a few others where the SPG pipeline did not produce Level 2.5 maps.

- PACS Point Source Catalogue. The PACS PSC contains more than half a million entries in the three PACS bands. The catalogue consists of several tables provided as compressed CSV format files: one PSC table for each band; a list of slightly extended sources (HPESL); and a rejected source list (HPRSL).

10.4.4.2 Spectrometer

The spectroscopy HPDPs offer data that are not present in the SPG product, or provide data complementary to the SPG-processed observations. The can be found in the HPDP cosmos page.

- Red leak spectra. PACS Spectrometer observations with wavelengths longward of 190 μm were not processed by the SPG pipeline, as these data are affected by order leakage. These data were instead processed with a non-standard calibration scheme for the chop-nod observations and the SPG calibration scheme for unchopped observations, in both cases with a dedicated relative spectral response function. The spectral cubes feature calibrated order 1 emission lines (i.e. those that originate in the red spectral range, rather than in the leaking range) in the 190–206 μm range, while the continuum remains uncalibrated.
  As the volume of the products is $\sim$ 170 GB, these are only available through the HSA.

- Blue edge spectra. The range between 51 μm and 55 μm cannot be calibrated, however there were data taken in this range (either because it is in the parallel camera or because the observer specifically requested it). These data will be released without a flux calibration as an HPDP.
  As the volume of the products is $\sim$ 83 GB, these are only available through the HSA.

- On-source and Off-source cubes. In order to make it easier for users to inspect the off-source data from an observation, e.g. to check for the presence of contamination (line emission, mainly), all the unchopped line-scan and chop-nod observations will be processed to produce separate on-source and off-source cubes, and the postcard will show the field-averaged spectrum

from the on-source and off-source together. For the unchopped range-scans it is not necessary to create separate cubes – the on-source and off-source are separate observations anyway – but postcards will be produced to show the field-average spectrum of the two observations together. As the volume of the products is $\sim$ 190 GB, these are only available through the HSA.

- Pointing Offset Correction point-source spectra. For point sources observed with the chop-nod pointed mode, the point-source calibrated spectra produced by the Pointing Offset Correction (POC) script may be superior to those produced from the SPG pipeline, if there was a large pointing offset (i.e. the source is not in the centre) or a lot of pointing jitter during the observation. This script – which is an interactive pipeline script in HIPE – is currently being run on all observations of this mode, and the results – the spectra and the diagnostic data created by the pipeline – will be provided as an HPDP. Also available from here.

10.5 Calibration products and the calibration tree

Each PACS ObservationContext downloaded from the HSA contains a calibration tree. The calibration tree contains all the calibration products necessary to reduce any – spectroscopy or photometry – observation, and is also the same calibration tree that was used to reduce that observation. The calibration tree can also be downloaded separately via HIPE (this is explained in the PDRG (spec)), where it is unpacked into a directory and consists of individual FITS files.

The calibration tree is organised into a spectroscopy, a photometry, and a common section, and these are listed in Tables 10.10, 10.11, and 10.12. If working with the calibration tree that comes with a downloaded observation, the organisation of the data on disk is the same as the organisation in HIPE. On disk these various calibration products are held as FITS files. The name of the FITS files are the same as the names of the calibration products in HIPE: "PCalPhotometer_TevCorrection_FM_v1.fits" on disk is called calibration.photometer.tevCorrection in HIPE. The datasets that contain the actual "tev" calibration are inside the "tevCorrection" product. ("FM" simply refers to "flight model", i.e. the PACS instrument that actually flew on Herschel.)

A new version of the tree was produced whenever new calibration products were added or updated, and users who next opened HIPE were offered the chance to update their calibration tree on disk (in the directory ".hcss/data/pcal-community"). However, after the final SPG processing for PACS, the calibration tree was frozen. Hence the calibration tree that comes with all observations gotten from the HSA from early 2017 onwards will be the final calibration tree, and there is no need to download it independently.

A history of the calibration tree versions can be found from the Herschel pages, here, and linked from there are the release notes for each version. These release notes are also included in the calibration tree directory on disk, as html files. Most of the calibration product FITS files also have an associated html "info" file on disk.

Table 10.10: The contents of the PACS Spectrometer calibration tree.

Product	Description
absoluteCapacitance	The measured capacitances for the red and blue detector arrays
arrayInstrument	Array to Instrument coordinate conversion
badPixelMask	Bad pixels mask
beamSize	Measured FWHM of the beam vs. wavelength
beams[B2A|B3A|B2B|R1]	Beam profiles used in the Pointing Offset Correction pipeline (for the named bands)
beamsPerSpaxel[B2A|B3A|B2B|R1]	Beam profiles for each spaxel (for the named bands)
calSourceFlux	The fluxes (Jy) of the internal calibration sources at the primary key wavelengths
calSourceFlux3x3	An update of calSourceFlux computed from an improved calibration scheme
capacitanceRatios	The capacitance ratios for the red and blue detector arrays
chopperThrowDescription	The CPR (chopper position readouts) with verbal descriptions
crosstalkMatrix	Crosstalk matrices for the red and blue detector arrays
darkCurrent	Dark current (V/s) for the red and blue detector arrays
detectorSortMatrix	Detector sorting matrices for the red and blue detector arrays
discardRampHooks	Number of discarded readouts at the hook-shaped start of the ramps
effectiveCapacitance	Effective measured capacitances of the four commandable capacitances of the spectrometer
extendedSourceLoss	Fraction of the signal of an extended source seen in a single spatial pixel
filterBandConversion	The wheel position (WPR) readout-to-band conversion
gprHall	The GPR (DM_GRAT_CUR_POS) versus Hall sensor readback calibration object
gprHallRedundant	The redundant GPR (DM_GRAT_CUR_POS) versus Hall sensor readback calibration object
gratingJitterThreshold	Value for the jitter threshold of the final grating positions in readout units
keyWavelengths	The primary and secondary key wavelengths
labelDescription	The bit-coded labels with verbal descriptions
littrowParameters	Littrow parameters for wavelength calibration
littrowPolynomes	Grating wavelength calibration: Littrow equation parameters / polynomial approximation for alpha per pixel

Table 10.10: con't

Product	Description
moduleArray	Module to Array coordinate conversion
noisyPixelMask	Noisy pixels for the red and blue detector arrays
nominalResponse	The nominal responses in V/s/Jy at the prime key wavelengths
nonLinearity	Coefficents of a second order polynomial fit to linearise the signals for the red and blue detector arrays
observedResponse	The responses (V/sJy) for red and blue detector arrays, computed via observations of astronomical standards
observedResponse3x3	An update of the observedResponse based on an improved calibration scheme
offRatio[B2A|B3A|B2B|R1]	Signal ratio of the off positions used in the Pointing Offset Correction pipeline (for the named bands)
pointSourceLoss	Fraction of the signal of a point source seen in a single spatial pixel, in the central 3x3 and in the 5x5 spatial pixels
psf	Point spread functions for the red and blue spectrometer
rampSatLimits	Ramp saturation limits (digits) for the red and blue detector arrays
readouts2Volts	The ramp readout to volt conversion
relCalSourceFlux	The flux ratios of the calibration sources at the key wavelengths to those at the prime key wavelengths
rsrf[B2A|B3A|B2B|R1]	The relative spectral response function at the key wavelengths (for the named bands)
sensitivity	The line and continuum RMS noise fluctuations for a 1 sec integration time
signalSatLimits	The signal saturation limits (digits/second) for the red and blue detector arrays scaled to 1 second reset interval
specProperties	Constants for calculating the spectral resolution vs. wavelength
telBackCor[B2A|B3A|B2B|R1]	The wavelength, position and time dependent correction factors for the telescope background (for the named bands)
telescopeBackground	Telescope background SED
timedep	The time dependency for the calibration products, and which version is current
wavePolynomes	Grating wavelength calibration: grating step parameters / polynomial coefficients
wavelengthGrid	The wavelength grid for the three grating orders and for different upsample values

Table 10.11: The contents of the PACS Photometer calibration tree

Product	Description
absorption	Absorption values Photometer
apertureCorrection	Aperture correction factors for pixfrac=1.0
arrayInstrument	Array to Instrument coordinate conversion
badPixelMask	Bad pixels mask for PACS Photometer
calSources	Flux per pixel from the internal calibration sources (CSs) in the blue and red channel
clSaturationLimits	CL saturation limits
clTransferFunction	SurfCal_20061120 calibration VRL-VH_BLIND for saturation limits computation
coolerRecyclingTimes	Cooler recycling Times
corrZeroLevel	Zero-level corr for PACS Photometer based on the low-freq noise observations of OD97
crosstalkMatrix	Photometer Crosstalk matrix for red and blue channel
detectorReadoutTimeShift	Time shifts for red and blue photometer detector readouts
detectorSortMatrix	Time shifts for red and blue photometer detector readouts
diffCS	Difference of CS1 and CS2
filterTransmission	FilterTransmissions calibration product for the red and blue photometer.
flatField	FlatFields calibration product for the red and blue photometer.
gain	Photometer Gain parameters for Digits to Volts conversion
invntt	Noise2Noise correlation for MadMap
invnttBL	BL band inverse noise time-time correlation for MadMap based on the Version 1 of the Invntt cal data.
invnttBS	BS band inverse noise time-time correlation for MadMap based on the Version 1 of the Invntt cal data.
invnttRed	RED band inverse noise time-time correlation for MadMap based on the Version 1 of the Invntt cal data.
masks	Boolean-2D arrays marking the positions of permanently damaged pixels
noisePerPixel	Noise for each pixel to populate the starting values in the noise cube (not used)
nonLinearCoef	Coefficients for non-linearity corrections from logarithmic fit to middle points
photometricStabilityThreshold	thresholds used to raise an alert on bad photometric stability
responsivity	Responsivity calibration product for red and blue photometers.
satLimits	Matrix of saturation values for Photometer
subArrayArray	Coordinate conversion (row, col) -¿ (U,V) for the bolometer arrays
tevCorrection	Evaporator temperature correction parameters for the red and blue photometer
timedep	Defines time dependency for calibration products

Table 10.12: The contents of the PACS Common calibration tree

Product	Description
chopperAngle	Chopper position readout vs. chopper angle calibration
chopperAngleRedundant	Ditto, for the redundant chopper
chopperJitterThreshold	The threshold, in position readouts, within which the required accuracy of the chopper positions for the science and calibration windows is reached
chopperSkyAngle	Conversion factor for the chopper deflection angle (degrees) to the angle on the sky (arcmin), and the offset between the mechanical and optical zero position
csResistanceTemperature	Resistance temperature conversion for the calibration sources
filterWheel2Band	Filter wheel position (wpr) to band conversion
obcpDescription	The on-board control procedure descriptions vs number
siam	The spacecraft to instrument alignment matrices
timedep	Defines the time dependencies for the calibration products

Chapter 11

Source-specific product and analysis advice

See the PACS overview page for a summary of working with PACS spectrometer and spectrometer products, for different types of observation and source, and with links to the most important user-focused documentation. Most of this linked documentation is on HELL L1 and HELL L2. For those more interested in video material, a series of video tutorials to various aspects of working with PACS data can be found on the legacy training site. The documentation that is mentioned in these tutorials, to be read along with them, can all be found on HELL L2.

On HELL L1 you can find the quick-start guides to the photometer and spectrometer. These are a good place to get an overview of the instruments, their calibration, and their data products.

Detailed lists of issues/problems/warnings about PACS photometry products are available in the Data Products Known Issues page. *This page should be consulted as the information is not repeated here.* In addition, all observations in the HSA have a qualitySummary in which any specific quality issues for the observation can be found; this can be most easily checked in the HSA search results tab, rather than in the observation downloaded.

11.1 Photometry

The Level 2.5 Unimap and JScanam maps (the latter also being SBPs) are both science-ready products that can be used for point sources or extended emission. The HPF+photProject maps can be used only for point-like emission, and those in Level 2.5 should be used in preference to those in Level 2, as the sensitivity will be higher (being combined scan+cross-scans). If Level 3 maps exist, these can be adopted instead of the Level 2.5 maps because of the better SNR (being the combination of several Level 2.5 products). For aperture photometry, the aperture and colour corrections as detailed in Chp. 7 should be used. It should also be noted that PACS maps are differential maps, where the absolute level is undefined as it is removed by the map-making process. Hence it is not a worry if the background level is negative. All measurements should be made with respect to the (source-free) background on the maps.

11.1.1 Using HIPE to work with PACS photometry

A number of scripts are provided in HIPE to work directly from SPG products. These are documented in the PDRG (phot) (chp. 1). The most interesting of these for the archive user are:

- Point-source photometry for a single or multiple sources
- Convolving images at a shorter wavelength to the beam of a longer wavelength

11.2 Spectroscopy

A decision tree to guide the user through the products to use depending on the nature of the target (point source, small source, extended sources) and the type of observation (mapping, pointed, unchopped, chop-nod) can be found on HELL L2. You may want to consult that while reading the advice offered here.

Also highly recommended are the following user notes, which contain the latest information and were written to be read with the video tutorials on the Herschel Academy YouTube channel:

- Dealing with Point Sources Observed with PACS Spectroscopy explains the point-source corrections; explains what to do if the point source is offset from the centre of the cube, including how to determine the offset; and explain the effects of offsets on the resulting spectrum.
- Dealing with Semi-Extended Sources Observed with PACS Spectroscopy explains how to compute corrections for small sources.
- Dealing with Extended Sources Observed with PACS Spectroscopy explains what the effect the spatial sampling has on the quality of the data on extended sources. Also discussed here are the flux correction for irregular extended sources. The fluxes in PACS spectrometer cubes are only fully calibrated for fully-extended, i.e. flat, sources. Among others, this is ensured by an extended source correction (ESC) that is applied by the pipeline to correct for the non-uniform spatial response of the system (Sec. 8.3.4). For flat sources, whether from mapping or pointed observations and for any Level 2/2.5 cube, nothing more needs to be done to the data before carrying out the science measurements. But for any other source morphology, the fluxes derived from the SPG cubes will be formally incorrect. Extra corrections to the spectrum of the observed source extracted from the cube or from within any aperture can be computed, and these are explained here.
- PACS Spectrometer: dealing with "contaminated" off-source data explains under what conditions you need to remove an unwanted source of emission from your cube in order to apply corrections or extract scientifically-valid fluxes, and how to do this. This note is coupled with the OnOff HPDP (Sec. 10.4.4.2).

HIPE tasks are available to apply the corrections for all of these cases, and the prime references are these user notes. The contents of those notes are summarised here.

11.2.1 Point sources

To recover the correct flux levels for point sources, an aperture efficiency is applied via the point-source correction factor (see Sec. 8.3.3), after having first removed the ESC (the extended source correction). Summing up the FoV of the cube will usually not produce a spectrum with the correct flux level. The point-source correction is a beam correction applied to a spectrum taken from the Level 2/2.5 rebinned cubes. Two separate tasks and two separate scripts are provided in HIPE to deal with point sources. *However, it is expected that in most cases the point-source table (HPSSPECxxx), which is found in any HSA-downloaded observation, can be used directly as the correct spectrum of a point source without needing to run a task in HIPE.*

The various scenarios for point sources are outlined below. The first thing that a user needs to determine is where the point source is located, as this leads directly to which tasks/scripts/products can be used. In many cases, more than one task or script can be used for any one observation. Note that the limits given for the offset of the point source from the centre of a rebinned cube in the scenarios outlined here are not strict, because it depends also on the brightness of the source and the direction of the offset (e.g. square with the cube's grid or diagonally across it).

(If working with unchopped observations, for which the continuum level has a significant uncertainty, it may be a good idea to perform a continuum subtraction before running any of HIPE tasks discussed below.)

11.2.1.1 Estimating the location of a point source in the FoV

Most point-source observations will have been done in the pointed mode, and hence the user will begin with the rebinned cube (HPS3DR[BS][R|B]: see Tables 10.4 and 10.5). How does one estimate the location of a point source (or any source) in the FoV of a rebinned cube (Level 2 or 2.5)? It is unfortunately difficult to directly *measure* the offset from the centre of the spaxel in a rebinned cube, since the beam is undersampled for pointed observations. However, it can be guestimated.

- Compare the requested coordinates (or known coordinates of the source) to that achieved during the observation. The FITS keywords "RA" and "DEC" in the cube FITS file (not those the meta data of the entire observation) contain the achieved pointing (i.e. that in the centre of the cube), "RA_NOM" and "DEC_NOM" the requested pointing. However, do bear in mind that there there can be an error of up to a few arcsec in these respective positions.
- Using the Spectrum Explorer or Cube Image Viewer in HIPE (PDRG (spec), chp. 10), look at the cube. If most of the flux is in spaxel 2,2 (i.e. the centre of the FoV), the source is well-centred; an off-centring of a few arcsec (just under half a spaxel) can usually be detected via an uneven flux distribution. Note that for unchopped observations, since the continuum level uncertainty in each spaxel is very high, it will be necessary to concentrate on emission lines (or do a continuum subtraction first) before the point-source can usefully be located in the FoV.
- Look also the interpolated cube (HPS3DI[BS][B|R]: which are also provided for pointed observations), where the smaller spaxel sizes make inspecting offsets slightly easier. The centre of the interpolated cube will be very close to be the centre of the rebinned cube.
- Use the PACS footprint viewer (PDRG (spec), chp. 10) to overplot the footprint of a rebinned cube on an image of the FoV (you need to provide the image, e.g. from PACS photometry). **This is usually the most sensitive measure of offset.**

- Compare the beam image (provided on HELL L2 as "PACS Spectrometer Beams (2016)") at the closest wavelength to an image of the rebinned cube from your observation (the two need to be resampled to the same pixel size). The beam image is that of a completely centred point source.
- Run the "Pointing Offset Correction" (Sec. 9.2.2) pipeline script in HIPE (for chop-nod AOTs only), which calculates the offset of a point source from the centre of the FoV (look for the task *plotPointingOffset*).

These points are further explained in Dealing with Point Sources Observed with PACS Spectroscopy.

If you are working with a mapping observation, to chose the rebinned cube to apply the point-source corrections on, you should locate the particular rebinned cube, from the entire raster of rebinned cubes in the observation, in which the point source is located in the centre. The same steps outlined here can then be followed.

11.2.1.2 Source offsets up to 5″ (half a spaxel)

For sources that are located mostly within the central spaxel, the HIPE task *extractCentralSpectrum* can be used to perform the point-source corrections. It is recommended that the interested user reads the PDRG (spec) (chp. 8) to learn more about this task; the task is also demonstrated in one of the Useful scripts of HIPE, and it is explained in Dealing with Point Sources ....

Three point-source spectra are created by *extractCentralSpectrum*: one based on the spectrum taken from the central spaxel only (called *c1* in the PDRG (spec)), one based on the sum of the central 3×3 spaxels (called *c9*), and one that is a combination of the two (the spectrum of *c1* adjusted to the flux level of *c9*, and called *c129* in the PDRG (spec)).

- The *c1* spectrum has had the essential beam correction applied to it, and is appropriate only for faint sources (where very little flux lies outside the central spaxel) and (faint or bright) sources with offsets of no more than $\sim 2''$.
- By using a larger area of the cube, the *c9* spectrum accounts for flux losses due to slight pointing offsets and pointing jitter during the observation, therefore this point-source spectrum is the recommended product for all unchopped observations (excluding the very faint, where *c1* is better), and for sources with offset between ~ 4–$9''$(whatever the flux level or observing mode).
- The *c129* spectrum will usually have the superior SNR of *c1* but the pointing offsets/jitter-robust flux level of *c9*, and is suitable for all sources from chop-nod observation with offset no more than $\sim 4''$.

The point-source table (HPSSPECxxx) at Level 2, 2.5, and 3, includes the fluxes and errors of *c1*, *c9*, and *c129* for all chop-nod pointed observations, and *c1*, *c9* for all the unchopped pointed observations (*c129* is inappropriate for unchopped observations). The organisation of the data in the point-source table is explained in the PPE: the column "pointSourceFlux" is *c1*, "pointSourceCen3x3Flux" is *c9*, and "pointSourceScaledFlux" is *c129*.

Note that the effect of the average pointing error is already included in the flux calibration scheme (specifically in the 15% calibration uncertainty given for PACS spectroscopy: Sec 5.2.1), accounting for the flux errors arising from pointing errors and including the repeatability error.

For unchopped observations, it should be born in mind that there is a high uncertainty in correcting for transient effects during an observation, and especially in correcting for response changes between when the on-source and off-source pointings/observations were made. *Continuum fluxes can vary by up to* ± 20 *Jy in each spaxel (e.g. Sec 5.2.6). As such, and especially when using the c9 point-source spectrum, it should be born in mind that the continuum level could be very wrong indeed.* In any case, this AOT was recommended only for science cases concentrating on emission lines: hence it is worth considering subtracting the baseline from the spectra before analysing the cubes.

11.2.1.3 Source offsets up to 10″ (one spaxel) or with pointing jitter during the observation

The "Pointing offset correction" (POC) pipeline script in HIPE can be run on pointed chop-nod observations of point sources: particular tasks in this script are used to estimate the offset of the source from the centre of the FoV of the rebinned cube, and to correct the flux levels for this offset. Since the offset can be measured for chunks of time throughout the observation, and therefore correct for pointing jitter as well as the average offset, the result can be a smoother spectrum with a more correct continuum shape and slightly higher flux levels (source-brightness, pointing-offset, and jitter-level dependent). (This is true whether the source has an average offset of 0″or 10″.) At the end of the pipeline, the Level 2 cubes are then processed though *extractCentralSpectrum* and the end results are the point-source corrected spectra (*c129* or *c9*, in that order of preference, but never *c1*), *not* the cubes. Use of this pipeline script is explained in the PDRG (spec) (the pipeline chapters and chp. 8) and discussed briefly here in Sec. 9.2.2.

This script can be used on any point source offset from 0″ to one spaxel, but is probably most useful for sources for which broad-band features or the continuum shape are of prime interest. It has been tested on sources down to 10 Jy continuum level, so for fainter sources more attention should be paid to the inspection tasks included in the pipeline script. It also works better on spectral ranges rather than line scans, as the longer spectral stretch allows for a better-determined offset determination. The results should be compared to those taken from the HPSPEC table Level 2, as large differences are not expected as long as the source lies within the central 3×3 spaxels.

An HPDP that provides POC-processed spectra for most chop-nod pointed observations is provided, see Sec. 10.4.4.2.

11.2.1.4 Sources fully centred a non-central spaxel

For sources which are not in the central spaxel but which are well-centred within another spaxel, the essential point-source correction can be applied with two simple tasks in HIPE: *extractSpaxelSpectrum+pointSourceLossCorrection*. These tasks are demonstrated in one of the Useful scripts of HIPE and explained in the PDRG (spec) (chp. 8). If applied to the central spaxel (coordinate 2,2), the result will be the same as *c1* (Sec. 11.2.1.2). The point source correction applied by *pointSourceLossCorrection* is based on the calibrated beam of spaxel 2,2, and since the beams of each spaxel are slightly different, this correction is not, strictly-speaking, fully appropriate for any other spaxel. However, the expected differences are much smaller than the point-source correction factors applied.

If the point source is located within the central 3×3 spaxels, the POC script (Sec. 11.2.1.3) is recommended over the two tasks mentioned here. However, the POC script may have difficulties measuring the pointing offsets of a faint source, and if the source is mostly contained within a single spaxel, the two tasks explained here may be preferred.

11.2.1.5 Source offsets $> 10''$ (one spaxel), or lying between spaxels, or from mapping observations

This final scenario concerns: point sources that are offset from the centre by more than a spaxel *and* which are fall substantially *between* spaxels (so the scenario of Sec. 11.2.1.4 cannot be followed); point sources with offsets of more than a spaxel, or which are just too faint (so the POC script of Sec. 11.2.1.3 either cannot be used or may not produce useful results); or if the user is working with a mapping observation and it is not possible to locate a rebinned cube in which the point source is nicely located. In this case the *Forward Modelling* script (FM script) can be used. The FM script is explained in Sec. 11.2.3, and the model input in this case would be that of a narrow Gaussian (= a point source) with the coordinates of the target. After using the FM script it will not be necessary to apply the point-source correction tasks explained above, as the result will be (or will lead directly to) the necessary point-source correction.

11.2.2 Slightly extended sources

For small sources which have a diameter of less than about 15–30$''$ and are from pointed observations, the calibrated spectrum of the source can be extracted from the rebinned cube using a combination of the HIPE tasks *extractCentralSpectrum* and *specExtendedToPointCorrection*. Again, summing up the spectra from the cube is *not* sufficient. The tasks work on the Level 2 or 2.5 rebinned cubes (HPS3DRxxx). The PDRG (spec) (chp. 8) and the in-HIPE software reference documentation can be consulted for instructions.

The main input to this task is a model of the surface brightness distribution of the source (shape, size, position angle: some simple cases are explained in the task documentation). Since the first step is to run *extractCentralSpectrum*, it is necessary that the source is not offset from the centre of the FoV of the rebinned cube by more than 1/2 spaxel. If the offset is greater than this, the FM script (Sec. 11.2.3) should be used.

11.2.3 Irregular extended sources: the forward modelling script

For extended sources, with an irregular or steep surface brightness distribution, the flux measured in any aperture (from one spaxel to the entire field) from any Level 2/2.5 cube will not be fully corrected for the non-uniform spatial response of the system (Sec 8.3.4), regardless of the pointing/mapping mode of the observation. It is possible to estimate the correct flux distribution using the *Forward Modelling script* in HIPE. The most important input to the FM script is a model of the surface brightness distribution of the source – the shape, size, position angle – and an input spectrum. The FM script turns the input into simulated rebinned cubes, which can then processed by any of the three mosaicking tasks of the pipeline. The results can then be compared to the SPG Level 2/2.5 cubes, for example the user can create the ratio between the spectral cubes of simulated and observed data and derive the correction over an aperture to be used for spatial extraction. The results depends on the shape of the source and the pointing pattern of the observation, which is why it needs to be calculated uniquely, for each observation and for each spectral range scanned during the observation. The FM script runs in HIPE and a package of scripts and documentation can be found on HELL level 2 (see the technical note also).

If no correction is applied, the degree of inaccuracy in the measured fluxes will be unique to each observation, and to every source in it.

The FM script will compute the correction to the fluxes of the source, but it does not correct for the distortions to the line profiles that are caused by point-like features moving out of/in to the PACS detector slit (Sec. 8.4.2.2). These distortions take the form of a skew to the line profile, which causes the line centre to shift and line profile to change. Therefore, the ratio values produced by the FM script in the wings of spectral lines should not be over-interpreted. This effect is averaged out when considering spatially symmetric apertures for spectra extraction over the spectral mosaic cube.

11.2.4 How to detect contamination in the off-source spectra

The science-readiness of an observation depends on the off-source pointings being free of unwanted line or continuum emission – for both unchopped and chop-nod AOTs. It was the responsibility of the observer to define the off-source position and therefore to ensure this was the case. Since the final product of the pipeline are background-*free* cubes, for most AOTs it is not possible to inspect the off-source pointing data from an ObservationContext gotten from the HSA to check for the presence (or not) of contamination. Instead, the user would need to do the following:

- Chop-nod (line or range, pointed or mapping): open HIPE and run the the Split On-Off script (Sec. 9.2.2). In this script, the on-source and off-source data are separated from each other and both processed to Level 2, where on-source and off-source rebinned cubes are created.

- Chop-nod (line or range, pointed or mapping): another possibility is to open HIPE and run the two pipelines scripts that use a different flux calibration scheme (internal calibration sources vs. telescope background spectrum), but which are otherwise exactly the same. When comparing the results of the two, spectra that are affected by line (and less reliably, continuum) emission in the off-source pointings should stand out. See Sec. 9.2.2 for more detail.

- Unchopped line (pointed or mapping): open HIPE and run the "Calibration source and RSRF" pipeline script (Sec. 9.2.2; the "...with transient correction" pipeline script can also be run, but for the purpose of looking only at the off-source spectrum this is not necessary). This script produces, near the very end of Level 2, an on-source and off-source set of rebinned cubes.

- Unchopped range (pointed or mapping): for unchopped range-scan observations it is not necessary to re-run the pipeline, since the on-source and off-source observations are two separate obsids. By comparing the Level 2 or 2.5 of the on-source observation to the Level 2 of the off-source observation, one can check for (sufficiently significant levels of) unwanted emission in the off-source data. A list of the off-source obsids linked to the on-source obsids can be found here.

As it is unlikely that most users will want to run a HIPE pipeline to simply check for contamination, an HPDP that provides separate on-source and off-source cubes for all PACS spectroscopy observations has been prepared (Sec. 10.4.4.2).

The design of the PACS pipeline does not allow for easy intervention to *remove* line or continuum contamination from the off-source pointings before they are subtracted from the on-source pointings. Such advice as can be offered can be found in PACS Spectrometer: dealing with "contaminated" off-source data.

11.2.5 Using HIPE to create new cubes or fitted cube maps

A number of scripts are provided in HIPE to work directly from SPG products (Level 2 or 2.5 cubes). These are documented in the PDRG (spec) (chp. 1). The most interesting of these for the archive user are:

- Fitting spectral lines in cubes and creating integrated intensity or velocity maps. A separate script for mapping observations and for pointed observations is provided. It is possible to either fit the mosaic cubes (projected, drizzled or interpolated) and create images from the fitting results, or fit the rebinned cubes and then project or interpolate the fitting results. Which method gives better results depends on the type of spectral lines in the data and how much they vary over the observed field. Differences of up to 10% in fluxes between the two methods can be found, but usually only in parts of the field where the SNR is low: on average the differences are less than this.
- Point-source corrections for point sources located inside the central spaxel or fully within any other spaxel.
- Creating cubes with any spaxel size: most useful for drizzled cubes, where cubes of different spectral ranges but for the same observation will have spaxels of slightly different sizes.

Bibliography

Abreu-Vicente, J., Stutz, A., Henning, T., Keto, E., Ballesteros-Paredes, J., and Robitaille, T. (2017). Fourier-space combination of Planck and Herschel images. *A&A*, 604:A65.

Absil, O., di Folco, E., Mérand, A., Augereau, J.-C., Coudé du Foresto, V., Aufdenberg, J. P., Kervella, P., Ridgway, S. T., Berger, D. H., ten Brummelaar, T. A., Sturmann, J., Sturmann, L., Turner, N. H., and McAlister, H. A. (2006). Circumstellar material in the ¡ASTROBJ¿Vega¡/ASTROBJ¿ inner system revealed by CHARA/FLUOR. *A&A*, 452:237–244.

Ade, P. A. R., Pisano, G., Tucker, C., and Weaver, S. (2006). A review of metal mesh filters. In *Society of Photo-Optical Instrumentation Engineers (SPIE) Conference Series*, volume 6275 of *Proc. SPIE*, page 62750U.

Balog, Z., Müller, T., Nielbock, M., Altieri, B., Klaas, U., Blommaert, J., Linz, H., Lutz, D., Moór, A., Billot, N., Sauvage, M., and Okumura, K. (2014). The Herschel-PACS photometer calibration. Point-source flux calibration for scan maps. *Experimental Astronomy*, 37:129–160.

Barbey, N., Sauvage, M., Starck, J.-L., Ottensamer, R., and Chanial, P. (2011). Feasibility and performances of compressed sensing and sparse map-making with Herschel/PACS data. *A&A*, 527:A102.

Beichmann, C. A. (1985). *Infrared Astronomical Satellite (IRAS) catalogs and atlases. Explanatory supplement*.

Berta, S., Magnelli, B., Nordon, R., Lutz, D., Wuyts, S., Altieri, B., Andreani, P., Aussel, H., Castañeda, H., Cepa, J., Cimatti, A., Daddi, E., Elbaz, D., Förster Schreiber, N. M., Genzel, R., Le Floc'h, E., Maiolino, R., Pérez-Fournon, I., Poglitsch, A., Popesso, P., Pozzi, F., Riguccini, L., Rodighiero, G., Sanchez-Portal, M., Sturm, E., Tacconi, L. J., and Valtchanov, I. (2011). Building the cosmic infrared background brick by brick with Herschel/PEP. *A&A*, 532:A49.

Bertincourt, B., Lagache, G., Martin, P. G., Schulz, B., Conversi, L., Dassas, K., Maurin, L., Abergel, A., Beelen, A., Bernard, J.-P., Crill, B. P., Dole, H., Eales, S., Gudmundsson, J. E., Lellouch, E., Moreno, R., and Perdereau, O. (2016). Comparison of absolute gain photometric calibration between Planck/HFI and Herschel/SPIRE at 545 and 857 GHz. *A&A*, 588:A107.

Billot, N. (2011). Non-linearity correction module for the PACS photometer. *PICC-NHSC-TR-031*, Issue 0.2.

Billot, N., Agnèse, P., Auguères, J.-L., Béguin, A., Bouère, A., Boulade, O., Cara, C., Cloué, C., Doumayrou, E., Duband, L., Horeau, B., le Mer, I., Lepennec, J., Martignac, J., Okumura, K., Revéret, V., Sauvage, M., Simoens, F., and Vigroux, L. (2006). The Herschel/PACS 2560 bolometers imaging camera. In *Society of Photo-Optical Instrumentation Engineers (SPIE) Conference Series*, volume 6265 of *Proc. SPIE*, page 62650D.

Billot, N., Sauvage, M., Rodriguez, L., Horeau, B., Kiss, C., Aussel, H., Okumura, K., Boulade, O., Altieri, B., Poglitsch, A., and Agnèse, P. (2010). CEA bolometer arrays: the first year in space. In *Millimeter, Submillimeter, and Far-Infrared Detectors and Instrumentation for Astronomy V*, volume 7741 of *Proc. SPIE*, page 774102.

Bobin, J., Starck, J.-L., and Ottensamer, R. (2008). Compressed Sensing in Astronomy. *IEEE Journal of Selected Topics in Signal Processing*, 2:718–726.

Bouwman, J., Nielbock, M., and Klaas, U. (2009). PACS Chopper Dynamic Behaviour Verification (H COP PAC CHP2 01) during CoP on June 1, 2009. *PICC-MA-TR-083*, Version 2.0.

Chase, Jr., S. C. (1969). Infrared radiometer for the 1969 Mariner mission to Mars. *Applied Optics*, 8:639–643.

Cohen, M. (2003). Stellar Calibration in the Infrared: Extending the Legacy of KAO, ISO, and MSX to SIRTF and beyond. In Metcalfe, L., Salama, A., Peschke, S. B., and Kessler, M. F., editors, *The Calibration Legacy of the ISO Mission*, volume 481 of *ESA Special Publication*, page 135.

Cohen, M., Walker, R. G., Barlow, M. J., and Deacon, J. R. (1992). Spectral irradiance calibration in the infrared. I - Ground-based and IRAS broadband calibrations. *AJ*, 104:1650–1657.

Cohen, M., Witteborn, F. C., Carbon, D. F., Davies, J. K., Wooden, D. H., and Bregman, J. D. (1996). Spectral Irradiance Calibration in the Infrared.VII.New Composite Spectra, Comparison with Model Atmospheres, and Far-Infrared Extrapolations. *AJ*, 112:2274.

Cohen, M., Witteborn, F. C., Walker, R. G., Bregman, J. D., and Wooden, D. H. (1995). Spectral Irradiance Calibration in the Infrared.IV. 1.2-35 micron spectra of six standard stars. *AJ*, 110:275.

Contursi, A. and Lutz, D. (2008). PACS spatial coordinates cheat-sheet. *PICC-ME-TN-027*, Issue 1.0.

Courtin, R., Swinyard, B. M., Moreno, R., Fulton, T., Lellouch, E., Rengel, M., and Hartogh, P. (2011). First results of Herschel-SPIRE observations of Titan. *A&A*, 536:L2.

Dannerbauer, H., Klaas, U., Bouwman, J., Nielbock, M., and Schreiber, J. (2007). Functional and performance tests of PACS internal calibration sources during cold FM ILT. *PACS-MA-TR-033*, Issue 1.1.

Decin, L. and Eriksson, K. (2007). Theoretical model atmosphere spectra used for the calibration of infrared instruments. *A&A*, 472:1041–1053.

Decin, L., Vandenbussche, B., Waelkens, C., Decin, G., Eriksson, K., Gustafsson, B., Plez, B., and Sauval, A. J. (2003). ISO-SWS calibration and the accurate modelling of cool-star atmospheres. IV. G9 to M2 stars. *A&A*, 400:709–727.

Dehaes, S., Bauwens, E., Decin, L., Eriksson, K., Raskin, G., Butler, B., Dowell, C. D., Ali, B., and Blommaert, J. A. D. L. (2011). Structure of the outer layers of cool standard stars. *A&A*, 533:A107.

Doi, Y., Takita, S., Ootsubo, T., Arimatsu, K., Tanaka, M., Kitamura, Y., Kawada, M., Matsuura, S., Nakagawa, T., Morishima, T., Hattori, M., Komugi, S., White, G. J., Ikeda, N., Kato, D., Chinone, Y., Etxaluze, M., and Cypriano, E. F. (2015). The AKARI far-infrared all-sky survey maps. *PASJ*, 67:50.

Draine, B. T. and Li, A. (2007). Infrared Emission from Interstellar Dust. IV. The Silicate-Graphite-PAH Model in the Post-Spitzer Era. *ApJ*, 657:810–837.

Duband, L. (1995). A Thermal Switch for Use at Liquid Helium Temperature in Space-Borne Cryogenic Systems. In Ross, R. G., editor, *Cryocoolers 8*, pages 731–741. Springer US, Boston, MA.

Duband, L., Clerc, L., Ercolani, E., Guillemet, L., and Vallcorba, R. (2008). Herschel flight models sorption coolers. *Cryogenics*, 48(3-4):95 – 105.

Ducati, J. R. (2002). VizieR Online Data Catalog: Catalogue of Stellar Photometry in Johnson's 11-color system. *VizieR Online Data Catalog*, 2237.

Esquej, P. and Sánchez-Portal, M. (2017). Astrometry correction for observations affected by a thermoelastic drift. *HERSCHEL-HSC-TN-2130*, Issue 1.1.

Fadda, D., Jacobson, J. D., and Appelton, P. N. (2016). Transient effects in Herschel/PACS spectroscopy. *A&A*, 594:A90.

Feuchtgruber, F., Sturm, E., and Poglitsch, A. (2010). PACS OBCPs and DMC Sequences. *PICC-ME-LE-005*, Issue 2.2.

Fletcher, L. N., Drossart, P., Burgdorf, B., Orton, G. S., and Encrenaz, T. (2016). Neptune's atmospheric composition from AKARI infrared spectroscopy. *A&A*, 514:A17.

Fruchter, A. S. and Hook, R. N. (2002). Drizzle: A Method for the Linear Reconstruction of Undersampled Images. *PASP*, 114:144–152.

Fulchignoni, M., Ferri, F., Angrilli, F., Ball, A. J., Bar-Nun, A., Barucci, M. A., Bettanini, C., Bianchini, G., Borucki, W., Colombatti, G., Coradini, M., Coustenis, A., Debei, S., Falkner, P., Fanti, G., Flamini, E., Gaborit, V., Grard, R., Hamelin, M., Harri, A. M., Hathi, B., Jernej, I., Leese, M. R., Lehto, A., Lion Stoppato, P. F., López-Moreno, J. J., Mäkinen, T., McDonnell, J. A. M., McKay, C. P., Molina-Cuberos, G., Neubauer, F. M., Pirronello, V., Rodrigo, R., Saggin, B., Schwingenschuh, K., Seiff, A., Simões, F., Svedhem, H., Tokano, T., Towner, M. C., Trautner, R., Withers, P., and Zarnecki, J. C. (2005). In situ measurements of the physical characteristics of Titan's environment. *Nature*, 438:785–791.

Gautier, III, T. N., Boulanger, F., Perault, M., and Puget, J. L. (1992). A calculation of confusion noise due to infrared cirrus. *AJ*, 103:1313–1324.

Geis, N. and Lutz, D. (2010). Herschel/PACS modeled point-spread functions. *PICC-ME-TN-029*, Issue 2.0.

Gordon, K. D., Engelbracht, C. W., Fadda, D., Stansberry, J., Wachter, S., Frayer, D. T., Rieke, G., Noriega-Crespo, A., Latter, W. B., Young, E., Neugebauer, G., Balog, Z., Beeman, J. W., Dole, H., Egami, E., Haller, E. E., Hines, D., Kelly, D., Marleau, F., Misselt, K., Morrison, J., Pérez-González, P., Rho, J., and Wheaton, W. A. (2007). Absolute Calibration and Characterization of the Multiband Imaging Photometer for Spitzer. II. 70 μm Imaging. *PASP*, 119:1019–1037.

Gustafsson, B., Bell, R. A., Eriksson, K., and Nordlund, A. (1975). A grid of model atmospheres for metal-deficient giant stars. I. *A&A*, 42:407–432.

Gustafsson, B., Edvardsson, B., Eriksson, K., Mizuno-Wiedner, M., Jørgensen, U. G., and Plez, B. (2003). A Grid of Model Atmospheres for Cool Stars. In Hubeny, I., Mihalas, D., and Werner, K., editors, *Stellar Atmosphere Modeling*, volume 288 of *Astronomical Society of the Pacific Conference Series*, page 331.

Hammersley, P. L., Jourdain de Muizon, M., Kessler, M. F., Bouchet, P., Joseph, R. D., Habing, H. J., Salama, A., and Metcalfe, L. (1998). Infrared standards for ISO. I. A new calibration of mid infrared photometry. *A&AS*, 128:207–219.

Hanel, R., Crosby, D., Herath, L., Vanous, D., Collins, D., Creswick, H., Harris, C., and Rhodes, M. (1980). Infrared spectrometer for Voyager. *Applied Optics*, 19:1391–1400.

Hauser, M. G., Arendt, R. G., Kelsall, T., Dwek, E., Odegard, N., Weiland, J. L., Freudenreich, H. T., Reach, W. T., Silverberg, R. F., Moseley, S. H., Pei, Y. C., Lubin, P., Mather, J. C., Shafer, R. A., Smoot, G. F., Weiss, R., Wilkinson, D. T., and Wright, E. L. (1998). The COBE Diffuse Infrared Background Experiment Search for the Cosmic Infrared Background. I. Limits and Detections. *ApJ*, 508:25–43.

Herbstmeier, U., Abraham, P., Lemke, D., Laureijs, R. J., Klaas, U., Mattila, K., Leinert, C., Surace, C., and Kunkel, M. (1998). Small-scale structures in the far-infrared background. *A&A*, 332:739–747.

Juvela, M., Demyk, K., Doi, Y., Hughes, A., Lefèvre, C., Marshall, D. J., Meny, C., Montillaud, J., Pagani, L., Paradis, D., Ristorcelli, I., Malinen, J., Montier, L. A., Paladini, R., Pelkonen, V.-M., and Rivera-Ingraham, A. (2015). Galactic cold cores. VI. Dust opacity spectral index. *A&A*, 584:A94.

Kawada, M., Baba, H., Barthel, P. D., Clements, D., Cohen, M., Doi, Y., Figueredo, E., Fujiwara, M., Goto, T., Hasegawa, S., Hibi, Y., Hirao, T., Hiromoto, N., Jeong, W.-S., Kaneda, H., Kawai, T., Kawamura, A., Kester, D., Kii, T., Kobayashi, H., Kwon, S. M., Lee, H. M., Makiuti, S., Matsuo, H., Matsuura, S., Müller, T. G., Murakami, N., Nagata, H., Nakagawa, T., Narita, M., Noda, M., Oh, S. H., Okada, Y., Okuda, H., Oliver, S., Ootsubo, T., Pak, S., Park, Y.-S., Pearson, C. P., Rowan-Robinson, M., Saito, T., Salama, A., Sato, S., Savage, R. S., Serjeant, S., Shibai, H., Shirahata, M., Sohn, J., Suzuki, T., Takagi, T., Takahashi, H., Thomson, M., Usui, F., Verdugo, E., Watabe, T., White, G. J., Wang, L., Yamamura, I., Yamauchi, C., and Yasuda, A. (2007). The Far-Infrared Surveyor (FIS) for AKARI. *PASJ*, 59:S389.

Kessler, M. F., Steinz, J. A., Anderegg, M. E., Clavel, J., Drechsel, G., Estaria, P., Faelker, J., Riedinger, J. R., Robson, A., Taylor, B. G., and Ximénez de Ferrán, S. (1996). The Infrared Space Observatory (ISO) mission. *A&A*, 315:L27–L31.

Kiss, C., Ábrahám, P., Klaas, U., Lemke, D., Héraudeau, P., del Burgo, C., and Herbstmeier, U. (2003). Small-scale structure of the galactic cirrus emission. *A&A*, 399:177–185.

Kiss, C., Klaas, U., and Lemke, D. (2005). Determination of confusion noise for far-infrared measurements. *A&A*, 430:343–353.

Klaas, U. (2014). PACS Calibration Document Overview. *PACS-MA-LI-003*, Issue 1.10.

Klaas, U. (2016). A Herschel telescope background model for the PACS photometer. *PICC-MA-TN-013*, Issue 1.3.

Klaas, U., Ali, B., Altieri, B., Blommaert, J., Bouwman, J., and PACS ICC Cal. WG (2014). PACS Calibration Document. *PACS-MA-GS-001*, Issue 1.10.

Klaas, U., Balog, Z., Nielbock, M., Müller, T., Linz, H., and Kiss, C. (2017). *Herschel*-PACS photometry of faint stars for sensitivity performance assessment and establishment of faint FIR primary photometric standards. *A&A*, submitted.

Klaas, U. and Linz, H. (2016). Noise characterization of high-pass filtered PACS photometer mini-maps. *PICC-MA-TN-014*, Issue 1.0.

Klaas, U. and Linz, H. (2017). Noise characterization of PACS mini-maps processed with JScanam. *PICC-MA-TN-015*, Issue 0.2.

Klaas, U. and Nielbock, M. (2014a). PACS Performance Verification Phase Plan. *PICC-MA-PL-001*, Issue 2.0.

Klaas, U. and Nielbock, M. (2014b). PACS Routine Science Phase Plan. *PICC-MA-PL-002*, Issue 4.01.

Krause, O., Lemke, D., Hofferbert, R., Böhm, A., Klaas, U., Katzer, J., Höller, F., and Salvasohn, M. (2006). The cold focal plane chopper of HERSCHEL's PACS instrument. In *Society of Photo-Optical Instrumentation Engineers (SPIE) Conference Series*, volume 6273 of *Proc. SPIE*, page 627325.

Lagerros, J. S. V. (1996). Thermal physics of asteroids. I. Effects of shape, heat conduction and beaming. *A&A*, 310:1011–1020.

Lagerros, J. S. V. (1997). Thermal physics of asteroids. III. Irregular shapes and albedo variegations. *A&A*, 325:1226–1236.

Lagerros, J. S. V. (1998). Thermal physics of asteroids. IV. Thermal infrared beaming. *A&A*, 332:1123–1132.

Laureijs, R. J., Klaas, U., Richards, P. J., Schulz, B., and Abraham, P. (2003). *The ISO Handbook, Volume IV - PHT - The Imaging Photo-Polarimeter*.

Lindal, G. F. (1992). The atmosphere of Neptune - an analysis of radio occultation data acquired with Voyager 2. *AJ*, 103:967–982.

Looney, L. W., Raab, W., Poglitsch, A., Geis, N., Rosenthal, D., Hoenle, R., Klein, R., Fumi, F., Genzel, R., and Henning, T. (2003). FIFI LS: a far-infared 3D spectral imager for SOFIA. In Melugin, R. K. and Roeser, H.-P., editors, *Airborne Telescope Systems II*, volume 4857 of *Proc. SPIE*, pages 47–55.

Lutz, D. (2015). PACS photometer point spread function. *PICC-ME-TN-033*, Issue 2.2.

Lutz, D. and Contursi, A. (2013). PACS spatial calibration files. *PICC-ME-TN-019*, Issue 1.0.

Lutz, D. and Feuchtgruber, H. (2013). In-orbit rederivation of PACS photometer FOV distortion. *PICC-ME-TN-044*, Issue 1.0.

Meisner, A. M. and Finkbeiner, D. P. (2015). Modeling Thermal Dust Emission with Two Components: Application to the Planck High Frequency Instrument Maps. *ApJ*, 798:88.

Miville-Deschênes, M.-A. and Lagache, G. (2005). IRIS: A New Generation of IRAS Maps. *ApJ Supp.*, 157:302–323.

Miville-Deschênes, M.-A., Lagache, G., Boulanger, F., and Puget, J.-L. (2007). Statistical properties of dust far-infrared emission. *A&A*, 469:595–605.

Miville-Deschênes, M.-A., Martin, P. G., Abergel, A., Bernard, J.-P., Boulanger, F., Lagache, G., Anderson, L. D., André, P., Arab, H., Baluteau, J.-P., Blagrave, K., Bontemps, S., Cohen, M., Compiegne, M., Cox, P., Dartois, E., Davis, G., Emery, R., Fulton, T., Gry, C., Habart, E., Huang, M., Joblin, C., Jones, S. C., Kirk, J., Lim, T., Madden, S., Makiwa, G., Menshchikov, A., Molinari, S., Moseley, H., Motte, F., Naylor, D. A., Okumura, K., Pinheiro Gonçalves, D., Polehampton, E., Rodón, J. A., Russeil, D., Saraceno, P., Schneider, N., Sidher, S., Spencer, L., Swinyard, B., Ward-Thompson, D., White, G. J., and Zavagno, A. (2010). Herschel-SPIRE observations of the Polaris flare: Structure of the diffuse interstellar medium at the sub-parsec scale. *A&A*, 518:L104.

Moór, A., Müller, T. G., Kiss, C., Balog, Z., Billot, N., and Marton, G. (2014). PACS photometer calibration block analysis. *Experimental Astronomy*, 37:225–238.

Moreno, R. (2012). Neptune and Uranus planetry brightness temperature tabulation. *Tech. rep., ESA Herschel Science Centre*, available from ftp://ftp.sciops.esa.int/pub/hsc-calibration/PlanetrayModels/ESA4/.

Moreno, R., Gurwell, M. A., Moullet, A., and Lellouch, E. (2008). The mm/submm spectrum of Galilean satellites. In *AAS/Division for Planetary Sciences Meeting Abstracts #40*, volume 40 of *Bulletin of the American Astronomical Society*, page 478.

Moreno, R., Lellouch, E., Lara, L. M., Feuchtgruber, H., Rengel, M., Hartogh, P., and Courtin, R. (2012). The abundance, vertical distribution and origin of H_2O in Titan's atmosphere: Herschel observations and photochemical modelling. *Icarus*, 221:753–767.

Moshir, M., Copan, G., Conrow, T., McCallon, H., Hacking, P., Gregorich, D., Rohrbach, G., Melnyk, M., Rice, W., Fullmer, L., and Chester, T. J. (1993). IRAS Faint Source Catalog, $|b| > 10$, Version 2.0. *VizieR IRAS FSC Online Data Catalog*.

Mueller, T. G. and Lagerros, J. S. V. (1998). Asteroids as far-infrared photometric standards for ISOPHOT. *A&A*, 338:340–352.

Müller, T., Balog, Z., Nielbock, M., Lim, T., Teyssier, D., Olberg, M., Klaas, U., Linz, H., Altieri, B., Pearson, C., Bendo, G., and Vilenius, E. (2014). Herschel celestial calibration sources. Four large main-belt asteroids as prime flux calibrators for the far-IR/sub-mm range. *Experimental Astronomy*, 37:253–330.

Müller, T., Okumura, K., and Klaas, U. (2011). PACS photometer passbands and colour correction factors for various source SEDs. *PICC-ME-TN-038*, Issue 1.0.

Müller, T. G., Balog, Z., Nielbock, M., Moreno, R., Klaas, U., Moór, A., Linz, H., and Feuchtgruber, H. (2016). Far-infrared photometric observations of the outer planets and satellites with Herschel-PACS. *A&A*, 588:A109.

Müller, T. G., Herschel Calibration Steering Group, and ASTRO-F Calibration Team (2005). The Asteroid Preparatory Programme for HERSCHEL, ASTRO-F & ALMA. In Wilson, A., editor, *ESA Special Publication*, volume 577 of *ESA Special Publication*, pages 471–472.

Murakami, H., Baba, H., Barthel, P., Clements, D. L., Cohen, M., Doi, Y., Enya, K., Figueredo, E., Fujishiro, N., Fujiwara, H., Fujiwara, M., Garcia-Lario, P., Goto, T., Hasegawa, S., Hibi, Y., Hirao, T., Hiromoto, N., Hong, S. S., Imai, K., Ishigaki, M., Ishiguro, M., Ishihara, D., Ita, Y., Jeong, W.-S., Jeong, K. S., Kaneda, H., Kataza, H., Kawada, M., Kawai, T., Kawamura, A., Kessler, M. F., Kester, D., Kii, T., Kim, D. C., Kim, W., Kobayashi, H., Koo, B. C., Kwon, S. M., Lee, H. M., Lorente, R., Makiuti, S., Matsuhara, H., Matsumoto, T., Matsuo, H., Matsuura, S., Müller, T. G., Murakami, N., Nagata, H., Nakagawa, T., Naoi, T., Narita, M., Noda, M., Oh, S. H., Ohnishi, A., Ohyama, Y., Okada, Y., Okuda, H., Oliver, S., Onaka, T., Ootsubo, T., Oyabu, S., Pak, S., Park, Y.-S., Pearson, C. P., Rowan-Robinson, M., Saito, T., Sakon, I., Salama, A., Sato, S., Savage, R. S., Serjeant, S., Shibai, H., Shirahata, M., Sohn, J., Suzuki, T., Takagi, T., Takahashi, H., Tanabé, T., Takeuchi, T. T., Takita, S., Thomson, M., Uemizu, K., Ueno, M., Usui, F., Verdugo, E., Wada, T., Wang, L., Watabe, T., Watarai, H., White, G. J., Yamamura, I., Yamauchi, C., and Yasuda, A. (2007). The Infrared Astronomical Mission AKARI. *PASJ*, 59:S369.

Nielbock, M. and Klaas, U. (2013). Zero magnitude conversion for the PACS Photometer. *PICC-MA-TN-011*, issue 1.0.

Nielbock, M., Klaas, U., and Bouwman, J. (2009). Analysis of Nominal He-II Open Loop Functional Tests of the PACS FM1 Chopper during the Commissioning Phase. *PICC-MA-TR-088*, Version 1.1.

Nielbock, M., Klaas, U., Bouwman, J., Dannerbauer, H., and Schreiber, J. (2007). Angular Calibration and Zero Point Offset Determination of PACS FM1 Chopper for cold He II (T = 4.2 K) conditions PCD req. 2.3.1. *PICC-MA-TR-021*, Version 2.4.

Nielbock, M., Müller, T., Klaas, U., Altieri, B., Balog, Z., Billot, N., Linz, H., Okumura, K., Sánchez-Portal, M., and Sauvage, M. (2013). The Herschel PACS photometer calibration. A time dependent flux calibration for the PACS chopped point-source photometry AOT mode. *Experimental Astronomy*, 36:631–660.

Oke, J. B. and Gunn, J. E. (1983). Secondary standard stars for absolute spectrophotometry. *ApJ*, 266:713–717.

Okumura, K. (2010). Faint linear artefact in PACS photometer. *SAp-PACS-KO-0716-10*, Issue 1.0.

Okumura, K. and Klaas, U. (2016). PACS photometer flat-field measurement. *SAp-PACS-KO-0735*, Issue 2.0.

Orton, G. S., Fletcher, L. N., Moses, J. I., Mainzer, A. K., Hines, D., Hammel, H. B., Martin-Torres, F. J., Burgdorf, M., Merlet, C., and Line, M. R. (2014). Mid-infrared spectroscopy of Uranus from the Spitzer Infrared Spectrometer: 1. Determination of the mean temperature structure of the upper troposphere and stratosphere. *Icarus*, 243:494–513.

Ottensamer, R. (2009). *Intelligent detectors: Data processing of n-dimensional detector arrays*. PhD thesis, University of Vienna.

Ottensamer, R., Belbachir, A. N., Bischof, H., Feuchtgruber, H., Kerschbaum, F., Poglitsch, A., and Reimers, C. (2004). Herschel/PACS on-board reduction/compression software implementation. In Mather, J. C., editor, *Optical, Infrared, and Millimeter Space Telescopes*, volume 5487 of *Proc. SPIE*, pages 481–490.

Ottensamer, R. and Kerschbaum, F. (2008). HERSCHEL/PACS on-board reduction flight software. In *Advanced Software and Control for Astronomy II*, volume 7019 of *Proc. SPIE*, page 70191B.

Pearl, J. C. and Conrath, B. J. (1991). The albedo, effective temperature, and energy balance of Neptune, as determined from Voyager data. *Journal of Geophysical Research Supplement*, 96:18.

Pearl, J. C., Conrath, B. J., Hanel, R. A., and Pirraglia, J. A. (1990). The albedo, effective temperature, and energy balance of Uranus, as determined from Voyager IRIS data. *Icarus*, 84:12–28.

Pezzuto, S., Ottensamer, R., Mazy, A., Feuchtgruber, H., Di Giorgio, A. M., Vandenbussche, B., Benedettini, M., Liu, S. J., Molinari, S., and Schito, D. (2012). The on-board software of the HERSCHEL/PACS instrument: three successful years of in-flight operations. In *Observatory Operations: Strategies, Processes, and Systems IV*, volume 8448 of *Proc. SPIE*, page 844823.

Piazzo, L., Calzoletti, L., Faustini, F., Pestalozzi, M., Pezzuto, S., Elia, D., di Giorgio, A., and Molinari, S. (2015). UNIMAP: a generalized least-squares map maker for Herschel data. *MNRAS*, 447:1471–1483.

Pilbratt, G. L., Riedinger, J. R., Passvogel, T., Crone, G., Doyle, D., Gageur, U., Heras, A. M., Jewell, C., Metcalfe, L., Ott, S., and Schmidt, M. (2010). Herschel Space Observatory. An ESA facility for far-infrared and submillimetre astronomy. *A&A*, 518:L1.

Planck Collaboration, Abergel, A., Ade, P. A. R., Aghanim, N., Alves, M. I. R., Aniano, G., Armitage-Caplan, C., Arnaud, M., Ashdown, M., Atrio-Barandela, F., and et al. (2014). Planck 2013 results. XI. All-sky model of thermal dust emission. *A&A*, 571:A11.

Planck Collaboration, Adam, R., Ade, P. A. R., Aghanim, N., Arnaud, M., Ashdown, M., Aumont, J., Baccigalupi, C., Banday, A. J., Barreiro, R. B., and et al. (2016a). Planck 2015 results. VIII. High Frequency Instrument data processing: Calibration and maps. *A&A*, 594:A8.

Planck Collaboration, Ade, P. A. R., Aghanim, N., Alves, M. I. R., Aniano, G., Arnaud, M., Ashdown, M., Aumont, J., and et al. (2016b). Planck intermediate results. XXIX. All-sky dust modelling with Planck, IRAS, and WISE observations. *A&A*, 586:A132.

Plez, B., Brett, J. M., and Nordlund, A. (1992). Spherical opacity sampling model atmospheres for M-giants. I - Techniques, data and discussion. *A&A*, 256:551–571.

Poglitsch, A., Waelkens, C., Geis, N., Feuchtgruber, H., Vandenbussche, B., Rodriguez, L., Krause, O., Renotte, E., van Hoof, C., Saraceno, P., Cepa, J., Kerschbaum, F., Agnèse, P., Ali, B., Altieri, B., Andreani, P., Augueres, J.-L., Balog, Z., Barl, L., Bauer, O. H., Belbachir, N., Benedettini, M., Billot, N., Boulade, O., Bischof, H., Blommaert, J., Callut, E., Cara, C., Cerulli, R., Cesarsky, D., Contursi, A., Creten, Y., De Meester, W., Doublier, V., Doumayrou, E., Duband, L., Exter, K., Genzel, R., Gillis, J.-M., Grözinger, U., Henning, T., Herreros, J., Huygen, R., Inguscio, M., Jakob, G., Jamar, C., Jean, C., de Jong, J., Katterloher, R., Kiss, C., Klaas, U., Lemke, D., Lutz, D., Madden, S., Marquet, B., Martignac, J., Mazy, A., Merken, P., Montfort, F., Morbidelli, L., Müller, T., Nielbock, M., Okumura, K., Orfei, R., Ottensamer, R., Pezzuto, S., Popesso, P., Putzeys, J., Regibo, S., Reveret, V., Royer, P., Sauvage, M., Schreiber, J., Stegmaier, J., Schmitt, D., Schubert, J., Sturm, E., Thiel, M., Tofani, G., Vavrek, R., Wetzstein, M., Wieprecht, E., and Wiezorrek, E. (2010). The Photodetector Array Camera and Spectrometer (PACS) on the Herschel Space Observatory. *A&A*, 518:L2.

Popesso, D., Magnelli, B., Buttiglione, S., Lutz, , D., Poglitsch, A., Berta, S., Nordon, R., Altieri, B., Aussel, H., Billot, N., Gastaud, R., Ali, B., Balog, Z., Cava, A., Feuchtgruber, H., Gonzalez Garcia, B., Geis, N., Kiss, C., Klaas, U., Linz, H., Liu, X., Moor, A., Morin, B., Müller, T., Nielbock, M., Okumura, K., Osterhage, S., Ottenmsamer, R., Paladini, R., Pezzuto, S., Doublier Pritchard, V., Regibo, S., Rodighiero, G., Royer, P., Sauvage, M., Sturm, E., Wetzstein, M., Wieprecht, E., and Wiezorrek, E. (2012). The effect of the high-pass filter data reduction technique on the *Herschel* PACS photometer PSF and noise. *arXiv:12114257v1 [astro-ph.IM]*, Issue 1.0.

Price, S. D., Paxson, C., Engelke, C., and Murdock, T. L. (2004). Spectral Irradiance Calibration in the Infrared. XV. Absolute Calibration of Standard Stars by Experiments on the Midcourse Space Experiment. *AJ*, 128:889–910.

Regibo, S. (2012). *Data Reduction and Analysis Algorithms for the Herschel Space Observatory*. PhD thesis, Katholieke Universiteit Leuven Faculty of Science.

Rieke, G. H., Lebofsky, M. J., and Low, F. J. (1985). An absolute photometric system at 10 and 20 microns. *AJ*, 90:900–906.

Rieke, G. H., Young, E. T., Engelbracht, C. W., Kelly, D. M., Low, F. J., Haller, E. E., Beeman, J. W., Gordon, K. D., Stansberry, J. A., Misselt, K. A., Cadien, J., Morrison, J. E., Rivlis, G., Latter, W. B., Noriega-Crespo, A., Padgett, D. L., Stapelfeldt, K. R., Hines, D. C., Egami, E., Muzerolle, J., Alonso-Herrero, A., Blaylock, M., Dole, H., Hinz, J. L., Le Floc'h, E., Papovich, C., Pérez-González, P. G., Smith, P. S., Su, K. Y. L., Bennett, L., Frayer, D. T., Henderson, D., Lu, N., Masci, F., Pesenson, M., Rebull, L., Rho, J., Keene, J., Stolovy, S., Wachter, S., Wheaton, W., Werner, M. W., and Richards, P. L. (2004). The Multiband Imaging Photometer for Spitzer (MIPS). *ApJS*, 154:25–29.

Rosenthal, D., Beeman, J. W., Geis, N., Grözinger, U., Hönl, R., Katterloher, R. O., Kraft, S., Looney, L. W., Poglitsch, A., Raab, W., and Richter, H. (2002). Stressed Ge:Ga detector arrays for PACS and FIFI LS. In *Far-IR, Sub-mm & MM Detector Technology Workshop*, Proc. SPIE.

Roussel, H. (2013). Scanamorphos: A Map-making Software for Herschel and Similar Scanning Bolometer Arrays. *PASP*, 125:1126–1163.

Royer, P., Exter, K., Schrieber, J., and Bouwman, J. (2009). Herschel-PACS Commissioning Phase GeGa Optimisation. *PICC-KL-TR-023*, Issue 1.0.

Russell, E. E., Brown, F. G., Chandos, R. A., Fincher, W. C., Kubel, L. F., Lacis, A. A., and Travis, L. D. (1992). Galileo Photopolarimeter/Radiometer experiment. *Space Science Reviews*, 60:531–563.

Safarzadeh, M., Ferguson, H. C., Lu, Y., Inami, H., and Somerville, R. S. (2015). A Novel Technique to Improve Photometry in Confused Images Using Graphs and Bayesian Priors. *ApJ*, 798:91.

Sánchez-Portal, M., Marston, A., Altieri, B., Aussel, H., Feuchtgruber, H., Klaas, U., Linz, H., Lutz, D., Merín, B., Müller, T., Nielbock, M., Oort, M., Pilbratt, G., Schmidt, M., Stephenson, C., and Tuttlebee, M. (2014). The pointing system of the Herschel space observatory. Description, Calibration, Performance and improvements. *Experimental Astronomy*, 37:453–479.

Sauvage, M., Billot, N., and Okumura, K. (2008). Saturation limits for the PACS Photometer. *SAp-PACS-MS-0680-08*, Version 1.0.

Sauvage, M., Okumura, K., and Billot, N. (2009). Vrl-Vhblind calibration - Readout circuit transfer function calibratio. *SAp-PACS-MS-0705-09*, Version 1.2.

Sauvage, M., Okumura, K., Klaas, U., Müller, T., Moór, A., Poglitsch, A., Feuchtgruber, H., and Duband, L. (2014). Operations and performance of the PACS instrument ^{3}He sorption cooler on board of the Herschel space observatory. *Experimental Astronomy*, 37:397–431.

Selby, M. J., Hepburn, I., Blackwell, D. E., Booth, A. J., Haddock, D. J., Arribas, S., Leggett, S. K., and Mountain, C. M. (1988). Narrow band 1 micron-4 micron infrared photometry of 176 stars. *A&AS*, 74:127–132.

Simoens, F., Agnese, P., Béguin, A., Carcey, J., Cigna, J.-C., Pornin, J.-L., Rey, P., Vandeneynde, A., Rodriguez, L., Boulade, O., Lepennec, J., Martignac, J., Doumayrou, E., Reveret, V., and Vigroux, L. (2004). Submillimeter bolometers arrays for the PACS/Herschel spectro-photometer. In Bradford, C. M., Ade, P. A. R., Aguirre, J. E., Bock, J. J., Dragovan, M., Duband, L., Earle, L., Glenn, J., Matsuhara, H., Naylor, B. J., Nguyen, H. T., Yun, M., and Zmuidzinas, J., editors, *Z-Spec: a broadband millimeter-wave grating spectrometer: design, construction, and first cryogenic measurements*, volume 5498 of *Proc. SPIE*, pages 177–186.

Spencer, J. R. (1987). *The Surfaces of Europa, Ganymede, and Callisto: an Investigation Using Voyager IRIS Thermal Infrared Spectra*. PhD thesis, THE UNIVERSITY OF ARIZONA.

Spencer, J. R., Lebofsky, L. A., and Sykes, M. V. (1989). Systematic biases in radiometric diameter determinations. *Icarus*, 78:337–354.

Stansberry, J. A., Gordon, K. D., Bhattacharya, B., Engelbracht, C. W., Rieke, G. H., Marleau, F. R., Fadda, D., Frayer, D. T., Noriega-Crespo, A., Wachter, S., Young, E. T., Müller, T. G., Kelly, D. M., Blaylock, M., Henderson, D., Neugebauer, G., Beeman, J. W., and Haller, E. E. (2007). Absolute Calibration and Characterization of the Multiband Imaging Photometer for Spitzer. III. An Asteroid-based Calibration of MIPS at 160 μm. *PASP*, 119:1038–1051.

Takita, S., Doi, Y., Ootsubo, T., Arimatsu, K., Ikeda, N., Kawada, M., Kitamura, Y., Matsuura, S., Nakagawa, T., Hattori, M., Morishima, T., Tanaka, M., and Komugi, S. (2015). Calibration of the AKARI far-infrared all-sky survey maps. *PASJ*, 67:51.

Vinatier, S., Bézard, B., Nixon, C. A., Mamoutkine, A., Carlson, R. C., Jennings, D. E., Guandique, E. A., Teanby, N. A., Bjoraker, G. L., Michael Flasar, F., and Kunde, V. G. (2010). Analysis of Cassini/CIRS limb spectra of Titan acquired during the nominal mission. I. Hydrocarbons, nitriles and CO $_2$ vertical mixing ratio profiles. *Icarus*, 205:559–570.

Werner, M. W., Roellig, T. L., Low, F. J., Rieke, G. H., Rieke, M., Hoffmann, W. F., Young, E., Houck, J. R., Brandl, B., Fazio, G. G., Hora, J. L., Gehrz, R. D., Helou, G., Soifer, B. T., Stauffer, J., Keene, J., Eisenhardt, P., Gallagher, D., Gautier, T. N., Irace, W., Lawrence, C. R., Simmons, L., Van Cleve, J. E., Jura, M., Wright, E. L., and Cruikshank, D. P. (2004). The Spitzer Space Telescope Mission. *ApJS*, 154:1–9.

Wheelock, S. L., Gautier, T. N., Chillemi, J., Kester, D., McCallon, H., Oken, C., White, J., Gregorich, D., Boulanger, F., and Good, J. (1994). IRAS sky survey atlas: Explanatory supplement. *NASA STI/Recon Technical Report N*, 95.

List of Figures

List of Tables